Low-temperature thermochronometric constraints on
Cenozoic intraplate deformation in the central Basin and Range

By

Tandis S. Bidgoli

Submitted to the graduate degree program in Geology and the Graduate Faculty of the University of Kansas in partial fulfillment of the requirements for the degree of Doctor of Philosophy.

_____
Chairperson, Dr. J. Douglas Walker

_____
Co-Chairperson, Dr. Daniel F. Stockli

_____
Dr. Michael H. Taylor

_____
Dr. Andreas Moeller

_____
Dr. Leigh Stearns

_____
Dr. Stephen Egbert

Date Defended: April 28, 2014

The Dissertation Committee for Tandis S. Bidgoli

certifies that this is the approved version of the following dissertation:

Low-temperature thermochronometric constraints on

Cenozoic intraplate deformation in the central Basin and Range

_____

Chairperson, Dr. J. Douglas Walker

_____

Co-Chairperson, Dr. Daniel F. Stockli

Date approved: April 28, 2014

ABSTRACT

The current form of the Pacific-North American plate boundary is the result of a complex evolution from a subduction zone to a transform boundary. Changes in the kinematics and dynamics of the plate boundary have predictable consequences for deformation within the central Basin and Range (CBR). However, uncertainties in the timing, magnitude, and spatial distribution of extension and later transtension have made reconstructions of Cenozoic intraplate deformation difficult. This study investigates the Cenozoic history of the CBR through a province-wide (U-Th)/He thermochronologic study of 16 fault-bounded ranges. Thermochronologic data are integrated with published geologic and structural data in order to determine a detailed history of extensional deformation in the region, and the timing and spatial progression of the transition to transtensional deformation. These data are used to address two main questions. (1) How closely in time do the structural style and fault kinematics of intraplate deformation match changes in plate motion? (2) If the timing is very different, either locally or regionally, are there other dynamic processes that must be considered during the Cenozoic tectonic evolution of the western U.S.?

These questions are addressed in this dissertation by results presented in 5 chapters. Chapter 1 provides an introduction and the plate tectonic setting. Chapter 2 focuses on the timing of onset, magnitude of exhumation, and spatial distribution of strain associated with the Castle Cliffs, Tule Springs, and Mormon Peak detachments, three significant low-angle normal faults in the eastern part of the CBR. Chapter 3 evaluates the middle Miocene to recent exhumation history of the Slate Range, located in the southwestern part of the CBR. Chapter 4 uses low- to moderate-temperature thermochronology data to evaluate space-time patterns of Miocene to Pliocene strain within the Death Valley area and the geodynamic drivers of that

deformation. Chapter 5 focuses on evidence and possible mechanisms for Late Cretaceous to early Cenozoic cooling over a large portion of the western CBR.

Zircon and apatite (U-Th)/He cooling ages from this study suggest that Basin and Range extension initiated at the eastern edge of the CBR at ~18 Ma and migrated westward with time. Extension in the western part of the CBR is overprinted by distinctly younger episodes of cooling that signal the onset of transtension associated with the development of the eastern California shear zone. For areas west of Death Valley, the initiation of dextral transtension occurs simultaneously at 3-4 Ma, matching the inferred timing of lithospheric delamination in the central and southern Sierras. The results suggest that the Cenozoic pattern of strain reflects a progression from plate boundary kinematics to intraplate drivers like lithospheric delamination.

This study also sheds light on the development of the Nevadaplano, a broad plateau in the hinterland of the Late Cretaceous to early Cenozoic Sevier retroarc fold-thrust belt. The new (U-Th)/He ages, combined with published thermochronology data, show that there are two distinct periods of pre-Miocene cooling that affect the western CBR and Mojave Desert. The first is a Late Cretaceous cooling event that may be related to widespread extension, crustal refrigeration, and/or erosion associated with Laramide flat-slab subduction. The second event corresponds to a pulse of exhumation during the Eocene that may be related to rapid erosion following major shifts in global climate. Collectively, the data suggest the rapid tectonic exhumation of the Nevadaplano occurred in the latest Cretaceous, whereas erosional beveling and stabilization of the plateau was dominantly an early to middle Eocene phenomenon related to a changing climate.

ACKNOWLEDGEMENTS

This research was supported by grants from the Geothermal Program Office of the U.S. Department of the Navy, China Lake; the National Science Foundation, EarthScope Program; the Geological Society of America; the American Association of Petroleum Geologists; the International Union of Geological Sciences; and the University of Kansas, Doctoral Student Research Fund. The University of Kansas, Department of Geology also provided funding through a Patterson Fellowship, Encana Energy Scholarship, Ernest E. Angino Geochemistry Scholarship, Phillips Petroleum Scholarship, and D.A. McGee Geology Scholarship.

I would like to acknowledge several people who were gracious enough to share samples, data, and other information that were critical to a more complete understanding of the geology of the central Basin and Range. They include Michael Giallorenzo from the University of Nevada – Las Vegas for sharing samples from the Resting Springs and Nopah ranges, and for sharing data and interpretations from the Spring Mountains; Erika Amir and John Caskey from San Francisco State University for sharing their data from the Black Mountains; and Chris Hager for sharing his thermal modeling software and related text.

Special thanks are in order for a number of people who assisted me in the field and/or laboratory over the course of my dissertation. I am grateful to Chad La Fever, Joseph Andrew, John Caskey, Sarah Evans, Kurt Sundell, Steve Alm, Gabriel Creason, Rachelle Warren, and Ted Morehouse for assistance with sample collection. Thank you for sacrificing your backs to carry my rocks. Jessica Savage, Matthew Meyers, Andrew Vohs, Ted Morehouse, and Ty Tenpenny processed many samples on my behalf. I appreciate all the long hours spent at the water table and Frantz, and under the fume hood. And last, but definitely not least, Roman Kislitsyn, for

guidance and support with sample preparation and analysis, for making sure my samples got analyzed in a timely manner, and for always making the lab a very enjoyable place to work.

I would like express my gratitude to Doug Walker for being a wonderful advisor over the last 4+ years. You have been a fantastic role model and mentor, and I have learned so much from you. I am indebted to Daniel Stockli for teaching me much of what I know about (U-Th)/He dating and for always accommodating me and my samples into his very busy lab. I would also like to acknowledge my committee members, Andreas Moeller, Michael Taylor, Leigh Stearns, and Stephen Egbert for their time, help, and support.

Finally, I would like to acknowledge my family and friends for their love and support. In particular, my daughter, Sonia La Fever, whose smiles and giggles are the brightest part of each day. You keep me motivated to be the best version of myself. And a very special thank you to my husband, Chad La Fever, who is my best friend, my biggest cheerleader, and the most outstanding field assistant I could ever ask for. I would be lost without you.

TABLE OF CONTENTS

LIST OF FIGURES

LIST OF TABLES

CHAPTER 1

INTRODUCTION

Background contents of the dissertation

The Pacific-North American plate boundary is best characterized as diffuse, with relative plate motion accommodated across a broad zone of variable-style deformation (Figure 1.1; Minster and Jordan, 1987; Dokka and Travis, 1990; Bennett et al., 2003). Although most of the plate boundary strain is focused on the San Andreas transform fault, ~25% of it is accommodated by right-lateral strike- and oblique-slip faults of the eastern California shear zone (ECSZ) and Walker Lane east of the Sierra Nevada, which currently account for 9-12 mm/yr of relative plate motion (Figure 1.1; Dokka and Travis, 1990; Dixon et al., 1995, 2000; Bennett et al., 2003;). An additional 2-3 mm/yr is accommodated by normal faults within the eastern part of the Basin and Range (Figure 1.1; Dixon et al., 1995; Bennett et al., 2003).

The current form of the Pacific-North American plate boundary is the result of a complex evolution that is well documented by plate circuit reconstructions of the Pacific plate relative to North America (Figure 1.2; Atwater, 1970; Atwater and Stock, 1998). Several important events are suggested by the reconstructions for the middle to late Cenozoic, including: (1) the change from a convergent to transform margin when the Pacific-Farallon ridge reaches the North-American plate at ~30 Ma; (2) a period of highly oblique motion between the Pacific and North American plates from ~16 to 8 Ma; and (3) a change from oblique motion to dominantly coast-parallel motion at ~8 Ma (Figure 2; Atwater and Stock, 1998). Although our understanding of the nature of the far-field kinematics is robust, the complex intraplate deformation within North America, such as development of the extensional Basin and Range province and subsequent

dominantly transcurrent Eastern California shear zone and Walker Lane belt, has been more difficult to reconcile with the far-field information.

A key region for studying intraplate deformation associated with the evolving Pacific-North American plate boundary is the central Basin and Range province (*sensu* Wernicke, 1992) (Figures 1.1). The relatively simple Paleozoic passive margin succession and the abundance of Mesozoic structural markers make the central Basin and Range an ideal area for deciphering intraplate deformation (e.g., Wernicke et al., 1988; Wernicke and Snow, 1998; Snow and Wernicke, 2000; McQuarrie and Wernicke, 2005). To date, research has focused primarily on palinspastic reconstructions that have become increasingly sophisticated; however, gaps in and inconsistencies between models (e.g., compare large differences between McQuarrie and Wernicke, 2005; Serpa and Pavlis, 1996; Snow and Wernicke, 2000; Andrew and Walker, 2009) show that there are important uncertainties in the timing, magnitude, and spatial pattern of strain.

One of the principal challenges in reconstructing ranges is determining robust and appropriate timing constraints on the motion of bounding faults. Most of the reconstructions rely on restorations of features or structures that are significantly older than the extensional and transtensional faults that overprint them (e.g., Stewart, 1983; Prave and Wright, 1986; Snow and Wernicke, 1989; Snow and Wernicke, 2000). The restored positions of many of these strain markers are also debated (e.g., Stewart, 1983 vs. Prave and Wright, 1986; Stevens et al., 1992 vs. Snow and Wernicke, 1989). Similarly, reconstructions using chronostratigraphic constraints have also been hampered by limited or incomplete exposures of Miocene to Pliocene strata, a lack of datable material, and "openness" for interpretation of the depositional setting (e.g., Snow and Lux, 1999; Niemi et al., 2001; Renik et al., 2008). These issues are compounded by the fact

that many of the faults in question were active during Basin and Range deformation and subsequently either abandoned or transitioned into or reactivated during later transcurrent strain.

In contrast to the above approaches, it is my opinion that thermochronologic methods, although widely applied, are still under-utilized in the central Basin and Range, and that more densely spaced data collection can yield a critical and independent dataset from those described above. Thermochronology determines ages that can be linked to specific temperatures and thus can be used to reconstruct the time-temperature history of a mountain range. When integrated with structural and stratigraphic data, these methods can capture information about a diverse range of tectonic and geomorphic processes (e.g., timing, magnitude, and rate of faulting; geothermal gradients; degree of tilting or rotation of crustal blocks; erosion magnitudes and rates; see summaries in Ehlers, 2005; Spotila, 2005; Stockli, 2005). In the central Basin and Range, thermochronologic methods have been applied to mostly the eastern region, in the Virgin Mountains (Fitzgerald et al., 1991, 2009; Reiners et al., 2000; Reiners, 2005; Quigley et al. 2010), northern White Hills (Fitzgerald et al., 2003, 2009), Lost Basin Range (Fitzgerald et al., 2009), southern McCullough Range (Mahan et al., 2009), the Funeral Mountains (Holm and Dokka, 1991; Hoisch and Simpson, 1993; Beyene, 2011), and the Black Mountains (Figure 3; Holm and Wernicke, 1990; Holm et al., 1992; Holm and Dokka, 1993). Where applied, this method has provided critical constraints on fault-related exhumation histories, even for fault blocks with multiple exhumation histories.

This dissertation presents the results of a comprehensive (U-Th)/He thermochronologic study of 16 fault-bounded ranges between the Sierra Nevada and Colorado Plateau (Figure 1.3) and adds greatly to our understanding of Cenozoic deformation within the central Basin and Range. The new thermochronometric data are integrated with published structural and

stratigraphic data to determine a more detailed history of extension and the transition to transtensional deformation.

The results are used to address two main questions. (1) How closely in time do the structural style and fault kinematics of intraplate deformation match changes in plate motion? (2) If the timing is very different, either locally or regionally, are there other dynamic processes that must be considered during the Cenozoic tectonic evolution of the western Cordillera? These questions are addressed in the dissertation by results presented in 4 chapters. These chapters cover the scale of observed complex faulting in a single range to the development of different zones of the region, to regional patterns of cooling that have not been and may not be able to be linked to individual structures but rather to larger scale lithospheric development.

Chapter 2 focuses on the timing of onset, magnitude of exhumation, and spatial distribution of strain associated with the Castle Cliffs, Tule Springs, and Mormon Peak detachments, three significant low-angle normal faults in the eastern part of the central Basin and Range (Figure 1.3). The primary dip of these faults, either low or high angle, is vigorously debated, as are both the origin of the structures and the magnitude of extension across them (e.g., Walker et al., 2007; Christie-Blick et al., 2007; Axen et al., 1990). In this chapter, I present new (U-Th)/He thermochronologic data from the footwalls of all of these detachments. The data suggest that extension initiated at 18 Ma, 2 m.y. earlier than previously estimated, and migrated westward with time. In addition to better bracketing the onset of extension and footwall cooling, the thermochronology results can be used to infer the magnitude of extension, providing an independent test of published geological cross-sections (e.g., Axen et al., 1990). The results indicate that previously determined extension estimates for the detachments may be too high (40 km for this study versus 54 km for previous ones – e.g., Wernicke et al., 1985; Wernicke et al,,

1988; Axen et al., 1990; Axen, 1993). That said, the protracted cooling history, magnitude of exhumation, and pattern of cooling ages provide compelling evidence for a low-angle normal fault origin for these structures.

Chapter 3 is a manuscript, already published in the Geological Society of America journal *Geosphere*, which evaluates the middle Miocene to recent exhumation history of the Slate Range (SR on Figure 1.3). The Slate Range, located in the southwestern part of the central Basin and Range, lies in a region that has experienced both Miocene Basin and Range extension, and Pliocene to recent transtension related to ECSZ. In this paper, structural interpretations are tied to three thermochronology transects across the range. Paleodepth reconstructions of apatite and zircon (U-Th) ages demonstrate two discrete periods of cooling. Middle Miocene cooling is linked to the west-directed extension along the Slate Range detachment, while rapid cooling in the Pliocene is best explained by exhumation along the cross-cutting Searles Valley fault system, part of a younger transtensional fault system. This work, when placed into the context of regional fault timing data, is a key datum for interpreting that the initiation of transtensional deformation occurs as a westward migrating wave that is not easily related to changes in plate boundary kinematics. This is critical to answering the first of the questions posed above.

Chapter 4 uses low- to moderate-temperature thermochronology data to evaluate space-time patterns of Miocene to Pliocene strain within the Death Valley area (Figure 1.3). In this chapter, new apatite and zircon (U-Th)/He ages obtained from the footwalls of detachments in the Black and Panamint mountains are integrated with published structural and stratigraphic data to show that, much like the Slate Range (Chapter 3), Miocene extension in the Death Valley area is overprinted by distinctly younger episodes of transtension. I show that transtension initiates north and east of Black Mountains at ~11-8 Ma, coincident with the timing of major changes in

plate boundary relative motion, and then migrates westward into Death Valley at ~6 Ma. In contrast, data from the Panamint Range and several ranges west of Death Valley suggest that the initiation of dextral transtension occurs simultaneously over a large area at 3-4 Ma, matching the inferred timing of lithospheric delamination in the central and southern Sierra Nevada (e.g., Farmer et al., 2002). The results suggest that the Cenozoic pattern of strain reflects a progression from plate boundary kinematics to intraplate drivers like lithospheric delamination. This chapter thus answers question 1 and proposes a mechanism to question 2.

Chapter 5 focuses on evidence and mechanisms for Late Cretaceous to early Cenozoic cooling over a large portion of the study area. New cooling ages from the Lava Mountains, Argus Range, Spring Mountains, Clark Mountains, and Lucy Gray Range are combined with a published (U-Th)/He, fission-track, $^{40}Ar/^{39}Ar$, and K/Ar ages from the Sierra Nevada, western Basin and Range, and Mojave Desert to show that there are two distinct periods of cooling that affect this geographically broad region. The first is a Late Cretaceous cooling event that may be related to widespread crustal refrigeration (e.g., Dumitru, 1991), low-angle normal faulting (Wells et al., 2008 and references therein), and/or erosion associated with Laramide flat-slab subduction. The second event corresponds to a pulse of rapid cooling during the Eocene. This Eocene cooling is problematic because there are no known structures of that age, suggesting the region was tectonically quiescent at that time. Instead, it appears that this cooling may be related to rapid erosion that follows prominent climatic anomalies. To strengthen this hypothesis, I link the thermal signature of this denudation event to the climate record and to the terrestrial and marine sedimentary record.

References cited

Andrew, J.E., and Walker, J.D., 2009, Reconstructing Cenozoic deformation in the Panamint Valley region, eastern California, with implications for timing and magnitude of faulting in parts of the Central Basin and Range: Geosphere, v. 5, p. 172–198.

Atwater, T., 1970, Implications of plate tectonics for the Cenozoic tectonic evolution of western North America: Bulletin of the Geological Society of America, v. 81, p. 3513–3536.

Atwater, T., and Stock, J., 1998, Pacific-North America plate tectonics of the Neogene southwestern United States: An update: International Geological Review, v. 40, p. 375–402.

Axen, G.J., 1993, Ramp-flat detachment faulting and low-angle normal reactivation of the Tule Springs thrust, southern Nevada: Geological Society of America Bulleting, v. 105, p. 1076-1090.

Axen, G.J., Wernicke, B.P., Skelly, M.F., Taylor, W.J., 1990, Mesozoic and Cenozoic tectonics of the Sevier thrust belt in the Virgin River Valley area, southern Nevada, in Wernicke, B.P., ed., Basin and Range Extensional Tectonics at the Latitude of Las Vegas, Nevada,: Geological Society of America Memoir 176, p. 123-153.

Bennett, R.A., Wernicke, B.P., Niemi, N.A., Friedrich, A.M., and Davis, J.L., 2003, Contemporary strain rates in the northern Basin and Range province from GPS data: Tectonics, v. 22, p. 1008.

Beyene, M., 2011, Mesozoic burial, and Mesozoic and Cenozoic exhumation of the Funeral Mountains core complex, Death Valley, southeastern California [Ph.D. thesis]: Las Vegas, University of Nevada, 362 p.

Christie-Blick, N., Anders, M.H., Wills, S., Walker, C.D., and Renik, B., 2007, Observations from the Basin and Range Province (western United States) pertinent to the interpretation of regional detachment faults, in Karner G.D., Manatschal, G., and Pinheiro, L.M., eds.,: Imaging, Mapping and Modeling Continental Lithosphere Extension and Breakup, Geological Society of London Special Publication 282, p. 421 – 481.

Dixon, T.H., Robaudo, S., Lee, J., and Reheis, M.C., 1995, Constraints on present-day Basin and Range deformation from space geodesy: Tectonics, v. 14, p. 755–772.

Dokka, R.K., and Travis, C.J., 1990, Role of the eastern California shear zone in accommodating Pacific-North American plate motion: Geophysical Research Letters, v. 17, p. 1323–1326.

Dumitru, T.A., Gans, P.B., Foster, D.A., and Miller, E.L., 1991, Refrigeration of the western Cordilleran lithosphere during Laramide shallow-angle subduction: Geology, v. 19, p. 1145-1148.

Farmer, G.L., Glazner, A.F., and Manley, C.R., 2002, Did lithospheric delamination trigger late Cenozoic potassic volcanism in the southern Sierra Nevada, California?: Geological Society of America Bulletin, v. 114, p. 754–768.

Fitzgerald, P.G., Fryxell, J.E., and Wernicke, B.P., 1991, Miocene crustal extension and uplift in southeastern Nevada: Constraints from apatite fission track analysis: Geology, v. 19, p. 1013-1016.

Fitzgerald, P.G., O'Sullivan, P.B., Duebendorfer, E.M., Faulds, J.E., and Fryxell, J.E., 2003, Thermochronologic constraints on extension via detachment faulting in the White Hills of NW Arizona and Gold Butte Block of SE Nevada: Geological Society of America Abstracts with programs, v. 35, p. 348.

Fitzgerald, P.G., Duebendorfer, E.M. Faulds, J.E and O'Sullivan, P., 2009, South Virgin–White Hills detachment fault system of SE Nevada and NW Arizona: Applying apatite fission track thermochronology to constrain the tectonic evolution of a major continental detachment fault: Tectonics, v. 28, p. TC2001, doi:10.1029/2007TC002194.

Holm, D.K., and Dokka, R.K., 1991, Major late Miocene cooling of the middle crust associated with extensional orogenesis in the Funeral Mountains, California, Geophysical Research Letters, v. 18, p. 1775–1778.

Holm, D. K., and Dokka, R.K., 1993, Interpretation and tectonic implications of cooling histories: An example from the Black Mountains, Death Valley extended terrane, California: Earth and Planetary Science Letters, v. 116, p. 63–80.

Holm, D.K., and Wernicke, B., 1990, Black Mountains crustal section, Death Valley extended terrain, California: Geology, v. 18, p. 520–523.

Holm, D.K., Snow, J.K., and Lux, D.R., 1992, Thermal and barometric constraints on the intrusive and unroofing history of the Black Mountains—Implications for timing, initial dip, and kinematics of detachment faulting in the Death Valley region, California: Tectonics, v. 11, p. 507–522.

Hoisch, T.D., and Simpson, C., 1993, Rise and tilt of metamorphic rocks in the lower plate of a detachment fault in the Funeral Mountains, Death Valley, California: Journal of Geophysical Research, v. 98, p. 6805-6827.

Liu, M., Wang, H., and Li, Q., 2010, Inception of the eastern California shear zone and evolution of the Pacific-North American plate boundary: From kinematics to geodynamics: Journal of Geophysical Research, v. 115, doi:10.1029/2009JB007055.

Mahan, K.H., Guest, B., Wernicke, B., and Niemi, N.A., 2009, Low-temperature thermochronologic constraints on the kinematic history and spatial extent of the Eastern California shear zone. Geosphere, v. 5, p. 1–13.

McQuarrie, N., and Wernicke, B.P., 2005, An animated tectonic reconstruction of southwestern North America since 36 Ma: Geosphere, v. 1, p. 147–172.

Minster, J.B., and Jordan, T.H., 1987, Vector constraints on Western US deformation from space geodesy, neotectonics, and plate motions: Journal of Geophysical Research, v. 92, p. 4798–4804.

Niemi, N.A., Wernicke, B.P., Brady, R.J., Saleeby, J.B., and Dunne, G.C., 2001, Distribution and provenance of the middle Miocene Eagle Mountain Formation, and implications for regional kinematic analysis of the Basin and Range province: Geological Society of America, Bulletin, v. 113, p. 419-442.

Prave, A.R., and Wright, L.A., 1986a, Isopach pattern of the Lower Cambrian Zabriskie Quartzite, Death Valley region, California-Nevada: How useful in tectonic reconstructions?: Geology, v. 14, p. 251-254.

Quigley, M.C., Karlstrom, K.E., Kelley, S., and Heizler, M., 2010, Time and mechanisms of basement uplift in the Colorado Plateau-Basin and Range transition zone, Virgin Mountain anticline, Nevada-Arizona, *in* Umhoefer, P.J., Beard, L.S., and Lamb, M.A., eds., Miocene Tectonics of the Lake Mead Region, Central Basin and Range: Geological Society of America Special Paper 463, p. 311-329.

Renik, B., Christie-Blick, N., Troxel, B.W., Wright, L.A., Niemi, N.A., 2008, Re-evaluation of the middle Miocene Eagle Mountain Formation and its significance as a piercing point for the interpretation of extreme extension across the Death Valley region, California, U.S.A.: Journal of Sedimentary Research, v. 78, p. 199–219.

Serpa, L., and Pavlis, T.L., 1996, Three-dimensional model of the Cenozoic history of the Death Valley region, southeastern California: Tectonics, v. 15, p. 1113–1128.

Spotila, J., 2005, Application of Low-Temperature Thermochronometry to Quantification of Recent Exhumation in Mountain Belts, in Reiners, P.W. and Ehlers, T.A. eds., Thermochronology, Reviews in Mineralogy and Geochemistry, v. 58, p. 449-466.

Snow, J.K., and Lux, D.R., 1999, Tectono-sequence stratigraphy of Tertiary rocks in the Cottonwood Mountains and northern Death Valley area, California and Nevada, *in* Wright, L.A., and Troxel, B.W., eds., Cenozoic Basins of the Death Valley Region: Geological Society of America, Special Paper 333, p. 17-64.

Snow, J.K., and Wernicke, B., 1989, Uniqueness of geological correlations: An example from the Death Valley extended terrain: Geological Society of America, Bulletin, v. 101, p. 1351-1362.

Snow, J.K., and Wernicke, B., 2000, Cenozoic tectonism in the central Basin and Range; magnitude, rate, and distribution of upper crustal strain: American Journal of Science, v. 300, p. 659–719.

Stevens, C.H., Stone, P., and Belasky, P., 1992, Paleogeographic and structural significance of an Upper Mississippian facies boundary in southern Nevada and east-central California: Reply: Geological Society of America, Bulletin, v. 104, p. 1069-1071.

Stewart, J.H., 1983, Extensional tectonics in the Death Valley area, California: Transport of the Panamint Range structural block 80 km northwestward: Geology, v. 11, p. 153-157.

Stockli, D.F., 2005, Application of low-temperature thermochronometry to extensional tectonic settings, *in* Reiners, P., and Ehlers, T., eds., Reviews in Mineralogy and Geochemistry, v. 58, p. 420–461.

Reiners, P.W., 2005, Zircon (U-Th)/He Thermochronometry, *in* Reiners, P.W. and Ehlers, T.A. eds., Thermochronology, Reviews in Mineralogy and Geochemistry, v. 58, p. 151-176.

Reiners, W., Brady, R., Farley, K. A., Fryxell, J. E., Wernicke, B., and Lux, D., 2000, Helium and argon thermochronometry of the Gold Butte Block, South Virgin Mountains, Nevada: Earth Planetary Science Letters, v. 178, p. 315–326.

Walker, C.D., Anders, M.H., and Christie-Blick, N., 2007, Kinematic evidence for downdip movement on the Mormon Peak detachment: Geology, v. 35, p. 259-262.

Wells, M.L. and Hoisch, T.D., 2008, The role of mantle delamination in widespread Late Cretaceous extension and magmatism in the Cordilleran orogen, western United States: Geological Society of America Bulletin, v. 120, p. 515-530.

Wernicke, B.P., 1992, Cenozoic extensional tectonics of the U.S. Cordillera, in Burchfield, B.C., Lipman, P.W., and Zoback, M.L., eds., Geology of North America, Volume G-3, The Cordilleran Orogen: Conterminous U.S: Geological Society of America, p. 553–581.

Wernicke, B. and Axen, G.J., 1988, On the role of isostasy in the evolution of normal fault systems: Geology, v. 16, p. 848-851.

Wernicke, B.P., Axen, G.J., and Snow, J.K., 1988, Basin and Range extensional tectonics at the latitude of Las Vegas, Nevada: Geological Society of America Bulletin, v. 100, p. 1738–1757.

Wernicke, B.P., Walker, J.D., and Beaufait, M.S., 1985, Structural discordance between Neogene detachments and frontal Sevier thrusts, central Mormon Mountains, southern Nevada: Tectonics, v. 4, p. 213-246.

Wernicke, B., and Snow, J.K., 1998, Cenozoic tectonism in the central Basin and Range: Motion of the Sierran-Great Valley block: International Geology Review, v. 40, p. 403–410.

Wills, C.J., Weldon II, R.J., and Bryant, W. A., 2007a, California fault parameters for the National Seismic Hazard Maps and Working Group on California Earthquake Probabilities 2007: U. S. Geological Survey Open File Report, 2007-1437-A, 96 p.

Figure captions

Figure 1.1. Shaded relief map of California, Nevada, eastern Utah, and western Arizona showing active faults (red), approximate fault slip rates, and historic earthquakes (circles). White dashed lines show the subprovinces of the Basin and Range from Wernicke (1992). Shaded area shows the bounds of the eastern California shear zone and Walker Lane belt. Earthquake data are from the United States Geological Survey (2014), Earthquake Archive (http://earthquake.usgs.gov/earthquakes/search). Fault slip rates from Dixon et al., 1995; Bennett et al., 2003; Wills et al., 2007. Figure adapted from Liu et al. (2010). CBR – Central Basin and Range; ECSZ – Eastern California shear zone, NBR – Northern Basin and Range; SBR – Southern Basin and Range.

Figure 1.2. Schematic diagram showing the tectonic evolution of the Pacific-North American plate boundary since ~30 Ma, modified from Dickinson (1981). See text for discussion. Teeth on upper plate. Fault motion shown by arrows. M – Mendocino triple junction; R – Riviera triple junction; SAF – San Andreas Fault.

Figure 1.3. Color shaded relief map of the central Basin and Range showing major faults, including high-angle normal faults (ball and stick), low-angle normal faults (ticks), and strike-slip faults (arrows with relative motion). Faults are modified from Snow and Wernicke (2000). Warm colors correspond to the ranges and cool colors to the basins. (U-Th)/He transect locations are shown with red circles. Sampled ranges are numbered. AR – Argus Range; BD – Beaver Dam Mountains; BM – Black Mountains; CM – Clark Mountains; CW – Cottonwood Mountains; FM – Frenchman Mountain; FN – Funeral Mountains; GM – Grapevine Mountains; HM – Hunter Mountains; KR – Kingston Range; LB – Lost Basin Range; MC – McCullough Range; MD – Muddy Mountains;

MM – Mormon Mountains; NR – Nopah Range; NVM – North PM – Panamint Mountains; PT – Pintwater Range; Panamint Valley – Panamint Valley; RS – Resting Spring Range; SP – Spotted Range; SR – Slate Range; ST – Striped Range; SVM – Southern Virgin Mountains; TS – Tule Springs Hills; WH – White Hills.

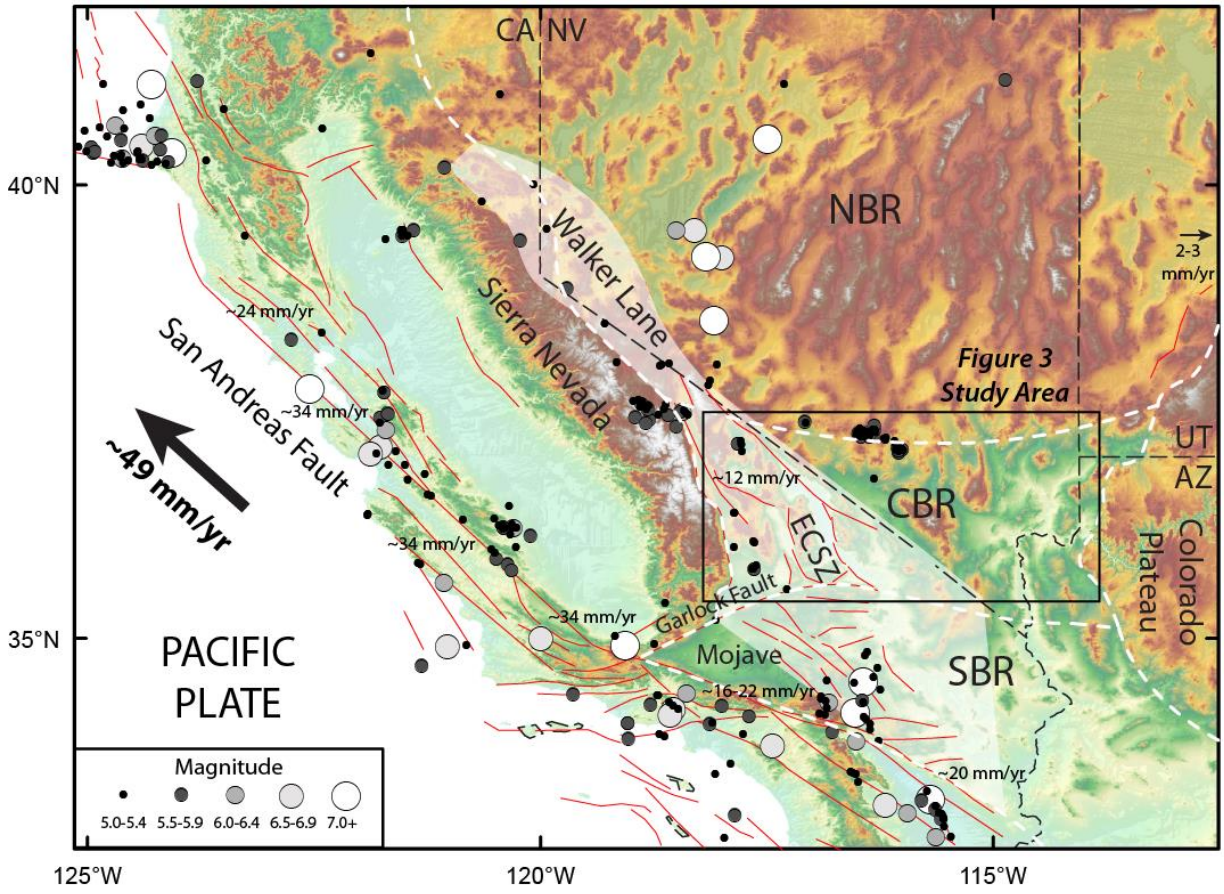
CA
NV
NBR
Walker Lane
Sierra Nevada
San Andreas Fault
~49 mm/yr
~24 mm/yr
~34 mm/yr
~34 mm/yr
~34 mm/yr
~12 mm/yr
~16-22 mm/yr
~20 mm/yr
2-3 mm/yr
Figure 3 Study Area
ECSZ
CBR
SBR
Garlock Fault
Mojave
PACIFIC PLATE
UT
AZ
Colorado Plateau
40°N
35°N
125°W
120°W
115°W
Magnitude
5.0-5.4 5.5-5.9 6.0-6.4 6.5-6.9 7.0+

Figure 1.1

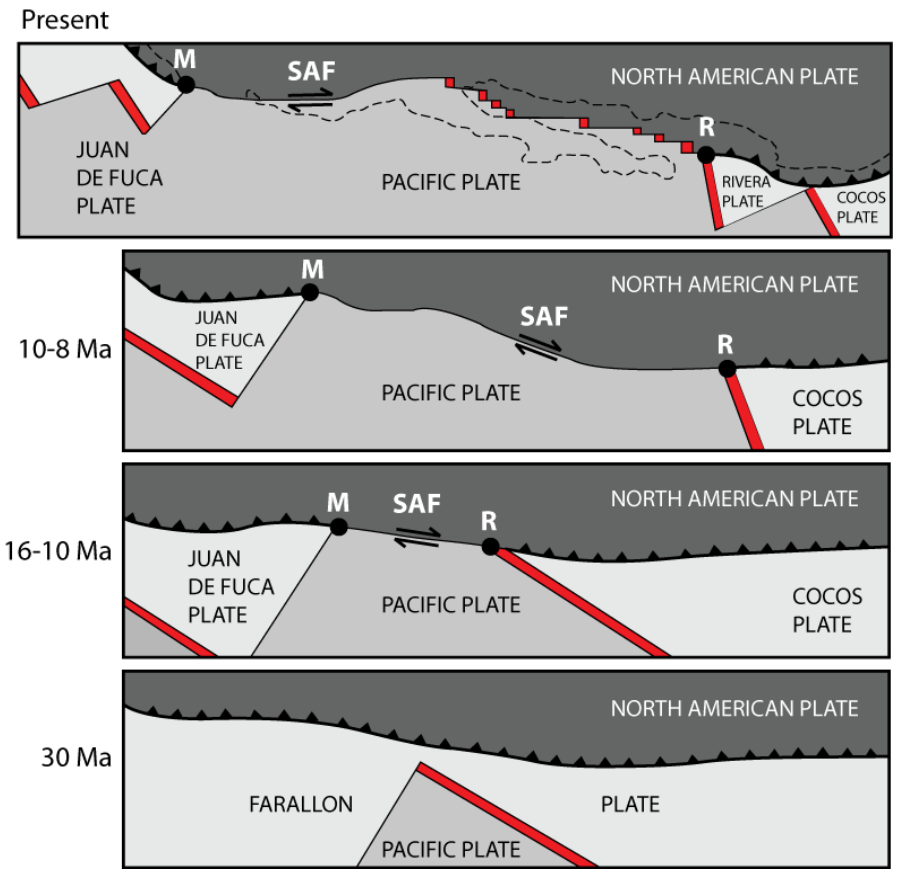
Present
M
SAF
NORTH AMERICAN PLATE
R
JUAN
DE FUCA
PLATE
PACIFIC PLATE
RIVERA
PLATE
COCOS
PLATE
10-8 Ma
M
NORTH AMERICAN PLATE
JUAN
DE FUCA
PLATE
SAF
R
PACIFIC PLATE
COCOS
PLATE
16-10 Ma
M
SAF
NORTH AMERICAN PLATE
R
JUAN
DE FUCA
PLATE
PACIFIC PLATE
COCOS
PLATE
30 Ma
NORTH AMERICAN PLATE
FARALLON
PLATE
PACIFIC PLATE

Figure 1.2

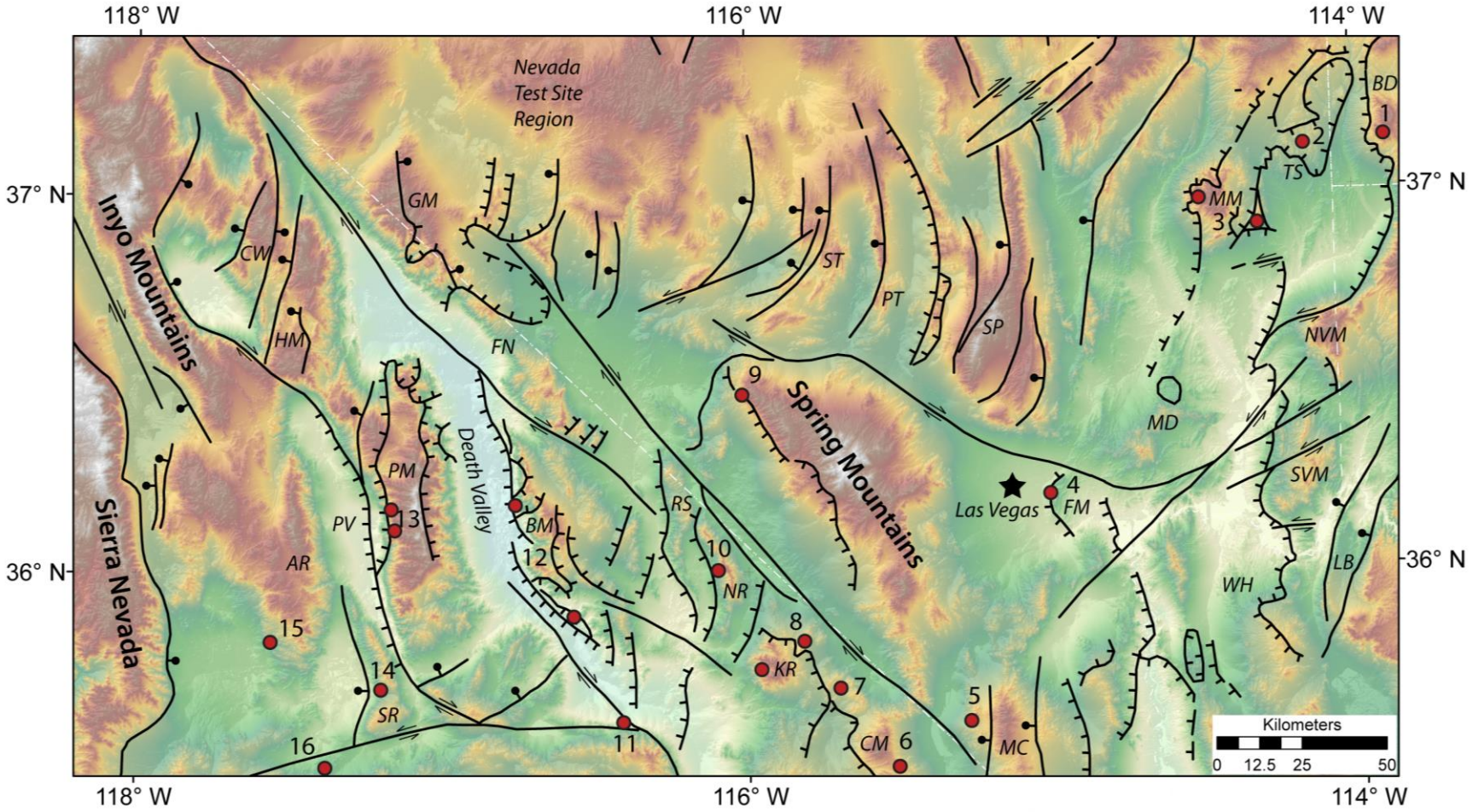
118° W
116° W
114° W
37° N
36° N
Nevada
Test Site
Region
Inyo Mountains
Sierra Nevada
Death Valley
Spring Mountains
Las Vegas
GM
CW
HM
FN
ST
PT
SP
MD
MM
TS
BD
NVM
SVM
LB
WH
PM
PV
AR
BM
RS
NR
KR
SR
CM
MC
1
2
3
4
5
6
7
8
9
10
11
12
13
14
15
16
Kilometers
0 12.5 25 50

Figure 1.3

CHAPTER 2

Low-temperature thermochronologic constraints on the kinematic histories of the Castle Cliffs, Tule Springs, and Mormon Peak detachments, southeastern Nevada and southwestern Utah

Tandis S. Bidgoli[1]

Daniel F. Stockli[2]

J. Douglas Walker[1]

[1]*Department of Geology, University of Kansas, Lawrence, Kansas 66045, USA*

[2]*Now at Jackson School of Geosciences, University of Texas, Austin, Texas 78712, USA*

Abstract

We use apatite and zircon (U-Th)/He thermochronometry to evaluate the timing, magnitude, and spatial pattern of Miocene strain within the Beaver Dam Mountains, Tule Springs Hills, and Mormon Mountains of southwestern Utah and southeastern Nevada. The region is host to three major low-angle structures, the Castle Cliffs, Tule Springs, and Mormon Peak detachments, whose origin and role in regional extension are vigorously debated. We analyzed 36 samples collected from Precambrian basement gneisses and Paleozoic to Jurassic siltstones and sandstones exposed in the footwalls of these detachments. Zircon He ages from the footwall of the Castle Cliffs detachment record rapid footwall exhumation at ~17-18 Ma. At structurally higher positions, apparent ages become progressively older, defining a zircon He partial retention zone. Paleodepth reconstructions of the data using published cross-sections suggest 180+˚C of cooling or 6.8 to 8.2 km of total exhumation, yielding a maximum of ~13 km of extension across this detachment. In contrast, zircon and apatite ages from the footwall of the Mormon Peak record rapid exhumation at 13-14 Ma and anywhere from 5.8 to 7.1 km of vertical

exhumation. Using a range of restored fault dips (20-28°) for the Mormon Peak detachment, the thermochronology data record 10.9 to 19.5 km horizontal extension. Data from the Tule Springs detachment also show a similar timing of exhumation and indicate there has been 5.0 to 6.8 km of vertical exhumation and a minimum of ~5 km of extension. The results demonstrate that extension initiated in the east along the Castle Cliffs detachment and migrated westward with time. Although our data indicate that existing extension estimates across this system of detachment faults are too high (40 km versus 54 km), the pattern of cooling ages and protracted cooling history recorded in these ranges are inconsistent with rootless gravity slide interpretations and low-magnitude extension models.

Introduction

The Basin and Range province is host to some of the best examples of low-angle normal faults (LANFs) or detachment faults (e.g., Whipple detachment; Davis et al. 1980, Snake Range; Bartley and Wernicke, 1984, Sevier Desert detachment; Allmendinger et al., 1983). Although these structures are now widely recognized in continental and oceanic rift systems, there is still significant debate surrounding these faults. The controversy is in large part due to an apparent conflict between well-documented examples of LANFs that are interpreted to have originated and slipped at low dips and current fault mechanical theory. According to such theory, only steep normal faults should form within the brittle part of the crust and faults that dip less than 30° should be frictionally locked (Anderson, 1942, 1951). Consequently, slip on LANFs can only occur by invoking some special circumstance, such as reactivation of a pre-existing weakness, rotation of the stress field, and/ or high pore-fluid pressures. The lack of convincing seismological evidence for large earthquakes on LANFs is also frequently used as an argument

against their mechanical feasibility (Jackson, 1987; Jackson and White, 1989; Thatcher and Hill, 1991; Collettini and Sibson, 2001).

This controversy is well typified by the geology of the Beaver Dam Mountains-Tule Springs Hills-Mormon Mountains area of southeastern Nevada and southwestern Utah where three of the best documented LANFs occur (Figure 2.1). Detailed geologic mapping and cross-section reconstructions of the Castle Cliffs, Tule Springs, and Mormon Peak detachments somewhat convincingly show that they formed and slipped at low angles and accommodated significant extension across this portion of the province (Wernicke, 1982; Wernicke et al., 1985; Axen et al., 1990; Axen, 1993). Other workers, however, have questioned a "rooted" LANF interpretation for these structures. Carpenter and Carpenter (1994a) provided some of the earliest criticism, suggesting instead that the low-angle features in these ranges form the bases to catastrophically emplaced "rootless" gravity slide blocks. A gravity slide interpretation has also been suggested by Anders et al. (2006) based on similarities between breccias found along the Mormon Peak detachment and deposits found at the base of known gravity slide blocks (e.g., Hart Mountain; Beutner and Gerbi, 2005). Inconsistencies in the orientations of kinematic indicators measured along the Mormon Peak detachment have also been cited as evidence of mass wasting (Walker et al., 2007). These workers, alternatively, suggest that extension in these ranges is much more modest and has been accomplished by high-angle range-bounding faults that have been imaged in subsurface seismic reflection profiles (e.g., Carpenter and Carpenter, 1994a) and interpreted from geophysical anomaly maps (e.g., Blank and Kucks, 1989).

The debate over the origin of low-angle features in these ranges, in part, stems from uncertainties in the magnitude, timing, and spatial pattern of strain. Cross-section-based restorations by Wernicke et al. (1985) and Axen et al. (1990) suggest these structures have

collectively accommodated more than 50 km of extension. Although extension estimates for the Mormon Peak and Tule Springs detachments are fairly well-constrained, much of the Castle Cliffs detachment is buried beneath the Virgin River Valley, representing a significant source of uncertainty in the total extension across this system of faults. Also, the timing of fault motion has only been loosely bracketed by cross-cutting relationships between faults and the volcanic units of the Kane Springs Wash caldera (ca. 13.5-17.4 Ma; Scott et al., 1995; Wernicke et al., 1985; Axen et al., 1990; Axen, 1993; Walker, 2008). Thermochronology data are also lacking in the region. The exception is the Beaver Dam Mountains, where fission track studies have provided some constraint on the exhumation history of the range (O'Sullivan et al., 1994; Stockli, 1999). Thermochronology determines ages that can be linked to specific temperatures and thus can be used to reconstruct the time-temperature history of a mountain range. When integrated with structural and stratigraphic data, these methods can capture information about a diverse range of tectonic and geomorphic processes (e.g., timing, magnitude, and rate of faulting; geothermal gradients; degree of tilting or rotation of crustal blocks; magnitude and rate of erosion; see summaries in Ehlers, 2005; Spotila, 2005; Stockli, 2005).

In this paper, we present new zircon and apatite (U-Th)/He thermochronologic data that better constrain the deformational histories of the Castle Cliffs, Tule Springs, and Mormon Peak detachments. Paleodepth reconstructions of the (U-Th)/He data, using published cross-sections, are evaluated to test competing models for the development of these low-angle structures and exhumation in the area. The results provide new constraints on the timing of fault initiation and the magnitude of extension. Our results suggest that earlier extension estimates may be too high; however, a gravity slide origin for low-angle structures in these ranges is inconsistent with the pattern of cooling ages and the protracted cooling history evident in the data.

Geologic background

The Beaver Dam Mountains, Tule Springs Hills, and Mormon Mountains are located within the eastern part of the central Basin and Range province (*sensu* Wernicke, 1992; Figures 2.1 and 2.2). The region experienced both Mesozoic contraction and Cenozoic extension (Tschanz and Pampeyan, 1970; Wernicke et al., 1985; Hintze, 1986; Axen et al., 1990; Axen, 1993). Mesozoic contractional structures are part of the dominantly east-directed Sevier orogenic belt (Armstrong, 1968). The Sevier orogenic belt, at this latitude, is a north-trending décollement-style thrust system, active between the mid-Cretaceous and early Tertiary (Longwell, 1949; Fleck, 1970; Bohannon, 1983; Carpenter, 1989; Axen et al., 1990; Carpenter and Carpenter, 1994b). The principal thrust belt structure is the Mormon-Tule Springs thrust, which has a well characterized flat-ramp-flat geometry (Wernicke et al., 1985; Axen et al., 1990, Axen, 1993) (Figure 2.2). This fault and its associated folds place important constraints on Miocene reconstructions (Wernicke et al., 1985; Axen et al., 1990; Axen, 1993).

Mesozoic contractional structures in the region are overprinted by low-angle and high-angle normal faults that formed during two major pulses of extension: one in the early to middle Miocene and the other in the late Miocene (?) to Pliocene (?), although the bulk of the extension in these ranges is interpreted to be middle Miocene in age (Figures 2.1 and 2.2; Wernicke et al., 1985; Axen et al., 1990; Axen, 1993). Miocene extensional structures within the study area include, from east to west, the Castle Cliffs, Tule Springs, and Mormon Peak detachment faults. These LANFs are part of what has been coined the Las Vegas normal fault system, a west-southwest-directed system of faults interpreted to be responsible for ~45-65 km extension between the western edge of the Colorado Plateau and Spring Mountains west of Las Vegas (Wernicke et al., 1988, Axen et al., 1990; Axen, 1993; 2004).

Late Miocene (?) to Pliocene (?) normal and strike-slip faults are also present within these ranges. The most prominent faults are the Sam's Camp-East Mormon, Gourd Springs, and Tule Corral faults (Figure 2.2; Olmore, 1971; Axen et al., 1990; Axen, 1993; Anderson and Barnhard, 1993a, 1993b). The kinematics and timing of these faults are not well-known; however, cross-cutting relationships with detachments faults and detachment-related structures, as well as with Pliocene (?) calcrete deposits suggest that they postdate middle to late Miocene faults (Axen, 1993). High-angle range-bounding faults have also been identified on the west side of the Mormon Mountains and Beaver Dam Mountains in seismic reflection profiles (e.g., Carpenter and Carpenter, 1994a) and geophysical anomaly maps (e.g., Blank and Kucks, 1989) (Figure 2.2). The timing of these structures is not known, but they also likely post-date detachment faulting.

Castle Cliffs detachment

The Castle Cliffs detachment (CCD), exposed in the Beaver Dam Mountains, is the easternmost detachment within the Las Vegas system (Figures 2.1 and 2.2). The fault forms the eastern edge of Basin and Range province, separating a region of moderately to highly extended crust on the west from the stable and relatively undeformed Colorado Plateau on the east (Figure 2.1). Where exposed, the detachment dips 10˚-20˚ westward, but geometric reconstructions suggest that the fault had an initial dip of 32˚ (Wernicke and Axen, 1988; Axen et al., 1990; Axen, 1993). The present low dip of the fault reflects a combination of detachment-related tilting or unloading (Wernicke and Axen, 1988; Axen et al., 1990; Axen, 1993) and possible tilting related to an inferred range-front fault (Hintze, 1986; Blank and Kucks, 1989).

The footwall of the CCD contains the Beaver Dam "anticline", a large-scale monocline that exposes Precambrian basement gneisses and Paleozoic through Mesozoic carbonate and

clastic strata. The fold is interpreted by Wernicke and Axen (1988) to have formed by flexural unloading of the footwall of the detachment during Miocene slip. The fold has also been interpreted as a Laramide-age, basement-involved contractional structure (Hintze, 1986; Carpenter and Carpenter, 1994a; Christie-Blick et al., 2007); however, tilted mid-Tertiary strata on the east flank of the monocline (Wernicke and Axen, 1988; Axen and Wernicke, 1989; Axen, 2004) and published fission-track ages (O'Sullivan et al., 1994; Stockli, 1999) from the footwall of the detachment support fold formation during the Miocene.

The hanging wall of the CCD consists of Paleozoic carbonates, principally Mississippian Redwall and Pennsylvanian Callville limestone, preserved as klippen on Precambrian basement rocks. These klippen were initially thought to be remnants of the hanging wall of the Castle Cliffs "thrust" (Dobbin, 1939), which is now interpreted to be a normal fault based on the younger-over-older relationship between geologic units (Wernicke and Axen, 1988; Axen, 2004). These klippen have also been interpreted by Cook (1960) and, more recently, by Christie-Blick and others (2007) as gravity slide blocks. Part of the difficulty with finding a satisfactory interpretation for the klippe is that similar blocks of Paleozoic strata are found in contact with Tertiary conglomerate at the Beaver Dam range front (Cook, 1960; Hintze, 1986). However, these known landslide deposits and underlying sediment are interpreted by Axen (2004) to have formed above the CCD and thus, record Neogene motion on the detachment.

Tule Springs detachment

The Tule Springs detachment (TSD), exposed in the Tule Springs Hills, is the middle of the three detachments within the study area (Figure 2.2). The detachment is one of the earliest documented examples of a LANF that originated and slipped at low dips. It is also the one of the

best examples of a LANF with a ramp-flat geometry. The description below follows Axen (1993).

Exposures of the TSD are presently subhorizontal, but geometric reconstructions show that the detachment ramp began with a moderate west dip and that the detachment flat reactivated a portion of the former Tule Springs thrust. Structural arguments indicate that this part of the fault initiated with a 3-15˚ dip to the west.

The footwall of the TSD is folded into a large-scale asymmetric syncline called the Abe-Steer Flat syncline. At the surface, the east limb of the syncline is made up of subhorizontal Jurassic Kayenta Formation, whereas the west limb comprises east-tilted Triassic and younger stratigraphic units. Like the Beaver Dam anticline, the Abe-Steer Flat syncline is also interpreted to have formed by flexural unloading of the footwall of the detachment during Miocene slip.

The hanging wall of the TSD is made up of klippen of Middle Cambrian to Carboniferous carbonates and minor Tertiary strata. These klippen are cut by closely spaced, low- and high-angle normal faults with as much as 3 km of stratigraphic throw. Most of these faults are interpreted to be synkinematic upper plate faults of the TSD because they either terminate at or merge with the detachment. Cross-cutting relationships between these faults and poorly-dated Tertiary volcanic and sedimentary units suggest that the TSD was active from the middle to late Miocene. Pliocene (?) calcretes deposited on the detachment indicate that activity ceased by that time. Klippen of the Mormon Peak detachment are also found in the hanging wall of the TSD in the western Tule Springs Hills, demonstrating that the TSD is the younger of the two (Wernicke et al., 1985; Axen, 1993).

Mormon Peak detachment

The Mormon Peak detachment (MPD) is the westernmost detachment within the study area (Figure 2.2), and perhaps, the most controversial of structures in the region. Exposures of the detachment presently dip 5-10˚ to the west; however, the detachment is interpreted to have initiated with a dip of 20-28˚westward (Wernicke et al., 1985; Axen, 2004). This range in initial dip was determined by reconstructing the cut-off angle between the fault and lower plate stratigraphy (17-20˚) and by allowing for some modest westward tilting (3-8˚) beneath the load of the pre-extensional fold-thrust belt (Wernicke et al., 1985; Axen, 2004). The restored dip is also supported by hanging wall reconstructions of the fold-thrust structure, between the Mormon Mountains and the Meadow Valley mountains to the west, relative to the detachment footwall (Wernicke et al., 1985; Axen et al., 1990; Axen, 2004).

The footwall of the MPD contains autochthonous Precambrian basement rocks and Paleozoic strata relative to the Mormon thrust (Wernicke et al., 1985; this reference applies to most of the rest of the description). The western part of the exposed footwall contains a number of high-angle (50-70˚) faults, most with normal-sense displacements of less than 100 m. These faults have contradictory cross-cutting relations with the detachment, suggesting that they formed during slip on the detachment, perhaps during its late history. High-angle footwall faults also occur in the east-central part of the range. These faults are mostly west-dipping normal faults that cross-cut and post-date the detachment. They are interpreted as faults that are part of the hanging wall of the Tule Springs detachment (Wernicke et al., 1985, Axen, 1993).

The hanging wall of the Mormon Peak detachments is made up of erosional remnants of Paleozoic and Tertiary strata that are extensively faulted and brecciated. These remnants are bounded at their base by the detachment. Kinematic indicators, including slickenlines and small-

scale groove and mullion structures, are common along the detachment, although the movement direction determined by them locally contrasts with the WSW extension direction determined by Wernicke et al., (1988; see Walker et al., 2007). Above the detachment is a thick carbonate gouge and breccia. Anders et al. (2006) documented a number of similarities between the breccia and deposits found at the base of known gravity slide blocks, providing the strongest evidence in support of a gravity-slide interpretation for the MPD. However, the origin and significance of these deposits needs additional investigation.

(U-Th)/He thermochronometry

(U-Th)/He thermochronometry is a powerful dating technique that is increasingly being applied to extensional settings. It is one of the few methods that can expressly date the exhumation and cooling of a footwall of a major normal fault (e.g., Axen et al., 2000; Stockli et al., 2000; Ehlers et al., 2003; Armstrong et al. 2004). These types of data can also be used to estimate geothermal gradients within the crust preceding and during extension (e.g., Fitzgerald and Gleadow, 1990; Howard and Foster, 1996; Miller et al., 1999; Stockli et al., 2002). The (U-Th)/He method is based on the decay ^{235}U, ^{238}U, ^{232}Th, and ^{147}Sm by alpha (^{4}He nucleus) emission. However, ^{4}He retention in minerals is temperature dependent and controlled principally by mineralogy; but grain size (e.g., Farley, 2000; Reiners and Farley, 2001), cooling rate (e.g., Dodson, 1973), and damage to the crystal lattice (e.g., Shuster et al., 2006) also play important roles.

Apatite is one of the most commonly used (U-Th)/He thermochronometers, in part, because it records cooling at low temperatures: ^{4}He is completely lost by thermally-activated volume diffusion above ~80˚C and mostly retained below ~40˚C (Wolf et al., 1996, 1998; House et al., 1999; Stockli et al., 2000). These temperatures define thermal sensitivity windows or

"partial retention zones" (PRZs; Wolf et al., 1998) that can be used to reconstruct temperature-time histories or apparent age-paleodepth/ elevation trends (summary in Stockli, 2005).

Zircon is also widely used as a (U-Th)/He thermochronometer in extensional settings (e.g., Reiners et al., 2000; 2002; Lee et al., 2009). Zircon retains helium over a higher temperature range, from ~130°C to as high as ~200°C (Reiners et al., 2002; 2004; Wolf and Stockli, 2010), but the zircon helium PRZ is not as well determined because diffusion kinetics in zircon are complicated by a number of factors, the most significant being the impact of radiation damage on He diffusion and (U-Th)/He ages. Several studies have shown that zircon (U-Th)/He ages can be considerably affected by radiation damage to the crystal lattice (e.g., Hurley, 1952; Reiners et al., 2002; 2004; Nasdala, 2004; Reich et al., 2007). The damage is mainly produced by recoil of heavy isotopes during alpha emission, but spontaneous fission events and ejected ^{4}He nuclei also contribute some to the total lattice damage. Radiation damage to grains is generally recognized by a strong correlation (positive or negative; Guenthner et al., 2013) between (U-Th)/He dates and both He concentration [He] and effective U concentration [U]e. The [U]e is calculated as [U] + 0.235 [Th] + 0.005 [Sm], which is concentration of U, Th, and Sm within the grain weighted for each isotopes α productivity. A positive correlation between dates and [U]e typically develops at low levels of radiation damage, suggesting a decrease in He diffusivity or trap-like behavior, similar to radiation damaged apatite (Guenthner et al., 2013; Shuster et al., 2006; Flowers et al., 2009). Conversely, a negative correlation between dates and [U]e typically develops at higher levels of radiation damage, as damage zones become interconnected forming fast networks or pathways for He diffusion within the grain (Nasdala et al., 2004; Reiners, 2005; Guenthner et al., 2013).

Sample collection

We collected a total of 49 samples from the study area; however, only 36 samples (Figure 2.2) yielded usable apatite and zircon. Samples from the Beaver Dam Mountains and Mormon Mountains were collected earlier by Stockli (1999); samples from the Tule Springs Hills were collected during the course of this study. Where possible, we collected samples systematically, in horizontal transects, parallel to the known extensional fault slip direction (WSW; Wernicke et al., 1985; Axen et al., 1990). Although our sample transects are tightly spaced (~500 m) and cover the exposed range of structural depths in the footwalls of the detachments, sample gaps occur where we cross Paleozoic carbonate rock. This was particularly problematic for the Mormon Mountains, where much of the exposed rock is carbonate.

Analytical procedures

We used standard mineral separation techniques to isolate and concentrate apatite and zircon from our rock samples. From our separates, individual grains were inspected, measured, and photographed using a 180X Nikon stereo microscope with crossed polarizers and mounted digital camera. When possible, we selected near euhedral grains, greater than 70 μm in width that appeared inclusion-free. These guidelines increase the accuracy and reproducibility of (U-Th)/He ages by minimizing the effects of: (1) U and Th-bearing inclusions that may incompletely dissolve, producing "parentless" He and anomalously older apatite He ages (House et al., 1999; Farley and Stockli, 2002) and (2) the alpha-ejection (Ft) correction, a standard morphometric age correction that accounts for the loss of alpha particles near the edge of a grain (Farley et al., 1996). Each single-grain was then loaded into a 1-mm platinum packet and heated using a continuous-mode laser. Apatite grains were heated for 5 minutes at 1070°C; whereas, zircon grains were heated for 10 minutes at 1300°C. The extracted He gas was spiked with ^{3}He,

purified using a gettering and cryogenic gas system, and measured on a Blazers Prisma QMS-200 quadrupole mass spectrometer. The degassed apatite grains were subsequently dissolved in a spiked (^{230}Th, ^{235}U, ^{149}Sm) HNO_3 solution and analyzed using a Thermo Scientific Element-2 inductively coupled plasma mass spectrometer (ICP-MS). In contrast, degassed zircon grains were removed from their platinum packets and dissolved using standard U-Pb high-pressure vessel digestion procedures (HF-HNO_3 and HCl). Following dissolution, zircon samples were spiked (^{230}Th, ^{235}U, ^{149}Sm) and analyzed for U, Th, and Sm using an ICP-MS. Laboratory and analytical work was performed at the Isotope Geochemistry Laboratories at the University of Kansas and at the (U-Th)/He Geo- and Thermochronometry Lab at the University of Texas at Austin.

Error reporting

Propagated analytical uncertainties for single-grain analyses are approximately 3-4% (2σ). However, these uncertainties generally underestimate sample reproducibility because errors related parent isotope distributions within grains and the Ft correction are difficult to quantify. Therefore, we follow a common (U-Th)/He dating practice and apply a percentage error to single-grain analyses, estimated from the reproducibility of laboratory standards: 6% for apatite and 8% for zircon (Farley et al., 2001; Reiners et al., 2002; see supplementary data[1]). For our mean ages, the error is reported as the standard deviation (1σ) of our replicates for a given sample (Table 2.1). However, 4 samples (11TS09; 96BR006, -13, and -14) are single grain ages; therefore, we show the error in the "mean" age as the standard error.

Paleodepth reconstructions

In order to properly evaluate the thermal structure of the crust within the study area, it is necessary to restore our thermochronology samples to their pre-extensional paleodepths. In this

study, we restore samples using published cross sections of Axen et al. (1990). Alternative interpretations for the structures in the region have been suggested (e.g., Anderson and Barnhard, 1993; Carpenter and Carpenter, 1994a; Anders et al., 2006; Walker et al., 2007); however, Axen et al. (1990) contains the only set of balanced cross sections across these specific ranges and is the most widely accepted interpretation.

These cross-sections and, consequently, our paleodepth reconstructions make several assumptions about the pre-extensional thrust belt structure, most importantly that Paleozoic through Mesozoic strata in the footwalls of the detachments were roughly horizontal prior to extension. This assumption is supported by the fact that the strata are part of the thrust autochthon, in the frontal portion of the Mesozoic Sevier thrust belt, and are, therefore, unlikely to have been significantly deformed prior to extension; although some modest westward tilting is expected (~3°-8°; see Wernicke et al. [1985] and Axen et al. [1990] for detailed discussions). This interpretation is also supported by the fact that there is little angular discordance (<5°) between Oligocene-Miocene strata and the footwall stratigraphy of the thrust (Wernicke et al., 1985; Wernicke and Axen, 1989; Axen et al., 1990).

For the Beaver Dam Mountain transect, we use the Precambrian nonconformity as our paleohorizontal datum, although any of the Paleozoic unit boundaries could have been selected since the stratigraphic thickness of these intervals does not change by any significant degree over the study area. All other samples are referenced relative to the sub-Tertiary unconformity, a regional marker that is important for restoring cross sections and for determining paleotopographic patterns in the area. The sub-Tertiary unconformity was chosen because there is a small degree of westward tilting (5°) to the fold-thrust structure and the Precambrian

nonconformity across the Tule Springs Hills and Mormon Mountains (Wernicke et al., 1985; Axen et al., 1990; Axen, 1993).

The above paleohorizontal references were selected because there are only limited exposures of Tertiary strata within the study area, making overburden and "true" paleodepth estimates difficult. Since we rely on published cross-sections to restore samples to their preextensional configuration, it is difficult for us to quantify our paleodepth uncertainties. A steeper tilt to the fold-thrust structure across the study area would certainly shift the positions of our samples downward, particularly for areas west of the Beaver Dam Mountains (the Beaver Dam Mountains are unlikely to be affected because they are located at the very frontal portion of the thrust belt where tilt is expected to be low). For the Tule Springs Hills and East Mormon Mountains a steeper tilt (to 8°) could amount to a shift of ~1.5 km; for the western Mormon Mountains, the steeper tilt could result in a shift of 2+ km. Although these shifts are large, the relative positions of our samples and reconstructed isotherms are unlikely to be significantly changed.

Thermochronology results

Table 2.1 shows our resulting (U-Th)/He mean ages and associated errors (1σ). For most samples (N=37), three or more replicates were used to calculate the mean; however, 7 of the 44 reported ages were calculated using less than three replicates. These samples contained outliers that were excluded from our calculated mean ages. Outliers were determined as dates that were greater than 2 standard deviations from the mean. Analyses with a large number of reextractions during laser He degassing were also excluded from the determined means, as this usually points to the presence of unseen mineral or fluid inclusions within the grain (House et al., 1999). In

total, 11 (~6%) of the 190 single-grain analyses completed were excluded (see data supplement, Tables SD2.1 and SD2.2).

Although most of our mean ages were calculated with an appropriate number of replicates, many of the reported standard deviations in Table 2.1 are quite large (>20%) and show that there is a wide spread of dates captured by our mean (U-Th)/He ages, particularly for zircon. Upon closer inspection, it appears that individual zircon dates for most of our samples are negatively correlated with both [He] and [U]e, a strong indication that radiation damage effects are likely at play (Figure 2.3; Reiners et al., 2002; 2004; Nasdala, 2004; Reich et al., 2007; Guenthner et al., 2013). The data also reveal that there is a wide range in [U]e for our samples, from less 50 ppm to greater than 1600 ppm (Table 2.1). Radiation damage and its effects our (U-Th)/He dates and interpretations are discussed in more detail in later sections.

Beaver Dam Mountains

Cross-section B-B' (Figure 2.4) is oriented WSW and shows the geometry of the Beaver Dam monocline and the projected positions of our thermochronology samples. We analyzed 16 samples from the footwall of the Castle Cliff detachment. The samples were collected from a large portion of the footwall section, including Precambrian gneiss and granite, Cambrian sandstone (Tapeats Sandstone), and Permian through Jurassic sandstone and conglomerate (Queantoweap Sandstone; and Chinle, Kayenta, and Navajo formations; Figures 2.2 and 2.4). A sample gap occurs where our transect crosses Cambrian through Mississippian miogeoclinal carbonates (Figures 2.2 and 2.4). Reported ages range from as young 17.1 Ma to as old as 649.1 Ma, but no systematic relationship between cooling age and elevation is observed in the data (Table 2.1 and Figure 2.4). The youngest mean ages, with the exception of sample 95BR111, are located in the very western part of the transect, collected just east of the detachment, clustering at

around 18 Ma (Figures 2.2 and 2.4). The samples increase in apparent age eastward, and the eastern half of the transect contains the oldest apparent ages, ranging from ~265 to 650 Ma (Table 2.1 and Figure 2.4).

To evaluate the samples further, we restored samples to their preextensional paleodepths (Figure 2.5). Depths in Figure 2.5 are referenced to a datum at the basal nonconformity, not the interpreted depth (see previous section). The paleodepth reconstruction reveals that, although the samples were collected from within a few hundred meters of elevation (1035-1450 m), they capture a wide section of Beaver Dam crust (~7 km). The structurally lowest and deepest samples (95BR102, -103, and -104) are invariant at around 17-18 Ma, recording rapid exhumation at that time. These ages overlap (within error) with apatite fission track ages of Stockli (1999) analyzed from the same samples (Figure 2.5). At structurally shallower depths, the samples form a broad grouping, with mean ages ranging from ~18 Ma to 75 Ma (Figure 2.5). These samples appear to define a zircon He partial retention zone. Ages then dramatically increase above the PRZ (above sample 95BR115); mean ages for these samples are, in most cases, older than the depositional ages of the units, suggesting that they have not been thermally reset (Table 2.1 and Figure 2.5).

The thermochronology data can also be used to evaluate the Miocene preextensional geothermal gradient. This is accomplished by using the relative positions of the top (~130°C) and base (~190°C) of the zircon He PRZ in our paleodepth reconstruction (Figure 2.6). The position of 130°C isotherm is constrained between 0.35 and 0.20 km by samples 95BR115 (shallowest Tertiary age) and 95BR116 (deepest Paleozoic age; Figure 2.6). Using a similar approach, the position of the 190°C isotherm is constrained between -2.1 and -1.6 km (Figure 2.6). The vertical difference between these isotherms is 1.9 to 2.4 km, resulting in a

preextensional geothermal gradient of 28 +/-3°C/km. Alternatively, we can calculate the geothermal gradient by using the difference between the base of apatite fission track partial annealing zone (~110°C) from Stockli (1999) and the base of our zircon He PRZ (~190°C) (Figure 2.6). Although the base of the zircon He PRZ is fairly well constrained, the base of the apatite fission track partial annealing zone is uncertain where our traverse crosses middle Cambrian to lower Permian carbonates (Figure 2.6). Factoring uncertainties, the difference between these isotherms ranges from as little as 1.9 km to as high as 4.9 km, resulting in a geothermal gradient of 29+/-13°C/km (Figure 2.6).

Mormon Mountains and Tule Springs Hills

We analyzed 7 samples from the footwall of the Mormon Peak detachment, collected from exposures of Precambrian gneiss and Cambrian Tapeats Sandstone in the western and central Mormon Mountains (Figure 2.2). Zircon (U-Th)/He ages are shown in cross-section C-C' (Figure 2.7), ranging from 13.4 Ma to 84.2 Ma. In the western part of the range, samples ages systematically increase to the east, from 14.3 Ma to 24.7 Ma. A similar pattern is present in the central Mormon Mountains where two samples cluster at 13-14 Ma. The next sample to east, however, increases in apparent age to 84.2 Ma. The cross-section also shows that a similar eastward increase in apparent ages occurs in the footwall of the Tule Springs detachment. Apatite (U-Th)/He ages from the MPD footwall range from 10.2 Ma to 13.7 Ma. However, the two westernmost samples (96BR013 and 96BR014) are single grain ages and are, therefore, not considered reliable.

Paleodepth reconstruction of the footwall of the MPD reveals that the preextensional depths of our samples fall within a narrow range, spanning less than 2 km (Figure 2.7). Figure 2.7 shows that most of our apatite ages and the structurally deepest zircon sample have similar

cooling ages, around 13-14 Ma. This implies that these samples cooled through both the zircon He PRZ and apatite He PRZ, indicative of rapid exhumation at that time. Zircon cooling ages then systematically increase at shallower depths, a pattern consistent with residence in a partial retention zone prior to the mid-Miocene. The base of the zircon He PRZ (190°C) is well constrained between our shallowest partially reset sample (96BR014) and our deepest 13-14 Ma sample (96BR016); however the top of the PRZ is uncertain in this reconstruction (Figure 2.7).

Cross section D-D' (Figure 2.8) is a deformed state cross-section across the Mormon Mountains and Tule Springs Hills, showing the projected positions of 13 samples collected from the footwall of the Tule Springs detachment. Samples from the East Mormon Mountains were collected from Precambrian gneiss and Cambrian Tapeats Sandstone (Figure 2.2). Samples from the Tule Springs Hills were collected from sandstones and siltstones of the Jurassic Kayenta Formation (Figure 2.2). Zircon (U-Th)/He mean ages range from 21.6 Ma to 347.6 Ma (Figure 2.8). Again, no systematic relationship between apparent age and elevation is evident in the data (samples are collected from within 150 m in elevation) (Table 2.1 and Figure 2.8). Instead, the youngest cooling ages occur in the western part of the transect, within the East Mormon Mountains, and the oldest cooling ages occur to the east, across the Tule Springs Hills (Figure 2.8). Apatite (U-Th)/He ages from the same transect range from 13.4 Ma to 27.6 Ma (Figure 2.8). The youngest apatite cooling ages occur in the western part of the transect, clustering at around 13-14Ma. Ages then get progressively older to the east (Figure 2.8).

It should be pointed out that three of the Tule Springs Hills zircon ages (11TS04, -06, and -09) shown in Table 2.1 have been excluded from the cross-section and our paleodepth reconstruction. These samples have very young dates (younger than our apatite He dates) and the very high [U]e when compared with other samples from the transect and study area (Table

2.1). We believe that these grains may have leaked He at relatively low temperatures and therefore do not reflect on the cooling history of the Tule Springs detachment. Alternatively, the samples may have experienced localized hydrothermal resetting, but given the relationship between dates and [U]e, we think that scenario is unlikely.

The restored positions of the samples in cross-section D-D' are shown in Figure 2.8. The paleodepth reconstruction reveals that samples from the TSD footwall span ~5 km of preextensional crust. Zircon (U-Th)/He ages form two groups: a broad cluster of Tertiary ages between 5.5 and 6.2 km, and a broad cluster of Jurassic and older ages between 2.0 and 2.4 km (Figures 2.8 and 2.9; depths in this case are relative to the basal Tertiary unconformity). The deeper cluster shows a fairly systematic increase in apparent age with depth, characteristic of a partial retention zone. However, the positions of the top and base of the zircon He PRZ are uncertain. The shallower cluster has zircon ages that are either close to or older than the depositional age of the sampled unit. These samples probably resided above the zircon He PRZ and are not thermally reset. Apatite (U-Th)/He ages also form two groups (Figure 2.8 and 2.9). The first includes a group of invariant samples at 13-14 Ma. The second group shows a somewhat orderly increase in apparent age with shallowing depth, suggestive of an apatite He partial retention zone; although its geometry is uncertain. Our best estimate is that the base of this zone resides between samples 11TS09, our shallowest partially reset sample, and 11TS07, whose age overlaps with 13-14 Ma samples that record the timing of exhumation.

Paleodepth reconstructions of our data from Mormon Mountains, East Mormon Mountains, and Tule Springs Hills indicate that the footwalls of the MPD and TSD experienced rapid cooling at the same time (ca. 13-14 Ma). The close proximity of these faults and the similarity in their cooling histories indicates that the preextensional thermal structure across the

region was relatively smooth. Figure 2.9a shows the combined data set and the approximate position of the zircon He PRZ. Figure 2.9b shows the same data rescaled to show the interpreted shape and position of the apatite He PRZ. The combined paleodepth reconstruction can be used to evaluate the Miocene preextensional geothermal gradient. To do this, we use the relative positions of the base of the apatite He PRZ (~80°C) and the base of the zircon He PRZ (~190°C) (Figure 2.9b). The vertical difference between these isotherms is 3.6 to 4.8 km, which yields a preextensional geothermal gradient of 27 +/-4°C/km (Figure 2.9b).

Discussion

Radiation damage effects

The strong correlation between our (U-Th)/He dates and the [U]e suggests that radiation damage effects may be modifying the diffusive behavior of He within our grains and closure temperatures, raising a question about the reliability of our zircon data and paleodepth interpretations. However, several factors make us believe that that the data are still reliable despite obvious radiation damage effects. In the Beaver Dam Mountains, the timing of exhumation from our (U-Th)/He ages is within error of apatite fission-track data from Stockli (1999) on these same samples, and compatible with the timing of exhumation regionally (e.g., Fitzgerald et al., 1991, 2003, 2009; Reiners et al., 2000; Bernet, 2002; Reiners, 2005; Quigley et al., 2010). The youngest ages are also consistently between 17-18 Ma. If grains were sufficiently leaky at ambient temperatures, we might expect an age reversal, with (U-Th)/He ages being younger than the published fission-track ages. Similar observations can be made in the Mormon Mountains and Tule Springs Hills, where most of our zircon (U-Th)/He ages are the same (within error) as the apatite (U-Th)/He ages. The exceptions are 11TS04, -06, and -09

(Table 2.1), which were excluded from our paleodepth reconstructions because they had younger cooling dates than apatite grains analyzed from the same samples and have very high [U]e.

The geothermal gradients calculated from our thermochronology data also seem to suggest that radiation damage effects are at a minimum. The geothermal gradients determined from our data are reasonable (23-31°C), invariable across the study area, and similar to the average continental geothermal gradient (~25°C) and published geothermal gradients from the region (e.g., Reiners et al., 2002; Fitzgerald et al., 1991; 2009; Karlstrom et al., 2010). This implies that the temperatures at the top and base of zircon He partial retention zone may close to their expected values.

Figure 2.10 illustrates the overall shape of the zircon He partial retention zone using our data from the Beaver Dam Mountains. The size of each He date symbol is scaled to the [U]e, and the approximate shape of the partial retention zone is shown at high (>600 ppm) and low (<200 ppm) [U]e. The sigmoidal shapes of the PRZs are similar to what would be expected for a typical zircon without significant radiation damage (e.g., Fish Canyon Tuff); however at high [U]e the PRZ is steep and abruptly flattens towards the ~130° C isotherm. The shape of this PRZ demonstrates that ages are younger at lower temperatures, consistent with a reduction in He retentivity in radiation-damaged zircon. In contrast, the shape of the low [U]e PRZ appears relatively flat at higher temperatures. In this case, ages are older at higher temperatures because undamaged zircons or those with lower levels of radiation damage have higher retention of He.

Our results seem to suggest that, although there are clear radiation damage effects on our zircon cooling ages, the data can still be interpreted in a robust way. This may be explained by the fact that our data capture a wide range of [U]e, minimizing uncertainties in the positions of paleoisotherms at the top and base of the PRZ. However, a more quantitative study of radiation

damage and its impact on He diffusivity in our samples is required to properly evaluate this claim (e.g., Nasdala et al., 2004; Shuster et al., 2006; Nasdala et al., 2011; Guenthner et al., 2013).

Temporal and spatial patterns

The new thermochronology data allow us to place constraints on the timing and spatial pattern of strain across the study area. The structurally lowest (deepest) zircon (U-Th)/He ages from the footwall of the Castle Cliffs detachment are invariant at 17-18 Ma and overlap (within error) with apatite fission track ages of Stockli (1999). This implies that samples rapidly cooled from below the zircon He PRZ and to above the apatite fission track PAZ at that time. Thus, we interpret the onset of rapid cooling and exhumation at ~17 Ma as marking the timing of initiation of the Castle Cliffs detachment.

The timing of initiation for the Castle Cliffs detachment is similar to that of other structures that lie along the western margin of the Colorado Plateau. Thermochronology studies of the Virgin Mountain anticline (Quigley et al. 2010), and of the South Virgin-White Hills detachment in the Gold Butte block (Fitzgerald et al., 1991, 2009; Reiners et al., 2000; Bernet, 2002; Reiners, 2005), Lost Basin Range (Fitzgerald et al., 2009), and northern White Hills (Fitzgerald et al., 2003, 2009) also show rapid cooling at 17-19 Ma. Sedimentological constraints from the region show a similar, but slightly younger age (ca. 16.5 Ma) for fault initiation and basin development based on the conglomerates within the lower Horse Springs Formation (Beard, 1996; Blythe et al., 2010; Lamb et al., 2010). This may imply that there is a lag between fault activity and the first appearance of sediment in catchments. It is also possible that the earliest synkinematic strata are just poorly dated, not well preserved, or not sampled because they are buried by younger strata.

Zircon and apatite (U-Th)/He ages from the footwalls of the Mormon Peak and Tule Springs detachments are invariant at 13-14 Ma, indicating that samples cooled by as much as ~150°C at that time. We interpret this rapid cooling as marking the onset of slip along these detachments. This interpretation is supported by cross-cutting relationships with regionally distributed ash-flow tuffs, which indicate that detachment faulting post-dates the 18.2±0.2 Ma Hiko tuff (Rowley et al., 1995) and at least some of the tuffs of the Kane Springs Wash caldera (ca. 13.5-17.4 Ma; Scott et al., 1995), although definitive correlations between volcanic units in these ranges and source calderas have not been made (Wernicke et al., 1985; Axen, 1993; Walker, 2008).

Our thermochronologically-based interpretations for the timing of fault initiation indicate that the Mormon Peak and Tule Springs detachments are younger than the Castle Cliffs detachment by as much as 5 Ma. This implies that extension and exhumation began at the eastern margin of the central Basin and Range and migrated westward with time. This is a somewhat surprising result since field relations between the detachments suggest that these structures young in an eastward direction; faults in the hanging wall of the TSD cut the MPD, and faults in the hanging wall of the CCD cut the TSD. The apparent paradox may be resolved, however, if activity along these structures ceased from west to east. If correct, it suggests that the Castle Cliffs detachment is a relatively long-lived structure, with its activity spanning more than 10 Ma. Such a lengthy tectonic history may imply that this structure serves as a fundamental boundary at the edge of this diffusely deforming province.

Vertical exhumation and magnitude of extension

In addition to providing critical timing constraints, the thermochronology data may be used to estimate vertical exhumation and preextensional overburden, and can provide an

independent test of cross-section-based extension estimates. It is important to note that the cross sections and consequently our paleodepth interpretations come from detailed geologic map data, whereas the partial retention zones and temperature estimates come entirely from the (U-Th)/He age data.

Our paleodepth reconstruction (Figure 2.6) indicates that the Beaver Dam Mountains have experienced a minimum of 180°C of cooling since ~17 Ma. This value is determined by assuming a mean surface temperature of 10°C, although a slightly warmer or cooler temperature (+/-5°C) may be used. Using our best estimate of the geothermal gradient (28 +/-3°C/km), this translates to 5.8 to 7.2 km of vertical exhumation. However, our structurally deepest sample resides almost 1 km below the approximate position of the 190°C isotherm in our reconstruction. Therefore, the total vertical exhumation is anywhere from 6.8 to 8.2 km. The estimated vertical exhumation indicates that the total overburden across the Beaver Dam Mountains never exceeded ~1.5 km.

The thermochronology data from the Beaver Dam Mountains can also be used to evaluate extension across the Castle Cliffs detachment. To do this, we trigonometrically convert the vertical exhumation (throw) to horizontal extension (heave) assuming a planar fault geometry. Using the restored fault dip of 32° from Axen et al. (1990), the estimated vertical exhumation results in a net extension or heave of 10.9 to 13.1 km. It is important to note that our estimate assumes that all of the exhumation is related to slip on the Castle Cliffs detachment, which is an unlikely scenario. A small component of the exhumation may be attributed to erosion and to buried faults at the Beaver Dam range front. Therefore, these estimates for exhumation related to detachment faulting should be considered maximums.

Using a similar set of assumptions, we can determine the vertical exhumation and horizontal extension along the Mormon Peak detachment. Figure 9 shows that the Mormon Mountains have experienced a maximum of 180°C of cooling since ~14 Ma. Using our calculated geothermal gradient (27 +/-4°C/km), this translates to 5.8 to 7.1 km of vertical exhumation, which suggests that the total overburden there never exceeded ~1 km. Using the range of restored fault dips (20-28°) from Wernicke et al. (1985), we estimate anywhere from 10.9 to 19.5 km of extension along the Mormon Peak detachment. Again, this calculation assumes all of the exhumation is related to slip on the MPD. Any exhumation associated with buried faults on the west side of the Mormon Mountains or related to erosion would certainly reduce this estimate.

A similar set of calculations can be made for the Tule Springs detachment. Because the deepest sample from the TSD footwall is 0.3 to 0.8 km shallower than the 190°C isotherm, we estimate that the total vertical exhumation is 5.0 to 6.8 km (Figure 2.9). Using the restored fault dip for the ramping portion of the fault in the cross-section D-D' (50°), we estimate a minimum of 4.2 to 5.7 km of horizontal extension. Calculations for the TSD, however, are complicated because it lies in the footwall of the MPD, which makes teasing out its thermal history difficult. It is also difficult to accurately estimate the heave on the fault because much of the fault is subhorizontal where it follows a footwall flat of the former Tule Springs thrust.

Cross-section based reconstructions suggest that there has been ~54 km of extension between the Beaver Dam and Meadow Valley mountains (Wernicke et al., 1985; Wernicke et al,, 1988; Axen et al., 1990; Axen, 1993). These reconstructions assign 24 km of extension to the Castle Cliffs detachment, 7 km to the Tule Springs detachment, and 23 km to the Mormon Peak detachment (Wernicke et al., 1985; Axen et al., 1990; Axen, 1993). These values have been

challenged by a number of studies (e.g., Anderson and Barnhard, 1993; Carpenter and Carpenter, 1994a; Anders et al., 2006; Anderson et al., 2010), with those authors preferring more modest extension across these ranges. Our data suggest that extension estimates for at least two of the detachment may be too high. At a minimum, ~3 km may be eliminated from the Mormon Peak detachment, and ~11 km from the Castle Cliffs, making the net extension across this system of faults closer to 40 km, ~25% lower than earlier estimates.

A lower value for extension across the Castle Cliffs detachment is not entirely surprising as cross-section reconstructions across the Virgin River Valley are largely unconstrained, with earlier workers citing extension errors of +/-10 km for that fault (Axen et al., 1990; Axen, 1993). However, the lower range of extension estimates for the Mormon Peak detachment, determined by our data above, seem unlikely given that the Meadow Valley syncline necessarily formed above the Mormon thrust ramp (Axen et al., 1990). It would be difficult to remove more than a few kilometers of heave given this fairly tight geological constraint. Reconciling the fold-fault relationship with our thermochronology results means that the range of fault dips proposed by Wernicke et al., (1985) and used in our calculations is too wide and that the initial fault dip was probably closer to 20°.

Low-angle normal faults or gravity-slide blocks?

Although our data do not allow us to say definitively what the origin of low-angle structures in these ranges is, we can say that the thermochronology data make good sense in the context of a low-angle normal fault interpretation. In particular, the pattern of cooling ages seems to support such an interpretation as samples systematically young in the presumed slip direction of the fault. The youngest samples are consistently from what would be the deepest

and most recently exhumed parts of the footwalls, while the oldest samples reside along the eastern portions of our transects.

Proponents of a gravity-slide interpretation for low-angle structures in these ranges prefer more modest extension models. These authors suggest that uplift and exhumation was accomplished by high-angle normal faults inferred at the range fronts of the Beaver Dam and Mormon Mountains (e.g., Carpenter and Carpenter, 1994a; Anders et al., 2006; Christie-Blick et al., 2007; Walker, 2008). However, our thermochronology data indicate that there may be problems with such interpretations. First, there is no systematic cooling age-elevation relationship observed in our data, as might be expected for exhumation along a high-angle fault (Stockli, 2005). Instead, samples collected from very similar elevations have vastly different cooling ages, a strong indication that paleoisotherms have been tilted or rotated. As such, an interpretation that invokes exhumation along a high-angle normal fault would narrow the distance between paleoisotherms and produce unreasonably high geothermal gradients. Second, models invoking extension along high-angle range-front faults would also require very deep basins west of the Beaver Dam and Mormon mountains, as our data demonstrate ~6-8 km of vertical exhumation. However, geophysical data gathered over these basins suggests they are shallow. For example, gravity modeling across the Meadow Valley Wash indicates that basement resides only ~1.5 km below the surface (Scheirer et al., 2006), consistent with seismic reflection data that show the top of basement at shallow two-way times (Carpenter and Carpenter, 1994a; Scheirer et al., 2006). Gravity data from the central and southern Virgin River Valley support the interpretation of a deep (~8 km) basin there, but the magnitude of the gravity anomaly diminishes significantly to north, suggesting that the portion of the basin adjacent to the

Beaver Dam Mountains is relatively shallow, inconsistent with the high-angle fault interpretation.

Conclusions

The new apatite and zircon (U-Th)/He thermochronometric data provide important insights into the kinematic histories of the Castle Cliffs, Tule Springs, and Mormon Peak detachments. Paleodepth reconstructions of the data, using published cross-section, demonstrate that the Beaver Dam Mountains have experienced more than 180˚C of cooling or ~7-8 km of exhumation since ~18 Ma; whereas, data from the Mormon Mountains and Tule Springs Hills show that these ranges have experienced ~5-7 km of exhumation since ~14 Ma.

The data from the Beaver Dam Mountains show that the Castle Cliffs Detachment initiated at the same time as other structures that lie along the western margin of the Colorado Plateau (Fitzgerald et al., 1991, 2003; 2009; Reiners et al., 2000; Bernet, 2002; Reiners, 2005; Quigley et al. 2010). This is a somewhat surprising result because it indicates that the detachment initiated as much as 5 Ma before faults to the west. The fault is interpreted to have remained active after slip on detachments to the west ceased, indicating the Castle Cliffs detachment is a long-lived structure and may be important boundary between tectonic provinces.

Our thermochronologically-based interpretations indicate that extension estimates for detachments in the region are too high (e.g., Wernicke et al., 1988; Axen et al., 1990); however, ~40 km of extension is allowed from our data, compatible with earlier assertions of large-magnitude extension between these ranges. Although we cannot rule out a gravity slide interpretation for low-angle structures in these ranges, the protracted cooling history, magnitude of exhumation, and pattern of cooling ages are most consistent with exhumation along a low-angle normal fault.

Acknowledgements

This research was supported by a Department of Defense, Research Assistantship and a University of Kanas, Patterson Fellowship to Bidgoli. We are grateful to Chad La Fever for assistance with sample collection and Roman Kislitsyn for guidance and support with sample preparation and analysis.

References cited

Allmendinger, R.W., Sharp, J.W., Von Tish, D., Serpa, L., Brown, L., Kaufman, S., and Oliver, J., 1983, Cenozoic and Mesozoic structure of the eastern Basin and Range province, Utah, from COCORP seismic reflection data: Geology, v. 11 p. 532-536.

Anders, M.H. and Christie-Blick, N., and Walker, C.D., 2006, Distinguishing between rooted and rootless detachments, a case from the Mormon Mountains of southeastern Nevada: Journal of Geology, v. 114, p. 645-664.

Anderson, E.M., 1942, The Dynamics of Faulting and Dyke Formation with Application to Britain: Oliver and Boyd, Edinburgh, 191 p.

Anderson, R.E., and Barnhard, T.P., 1993a, Heterogeneous Neogene strain and its bearing on horizontal extension and horizontal and vertical contraction at the margin of the extensional orogen, Mormon Mountains area, Nevada and Utah: U.S. Geological Survey Bulletin B2011, 113 p.

Anderson, R.E. and Barnhard, T.P., 1993b, Aspects of three-dimensional strain at the margin of the extensional orogen, Virgin River depression area, Nevada, Utah, and Arizona: Geological Society of America Bulletin, v.105, p. 1019-1052.

Anderson, R.E., Felger, T.J., Diehl, S.E., Page, W.R., and Workman, J.B., 2010, Integration of tectonic, sedimentary, and geohydrologic processes leading to a small-scale extension model for the Mormon Mountains area north of Lake Mead, Lincoln County, Nevada, *in* Umhoefer, P.J., Beard, L.S., and Lamb, M.A., eds., Miocene Tectonics of the Lake Mead Region, Central Basin and Range: Geological Society of America Special Paper 463, p. 395-426.

Armstrong, R.L., 1968, Sevier orogenic belt in Nevada and Utah: Geological Society of America Bulletin, v. 79, p. 429-458.

Armstrong, P.A., Taylor, A.R., and Ehlers, T.A., Is the Wasatch fault footwall (Utah, United States) segmented over million-year time scales?: Geology, v. 32, p. 385-388.

Axen, G.J., 1993, Ramp-flat detachment faulting and low-angle normal reactivation of the Tule Springs thrust, southern Nevada: Geological Society of America Bulleting, v. 105, p. 1076-1090.

Axen, G.J., 2004, Low-angle normal fault mechanics and crustal strength: in Karner, G.D., et al., (eds.), Rheology and deformation of the lithosphere at continental margins: New York, Columbia University Press, p. 46 – 91.

Axen, G.J., Grove, M., Stockli, D., Lovera, O.M., Rothstein, D.A., Fletcher, J.M., Farley, K., and Abbott, P.L., Thermal evolution of Monte Blanco dome: Low-angle normal faulting during Gulf of California rifting and late Eocene denudation of the eastern Peninsular Ranges: Tectonics, v. 19, p. 197-212.

Axen, G.J., and Wernicke, B.P., 1989, On the role of isostasy in the evolution of normal fault systems – Reply: Geology, v. 17, p. 775-556.

Axen, G.J., Wernicke, B.P., Skelly, M.F., Taylor, W.J., 1990, Mesozoic and Cenozoic tectonics of the Sevier thrust belt in the Virgin River Valley area, southern Nevada, in Wernicke, B.P., ed., Basin and Range Extensional Tectonics at the Latitude of Las Vegas, Nevada,: Geological Society of America Memoir 176, p. 123-153.

Bartley, J.M., and Wernicke, B.P., 1984, The Snake Range décollement interpreted as a major extensional shear zone: Tectonics, v. 3, p.647-657.

Bernet, M., Brandon, M., Garver, J. Reiners, P. Fitzgerald, P.G, 2002, Determining the zircon fission-track closure temperature: Geological Society of America Abstracts with Program, v. 34, p. 18.

Beutner, E.C., and Gerbi, G.P., 2005, Catastrophic emplacement of the Heart Mountain block slide, Wyoming and Montana, USA: Geological Society of America Bulletin, v. 117, p. 724-735.

Blank, H.R., and Kucks, R.P., 1989, Preliminary aeromagnetic, gravity, and generalized geologic maps of the USGS Basin and Range-Colorado Plateau transition zone study area in southwestern Utah, southeastern Nevada, and northwestern Arizona (the "BARCO" project): U.S. Geological Survey Open-File Report 89-432, 16 p. text, 3 plates, 1:250,000 scale.

Blythe, N. Umhoefer, P.J., Duebendorfer, E.M. and Beard, L.S., 2010, Development of Salt Spring Wash basin in the hanging wall of the White Hills detachment fault, Lake Mead domain, in Umhoefer, Paul J., Lamb, Melissa A., Beard, L.S., eds., Miocene Tectonics of the Lake Mead region: Geological Society of America Special Paper 463, p. 61-85.

Bohannon, R.G., 1983, Mesozoic and Cenozoic tectonic development of the Muddy, North Muddy, and northern Black Mountains, Clark County, Nevada, in Miller, D.M., Todd,

V.R., and Howard, K.A., eds., Tectonic and stratigraphic studies in the eastern Great Basin: Geological Society of America Memoir, v. 157, p. 125-148.

Carpenter, D.G., 1989, Geology of the North Muddy Mountains, Clark County, Nevada and regional structural synthesis: fold-thrust and basin-range structure in southern Nevada, southwest Utah, and northwest Arizona: [M.S. thesis], Corvallis, Oregon, Oregon State University, 145 p.

Carpenter, J.A. and Carpenter, D.G., 1994a, Analysis of basin-range and fold-thrust structure, and reinterpretation of the Mormon Peak detachment and similar features as gravity slide systems, southern Nevada, southwest Utah and northwest Arizona, *in* Dobbs, S.W., and Taylor, W.J., eds., Structural and stratigraphic investigations and petroleum potential of the Nevada, with special emphasis south of Railroad Valley producing trend: Reno, Nevada Petroleum Society Conference, v. 2, p. 15-52.

Carpenter, J.A. and Carpenter, D.G., 1994b, Fold-thrust structure , synorogenic rocks, and structural analysis of the North Muddy and Muddy Mountains, Clark County, Nevada, *in* Dobbs, S.W., and Taylor, W.J., eds., Structural and stratigraphic investigations and petroleum potential of the Nevada, with special emphasis south of Railroad Valley producing trend: Reno, Nevada Petroleum Society Conference, v. 2, p. 65-94.

Christie-Blick, N., Anders, M.H., Wills, S., Walker, C.D., and Renik, B., 2007, Observations from the Basin and Range Province (western United States) pertinent to the interpretation of regional detachment faults, *in* Karner G.D., Manatschal, G., and Pinheiro, L.M., eds.,: Imaging, Mapping and Modeling Continental Lithosphere Extension and Breakup, Geological Society of London Special Publication 282, p. 421 – 481.

Collettini, C. and Sibson, R.H., 2001, Normal faults, normal friction?: Geology, v. 29, p. 927-930.

Cook, E. F., 1960b, Breccia blocks (Mississippian) of the Welcome Springs area, southwest Utah: Geological Society of America Bulleting, v. 71, p. 1709–1712.

Davis, G.A., Anderson, J.L., Frost, E.G., and Shackelford, T.S., 1980, Mylonitization and detachment faulting in the Whipple-Buckskin-Rawhide Mountains terrane, southeastern California and western Arizona, *in* Crittenden, M.D., Jr., Coney, P.J., and Davis, G.H., eds., Cordilleran Metamorphic Core Complexes: Geological Society of America Memoir 153, p. 79-130.

Dobbin, C. E., 1939, Geologic structure of St. George District, Washington County, Utah: American Association of Petroleum Geologists Bulleting, v. 23, p. 121–144.

Dodson, M. H., 1973, Closure temperatures in cooling geological and petrological systems, Contributions to Mineralogy and Petrology, v. 40, p. 259–274.

Ehlers, T.A., 2005, Crustal Thermal Processes and the Interpretation of Thermochronometer Data, *in* Reiners, P.W. and Ehlers, T.A. eds., Thermochronology, Reviews in Mineralogy and Geochemistry, v. 58, p. 315-350.

Ehlers, T.A., Willett, S.D., Armstrong, P.A., and Chapman, D.S., 2003, Exhumation of the Central Wasatch Mountains, Utah: 2. Thermo-kinematics of exhumation, erosion and thermochronometer interpretation: Journal of Geophysical Research., v. 108, 2173

Farley, K.A., 2000, Helium diffusion from apatite: General behavior as illustrated by Durango fluorapatite: Journal of Geophysical Research: v. 105, p. 2903–2914, doi:10.1029/1999JB900348.

Farley, K.A., Rusmore, M.E., and Bogue, S.W., 2001, Exhumation and uplift history of the central Coast Mountains, British Columbia, from apatite (U-Th)/He Thermochronometry: Geology, v. 29, p. 99-102.

Farley, K.A., and Stockli, D.F., 2002, (U-Th)/ He dating of phosphates; apatite, monazite, and xenotime, *in* Kohn, M.J., Rakovan, J., and Hughes, J.M., eds., Phosphates; geochemical, geobiological, and materials importance., Mineralogical Society of America and Geochemical Society. Washington, DC, United States.

Farley, K.A., Wolf, R.A., and Silver, L.T., 1996, The effects of long alpha-stopping distances on (U-Th)/ He ages: Geochimica et Cosmochimica Acta, v. 60, p. 4223-4229.

Felger, T.J. and Beard, L.S., 2010, Geologic Map of Lake Mead and surrounding regions, southern Nevada, southwestern Utah, and northwestern Arizona, *in* Umhoefer, P.J., Beard, L.S., and Lamb, M.A., eds., Miocene Tectonics of the Lake Mead Region, Central Basin and Range: Geological Society of America Special Paper 463, p. 29-38.

Fitzgerald, P.G. and Gleadow, A.J.W., 1990, New approaches in fission track geochronology as a tectonic tool: Examples from the Transantarctic Mountains: Nuclear Tracks and Radiation Measurements, v. 17, p. 351-357.

Fitzgerald, P.G., Fryxell, J.E., and Wernicke, B.P., 1991, Miocene crustal extension and uplift in southeastern Nevada: Constraints from apatite fission track analysis: Geology, v. 19, p. 1013-1016.

Fitzgerald, P.G., O'Sullivan, P.B., Duebendorfer, E.M., Faulds, J.E., and Fryxell, J.E., 2003, Thermochronologic constraints on extension via detachment faulting in the White Hills of NW Arizona and Gold Butte Block of SE Nevada: Geological Society of America Abstracts with programs, v. 35, p. 348.

Fitzgerald, P.G., Duebendorfer, E.M. Faulds, J.E and O'Sullivan, P., 2009, South Virgin–White Hills detachment fault system of SE Nevada and NW Arizona: Applying apatite fission track thermochronology to constrain the tectonic evolution of a major continental detachment fault: Tectonics, v. 28, p. TC2001, doi:10.1029/2007TC002194.

Fleck, R.J., 1970, Tectonic style, magnitude, and age of deformation in the Sevier orogenic belter in southern Nevada and eastern California: Geological Society of America Bulletin, v. 81, p. 1705-1720.

Flowers R.M., Ketcham R.A., Shuster D.L., Farley K.A., 2009, Apatite (U-Th)/He thermochronometry using a radiation damage accumulation and annealing model, Geochimica et Cosmochimica Acta, v. 73, p. 2347-2365.

Flowers, R.M., Shuster, D.L., Wernicke, B.P., and Farley, K.A., 2007, Radiation damage control on apatite (U-Th)/He dates from the Grand Canyon region, Colorado Plateau: Geology, v. 35, p. 447–450, doi: 10.1130/G23471A.1.

Guenthner, W., Reiners, P.W., Ketcham, R.A., Nasdala, L., and Giester, G., 2013, Helium diffusion in natural zircon: Radiation damage, anisotropy, and the interpretation of zircon (U-Th)/He thermochronology: American Journal of Science, v. 313, p. 145-198.

Hintze, L.F., 1986, Stratigraphy and structure of the Beaver Dam Mountains, Utah, *in* Griffin, D.T., and Phillips, W.R., eds., Thrusting and Extensional Structures and Mineralization in the Beaver Dam Mountains, Southwestern Utah: Special Publication of Utah Geological Association, p. 1-36.

Hourigan, J. K., Reiners, P. W., and Brandon, M. T., 2005, U-Th zonation-dependent alpha-ejection in (U-Th)/He chronometry: Geochimica et Cosmochimica Acta, v. 69, p. 3349-3365.

House, M.A., Farley, K.A., and Kohn, B.P., 1999, An empirical test of helium diffusion in apatite; borehole data from the Otway Basin, Australia: Earth and Planetary Science Letters, v. 170, p. 463-474.

House, M.A., Farley, K.A., and Stockli, D., 2000, Helium chronometry of apatite and titanite using Nd-YAG laser heating: Earth and Planetary Science Letters, v. 183, p. 365-368.

Howard, K. A., and D. A. Foster, 1996, Thermal and unroofing history of a thick, tilted Basin-and-Range crustal section in the Tortilla Mountains, Arizona: Journal of Geophysical Research, v. 101, p. 511–522.

Hurley, P.M., 1952, Alpha ionization damage as a cause of low helium ratios: Transactions of the American Geophysical Union, v. 33, p. 174-183.

Jackson, J.A., 1987, Active normal faulting and crustal extension, in Coward, M.P., Dewey, J.F., and Hancock, P.L., eds., Continental Extensional Tectonics: Geological Society Special Publication 28, p. 3-18.

Jackson, J.A., and White N.J., 1989, Normal faulting in the upper continental crust: observations from regions of active extension: Journal of Structural Geology, v. 11, p. 15-36.

Karlstrom, K.E., Heizler, M., and Quigley, M.C., 2010, Structure and 40Ar/39Ar K-feldspar thermal history of the Gold Butte block: Reevaluation of the tilted crustal section model, *in* Umhoefer, P.J., Beard, L.S., and Lamb, M.A., eds., Miocene Tectonics of the Lake Mead Region, Central Basin and Range: Geological Society of America Special Paper 463, p. 331-352.

Lachenbruch, A. H., and Sass, J. H., 1980, Models of an extending lithosphere and heat flow in the Basin and Range province, *in* R. B. Smith and G. P. Eaton, eds., Cenozoic Tectonics and Regional Geophysics of the Western Cordillera, Memoir of the Geological Society of America, v.152, p. 209 – 250.

Lamb, M., K.L. Martin, T. Hickson, P.J. Umhoefer, L. Eaton, 2010, Deposition and age of the lower Horse Spring Formation in the Longwell Ridges area, *in* Umhoefer, Paul J., Lamb, Melissa A., Beard, L.S., eds., Miocene Tectonics of the Lake Mead region: Geological Society of America Special Paper 463, p. 171-201.

Lee, J., Stockli, D.F., Owen, L.A., Finkel, R.C., and Kislitsyn, R., 2009, Exhumation of the Inyo Mountains, California: Implications for the timing of extension along the western boundary of the Basin and Range Province and distribution of dextral fault slip rates across the eastern California shear zone: Tectonics, v. 28, TC1001, doi:10.1029/2008TC002295.

Lippolt, H.J., Leitz, M., Wernicke, R.S., and Hagedorn, B., 1994, (Uranium+thorium)/ helium dating of apatite; experience with samples from different geochemical environments: Chemical Geology, v. 112, p. 179-191.

Longwell, C.R., 1949, Structure of the Northern Muddy Mountains area, Nevada: Geological Society of America Bulletin, v. 60, p. 923-968.

Miller, E. L., T. A. Dumitru, R. Brown, and B. Gans, 1999, Rapid Miocene slip on the Snake Range-Deep Creek Range fault system, east-central Nevada: Geological Society of America Bulletin, v. 111, p. 886–905.

Nasdala, L., Reiners, P.W., Garver, J.I., Kennedy, A.K., Stern, R.A., Balan, E., and Wirth, R., 2004, Incomplete retention of radiation damage in zircon from Sri Lanka: American Mineralogist, v. 89, p. 219-231.

Nasdala, L., Grambole, D., Gotze, J., Kempe, U., and Vaczi, T., 2011, Helium irradiation study on zircon: Contributions to Mineralogy and Petrology, v. 161, p. 777-789.

Olmore, S.D., 1971, Style and evolution of thrusts in the region of the Mormon Mountains, Nevada [Ph.D. thesis]: Salt Lake City, Utah, University of Utah, 213 p.

O'Sullivan, P., Carpenter, D. G. and Carpenter, J. A., 1994, Cooling history of the Beaver Dam Mountains, Utah: Determined by apatite fission track analysis, *in* Dobbs, S.W., and Taylor, W.J., (eds.): Structural and stratigraphic investigations and petroleum potential of

Nevada, with special emphasis south of the Railroad Valley producing trend, Nevada Petroleum Society, Reno, Nevada, p. 53 – 64.

Quigley, M.C., Karlstrom, K.E., Kelley, S., and Heizler, M., 2010, Time and mechanisms of basement uplift in the Colorado Plateau-Basin and Range transition zone, Virgin Mountain anticline, Nevada-Arizona, *in* Umhoefer, P.J., Beard, L.S., and Lamb, M.A., eds., Miocene Tectonics of the Lake Mead Region, Central Basin and Range: Geological Society of America Special Paper 463, p. 311-329.

Reich, M., Ewing, R.C., Ehlers, T.A., and Becker, U., 2007, Low-temperature anisotropic diffusion of helium in zircon: Implications for zircon (U-Th)/He thermochronometry, Geochimica et Cosmochimica Acta, v. 71, p. 3119-3130.

Reiners, P.W., 2005, Zircon (U-Th)/He Thermochronometry, *in* Reiners, P.W. and Ehlers, T.A. eds., Thermochronology, Reviews in Mineralogy and Geochemistry, v. 58, p. 151-176.

Reiners, P.W., Brady, R., Farley, K.A., Fryxell, J.E., Wernicke, B.P., and Lux, D., 2000, Helium and Argon thermochronometry of the Gold Butte block, South Virgin Mountains, Nevada: Earth and Planetary Science Letters, v. 178, p. 315-326.

Reiners, P.W., and Farley, K.A., 2001, Influence of crystal size on apatite (U-Th)/He thermochronology: An example from the Bighorn Mountains, Wyoming: Earth and Planetary Science Letters, v. 188, p. 413-420.

Reiners, P.W., Farley, K.A., and Hickes, H.J., 2002, He diffusion and (U-Th)/He thermochronometry of zircon: Initial results from Fish Canyon Tuff and Gold Butte: Tectonophysics, v. 349, p. 247–308.

Reiners, P.W., Spell, T.L., Nicolescu, S., and Zanetti, K.A., 2004, Zircon (U-TH)/He thermochronometry: He diffusion and comparison with 40Ar/39Ar dating: Geochimica et Cosmochimica Acta, v. 68, p. 1857-1887.Shuster, D.L., Flowers, R.M., and Farley, K.A., 2006, The influence of natural radiation damage on helium diffusion kinetics in apatite: Earth and Planetary Science Letters, v. 249, doi: 10.1016/j.epsl.2006.07.028.

Rowley, P.D., Nealey, L.D., Unruh, D.M., Snee, L.W., Mehnert, H.H., Anderson, R.E., and Gromme, C.S., 1995, Stratigraphy of Miocene ash-flow tuffs in and near the Caliente caldera complex, southeastern Nevada and southwestern Utah, *in* Scott, R.B. and Swadley, W.C., eds., Geologic studies in the Basin and Range–Colorado Plateau transition in southeastern Nevada, southwestern Utah and northwestern Arizona: U.S. Geological Survey Bulletin 2056-A, p. 42-87.

Scheirer, D. S., Page, W.R., and Miller, J. J., 2006, Geophysical studies based on gravity and seismic data of Tule Desert, Meadow Valley Wash, and California Wash Basins, Southern Nevada; U.S. Geological Survey Open-File Report 2006-1396, 44 pp.

Scott, R.B., Gromme, C.S., Best, M.G., Rosenbaum, J.G., and Hudson, M.R., 1995, Stratigraphic relations of Tertiary volcanic rocks in central Lincoln County, southeastern Nevada, *in* Scott, R.B. and Swadley, W.C., eds., Geologic Studies in the Basin and Range–Colorado Plateau Transition in Southeastern Nevada, Southwestern Utah and Northwestern Arizona: U.S. Geological Survey Bulletin 2056-A, p. 5-41.

Shuster D. L., Flowers R. M., and Farley K. A., 2006, The influence of natural radiation damage on helium diffusion kinetics in apatite. Earth and Planetary Science Letters 249(3-4), 148-161.

Spotila, J., 2005, Application of Low-Temperature Thermochronometry to Quantification of Recent Exhumation in Mountain Belts, *in* Reiners, P.W. and Ehlers, T.A. eds., Thermochronology, Reviews in Mineralogy and Geochemistry, v. 58, p. 449-466.

Stockli, D.F., 1999, Regional timing and spatial distribution of Miocene extension in the northern Basin and Range province [Ph.D. thesis]: Stanford, California, Stanford University, 239 pp.

Stockli, D.F., 2005, Application of Low-Temperature Thermochronometry to Extensional Tectonic Settings, *in* Reiners, P.W. and Ehlers, T.A. eds., Thermochronology, Reviews in Mineralogy and Geochemistry, v. 58, p. p. 420-461.

Stockli, D.F., Farley, K.A. and Dumitru, T.A., 2000, Calibration of the (U-Th)/He thermochronometer on an exhumed normal fault block in the White Mountains, eastern California and western Nevada: Geology, v. 28; no. 11, p. 983-986.

Stockli, D.F., Dumitru, T.A., McWilliams, M.O., and Farley, K.A., 2003, Cenozoic tectonic evolution of the White Mountains, California and Nevada: Geological Society of America Bulletin, v. 115, p. 788-816.

Stockli, D.F., Farley, K.A., and Dumitru, T.A., 2000, Calibration of the apatite (U-Th)/ He thermochronometer on an exhumed fault block, White Mountains, California: Geology, v. 28, p. 983-986.

Stockli, D.F., Surpless, B.E., and Dumitru, T.A., 2002, Thermochronological constraints on the timing and magnitude of Miocene and Pliocene extension in the central Wassuk Range, western Nevada: Tectonics, v. 21, p. 10-1 – 10-19.

Thatcher, W. and Hill, D.P., 1991, Fault orientations in extensional and conjugate strike-slip environments and their implications: Geology, v. 19, p. 1116-1120.

Tschanz, C.M., and Pampeyan, E.H., 1970, Geology and mineral deposits of Lincoln County, Nevada: Nevada Bureau of Mines and Geology Bulletin 73, 188 p.

Walker, C.D., Anders, M.H., and Christie-Blick, N., 2007, Kinematic evidence for downdip movement on the Mormon Peak detachment: Geology, v. 35, p. 259-262.

Walker, C.D., 2008; A gravity slide origin for the Mormon Peak detachment: Re-examining the evidence for extreme extension in the Mormon Mountains, southeastern Nevada, U.S.A. [Ph.D. thesis]: New York, New York, Columbia University, 690 p.

Wernicke, B.P., 1992, Cenozoic extensional tectonics of the U.S. Cordillera, in Burchfield, B.C., Lipman, P.W., and Zoback, M.L., eds., Geology of North America, Volume G-3, The Cordilleran Orogen: Conterminous U.S: Geological Society of America, p. 553–581.Wernicke, B. and Axen, G.J., 1988, On the role of isostasy in the evolution of normal fault systems: Geology, v. 16, p. 848-851.

Wernicke, B, Axen, G.J. and Snow, J.K., 1988, Basin and Range extensional tectonics at the latitude of Las Vegas, Nevada: Geological Society of America Bulletin, v. 100, p. 1738-1757.

Wernicke, B.P., Walker, J.D., and Beaufait, M.S., 1985, Structural discordance between Neogene detachments and frontal Sevier thrusts, central Mormon Mountains, southern Nevada: Tectonics, v. 4, p. 213-246.

Wernicke, B, Axen, G.J. and Snow, J.K., 1988, Basin and Range extensional tectonics at the latitude of Las Vegas, Nevada: Geological Society of America Bulletin, v. 100, p. 1738-1757.

Wolf, R.A., Farley, K.A., and Silver, L.T., 1996, Helium diffusion and low temperature thermochronometry of apatite: Geochimica et Cosmochimica Acta, v. 60, p. 4231-4240.

Wolf, R.A., Farley, K.A., and Kass, D.M., 1998, Modeling of the temperature sensitivity of the apatite (U-Th)/ He thermochronometer: Chemical Geology, v. 148, p. 105-114.

Wolfe, M.R., and Stockli, D.F., 2010, Zircon (U-Th)/He thermochronometry in the KTB drillhole, Germany, and its implications for bulk He diffusion kinetics in zircon: Earth And Planetary Science Letters, v. 295, p. 69-82.

Figure captions

Figure 2.1. (a) Color shaded relief map of the study area and surrounding region. Warm colors correspond to the ranges and cool colors to the basins. Major faults (after Wernicke et al., 1988) are shown in black. BD – Beaver Dam Mountains; CM – Clark Mountains; FM – Frenchman Mountain; KR – Kingston Range; MC – McCullough Range; MD – Muddy Mountains; MM – Mormon Mountains; NR – Nopah Range; NVM – North Virgin Mountains; PT – Pintwater Range; SP – Sheep Range; ST – Spotted Range; SVM

– South Virgin Mountains; TS – Tule Springs Hills. (b) Simplified deformed-state cross-section showing major low-angle normal faults between the Beaver Dam Mountains and Meadow Valley Mountains. Modified from Axen et al., (1990). Cross-section location is show in Figure 1a.

Figure 2.2. Simplified geologic map of the of the study area showing the locations of the Castle Cliffs, Tule Springs, and Mormon Peak detachments. Red dots correspond to the locations of our thermochronology samples. Geology simplified from compilation by Felger and Beard (2010).

Figure 2.3. (a) (U-Th)/He dates versus [U]e for samples from the Beaver Dam Mountains. The data show a strong negative correlation. (b) The same data rescaled to show only samples < 200 Ma. (c) (U-Th)/He date versus [U]e plot for the Mormon Mountains and Tule Springs Hills, showing a similar negative correlation.

Figure 2.4. Geologic cross section B-B' across the Beaver Dam Mountains showing geometries of the Beaver Dam "anticline" and the Castle Cliffs detachment. Thermochronology samples, shown as red dots, have been projected into the plane of the cross-section, which is oriented ~parallel to the inferred slip direction of the fault. Although all samples came from the footwall of the detachment, in this projected view they may lie above or below topography of the section line. Mean zircon (U-Th)/He ages and errors (1σ standard deviation) are shown above each sample. Cross section location is shown in Figure 2. Cross section modified from Axen et al., (1990) and Stockli (1999).

Figure 2.5. (a) Restored-state cross section across the Beaver Dam Mountains showing the initial dip of the Castle Cliffs detachment and the pre-extensional configuration of our thermochronology samples. Modified from Axen et al. 1990. (b) Mean zircon (U-Th)

He ages (black diamonds) versus distance from the Precambrian nonconformity. Error bars are 1σ standard deviations. Data reveal an exhumed zircon He partial retention zone. Apatite fission-track ages (red squares) and exhumed partial annealing zone from Stockli (1999) are also shown. AFT – Apatite Fission Track; AFT PAZ – Apatite Fission-Track Partial Annealing Zone; ZHe – Zircon Helium; ZPRZ – Zircon Helium Partial Retention Zone.

Figure 2.6. (a) Mean zircon (U-Th)/He ages (black diamonds) versus distance from the Precambrian nonconformity. Error bars are 1σ standard deviations. Sample numbers refer to Table 2.1. Apatite fission-track ages (red squares) and exhumed partial annealing zone from Stockli (1999) are also shown. Shaded area corresponds to the approximate position of the zircon He partial retention zone. Hachured area shows uncertainty in position of the ~190°C isotherm. Given the uncertainty, the distance between the top and base of the partial retention zone may be anywhere from 1.9 to 2.4 km, resulting in a geothermal gradient of 28 +/-3°C/km. (b) The same paleodepth reconstruction can be used to calculate the distance between the base of the apatite fission-track partial annealing zone (~110°C isotherm) from Stockli (1999) and the base of zircon He partial retention zone (~190°C isotherm). However, the high degree of uncertainty in the position of the isotherms (hachured areas), results in anywhere from 1.9 to 4.9 km between paleoisotherms and a geothermal gradient of 29+/-13°C/km. AFT – Apatite Fission Track; AFT PAZ – Apatite Fission-Track Partial Annealing Zone; ZHe – Zircon Helium; ZPRZ – Zircon Helium Partial Retention Zone.

Figure 2.7. Geologic cross section C-C' across the Mormon Mountains showing the geometries of the Mormon Peak and Tule Springs detachments. Cross section is oriented ~parallel to

the slip direction of the faults. Thermochronology samples, shown as red dots, are projected into the plane of the cross-section. In this projected view, samples may lie above or below topography of the section line. Mean zircon and apatite (U-Th)/He ages and errors (1σ standard deviation) are shown above each sample. Cross section location is shown in Figure 2. (b) Restored-state cross section shows the initial dips of the detachments and the pre-extensional configuration of our thermochronology samples. Cross-sections are modified from Axen et al. 1990. (c) Mean zircon and apatite (U-Th) He ages versus distance from the Tertiary unconformity. Error bars are 1σ standard deviations. Cross-sections are modified from Axen et al. 1990. AHe - Apatite Helium; MPD – Mormon Peak Detachment; St Dev – Standard Deviation; ZHe – Zircon Helium.

Figure 2.8. Geologic cross section D-D' across the Mormon Mountains and Tule Springs Hills showing the geometries of the Tule Springs and Castle Cliffs detachments. Cross section is oriented ~parallel to the slip direction of the faults. Thermochronology samples, shown as red dots, are projected into the plane of the cross-section. In this projected view, samples may lie above or below topography of the section line. Mean zircon and apatite (U-Th)/He ages and errors (1σ standard deviation) are shown above each sample. Cross section location is shown in Figure 2. (b) Restored-state cross section shows the initial dips of the detachments and the pre-extensional configuration of our samples. Cross-sections are modified from Axen et al. 1990. (c) Mean zircon and apatite (U-Th) He ages versus distance from the Tertiary unconformity. Error bars are 1σ standard deviations. AHe - Apatite Helium; MPD – Mormon Peak Detachment; St Dev – Standard Deviation; ZHe – Zircon Helium.

Figure 2.9. (a) Mean zircon and apatite (U-Th)/He ages from the footwalls of the Mormon Peak and Tule Springs detachments plotted against distance from the Tertiary unconformity. Error bars are 1σ standard deviations. Sample numbers refer to Table 2.1. Shaded area corresponds to the approximate position of the zircon He partial retention zone. Hachured area shows uncertainty in position of the ~190°C isotherm. (b) Shows the same paleodepth reconstruction rescaled to only show samples <40 Ma. Shaded area corresponds to the approximate position of the apatite He partial retention zone. Hachured areas show uncertainties in position of the ~80°C and 190°C isotherms. AHe – Apatite Helium; APRZ – Apatite Helium Partial Retention Zone; MPD – Mormon Peak detachment; TSD – Tule Springs detachment; ZHe – Zircon Helium; ZPRZ – Zircon Helium Partial Retention Zone.

Figure 2.10. Zircon (U-Th)/He date versus distance from the Precambrian nonconformity for the Beaver Dam Mountains. The size of each He date is scaled to the [U]e. Black lines correspond to approximate shape of the zircon He partial retention zone at high (>600 ppm) and low (<200 ppm) [U]e. The interpreted positions of the isotherms at the top and base of the zircon He partial retention zone are shown as dashed lines.

Table 2.1. Zircon and apatite (U-Th)/He data

Beaver Dam Mountains zircon data

Sample	Latitude	Longitude	Elev. (m)	Mass (mg)	Ft*	U (ppm)	Th (ppm)	Sm (ppm)	[U]e	Th/U	He (nmol/g)	Mean age (Ma)	St.Dev.† (Ma.	Replicates
95BR102	37.084090	-113.911868	1250	5.88	0.77	573.5	35.7	1.1	581.8	0.1	45.587	18.8	1.7	3
95BR103	37.086105	-113.908844	1300	5.59	0.76	613.3	216.6	1.4	663.2	0.3	49.142	18.2	1.6	3
95BR104	37.084152	-113.902723	1390	3.58	0.74	724.8	22.6	1.6	730.0	0.0	49.874	17.1	1.9	3
95BR105	37.090440	-113.896418	1450	4.18	0.75	324.6	81.8	2.0	343.4	0.2	91.667	72.6	26.5	6
95BR106	37.089592	-113.893245	1420	4.27	0.75	263.2	58.1	1.3	276.6	0.2	80.658	75.7	58.5	6
95BR109	37.084821	-113.886686	1340	6.27	0.77	450.5	91.5	2.9	471.5	0.2	105.701	56.5	21.0	5
95BR110	37.086551	-113.881132	1335	4.19	0.75	420.3	85.6	1.6	440.0	0.2	112.365	74.7	43.4	7
95BR111	37.089775	-113.875986	1145	4.25	0.74	664.3	250.5	11.7	722.0	0.4	53.864	18.8	1.9	3
95BR112	37.087679	-113.870951	1335	5.37	0.76	498.6	78.2	6.4	516.6	0.2	104.105	59.1	32.3	7
95BR113	37.087800	-113.865790	1405	4.40	0.75	635.6	94.1	4.3	657.2	0.2	90.678	38.0	11.9	7
95BR115	37.094251	-113.853044	1400	5.26	0.76	416.6	66.2	3.4	431.8	0.2	105.204	62.3	12.7	6
95BR116	37.094099	-113.851708	1430	6.86	0.76	121.3	218.1	7.0	171.6	2.0	238.871	340.2	91.1	7
95BR119	37.131019	-113.819133	1315	8.93	0.79	99.8	55.9	5.8	112.7	1.0	163.789	445.1	318.8	7
95BR120	37.134219	-113.817980	1320	3.21	0.72	403.6	170.2	9.1	442.9	0.5	392.207	276.3	134.7	3
95BR122	37.185778	-113.781115	1035	6.80	0.78	252.5	90.7	2.3	273.4	0.4	293.450	265.2	52.0	3
95BR124	37.244919	-113.778249	1035	11.28	0.81	59.2	32.5	0.7	66.6	0.5	208.257	649.1	350.4	3
Tule Springs Hills zircon data														
11TS01	37.091740	-114.219914	1065	3.74	0.72	181.2	118.5	0.8	208.5	0.7	168.187	217.9	87.1	3
11TS02	37.085329	-114.224719	1040	10.33	0.80	296.8	111.3	1.0	322.5	0.4	309.009	222.9	31.7	3
11TS04	37.065468	-114.240961	1015	16.76	0.83	853.0	300.8	5.7	922.3	0.4	36.502	8.8	0.4	3
11TS06	37.060374	-114.252700	980	5.41	0.75	1086.5	492.9	2.2	1200.0	0.5	54.620	11.2	0.2	3
11TS08	37.057649	-114.266847	1005	7.44	0.78	129.6	61.6	1.3	143.8	0.5	199.323	347.6	171.7	3
11TS09	37.055451	-114.258261	975	8.25	0.78	808.7	330.2	1.9	884.7	0.5	53.408	34.9	45.3	3

(continued)

Table 2.1. Zircon and apatite (U-Th)/He data (continued)

Sample	Latitude	Longitude	Elev. (m)	Mass (µg)	Ft*	U (ppm)	Th (ppm)	Sm (ppm)	[U]e	Th/U	He (nmol/g)	Mean age (Ma)	St.Dev.† (Ma)	Replicates
Tule Springs Hills apatite data														
11TS02	37.085329	-114.224719	1040	2.35	0.67	6.2	5.3	36.4	7.6	1.0	0.631	24.0	7.3	3
11TS03	37.072333	-114.239118	1060	1.64	0.63	29.1	52.0	57.3	41.4	1.5	3.560	25.0	1.5	2
11TS06	37.060374	-114.252700	980	1.26	0.60	6.7	12.4	43.1	9.8	2.1	1.001	27.6	6.2	4
11TS07	37.053699	-114.273554	1000	0.39	0.45	6.3	7.3	32.2	8.2	1.9	0.327	16.0	3.7	4
11TS09	37.055451	-114.258261	975	0.30	0.41	10.7	18.0	33.5	15.0	3.0	0.613	18.0	2.7	4
Mormon Mountain zircon data														
96BR003	36.916151	-114.277625	930	2.73	0.71	310.7	216.1	10.4	360.5	0.6	61.842	66.3	47.9	5
96BR005	36.949433	-114.286667	945	5.03	0.76	309.7	85.5	2.4	329.4	0.3	69.990	54.9	23.3	5
96BR006	36.970822	-114.299497	935	4.48	0.74	377.1	170.8	3.8	416.4	0.5	75.945	85.1	149.4	6
96BR008	36.938966	-114.293648	1030	3.93	0.73	303.5	134.5	3.0	334.4	0.4	28.676	21.6	1.0	3
96BR009	36.923159	-114.454233	1700	4.35	0.75	442.0	85.2	15.5	461.7	0.2	25.051	13.4	1.0	3
96BR010	36.920278	-114.451065	1660	3.58	0.73	532.7	48.5	3.8	543.8	0.1	29.880	13.9	0.8	3
96BR011	36.917119	-114.439676	1540	8.30	0.78	129.9	118.0	4.6	157.1	1.0	44.090	84.2	78.4	7
96BR012	36.971732	-114.544837	1290	4.93	0.75	146.7	47.5	4.0	157.7	0.4	16.245	24.7	10.9	7
96BR014	36.973663	-114.555490	1170	3.68	0.74	292.2	48.9	6.7	303.5	0.2	21.075	17.2	3.1	7
96BR016	36.975915	-114.563448	1110	4.49	0.75	394.3	80.3	2.7	412.8	0.2	23.171	14.3	2.1	7
Mormon Mountain apatite data														
96BR004	36.946503	-114.283040	915	1.91	0.63	3.7	3.4	40.6	4.7	1.2	0.215	13.8	2.2	2
96BR005	36.949433	-114.286667	945	1.29	0.61	7.8	6.2	40.0	9.5	0.8	0.465	14.6	0.5	3
96BR006	36.970822	-114.299497	935	0.24	0.39	15.2	2.2	99.4	16.2	0.1	0.461	13.4	-	1
96BR009	36.923159	-114.454233	1700	1.78	0.66	16.1	5.2	22.7	17.5	0.3	0.916	13.7	2.2	2
96BR010	36.920278	-114.451065	1660	0.72	0.55	4.8	3.1	55.5	5.8	0.7	0.218	12.1	0.2	2
96BR013	36.972881	-114.551783	1200	1.30	0.64	7.6	1.4	9.1	8.0	0.2	0.291	10.5	-	1
96BR014	36.973663	-114.555490	1170	1.24	0.60	1.6	3.2	9.4	2.4	2.0	0.082	10.2	-	1

Note: Individual aliquot analyses are given in supplementary data tables

*Ft is the alpha ejection correction of Farley et al. (1996)

†St. Dev.—standard deviation.

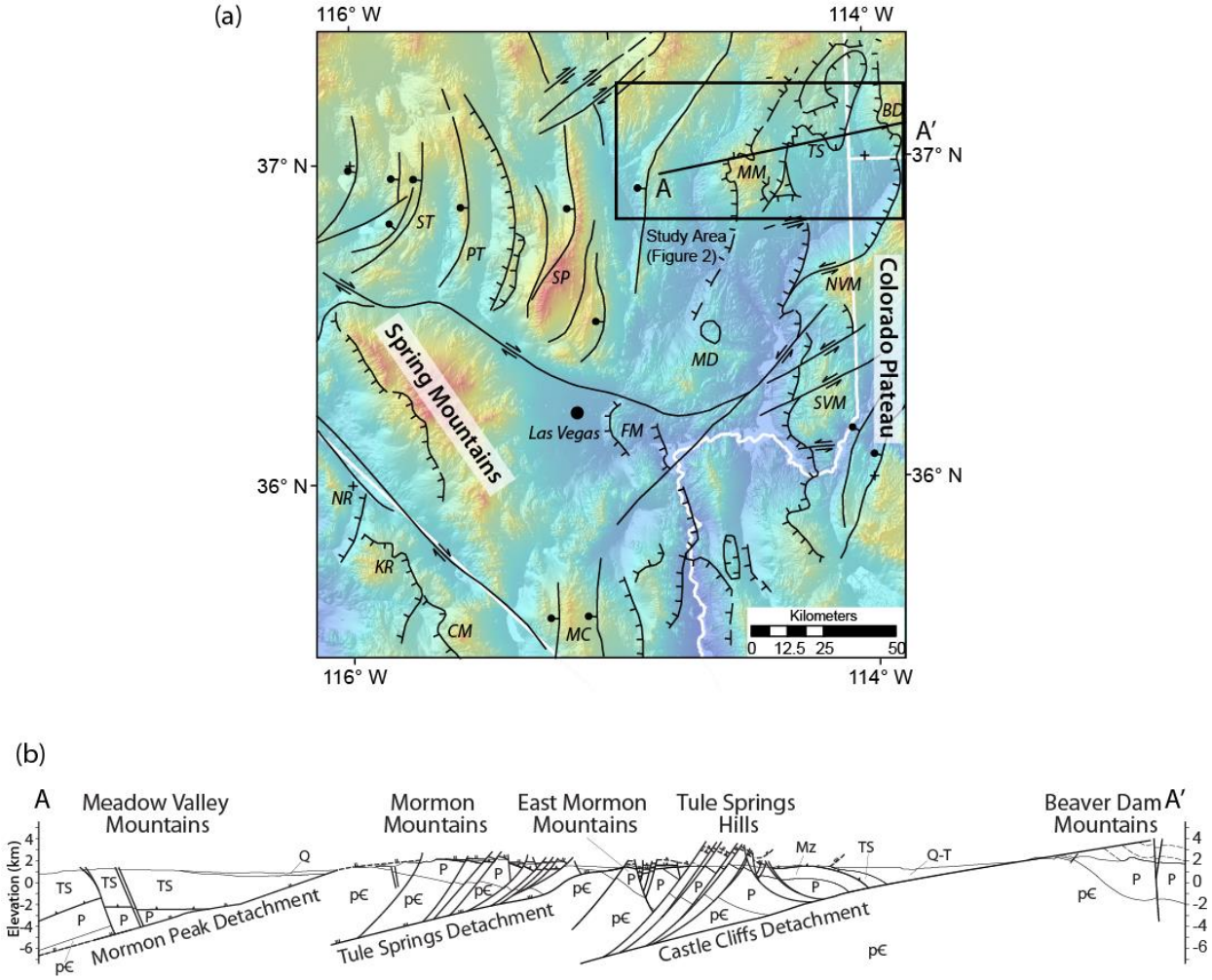
(a)
116° W
114° W
37° N
36° N
A
A′
BD
TS
MM
ST
PT
SP
Study Area
(Figure 2)
NVM
Colorado Plateau
MD
SVM
Spring Mountains
Las Vegas
FM
NR
KR
CM
MC
Kilometers
0 12.5 25 50
(b)
A
Meadow Valley
Mountains
Mormon
Mountains
East Mormon
Mountains
Tule Springs
Hills
Beaver Dam
Mountains
A′
Elevation (km)
Q
TS
P
Mz
Q-T
pЄ
Mormon Peak Detachment
Tule Springs Detachment
Castle Cliffs Detachment

Figure 2.1

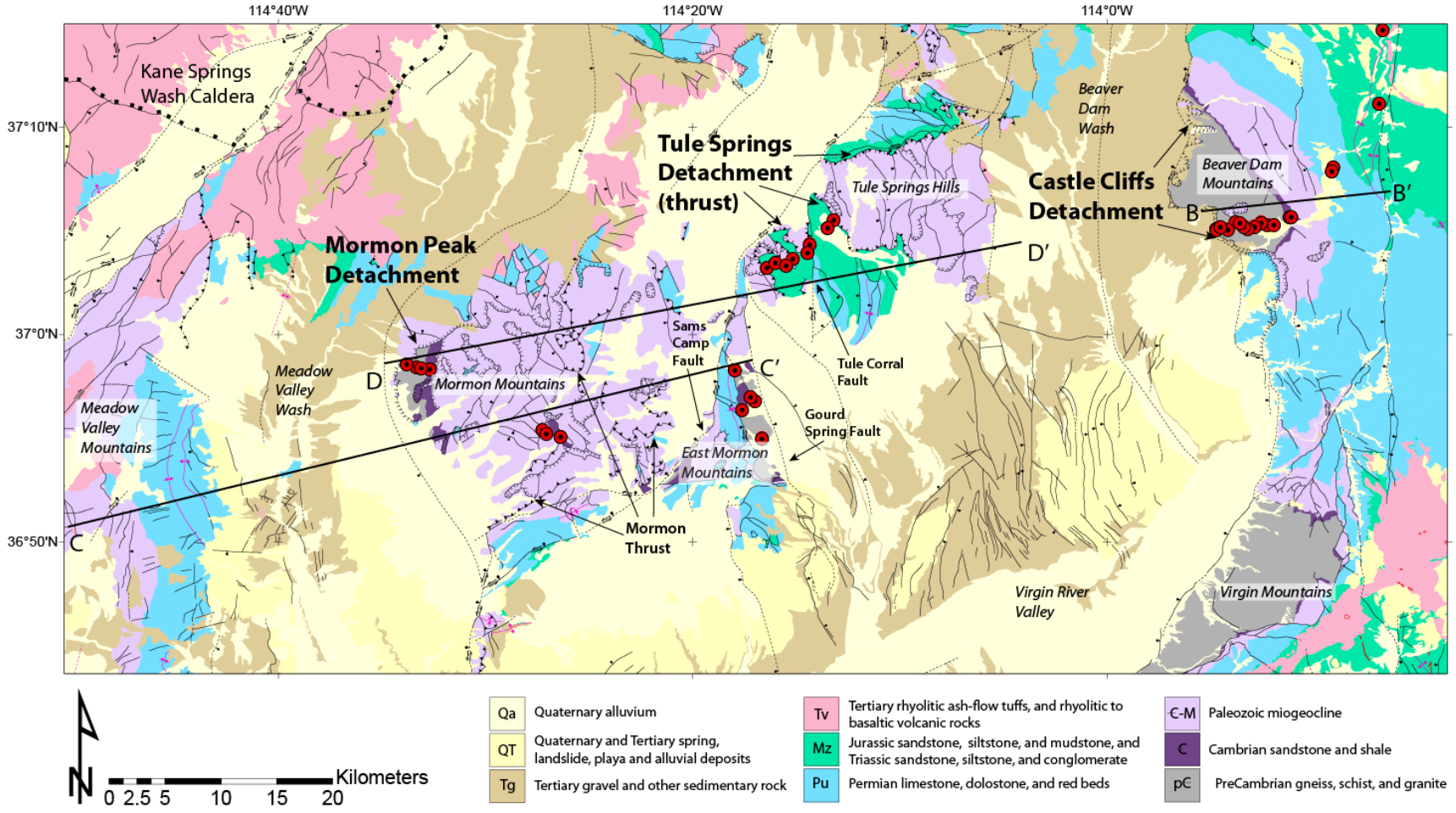
114°40'W
114°20'W
114°0'W
37°10'N
37°0'N
36°50'N
Kane Springs Wash Caldera
Tule Springs Detachment (thrust)
Mormon Peak Detachment
Castle Cliffs Detachment
Beaver Dam Wash
Beaver Dam Mountains
Tule Springs Hills
Sams Camp Fault
Tule Corral Fault
Gourd Spring Fault
Meadow Valley Wash
Meadow Valley Mountains
Mormon Mountains
East Mormon Mountains
Mormon Thrust
Virgin River Valley
Virgin Mountains
A
A′
B
B′
C
C′
D
D′
N
0 2.5 5 10 15 20
Kilometers
Qa Quaternary alluvium
QT Quaternary and Tertiary spring, landslide, playa and alluvial deposits
Tg Tertiary gravel and other sedimentary rock
Tv Tertiary rhyolitic ash-flow tuffs, and rhyolitic to basaltic volcanic rocks
Mz Jurassic sandstone, siltstone, and mudstone, and Triassic sandstone, siltstone, and conglomerate
Pu Permian limestone, dolostone, and red beds
Є-M Paleozoic miogeocline
C Cambrian sandstone and shale
pC PreCambrian gneiss, schist, and granite

Figure 2.2

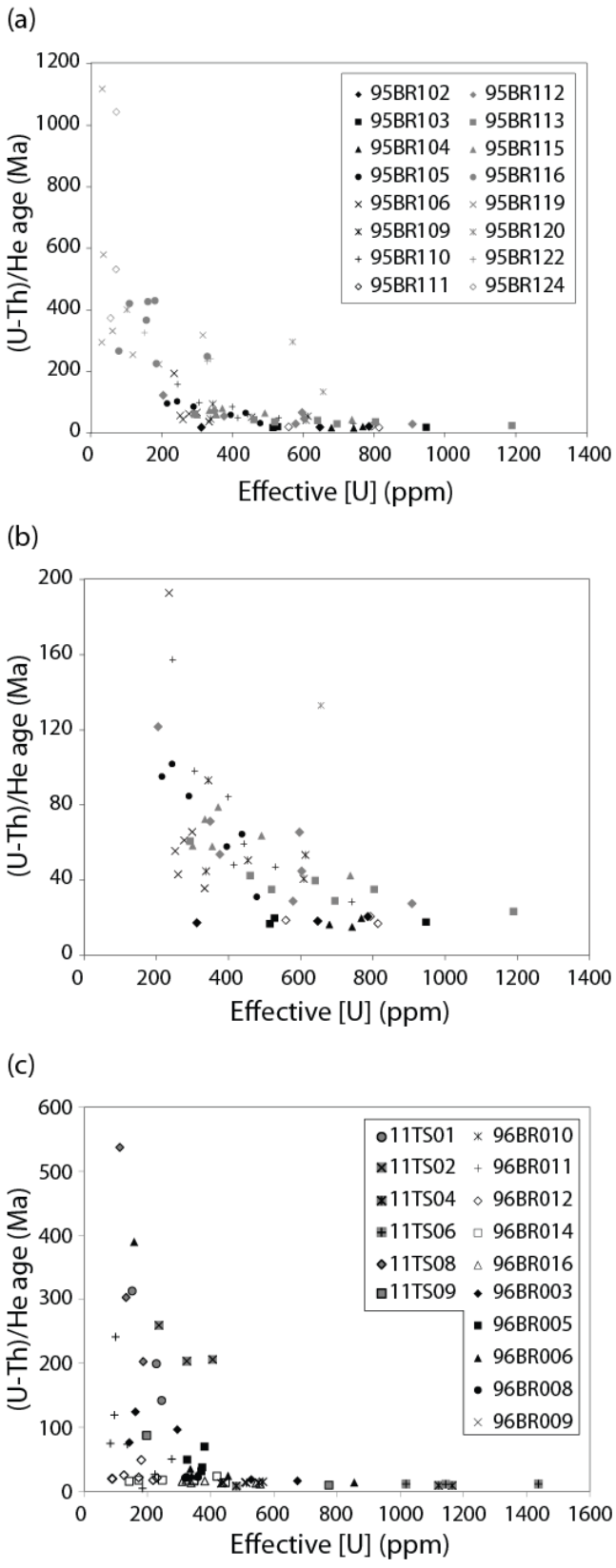
(a)
(U-Th)/He age (Ma)
Effective [U] (ppm)
95BR102
95BR103
95BR104
95BR105
95BR106
95BR109
95BR110
95BR111
95BR112
95BR113
95BR115
95BR116
95BR119
95BR120
95BR122
95BR124
(b)
(U-Th)/He age (Ma)
Effective [U] (ppm)
(c)
(U-Th)/He age (Ma)
Effective [U] (ppm)
11TS01
11TS02
11TS04
11TS06
11TS08
11TS09
96BR010
96BR011
96BR012
96BR014
96BR016
96BR003
96BR005
96BR006
96BR008
96BR009

Figure 2.3

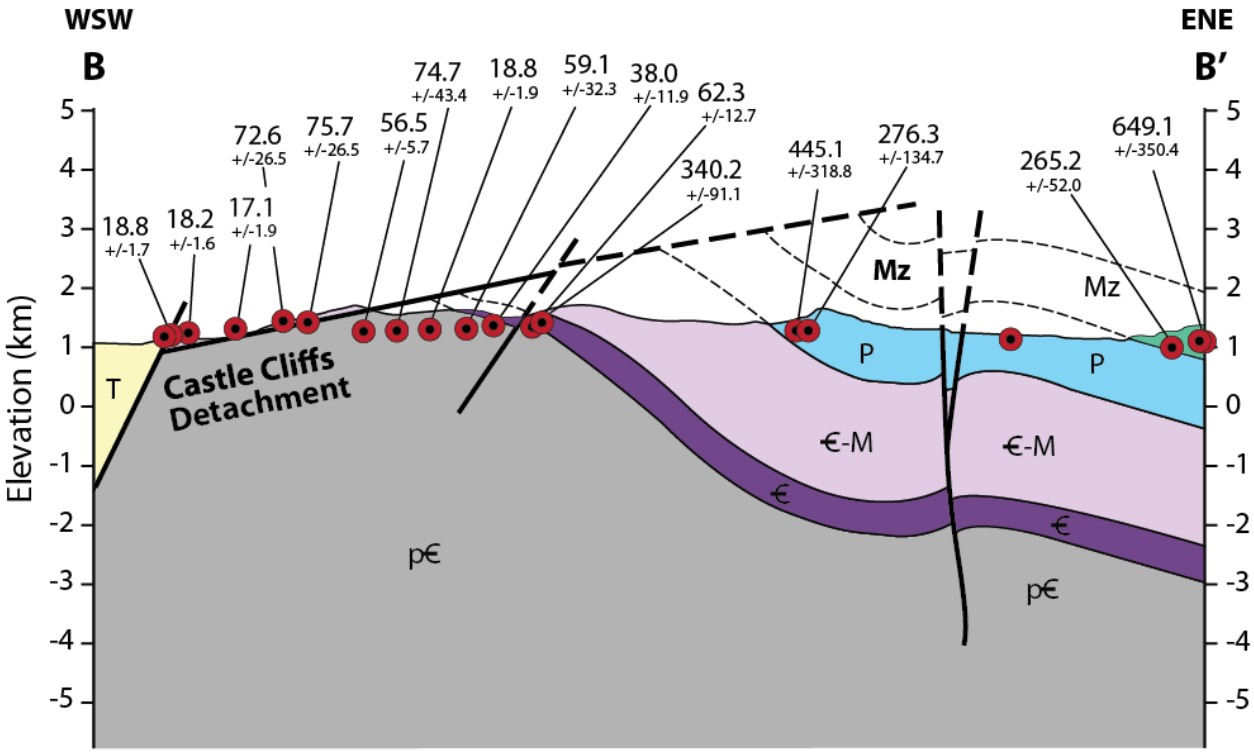
WSW
B
ENE
B′
Elevation (km)
5
4
3
2
1
0
-1
-2
-3
-4
-5
18.8 +/-1.7
18.2 +/-1.6
17.1 +/-1.9
72.6 +/-26.5
75.7 +/-26.5
56.5 +/-5.7
74.7 +/-43.4
18.8 +/-1.9
59.1 +/-32.3
38.0 +/-11.9
62.3 +/-12.7
340.2 +/-91.1
445.1 +/-318.8
276.3 +/-134.7
265.2 +/-52.0
649.1 +/-350.4
T
Castle Cliffs Detachment
Mz
Mz
P
P
€-M
€-M
€
€
p€
p€

Figure 2.4

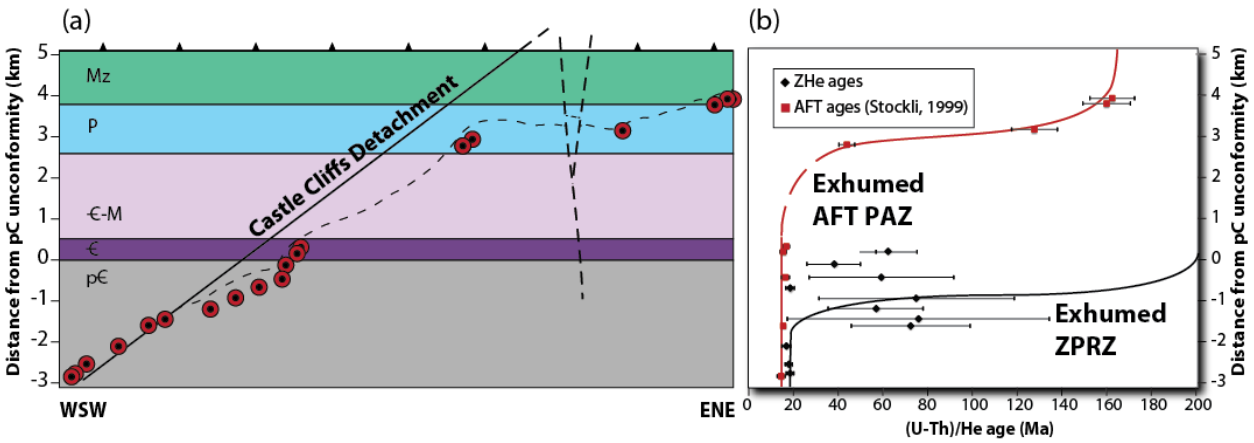
(a)
(b)
Mz
P
€-M
€
p€
Castle Cliffs Detachment
WSW
ENE
Distance from pC unconformity (km)
ZHe ages
AFT ages (Stockli, 1999)
Exhumed
AFT PAZ
Exhumed
ZPRZ
(U-Th)/He age (Ma)

Figure 2.5

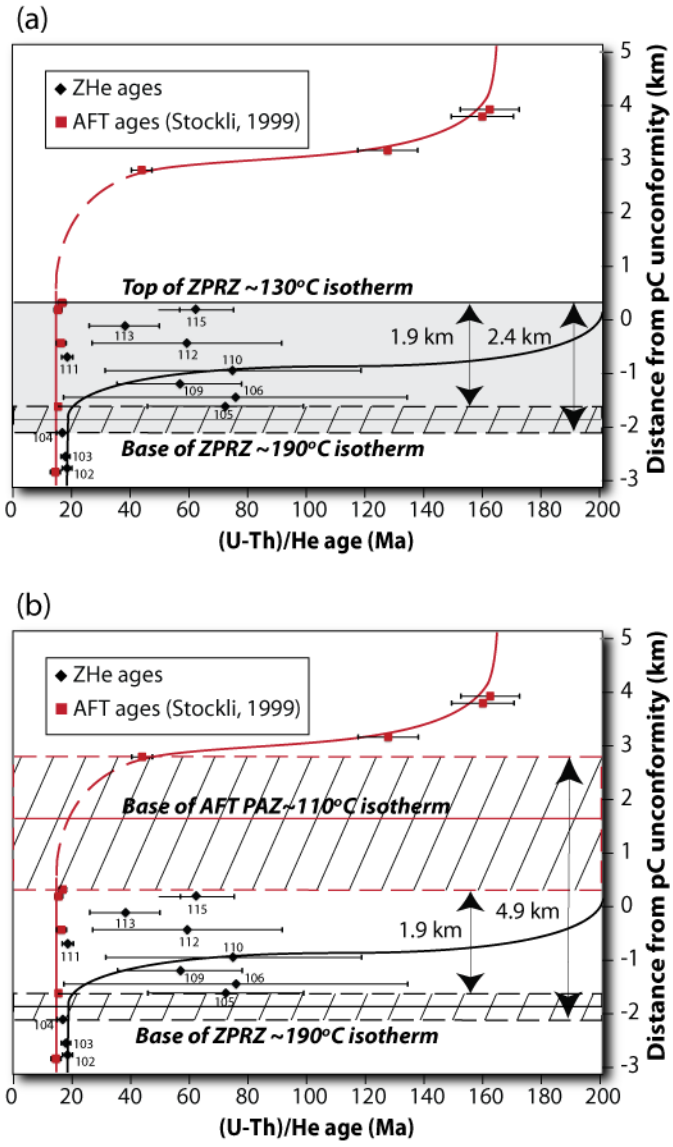
(a)
ZHe ages
AFT ages (Stockli, 1999)
Top of ZPRZ ~130°C isotherm
1.9 km
2.4 km
Base of ZPRZ ~190°C isotherm
Distance from pC unconformity (km)
(U-Th)/He age (Ma)
(b)
ZHe ages
AFT ages (Stockli, 1999)
Base of AFT PAZ~110°C isotherm
1.9 km
4.9 km
Base of ZPRZ ~190°C isotherm
Distance from pC unconformity (km)
(U-Th)/He age (Ma)

Figure 2.6

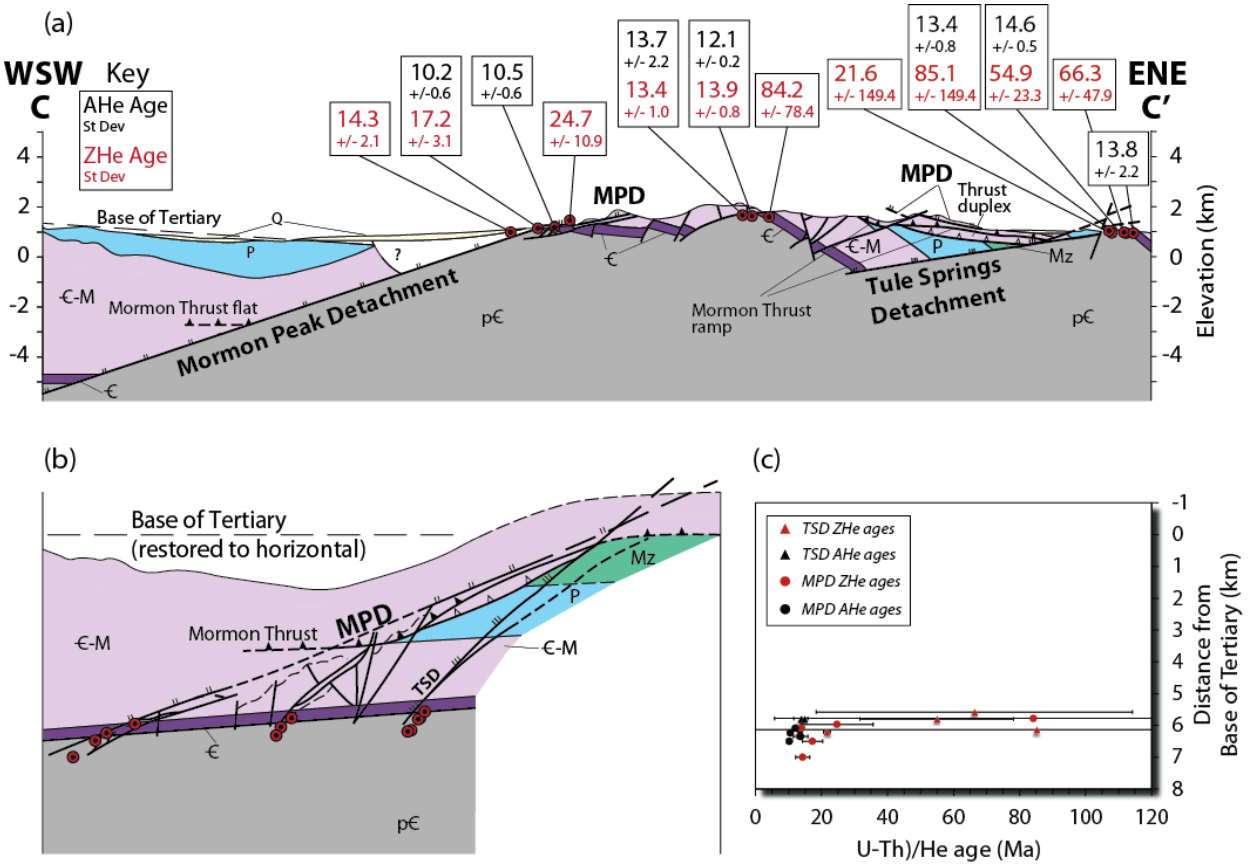
(a)
WSW
C
Key
AHe Age
St Dev
ZHe Age
St Dev
14.3
+/- 2.1
10.2
+/-0.6
17.2
+/- 3.1
10.5
+/-0.6
24.7
+/- 10.9
13.7
+/- 2.2
13.4
+/- 1.0
12.1
+/- 0.2
13.9
+/- 0.8
84.2
+/- 78.4
21.6
+/- 149.4
13.4
+/-0.8
85.1
+/- 149.4
14.6
+/- 0.5
54.9
+/- 23.3
66.3
+/- 47.9
13.8
+/- 2.2
ENE
C'
MPD
MPD
Thrust
duplex
Base of Tertiary
Q
P
?
€-M
Mormon Thrust flat
Mormon Peak Detachment
p€
€
Mormon Thrust
ramp
Tule Springs
Detachment
Mz
Elevation (km)
(b)
Base of Tertiary
(restored to horizontal)
Mz
P
€-M
Mormon Thrust
MPD
TSD
€
p€
(c)
TSD ZHe ages
TSD AHe ages
MPD ZHe ages
MPD AHe ages
Distance from
Base of Tertiary (km)
U-Th)/He age (Ma)

Figure 2.7

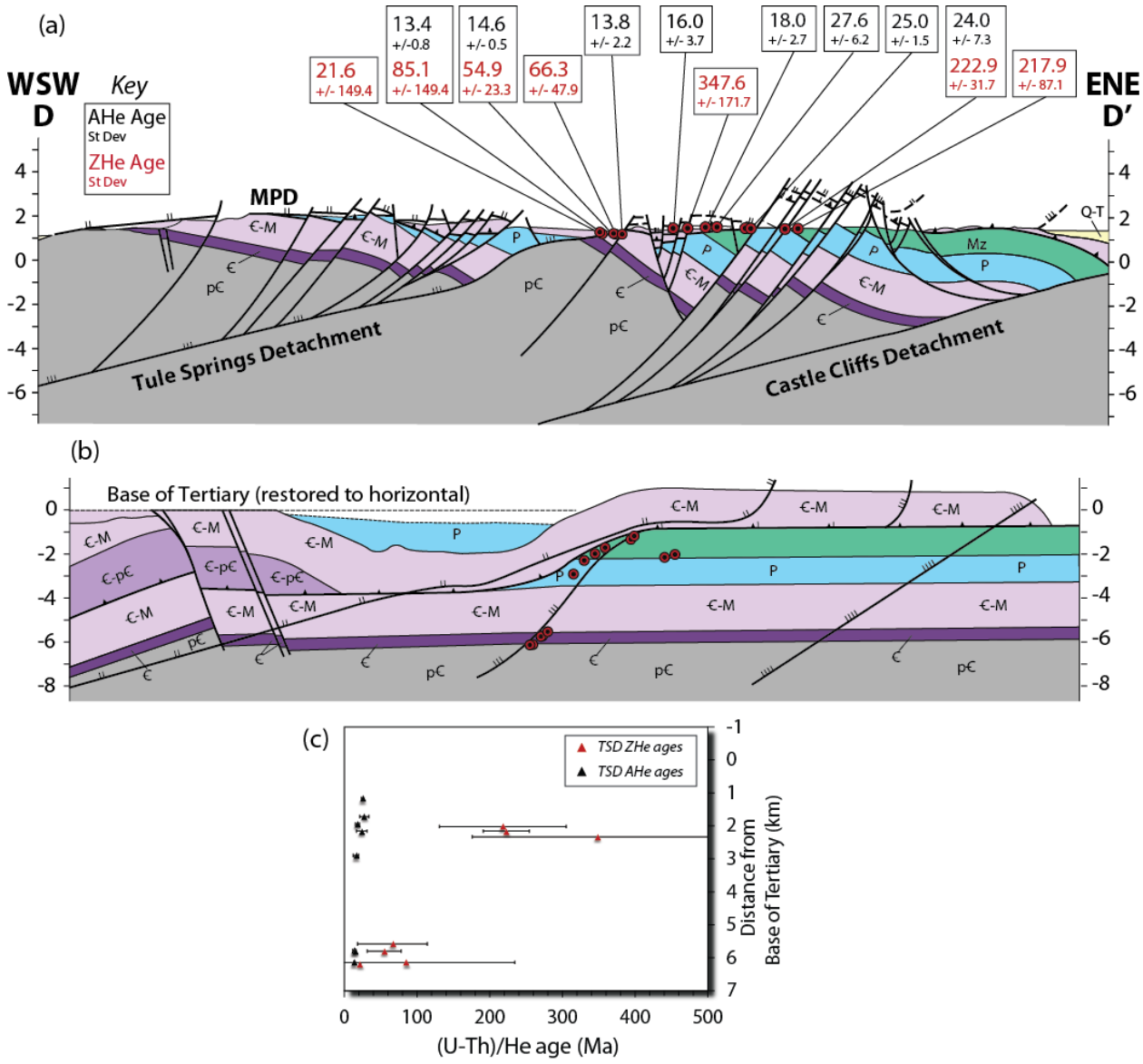
(a)
WSW
D
Key
AHe Age
St Dev
ZHe Age
St Dev
ENE
D'
21.6
+/- 149.4
13.4
+/-0.8
85.1
+/- 149.4
14.6
+/- 0.5
54.9
+/- 23.3
66.3
+/- 47.9
13.8
+/- 2.2
16.0
+/- 3.7
347.6
+/- 171.7
18.0
+/- 2.7
27.6
+/- 6.2
25.0
+/- 1.5
24.0
+/- 7.3
222.9
+/- 31.7
217.9
+/- 87.1
MPD
Q-T
Mz
P
€-M
€
pC
Tule Springs Detachment
Castle Cliffs Detachment
(b)
Base of Tertiary (restored to horizontal)
€-pC
(c)
TSD ZHe ages
TSD AHe ages
Distance from Base of Tertiary (km)
(U-Th)/He age (Ma)

Figure 2.8

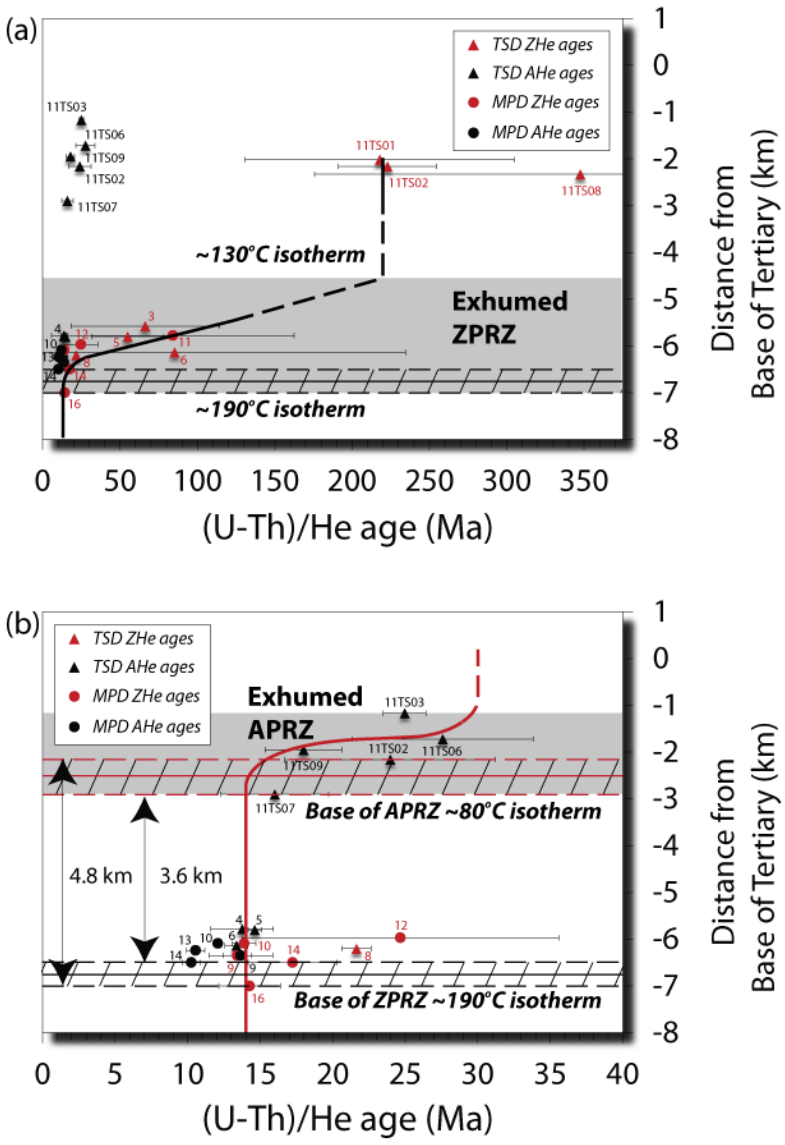
(a)
TSD ZHe ages
TSD AHe ages
MPD ZHe ages
MPD AHe ages
11TS03
11TS06
11TS09
11TS02
11TS07
11TS01
11TS02
11TS08
~130°C isotherm
Exhumed
ZPRZ
~190°C isotherm
0 50 100 150 200 250 300 350
(U-Th)/He age (Ma)
1 0 -1 -2 -3 -4 -5 -6 -7 -8
Distance from
Base of Tertiary (km)
(b)
TSD ZHe ages
TSD AHe ages
MPD ZHe ages
MPD AHe ages
Exhumed
APRZ
11TS03
11TS02
11TS06
11TS09
11TS07
Base of APRZ ~80°C isotherm
4.8 km
3.6 km
Base of ZPRZ ~190°C isotherm
0 5 10 15 20 25 30 35 40
(U-Th)/He age (Ma)
1 0 -1 -2 -3 -4 -5 -6 -7 -8
Distance from
Base of Tertiary (km)

Figure 2.9

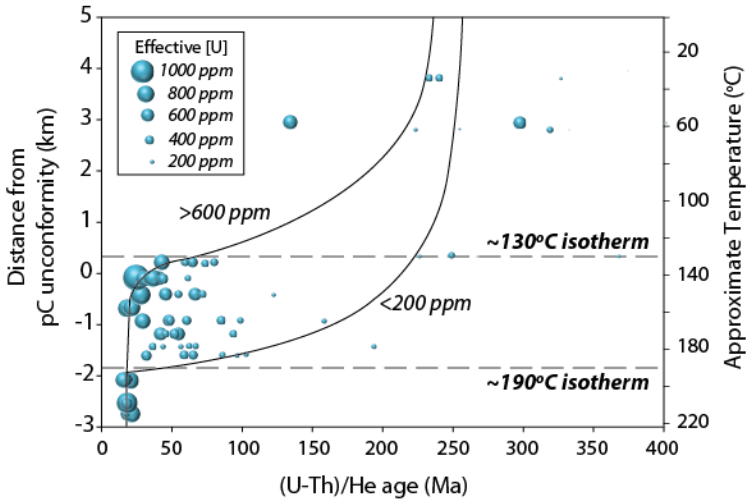
Effective [U]
1000 ppm
800 ppm
600 ppm
400 ppm
200 ppm
>600 ppm
<200 ppm
~130°C isotherm
~190°C isotherm
Distance from pC unconformity (km)
Approximate Temperature (°C)
(U-Th)/He age (Ma)
5
4
3
2
1
0
-1
-2
-3
20
60
100
140
180
220
0
50
100
150
200
250
300
350
400

Figure 2.10

Table SD2.1. Zircon (U-Th)/He data for the Beaver Dam Mountains

Sample	L (mm)	W (mm)	Mass (µg)	Ft*	U (ppm)	Th (ppm)	Sm (ppm)	[U]e	Th/U	He (nmol/g)	Corrected Age (Ma)	err. (Ma)	Mean age (Ma)	St.Dev.† (Ma)
95BR102	**185.12**	**80.85**	**5.88**	**0.77**	**573.5**	**35.7**	**1.1**	**581.8**	**0.06**	**45.6**	-	**1.5**	**18.8**	**1.7**
z95BR102-1	162.14	69.41	3.63	0.74	636.3	46.3	1.7	647.0	0.07	47.1	18.3	1.5		
z95BR102-2	197.10	73.16	4.91	0.76	775.8	43.7	1.1	785.8	0.06	66.1	20.6	1.7		
z95BR102-3	196.10	99.99	9.12	0.81	308.5	17.2	0.6	312.5	0.06	23.6	17.4	1.4		
95BR103	**187.06**	**79.41**	**5.59**	**0.76**	**613.3**	**216.6**	**1.4**	**663.2**	**0.32**	**49.1**	-	**1.5**	**18.2**	**1.6**
z95BR103-1	191.77	75.88	5.13	0.76	498.4	126.1	0.8	527.5	0.25	43.0	19.9	1.6		
z95BR103-2	171.74	72.11	4.15	0.74	851.3	416.6	2.0	947.2	0.49	67.3	17.8	1.4		
z95BR103-3	197.67	90.25	7.49	0.79	490.2	107.2	1.3	514.9	0.22	37.1	16.9	1.4		
95BR104	**158.58**	**69.80**	**3.58**	**0.74**	**724.8**	**22.6**	**1.6**	**730.0**	**0.03**	**49.9**	-	**1.4**	**17.1**	**1.9**
z95BR104-1	173.75	67.33	3.66	0.74	762.1	25.7	1.5	768.0	0.03	60.2	19.8	1.6		
z95BR104-2	164.60	70.79	3.84	0.74	675.9	15.4	1.2	679.4	0.02	44.8	16.5	1.3		
z95BR104-3	137.38	71.27	3.25	0.74	736.4	26.6	2.1	742.6	0.04	44.6	15.2	1.2		
95BR105	**164.93**	**73.62**	**4.18**	**0.75**	**324.6**	**81.8**	**2.0**	**343.4**	**0.25**	**91.7**	-	**5.8**	**72.6**	**26.5**
z95BR105-1	172.99	71.15	4.07	0.74	449.9	123.9	1.2	478.5	0.28	59.7	31.1	2.5		
z95BR105-2	166.82	79.11	4.85	0.76	274.3	69.4	1.3	290.3	0.25	101.4	84.8	6.8		
z95BR105-3	139.04	73.00	3.45	0.74	205.5	43.9	1.0	215.6	0.21	82.1	95.2	7.6		
z95BR105-4	188.63	78.06	5.34	0.76	415.8	93.6	1.8	437.3	0.23	116.6	64.5	5.2		
z95BR105-5	160.78	69.32	3.59	0.73	233.0	47.4	1.1	243.9	0.20	98.9	101.8	8.1		
z95BR105-6	161.32	71.10	3.79	0.74	369.1	112.6	5.5	395.1	0.31	91.4	57.9	4.6		
95BR106	**153.67**	**77.03**	**4.27**	**0.75**	**263.19**	**58.10**	**1.29**	**276.57**	**0.23**	**80.66**	-	**6.1**	**75.7**	**58.5**
z95BR106-1	135.80	86.16	4.69	0.77	325.0	39.4	0.9	334.0	0.12	49.4	35.7	2.9		
z95BR106-2	157.98	75.13	4.15	0.75	248.3	52.7	1.3	260.4	0.21	45.4	43.1	3.4		
z95BR106-3	126.49	73.12	3.14	0.73	264.7	54.7	1.2	277.3	0.21	67.4	61.3	4.9		
z95BR106-4	167.74	67.81	3.59	0.73	279.6	87.9	1.1	299.8	0.31	77.8	65.7	5.3		
z95BR106-5	160.09	74.58	4.14	0.75	220.6	63.6	2.2	235.2	0.29	185.1	192.8	15.4		
z95BR106-6	173.92	85.37	5.89	0.78	241.0	50.2	1.0	252.6	0.21	58.8	55.5	4.4		
95BR109	**212.60**	**78.98**	**6.27**	**0.77**	**450.45**	**91.54**	**2.93**	**471.54**	**0.20**	**105.70**	-	**4.5**	**56.5**	**21.0**
z95BR109-1	169.63	73.38	4.25	0.75	332.0	53.1	2.1	344.2	0.16	130.1	93.1	7.4		
z95BR109-2	255.64	83.34	8.26	0.78	586.3	96.5	3.8	608.5	0.16	105.2	40.8	3.3		
z95BR109-3	211.92	89.57	7.91	0.79	329.5	36.7	2.1	338.0	0.11	64.9	44.8	3.6		

Sample	L (mm)	W (mm)	Mass (µg)	Ft*	U (ppm)	Th (ppm)	Sm (ppm)	[U]e	Th/U	He (nmol/g)	Corrected Age (Ma)	err. (Ma)	Mean age (Ma)	St.Dev.† (Ma)
z95BR109-4	230.43	73.99	5.87	0.76	577.4	152.9	2.7	612.6	0.26	134.5	53.5	4.3		
z95BR109-5	195.37	74.60	5.06	0.75	427.0	118.5	3.9	454.3	0.28	93.9	50.6	4.0		
95BR110	**164.36**	**73.79**	**4.19**	**0.75**	**420.29**	**85.58**	**1.57**	**440.00**	**0.21**	**112.36**	-	**6.0**	**74.7**	**43.4**
z95BR110-1	127.11	68.58	2.78	0.72	417.4	109.3	1.8	442.6	0.26	102.4	59.4	4.8		
z95BR110-2	148.73	69.46	3.34	0.73	499.4	132.8	2.5	530.0	0.27	98.4	47.0	3.8		
z95BR110-3	158.03	83.57	5.13	0.77	400.0	64.7	1.0	414.9	0.16	83.0	48.2	3.9		
z95BR110-4	174.78	76.19	4.72	0.76	233.7	51.0	1.0	245.4	0.22	159.0	157.4	12.6		
z95BR110-5	189.29	67.70	4.03	0.73	289.4	73.7	1.3	306.3	0.25	119.9	98.1	7.8		
z95BR110-6	174.76	74.82	4.55	0.75	387.8	49.8	1.4	399.3	0.13	137.5	84.3	6.7		
z95BR110-7	177.79	76.21	4.80	0.76	714.5	117.7	2.0	741.6	0.16	86.5	28.5	2.3		
95BR111	**197.37**	**67.98**	**4.25**	**0.74**	**664.3**	**250.5**	**11.7**	**722.0**	**0.36**	**53.9**	-	**1.5**	**18.8**	**1.9**
z95BR111-1	210.74	69.04	4.67	0.74	722.4	397.0	18.5	813.9	0.55	55.1	17.0	1.4		
z95BR111-2	192.94	69.44	4.33	0.74	543.7	65.6	2.0	558.8	0.12	42.0	18.7	1.5		
z95BR111-3	188.41	65.45	3.75	0.72	726.8	289.0	14.5	793.4	0.40	64.5	20.7	1.7		
95BR112	**203.6**	**74.9**	**5.4**	**0.8**	**498.6**	**78.2**	**6.4**	**516.6**	**0.2**	**104.1**	-	**4.7**	**59.1**	**32.3**
z95BR112-1	186.08	76.70	5.09	0.76	360.3	69.4	4.7	376.3	0.19	83.1	53.8	4.3		
z95BR112-2	219.89	72.26	5.34	0.75	192.2	54.6	1.4	204.8	0.28	102.0	121.7	9.7		
z95BR112-3	148.69	74.03	3.79	0.74	577.2	83.6	6.2	596.4	0.14	157.5	65.5	5.2		
z95BR112-4	239.24	78.52	6.86	0.77	583.5	82.9	1.2	602.6	0.14	113.0	44.9	3.6		
z95BR112-5	189.93	68.58	4.15	0.74	336.4	55.9	1.1	349.2	0.17	99.7	71.3	5.7		
z95BR112-6	203.79	72.95	5.04	0.75	560.5	79.1	15.3	578.8	0.14	68.1	28.9	2.3		
z95BR112-7	237.38	81.27	7.29	0.78	880.2	121.6	15.0	908.2	0.14	105.3	27.6	2.2		
95BR113	**182.0**	**71.9**	**4.4**	**0.7**	**635.6**	**94.1**	**4.3**	**657.2**	**0.2**	**90.7**	-	**3.0**	**38.0**	**11.9**
z95BR113-1	183.77	81.32	5.65	0.77	1155.9	144.1	13.1	1189.2	0.12	115.7	23.4	1.9		
z95BR113-2	190.33	73.02	4.72	0.75	499.3	86.6	3.5	519.3	0.17	74.0	35.1	2.8		
z95BR113-3	173.49	73.55	4.36	0.75	671.8	100.1	4.1	694.9	0.15	81.9	29.1	2.3		
z95BR113-4	175.78	69.14	3.91	0.74	620.5	85.7	2.2	640.3	0.14	101.8	39.8	3.2		
z95BR113-5	169.67	67.14	3.56	0.73	776.8	115.7	2.5	803.5	0.15	111.7	35.2	2.8		
z95BR113-6	179.59	65.91	3.63	0.73	443.0	75.6	3.4	460.4	0.17	77.0	42.4	3.4		
z95BR113-7	201.49	72.95	4.99	0.75	281.5	51.0	1.3	293.2	0.18	72.7	60.8	4.9		

Sample	L (mm)	W (mm)	Mass (µg)	Ft*	U (ppm)	Th (ppm)	Sm (ppm)	[U]e	Th/U	He (nmol/g)	Corrected Age (Ma)	err. (Ma)	Mean age (Ma)	St.Dev.† (Ma).
95BR115	**198.0**	75.3	**5.3**	**0.8**	**416.6**	**66.2**	**3.4**	**431.8**	**0.2**	**105.2**	-	**5.0**	**62.3**	**12.7**
z95BR115-1	200.17	69.93	4.55	0.74	338.4	71.1	2.8	354.8	0.21	82.8	58.0	4.6		
z95BR115-2	136.84	81.85	4.26	0.76	360.7	46.7	2.9	371.4	0.13	120.4	78.9	6.3		
z95BR115-3	178.85	69.58	4.03	0.74	471.5	88.1	1.9	491.7	0.19	125.5	63.7	5.1		
z95BR115-4	202.05	76.03	5.43	0.76	290.6	43.8	3.2	300.7	0.15	72.3	58.4	4.7		
z95BR115-5	255.63	84.01	8.39	0.79	321.7	56.9	3.0	334.9	0.18	103.3	72.4	5.8		
z95BR115-6	214.22	70.28	4.92	0.75	716.5	90.8	6.7	737.4	0.13	126.9	42.5	3.4		
95BR116	**203.52**	**83.97**	**6.86**	**0.76**	**121.3**	**218.1**	**7.0**	**171.6**	**1.98**	**238.9**	-	**27.2**	**340.2**	**91.1**
z95BR116-1	243.42	90.48	9.27	0.79	257.8	308.6	9.6	328.9	1.20	354.1	248.1	19.8		
z95BR116-2	208.31	74.21	5.33	0.74	110.4	219.6	9.3	161.0	1.99	284.6	426.4	34.1		
z95BR116-3	190.24	79.42	5.58	0.75	70.9	166.0	4.5	109.2	2.34	192.5	420.5	33.6		
z95BR116-4	191.73	98.53	8.66	0.79	51.8	117.8	1.6	78.9	2.27	91.6	265.8	21.3		
z95BR116-5	179.61	72.61	4.40	0.73	111.8	195.6	2.7	156.9	1.75	234.0	366.0	29.3		
z95BR116-6	218.46	98.90	9.94	0.80	131.8	213.7	12.2	181.0	1.62	346.0	429.4	34.4		
z95BR116-7	192.88	73.63	4.86	0.74	114.7	305.1	9.1	185.0	2.66	169.3	225.0	18.0		
95BR119	**184.73**	**99.08**	**8.93**	**0.79**	**99.8**	**55.9**	**5.8**	**112.7**	**0.98**	**163.8**	-	**35.6**	**445.1**	**318.8**
z95BR119-1	165.86	92.32	6.57	0.78	168.1	105.2	21.2	192.4	0.63	183.2	222.1	17.8		
z95BR119-2	182.01	102.32	8.86	0.80	105.8	57.1	13.1	119.0	0.54	133.1	253.7	20.3		
z95BR119-3	208.52	128.51	16.01	0.83	21.6	46.4	0.8	32.3	2.15	177.2	1118.2	89.5		
z95BR119-4	192.46	88.10	6.95	0.77	23.0	35.3	1.6	31.1	1.54	39.1	293.8	23.5		
z95BR119-5	221.02	114.44	13.46	0.82	29.8	27.0	0.6	36.1	0.90	97.1	579.3	46.3		
z95BR119-6	160.70	77.61	4.50	0.75	51.6	43.0	1.2	61.5	0.83	84.1	330.8	26.5		
z95BR119-7	162.52	90.25	6.15	0.78	298.6	77.2	2.3	316.4	0.26	432.7	317.3	25.4		
95BR120	**144.88**	**68.95**	**3.21**	**0.72**	**403.6**	**170.2**	**9.1**	**442.9**	**0.49**	**392.2**	-	**22.1**	**276.3**	**134.7**
z95BR120-1	148.64	72.06	3.59	0.73	88.8	58.7	1.6	102.4	0.66	166.4	400.3	32.0		
z95BR120-2	151.40	67.42	3.20	0.72	523.0	204.1	10.3	570.0	0.39	670.0	295.6	23.6		
z95BR120-3	134.60	67.38	2.84	0.72	599.1	247.8	15.4	656.2	0.41	340.2	133.0	10.6		
95BR122	**209.67**	**83.41**	**6.80**	**0.78**	**252.5**	**90.7**	**2.3**	**273.4**	**0.41**	**293.4**	-	**21.2**	**265.2**	**52.0**
z95BR122-1	190.35	81.98	5.95	0.77	309.1	87.5	3.2	329.2	0.28	321.9	231.4	18.5		
z95BR122-2	213.89	82.80	6.82	0.78	315.7	100.5	1.9	338.8	0.32	345.2	239.2	19.1		
z95BR122-3	224.77	85.44	7.63	0.78	132.8	84.0	1.9	152.2	0.63	213.3	325.1	26.0		

Sample	L (mm)	W (mm)	Mass (µg)	Ft*	U (ppm)	Th (ppm)	Sm (ppm)	[U]e	Th/U	He (nmol/g)	Corrected Age (Ma)	err. (Ma)	Mean age (Ma)	St.Dev.† (Ma)
95BR124	**215.11**	**105.59**	**11.28**	**0.81**	**59.16**	**32.49**	**0.73**	**66.64**	**0.54**	**208.26**	-	**51.9**	**649.1**	**350.4**
z95BR124-1	223.59	112.68	13.20	0.82	52.9	13.6	0.6	56.0	0.26	95.7	372.8	29.8		
z95BR124-2	234.77	106.35	12.35	0.81	61.0	45.5	0.5	71.5	0.75	174.1	531.1	42.5		
z95BR124-3	186.96	97.76	8.31	0.79	63.6	38.3	1.0	72.4	0.60	354.9	1043.3	83.5		
11TS01	**161.3**	**69.3**	**3.7**	**0.7**	**181.2**	**118.5**	**0.8**	**208.5**	**0.7**	**168.2**	-	**17.4**	**217.9**	**87.1**
z11TS01-1	187.41	75.14	4.92	0.75	124.7	117.8	1.3	151.8	0.94	196.0	312.9	25.0		
z11TS01-2	144.53	54.71	2.01	0.67	199.5	125.6	0.4	228.4	0.63	166.6	199.1	15.9		
z11TS01-3	151.91	77.92	4.29	0.75	219.5	112.0	0.6	245.3	0.51	141.9	141.7	11.3		
11TS02	**231.1**	**96.9**	**10.3**	**0.8**	**296.8**	**111.3**	**1.0**	**322.5**	**0.4**	**309.0**	-	**17.8**	**222.9**	**31.7**
z11TS02-1	205.12	88.36	7.45	0.78	214.2	96.1	1.3	236.3	0.45	264.4	259.5	20.8		
z11TS02-2	243.25	113.24	14.50	0.83	292.8	138.3	1.2	324.7	0.47	299.2	203.4	16.3		
z11TS02-3	244.82	89.13	9.04	0.79	383.5	99.5	0.4	406.4	0.26	363.5	205.9	16.5		
11TS04	***265.3***	***113.6***	***16.8***	***0.8***	***853.0***	***300.8***	***5.7***	***922.3***	***0.4***	***36.5***	***-***	***0.7***	***8.8***	***0.4***
z11TS04-1	*223.62*	*93.91*	*9.17*	*0.80*	*1043.2*	*339.7*	*6.4*	*1121.4*	*0.33*	*44.4*	*9.2*	*0.7*		
z11TS04-2	*350.95*	*126.88*	*26.27*	*0.85*	*437.7*	*188.7*	*5.6*	*481.2*	*0.43*	*18.5*	*8.4*	*0.7*		
z11TS04-3	*221.23*	*120.09*	*14.84*	*0.83*	*1078.2*	*374.0*	*4.9*	*1164.3*	*0.35*	*46.6*	*8.9*	*0.7*		
11TS06	***214.4***	***73.4***	***5.4***	***0.8***	***1086.5***	***492.9***	***2.2***	***1200.0***	***0.5***	***54.6***	***-***	***0.9***	***11.2***	***0.2***
z11TS06-1	*232.38*	*77.90*	*6.56*	*0.77*	*1342.3*	*412.5*	*2.0*	*1437.3*	*0.31*	*67.4*	*11.3*	*0.9*		
z11TS06-2	*218.27*	*71.90*	*5.25*	*0.75*	*925.0*	*406.8*	*1.9*	*1018.7*	*0.44*	*46.3*	*11.2*	*0.9*		
z11TS06-3	*192.57*	*70.29*	*4.42*	*0.74*	*992.1*	*659.5*	*2.6*	*1143.9*	*0.66*	*50.2*	*11.0*	*0.9*		
11TS08	**226.6**	**83.7**	**7.4**	**0.8**	**129.6**	**61.6**	**1.3**	**143.8**	**0.5**	**199.3**	-	**27.8**	**347.6**	**171.7**
z11TS08-1	241.26	84.87	8.08	0.78	99.6	57.5	1.6	112.8	0.58	266.3	537.3	43.0		
z11TS08-2	228.69	88.11	8.26	0.79	167.1	83.8	1.2	186.4	0.50	162.7	202.6	16.2		
z11TS08-3	209.80	78.24	5.97	0.76	122.2	43.6	1.1	132.3	0.36	168.9	302.9	24.2		
11TS09	**213.0**	**87.6**	**8.2**	**0.8**	**808.7**	**330.2**	**1.9**	**884.7**	**0.5**	**53.4**	-	**2.8**	**34.9**	**45.3**
z11TS09-1	*262.44*	*104.68*	*13.37*	*0.82*	*1556.6*	*540.9*	*3.4*	*1681.1*	*0.35*	*60.6*	*8.1*	*0.7*		
z11TS09-2	*222.11*	*85.99*	*7.64*	*0.78*	*699.3*	*327.5*	*1.9*	*774.7*	*0.47*	*30.8*	*9.4*	*0.8*		
z11TS09-3	154.32	72.07	3.73	0.73	170.2	122.2	0.3	198.3	0.72	68.9	87.2	7.0		
96BR003	**135.81**	**67.14**	**2.83**	**0.71**	**282.63**	**156.01**	**7.88**	**318.58**	**0.49**	**68.31**	-	**6.26**	**78.3**	**45.8**
z96BR003-1	116.41	82.40	3.68	0.75	150.7	49.3	2.4	162.0	0.33	81.7	124.1	9.9		

Sample	L (mm)	W (mm)	Mass (µg)	Ft*	U (ppm)	Th (ppm)	Sm (ppm)	[U]e	Th/U	He (nmol/g)	Corrected Age (Ma)	err. (Ma)	Mean age (Ma)	St.Dev.† (Ma)
z96BR003-3	128.81	62.57	2.35	0.69	583.9	394.2	21.2	674.8	0.68	41.0	16.2	1.3		
z96BR003-4	158.80	62.66	2.90	0.71	269.2	110.0	6.2	294.5	0.41	109.3	96.4	7.7		
z96BR003-5	139.21	60.94	2.40	0.69	126.7	70.5	1.7	143.0	0.56	41.2	76.4	6.1		
96BR005	**181.09**	**77.46**	**5.03**	**0.76**	**309.7**	**85.5**	**2.4**	**329.42**	**0.28**	**70.0**	-	**4.4**	**54.9**	**23.3**
z96BR005-1	184.79	76.42	5.02	0.76	310.8	66.2	2.6	326.0	0.21	65.8	49.2	3.9		
z96BR005-2	195.33	67.61	4.15	0.73	343.7	116.2	2.8	370.4	0.34	45.9	31.2	2.5		
z96BR005-3	195.24	73.51	4.91	0.75	352.0	93.7	2.8	373.6	0.27	56.6	37.3	3.0		
z96BR005-4	161.54	89.26	5.98	0.78	181.7	64.3	1.6	196.5	0.35	72.4	87.3	7.0		
z96BR005-5	168.54	80.51	5.08	0.76	360.4	87.3	2.3	380.5	0.24	109.3	69.4	5.6		
96BR006	**165.4**	**75.3**	**4.5**	**0.7**	**377.1**	**170.8**	**3.8**	**416.4**	**0.5**	**75.9**	-	**6.8**	**85.1**	**149.4**
z96BR006-1	196.73	87.77	7.05	0.78	404.7	219.3	7.3	455.3	0.54	45.9	23.9	1.9		
z96BR006-2	101.93	71.71	2.44	0.71	306.7	127.6	3.0	336.1	0.42	45.1	34.8	2.8		
z96BR006-3	203.54	80.50	6.13	0.77	799.2	238.8	5.3	854.2	0.30	48.4	13.6	1.1		
z96BR006-4	139.59	73.10	3.47	0.73	135.8	96.0	1.9	157.9	0.71	249.5	389.8	31.2		
z96BR006-5	178.35	68.22	3.86	0.73	309.2	135.2	2.8	340.4	0.44	32.3	24.0	1.9		
z96BR006-6	172.22	70.29	3.96	0.73	307.0	208.0	2.5	354.9	0.68	34.5	24.5	2.0		
96BR008	**168.38**	**70.34**	**3.93**	**0.73**	**303.5**	**134.5**	**3.0**	**334.43**	**0.44**	**28.7**	-	**1.7**	**21.6**	**1.0**
z96BR008-1	170.35	81.11	5.21	0.76	292.5	135.8	3.2	323.8	0.46	29.8	22.3	1.8		
z96BR008-2	163.01	63.56	3.06	0.71	325.1	153.2	3.7	360.3	0.47	30.7	22.1	1.8		
z96BR008-3	171.78	66.36	3.52	0.72	292.8	114.6	2.0	319.2	0.39	25.6	20.5	1.6		
96BR009	**175.87**	**72.97**	**4.35**	**0.75**	**442.0**	**85.2**	**15.5**	**461.68**	**0.19**	**25.1**	-	**1.1**	**13.4**	**1.0**
z96BR009-1	182.71	69.00	4.04	0.74	431.8	41.4	7.8	441.3	0.10	24.0	13.6	1.1		
z96BR009-2	134.18	75.20	3.53	0.74	409.4	105.9	33.5	434.0	0.26	21.4	12.4	1.0		
z96BR009-3	210.72	74.72	5.47	0.76	484.7	108.4	5.1	509.7	0.22	29.7	14.2	1.1		
96BR010	**161.67**	**67.99**	**3.58**	**0.73**	**532.7**	**48.5**	**3.8**	**543.83**	**0.09**	**29.9**	-	**1.1**	**13.9**	**0.8**
z96BR010-1	208.06	74.58	5.38	0.76	545.6	87.6	7.6	565.8	0.16	34.1	14.7	1.2		
z96BR010-2	129.91	66.78	2.69	0.72	547.1	22.9	0.9	552.4	0.04	29.6	13.8	1.1		
z96BR010-3	147.05	62.60	2.68	0.71	505.3	34.9	2.8	513.3	0.07	25.9	13.1	1.1		
96BR011	**219.1**	**90.9**	**8.5**	**0.8**	**125.9**	**115.1**	**4.5**	**152.4**	**1.1**	**50.9**	-	**7.8**	**97.4**	**76.8**
z96BR011-1	252.99	85.53	8.61	0.78	241.0	157.1	3.0	277.2	0.65	59.4	50.5	4.0		
z96BR011-2	181.64	92.41	7.21	0.78	71.1	122.7	6.0	99.4	1.73	102.9	241.1	19.3		

Sample	L (mm)	W (mm)	Mass (µg)	Ft*	U (ppm)	Th (ppm)	Sm (ppm)	[U]e	Th/U	He (nmol/g)	Corrected Age (Ma)	err. (Ma)	Mean age (Ma)	St.Dev.† (Ma)
z96BR011-4	246.26	89.02	9.07	0.79	104.7	138.4	11.8	136.6	1.32	42.8	73.3	5.9		
z96BR011-5	215.64	88.44	7.84	0.78	77.2	78.3	3.3	95.3	1.01	48.4	119.2	9.5		
z96BR011-6	259.82	102.83	12.78	0.81	68.2	63.2	1.4	82.7	0.93	27.2	74.5	6.0		
z96BR011-7	158.12	87.26	5.60	0.77	193.4	130.8	1.7	223.5	0.68	24.4	26.2	2.1		
96BR012	**168.2**	**78.5**	**4.9**	**0.8**	**146.7**	**47.5**	**4.0**	**157.7**	**0.4**	**16.2**	-	**2.0**	**24.7**	**10.9**
z96BR012-1	160.60	87.98	5.78	0.78	209.4	36.9	3.9	217.9	0.18	15.9	17.4	1.4		
z96BR012-2	169.26	83.38	5.47	0.77	163.0	75.9	6.8	180.5	0.47	36.6	48.8	3.9		
z96BR012-3	159.60	79.75	4.72	0.76	168.0	19.0	4.5	172.4	0.11	15.3	21.6	1.7		
z96BR012-4	132.70	71.07	3.12	0.73	216.2	60.2	1.6	230.0	0.28	19.0	20.9	1.7		
z96BR012-5	135.45	69.69	3.06	0.72	77.6	42.4	5.9	87.4	0.55	6.8	19.8	1.6		
z96BR012-6	220.47	85.75	7.54	0.78	114.9	47.3	3.5	125.8	0.41	13.3	24.9	2.0		
z96BR012-7	199.38	72.18	4.83	0.74	78.1	51.1	2.0	89.9	0.65	7.0	19.3	1.5		
96BR014	**150.3**	**72.5**	**3.7**	**0.7**	**292.2**	**48.9**	**6.7**	**303.5**	**0.2**	**21.1**	-	**1.4**	**17.2**	**3.1**
z96BR014-1	128.07	78.33	3.65	0.75	333.2	67.1	2.2	348.7	0.20	24.2	17.2	1.4		
z96BR014-2	150.90	60.35	2.56	0.70	436.5	41.3	18.8	446.1	0.09	22.8	13.4	1.1		
z96BR014-3	170.64	60.29	2.88	0.71	237.4	42.1	19.1	247.2	0.18	16.6	17.5	1.4		
z96BR014-4	148.77	73.08	3.69	0.74	162.6	43.4	0.5	172.6	0.27	12.1	17.6	1.4		
z96BR014-5	138.01	85.50	4.69	0.76	332.2	66.2	1.4	347.4	0.20	22.9	15.9	1.3		
z96BR014-6	186.79	76.51	5.08	0.76	408.8	49.6	4.4	420.3	0.12	40.3	23.3	1.9		
z96BR014-7	128.99	73.26	3.22	0.73	135.0	32.3	0.3	142.4	0.24	8.8	15.6	1.2		
96BR016	**177.04**	**73.55**	**4.49**	**0.75**	**394.3**	**80.3**	**2.7**	**412.8**	**0.20**	**23.2**		**1.1**	**14.3**	**2.1**
z96BR016-1	178.21	74.24	4.57	0.75	309.5	58.1	2.4	322.8	0.19	23.0	17.5	1.4		
z96BR016-2	173.84	72.36	4.23	0.75	364.0	75.6	5.4	381.5	0.21	24.5	16.0	1.3		
z96BR016-3	179.94	82.29	5.67	0.77	516.4	119.7	1.9	544.0	0.23	28.3	12.5	1.0		
z96BR016-4	160.63	63.23	2.99	0.72	419.0	73.9	1.9	436.0	0.18	22.7	13.5	1.1		
z96BR016-5	188.82	69.80	4.28	0.74	293.8	71.1	1.4	310.2	0.24	19.2	15.5	1.2		
z96BR016-6	213.98	76.01	5.75	0.76	323.8	63.4	3.4	338.4	0.20	18.6	13.4	1.1		
z96BR016-7	143.85	76.88	3.95	0.75	533.8	100.0	2.8	556.9	0.19	25.9	11.5	0.9		

Notes: See text for discussion of analytical procedures and errors; samples in italics were not used in the calculation of mean ages

*Ft is the alpha ejection correction of Farley et al. (1996).

†St. Dev.—standard deviation.

Table SD2.2. Apatite (U-Th)/He data

Sample	L (um)	W (um)	Mass (µg)	Ft*	U (ppm)	Th (ppm)	Sm (ppm)	[U]e	Th/U	He (nmol/g)	Corrected Age (Ma)	err. (Ma)	Mean age (Ma)	St.Dev.† (Ma)
11TS02	**137.80**	**90.82**	**2.35**	**0.67**	**6.2**	**5.3**	**36.4**	**7.6**	**0.98**	**0.6**	-	**1.9**	**24.0**	**7.3**
11TS02-1	153.97	102.90	3.28	0.71	3.3	3.1	15.6	4.1	0.95	0.3	19.4	1.5		
11TS02-2	145.83	86.87	2.22	0.66	3.6	4.7	76.9	5.1	1.28	0.6	32.3	2.6		
11TS02-3	113.61	82.70	1.56	0.64	11.8	8.2	16.7	13.7	0.70	1.0	20.2	1.6		
11TS03	**120.22**	**81.65**	**1.64**	**0.63**	**29.1**	**52.0**	**57.3**	**41.4**	**1.54**	**3.6**	-	**2.0**	**25.0**	**1.5**
11TS03-1	121.52	90.99	2.03	0.66	45.7	90.3	67.7	66.9	1.98	5.7	23.9	1.9		
11TS03-2	*165.60*	*92.40*	*2.85*	*0.68*	*4.3*	*16.2*	*14.2*	*8.1*	*3.72*	*0.0*	*0.2*	*0.0*		
11TS03-3	118.93	72.30	1.25	0.61	12.5	13.8	46.8	15.9	1.10	1.4	26.0	2.1		
11TS06	**101.41**	77.52	**1.26**	**0.60**	**6.7**	**12.4**	**43.1**	**9.8**	**2.06**	**1.0**	-	**2.2**	**27.6**	**6.2**
11TS06-1	117.66	87.71	1.82	0.65	2.9	5.2	13.6	4.2	1.78	0.3	19.9	1.6		
11TS06-2	96.14	77.12	1.15	0.60	17.9	29.5	111.4	25.2	1.65	2.8	33.7	2.7		
11TS06-3	83.11	71.27	0.85	0.56	3.2	12.9	33.2	6.3	4.09	0.6	31.5	2.5		
11TS06-4	108.73	73.97	1.20	0.61	2.8	2.0	14.3	3.3	0.70	0.3	25.3	2.0		
11TS07	**80.45**	**49.86**	**0.39**	**0.45**	**6.3**	**7.3**	**32.2**	**8.2**	**1.91**	**0.3**	-	**1.3**	**16.0**	**3.7**
11TS07-1	60.68	55.33	0.37	0.47	3.3	2.3	17.8	3.9	0.69	0.2	21.1	1.7		
11TS07-2	76.24	50.36	0.39	0.44	1.5	7.6	62.8	3.5	5.23	0.1	13.1	1.0		
11TS07-3	125.22	45.10	0.51	0.46	15.6	15.9	39.2	19.5	1.01	0.8	16.4	1.3		
11TS07-4	59.68	48.63	0.28	0.43	5.0	3.4	8.9	5.8	0.69	0.2	13.4	1.1		
11TS09	72.17	**45.85**	**0.30**	**0.41**	**10.7**	**18.0**	**33.5**	**15.0**	**3.01**	**0.6**	-	**1.4**	**18.0**	**2.7**
11TS09-1	90.77	40.70	0.30	0.38	7.5	35.3	12.1	15.7	4.72	0.5	15.2	1.2		
11TS09-2	64.46	46.78	0.28	0.42	25.2	18.8	46.9	29.8	0.74	1.4	19.8	1.6		
11TS09-3	65.46	49.05	0.32	0.41	2.1	12.1	50.9	5.1	5.83	0.2	20.7	1.7		
11TS09-4	67.99	46.88	0.30	0.43	8.0	5.9	24.0	9.5	0.74	0.4	16.3	1.3		
96BR004	**119.60**	**84.14**	**1.91**	**0.63**	**3.7**	**3.4**	**40.6**	**4.7**	**1.17**	**0.2**	-	**1.1**	**13.8**	**2.2**
96BR004-1	85.30	70.22	0.85	0.58	5.5	3.3	45.7	6.5	0.59	0.3	12.2	1.0		
96BR004-2	*113.35*	*93.57*	*2.00*	*0.66*	*1.1*	*2.1*	*45.5*	*1.8*	*1.83*	*1.6*	*219.6*	*17.6*		
96BR004-3	153.89	98.06	2.98	0.69	2.0	3.5	35.4	2.9	1.75	0.2	15.3	1.2		

Sample	L (um)	W (um)	Mass (µg)	Ft*	U (ppm)	Th (ppm)	Sm (ppm)	[U]e	Th/U	He (nmol/g)	Corrected Age (Ma)	err. (Ma)	Mean age (Ma)	St.Dev.† (Ma)
96BR005	**117.32**	**74.10**	**1.29**	**0.61**	**7.8**	**6.2**	**40.0**	**9.46**	**0.82**	**0.47**	-	**0.9**	**14.6**	**0.5**
96BR005-1	123.41	64.25	1.03	0.58	8.3	7.2	58.4	10.3	0.87	0.5	14.4	0.9		
96BR005-2	*126.48*	*75.09*	1.44	0.62	10.5	7.4	35.3	12.4	0.70	0.6	15.2	0.9		
96BR005-3	*102.07*	*82.96*	1.41	0.63	4.6	4.1	26.2	5.7	0.90	0.3	14.4	0.9		
96BR006	**82.68**	**37.83**	**0.24**	**0.39**	**15.2**	**2.2**	**99.4**	**16.24**	**0.14**	**0.46**	-	**0.8**	**13.4**	**-**
96BR006-1	*119.46*	*57.54*	*0.80*	*0.56*	*12.9*	*3.3*	*149.0*	*14.4*	*0.25*	*3.2*	*70.7*	*4.2*		
96BR006-2	*85.14*	*38.71*	*0.26*	*0.38*	*6.3*	*3.4*	*124.0*	*7.7*	*0.54*	*2.6*	*154.4*	*9.3*		
96BR006-3	82.68	37.83	0.24	0.39	15.2	2.2	99.4	16.2	0.14	0.5	13.4	0.8		
96BR006-4	*138.13*	*46.08*	*0.59*	*0.48*	*9.9*	*3.6*	*116.1*	*11.3*	*0.37*	*2.2*	*72.0*	*4.3*		
96BR009	**110.15**	**89.68**	**1.78**	**0.66**	**16.14**	**5.23**	**22.66**	**17.45**	**0.32**	**0.92**	-	**0.8**	**13.7**	**2.2**
96BR009-1	103.85	92.65	1.79	0.67	6.1	2.0	20.1	6.7	0.32	0.3	12.1	0.7		
96BR009-2	116.46	86.71	1.76	0.66	26.2	8.5	25.2	28.2	0.32	1.5	15.2	0.9		
96BR009-3	*92.88*	*70.28*	*0.92*	*0.59*	*7.4*	*2.9*	*53.2*	*8.4*	*0.38*	*0.5*	*18.9*	*1.1*		
96BR010	**76.47**	**67.94**	**0.72**	**0.55**	**4.8**	**3.1**	**55.5**	**5.83**	**0.65**	**0.22**	-	**0.7**	**12.1**	**0.2**
96BR010-1	*87.19*	*67.92*	*0.81*	*0.57*	*6.5*	*3.3*	*36.7*	*7.4*	*0.52*	*1.0*	*41.8*	*2.5*		
96BR010-2	79.22	73.45	0.86	0.58	5.1	2.8	48.4	5.9	0.55	0.2	12.2	0.7		
96BR010-3	*73.72*	*62.44*	0.58	0.53	4.6	3.5	62.6	5.7	0.76	0.2	11.9	0.7		
96BR013	**94.97**	**82.61**	**1.30**	**0.64**	**7.6**	**1.4**	**9.1**	**7.98**	**0.18**	**0.29**	-	**0.6**	**10.5**	**-**
96BR013-1	94.97	82.61	1.30	0.64	7.6	1.4	9.1	8.0	0.18	0.3	10.5	0.6		
96BR013-2	*108.96*	*52.65*	*0.61*	*0.52*	*11.9*	*3.3*	*20.0*	*12.8*	*0.28*	*0.6*	*16.6*	*1.0*		
96BR013-3	*133.98*	*62.28*	*1.05*	*0.58*	*8.6*	*2.7*	*12.7*	*9.3*	*0.31*	*0.5*	*18.5*	*1.1*		
96BR014	**115.79**	**73.00**	**1.24**	**0.60**	**1.6**	**3.2**	**9.4**	**2.42**	**2.00**	**0.08**	-	**0.6**	**10.2**	**-**
96BR014-1	*85.24*	*67.27*	*0.78*	*0.55*	*3.6*	*5.4*	*6.8*	*4.9*	*1.48*	*0.1*	*7.3*	*0.4*		
96BR014-2	*93.67*	*60.36*	*0.69*	*0.54*	*4.2*	*2.5*	*7.2*	*4.8*	*0.58*	*0.1*	*5.3*	*0.3*		
96BR014-3	115.79	73.00	1.24	0.60	1.6	3.2	9.4	2.4	2.00	0.1	10.2	0.6		

Notes: See text for discussion of analytical procedures and errors; samples in italics were not used in the calculation of mean ages

*Ft is alpha ejection correction of Farley et al. (1996).

†St. Dev.—standard deviation.

CHAPTER 3

Middle Miocene to recent exhumation of the Slate Range, eastern California, and implications for the timing of extension and the transition to transtension

J. Douglas Walker[1]

Tandis S. Bidgoli[1]

Brad D. Didericksen[2]

Daniel F. Stockli[3]

Joseph E. Andrew[1]

[1]*Department of Geology, University of Kansas, Lawrence, Kansas 66045, USA*

[2] *Now at Platte River Associates Inc., Houston, Texas, 77270, USA*

[3]*Now at Jackson School of Geosciences, University of Texas, Austin, Texas 78712, USA*

Abstract

New mapping combined with fault-slip and thermochronological data show middle Miocene to recent extension and exhumation of the Slate Range, eastern California, is produced by the active Searles Valley fault system and the Slate Range detachment, an older middle Miocene low-angle normal fault. Offset middle Miocene rocks record a combined ~7.5 km of west-directed extension over the last ~14 Ma for the fault zones. (U-Th)/He apatite cooling ages of samples from the central and southern Slate Range indicate that footwall cooling began around 14 Ma; we interpret this as the age of initiation of motion on the Slate Range detachment. This timing is consistent with inferences made using stratigraphic and structural criteria. Data from the northern Slate range show rapid fault slip began along the Searles Valley fault at ~4 Ma; data from the central and southern Slate Range can be interpreted to present cooling at 5 to 6 Ma. This timing correlates to the results of nearby studies, suggesting a strain transition in the

surrounding area between ~6-3 Ma. Data collected are most consistent with a westward migration in the locus of transtensional deformation, and show that the initiation of that deformation commonly lags the timing predicted by plate reconstructions by a few million years.

Introduction

The Miocene Basin and Range extensional province and the latest Miocene to recent eastern California shear zone/Walker Lane transtensional belt at the latitude of Las Vegas, Nevada may have been stretched up to 300% since ca. 16 Ma (e.g., Wernicke et al., 1988; Niemi et al., 2001). The earlier deformation resulted in primarily east-west extension across the region (Wernicke et al., 1982, 1988). Extension in the southwestern Basin and Range started at around 15 Ma as inferred by the ages of early basin deposits of the Panuga (Snow and Lux, 1999) and Eagle Mountain formations (Niemi et al., 2001) of the northern Death Valley area, and of the Panamint Valley volcanic sequence in the Argus, Panamint and Slate Range region (Figure 3.1; Andrew and Walker, 2009). Peak extension, however, probably occurred after 15 Ma (Snow and Wernicke, 2000, p. 687) and lasted until late Miocene time; the locus of the major deformation is interpreted to be well east of Panamint Valley.

Later deformation is primarily transtensional in character, expressed as dextral-oblique normal faults and strike-slip faults active in the region from Spring Mountains to the Sierran front. At this latitude, this later deformation belt is variously referred to as the eastern California shear zone or Walker Lane belt, and to a first order, affects the western half of the older Basin and Range extensional province.

Using plate reconstructions, Atwater and Stock (1998) have interpreted a change in plate motions at around 10 Ma, from a more westerly to a more northerly motion of the Pacific plate relative to North America, and associated this change to the transition to dextral-transtensional

deformation. Geological evidence paints a more complex picture of the deformational history. Mahan et al. (2009) suggested initiation of dextral transtension along the Stateline fault in southern Nevada at around 5 Ma (Figure 3.1). Wernicke et al. [1988, and subsequent works of Snow and Wernicke (2000), and McQuarrie and Wernicke (2005)] consider the Furnace Creek fault to be active from about 9 to 5 Ma, and that this fault is a component of the dextral regime (Figure 3.1). Snow and Lux (1999) interpreted the change to dextral deformation in Death Valley to have started around 11 Ma (Figure 3.1). Other studies that focus on different areas interpret younger ages for this change to transtension. Hodges et al. (1989) placed the transition at ~3.7 Ma in Panamint Valley (Figure 3.1). Monastero et al. (2002) considered this transition to have occurred at around 3 to 2 Ma in the Indian Wells Valley based on mostly subsurface stratigraphic data. Bellier and Zoback (1995) consider the transition to have occurred in the last 300 k.y. using Holocene fault scarp slip data. Lastly, Stockli et al. (2003) reported a general westward migration of the transition, starting at 6 Ma and progressing westward to 4 Ma based on fault kinematic and thermochronometric data from the Fish Lake Valley – White Mountain area. Thus, the precise timing and associated spatial pattern(s) of the onset of significant dextral deformation remains uncertain: The transition from east-west extension to northwest-directed oblique extension is apparently complex in both timing and location. The resolution of this problem requires more complete documentation of the age of transtensional slip on specific structures.

This paper aims to more closely bracket the initiation of extension and to better define the age of the transition from extension to transtension for the Slate Range and adjacent Searles Valley, which are west of both Panamint and Death valleys (Figure 3.1). To do this, we present new structural interpretations tied to three thermochronologic transects from the northern,

central, and southern Slate Range. The northern transect (roughly along cross section A-A' on Figure 3.2) trends east-west across the northern Slate Range, near where the SW-striking Manly Pass fault joins the north-striking Searles Valley fault; the central transect (along cross section B-B' on Figure 2) crosses the Slate Range just north of Tank Canyon; and the southern transect (cross-section C-C' on Figure 3.2) parallels Layton Canyon. This work complements studies of late Cenozoic deformation in the southern and northern Slate Range (Walker et al., 2005; Numelin et al., 2007; Andrew and Walker, 2009).

Geologic setting

The Slate Range trends north-south and the southern two-thirds of the range is bound on its western flank by a west dipping, low- to moderate-angle normal fault zone (Figure 3.2; Moore, 1976; Smith et al., 1968; Walker et al., 2005, Numelin et al., 2007). Pre-Cenozoic rocks along the northern transect consist of 100 Ma Stockwell diorite, 159 Ma Copper Queen alaskite, and 166 Ma Isham Canyon granite (Moore, 1976; Dunne and Walker, 2004) containing pendants of Paleozoic and Mesozoic sedimentary rocks. The central and southern transects cross Jurassic plutonic rocks that contain pendants of Jurassic meta-volcanic and meta-epiclastic rocks (Smith et al., 1968; Dunne and Walker, 2004). These assemblages represent portions of the Mesozoic Sierran magmatic arc and the Paleozoic continental passive margin. There is an ~85 m.y. time-gap between the youngest Cretaceous intrusive rock and middle Miocene sedimentary-volcanic units, which is marked by an extensive erosion surface (Moore, 1976; Andrew and Walker, 2003, 2009). Miocene rocks dip eastward, and comprise a ~14.5 to 12.5 Ma sequence consisting of basal sandstone and conglomerate with locally interbedded limestones overlain by basaltic rocks, rhyolite lava flows, pumaceous epiclastic rocks, and andesitic to dacitic laharic deposits (Smith et al., 1968; Andrew and Walker, 2003, 2009; Didericksen, 2005). A similar volcanic and

sedimentary sequence is also found to the northwest in the Argus Range (Moore, 1976; Andrew and Walker, 2003, 2009), to the east in the Panamint Range (Johnson, 1957; Andrew and Walker, 2009) and Owlshead Mountains (Davis, 1988; Davis and Fleck, 1977; Luckow et al., 2005), and to the southeast in the Quail Mountains (Muehlberger, 1954; Andrew, 2002), although thicknesses vary greatly between the sections to the east and south of the study area.

The relatively uniform nature of the Miocene sections in the Slate Range and nearby areas probably means that the basal nonconformity was relatively planar (Andrew and Walker, 2009), although the thickness of the lowest Miocene sedimentary deposits varies from 0 to 30 m. The thickest sections were deposited against subvertical buttress nonconformities and depositional half grabens (Andrew and Walker, 2009). The nonconformity on the eastern flank of the central Slate Range appears to be a laterally continuous surface dipping between 14° and 25° eastward (calculated using three point solutions; Table 3.1). Volcanic rocks of the same age in the northern Slate Range and in the southern Panamint Valley region are tilted to moderate east-northeast dips and are locally capped by rock avalanche deposits, suggesting the most significant tilting event occurred in the Pliocene (Andrew, 2005). Bedding above the nonconformity in the Panamint Valley area averages 35° and ranges from 20° to 50° (Andrew and Walker, 2009).

Structural setting

The structural geology presented here is based on our 1:24,000 scale geologic mapping and previous work by Moore (1976) and Smith et al. (1968). Structural interpretations come mostly from the mapping of Andrew and Walker (2009; also Walker et al., 2005) for the northern Slate Range, and Didericksen (2005) and Numelin et al. (2007) for the central Slate Range.

There are two Tertiary-age extensional fault systems in the Slate range – the Slate Range detachment fault and the active Searles Valley and Manly Pass faults (Figure 3.2). The Searles Valley and Manly Pass fault zones constitute a younger, segmented fault system (Walker et al., 2005; Numelin et al., 2007) that we refer to as the Searles Valley fault zone. The Slate Range detachment is the older structure, because it is variously exposed in the footwall and hanging wall of the Searles Valley fault and the hanging wall of the Manly Pass fault (Figure 3.2; Andrew, 2005; Andrew and Walker, 2009; Didericksen et al., 2005). Geologic relationships from the Layton Canyon area, in the central Slate Range, indicate that collectively the Searles Valley fault and Slate Range detachment accommodate a minimum of ~9 km of horizontal extension in an apparent westward direction (Figure 3.3; Didericksen, 2005). The geometry and kinematics of these faults are critical to establishing paleodepth estimates for thermochronology samples and are examined in more detail below.

Faulting history of the central Slate Range

The Slate Range detachment is currently inactive, rotated to near horizontal dips, and is offset across the Searles Valley fault zone (Figures 3.2 and 3.3). The fault is interpreted to have initiated as a roughly north- to northwest-striking normal fault that dipped westward between 25° and 50° (Didericksen, 2005). The interpreted initial dip is derived from its apparent 25° cutoff angle with Miocene strata east of the breakaway in the footwall (Figure 3.4A); it cannot be any steeper than 50°, the cutoff angle of Miocene rocks in fault horses in the hanging wall. The Slate Range detachment probably initiated during Miocene deposition because the volcanic sequences (~12 to 15 Ma) contain interbedded rock avalanche deposits, some basal conglomerates, and locally consist almost entirely of footwall-derived clasts, indicative of significant topographic relief (see additional discussion in Andrew and Walker, 2009). Definitive Pliocene and younger

rocks are not found in the hanging wall of the Slate Range detachment suggesting the fault was uplifted and inactive before Pliocene volcanism began in the nearby Argus Range (Andrew and Walker, 2009). In the central Slate Range, middle Miocene units in the hanging wall dip eastward up to 50° into a 2-3m thick zone of fault gouge which grades into brecciated Jurassic basement (Figure 3.2 and 3.4B). The detachment in the northern central Slate Range is exposed west of the Manly Pass fault; there are several fault splays which dip 5° to 10° westward cutting Mesozoic plutonic rocks. A several meter thick gouge zone separates the Mesozoic plutonic rocks from hanging wall faulted and brecciated Miocene basaltic-andesite lava flows and an overlying carbonate-cemented footwall-derived fanglomerate (Figure 3.4C). This fanglomerate is undated, but the deformed nature of it along with poorly exposed, but east-tilted bedding argue that it is older than the nearby 4-5 Ma relatively untilted basalt flows in the Argus Range (Andrew and Walker, 2009).

The Searles Valley fault zone as defined by Walker et al. (2005) is a curviplanar fault zone striking between 155° to 180° and dipping 15-35° to the west-southwest in the southern and central Slate Range (Figure 3.2). The dip steepens to ~50° as the fault is traced northward into the north-central Slate Range. Fault-slip data for the southern and central Slate Range, measured along the fault zone in the Mesozoic bedrock, indicate overall motion is west directed (Didericksen, 2005). This structure continues to the northern portion of the central Slate Range where it has been historically mapped as the Manly Pass fault (Moore, 1976). As noted above, we consider the Manly Pass and Searles Valley faults to constitute a single segmented fault system. South of cross section line A-A' (Figure 3.2), the Manly Pass fault is indistinguishable from the Searles Valley fault; north of A-A' it bends to the northeast, dips moderately to gently northwest, and has left-lateral oblique normal motion (Walker et al., 2005; Andrew and Walker

2009). The fault continues northeastward into Panamint Valley where it intersects with the Panamint Valley fault zone and the Panamint detachment (Walker et al., 2005; Andrew and Walker, 2009).

We interpret the above relationships to indicate that the Slate Range detachment is an older structure related to middle Miocene, west-directed extension in the Death Valley region. The Searles Valley fault zone is a younger structure related to transtension because it: (1) clearly cuts the Slate Range detachment; (2) appears to be moving with active fault systems (Walker et al., 2005; Numelin et al., 2007); and (3) is coincident with arrays of earthquake foci (e.g., Unruh and Hauksson, 2009).

In the following section, we present pre-extensional paleodepth estimates for our rock samples, which are critical to properly evaluating the thermal histories of the Slate Range detachment and Searles Valley fault systems. These estimates are independent of the cooling ages, which are discussed in subsequent sections. The thermochronologic data better delineates the timing of initiation and exhumation of structures described above.

Pre-extensional paleodepth estimates

The pre-extensional paleodepths of rock samples in the Slate Range are essential to placing the thermochronologic data into a cooling history (Stockli, 2005). Middle Miocene sedimentary and volcanic rocks rest nonconformably on basement along the eastern flank of the Slate Range, providing a pre-extensional paleohorizontal datum (Figure 3.4A). However, the topography of the nonconformity, thickness of volcanic and sedimentary overburden, and potential errors in post-14 Ma tilt corrections need to be considered in order to accurately estimate the paleodepths of thermochronology samples (e.g. Stockli et al., 2002). The thickness of basal sediments overlying the nonconformity provides evidence for only minor, short-

wavelength topographic relief (~30 m) prior to the deposition of the remainder of the middle Miocene sedimentary and volcanic sequence. It is unlikely that these small amplitude variations perturbed the thermal structure (e.g. Stockli, 2005).

The orientation of the paleohorizontal/nonconformity surface in the footwall block of the Slate Range detachment and Searles Valley fault zone was calculated as the mean of 11 measurements made in middle Miocene units on the east-central flank of the central Slate Range, yielding a strike of 349° +/- 16° and dip of 24° +/- 6° (2σ) (Figure 3.5 and Table 3.1). The pre-extensional volcanic and sedimentary overburden above the Miocene nonconformity at the onset of faulting was estimated based on the preserved stratigraphic thickness. Our observations and those of Smith et al. (1968) suggest the basal sandstones and limestones could collectively be up to 50 m thick, and conglomerate sections less than 30 m thick; overlying pyroclastic rocks may be up to ~30 m thick; and the capping basaltic and andesitic volcanic section is commonly over 50 m thick and locally may be up to 100 m thick. Thus, an overburden value of ~200 m is added to all sample paleodepths. This thickness is at the high-end of measurements by Andrew and Walker (2009) who present values of ~100 to 200 m for the section in the northern Slate Range. A difference of 100 m, however, has little effect on the reconstructions, and is minor compared to the other uncertainties. Although not seen or preserved in the Slate Range sections, correlative rocks thicken to over 700 m to the south and east in the southern Panamint Range and Brown Mountains areas.

These values and orientations bracket paleodepths in the central and southern Slate Range relatively well (Figures 3.2 and 3.3) because Miocene strata rest directly on the basement rocks in the line of section. Assuming a ~25° dip for this surface gives paleodepth values ranging from 0.3 to 3.2 km. This estimate is possible because the range can be considered a simple, tilted fault

block, thus eliminating the need to consider the hinge position for tilting (e.g., Armstrong et al., 2003). These depths apply to the area in Middle Miocene time since they are computed using the Miocene nonconformity. The removal of hanging wall rocks by the Slate Range detachment as well as possible footwall tilting makes estimates of depths for later Miocene to recent times less certain as most of the samples sit below the detachment (Figures 3.3 and 3.6). We assume that the main eastward tilting of this section occurred during Pliocene due to recent motions on the Searles Valley and Panamint Valley fault systems, although it is possible that some tilting accompanied movement on the detachment: we present information below that supports former interpretation for timing of the tilting.

For the northern Slate Range, the paleohorizontal/nonconformity reference plane was projected northward to the latitude of the thermochronologic transect as Miocene units are not present to the east of the Manly Pass fault in this area (Figures 3.2 and 3.3). The projection was made in the direction of mean strike from the northernmost exposure of the nonconformity (Figure 3.2) at an elevation of ~510 m. In addition, there are three small faults that cut across or project into the area. These were initially ignored in estimating the paleodepths.

For all three areas, paleodepth estimate errors are primarily a function of the uncertainty in the timing and amount of eastward footwall tilting and, for the northern transect, the projection of the paleohorizontal surface northward ~6 km. Timing of tilting is important as rotation of the block changes the estimated depths. If tilting is prior to cooling age, then depth estimates would become shallower. Uncertainties for tilt correction of the central (B-B') and southern (C-C') transects mainly result from the variation in dip of the nonconformity and the assumption that the block behaves in a rigid manner, and only amount to a few hundred meters for this transect (with probable uncertainty of 500 m for the deepest samples). For the northern transect, projection

uncertainties are computed using the extreme high and low values for dip and strike of the section. This results in a possible variation of up to 1.5 km of depth (2σ). (This uncertainty is not plotted on any figures but is included in the paleogeothermal gradient calculation.) Because the sample locations are mostly adjacent to or east of the projected breakaway for the Slate Range detachment (Figures 3.3 and 3.6), we assume that tilting was minor prior to movement on the Searles Valley fault zone. Structural reconstructions based on interpretations of the thermochronologic data will help evaluate this uncertainty. The paleodepth estimates for samples 1, 2, 8, and 37 (located in the hanging wall of the Searles Valley fault zone) were not calculated. Thermochronologic data do give some information about their possible reconstructed positions (Figure 3.6; see detailed discussions below for how positions were determined).

(U-Th)/He thermochronometry

To better understand the timing and magnitude of fault motion, we analyzed 43 samples from the Slate Range using (U-Th)/He thermochronometry (Figure 3.2). The (U-Th)/He method is a well-established and effective technique for directly dating the exhumation and cooling of footwalls of major normal faults (e.g., Axen et al., 2000; Stockli et al., 2000; Ehlers et al., 2003; Armstrong et al. 2004), as well as the initiation of transtensional structures (e.g., Stockli et al., 2003; Lee et al., 2009; Mahan et al., 2009). The method is based on the production of ^{4}He through the decay of ^{235}U, ^{238}U, ^{232}Th, and ^{147}Sm. However, ^{4}He retention in minerals is temperature dependent. In apatite, ^{4}He is completely lost by thermally activated volume diffusion above ~80˚C and mostly retained below ~40˚C (Wolf et al., 1996, 1998; House et al., 1999; Stockli et al., 2000). For zircon, helium is retained over a higher temperature range, from 190˚C to 130˚C (Reiners et al., 2002; 2004). These temperatures define thermal sensitivity windows or partial retention zones (PRZs) (Wolf et al., 1998) that can be used to reconstruct

temperature-time paths or apparent age-paleodepth/ elevation trends for a range of common accessory mineral (e.g., apatite, zircon, titanite, etc.), ideal for evaluating upper crustal processes (see summary in Stockli, 2005).

Apatite and zircon separates from rock samples were prepared by standard mineral separation techniques. Each single- or multi-grain apatite or zircon sample was loaded into 1-mm platinum packet. Apatite grains were heated for 5 minutes at 1050°C using a continuous-mode 20W Nd-YAG laser (House et al., 2000). Extracted He gas was spiked with ^{3}He, purified using a gettering and cryogenic gas system, and measured on a quadrupole mass spectrometer. Degassed apatite grains were then dissolved (in their platinum packets) in a spiked HNO_3 solution in preparation for U Th, and Sm determinations using inductively coupled plasma mass spectrometry (ICP-MS). Zircon grains were heated for 10 minutes at 1300°C. After laser degassing, zircon grains were removed from their platinum packets and dissolved using standard U-Pb double pressure-vessel digestion procedures. Following dissolution, samples were spiked and analyzed for U, Th, and Sm using ICP-MS. Laboratory and analytical work was performed at the Isotope Geochemistry Lab at the University of Kansas and at the (U-Th)/He Geo- and Thermochronometry Lab at the University of Texas at Austin.

A major challenge in (U-Th)/He dating of apatite is the presence of small U and Th-bearing impurities or inclusions such as zircon and monazite microlites (House et al., 1999; Lippolt et al., 1994). These impurities can bias the Ft correction (see below), modify diffusive behavior by changing the He concentration gradient, and/or incompletely dissolve during dilution of the grain in HNO_3. The latter is particularly problematic as a significant portion of the measured He is “parentless”, resulting in anomalously older ages (Farley and Stockli, 2002). In order to minimize these problems, inclusion-free grains were handpicked from separates with a

160X Nikon stereo petrographic microscope under crossed polarized light before being loaded into the Pt packets for analysis.

During α-decay, a portion of the ^{4}He produced is ejected out of the grain. This effect is the single greatest impediment to high precision (U-Th)/He ages in common accessory minerals (Farley et al., 1996). Unaccounted for ^{4}He ejected from the grain will result in a younger (U-Th)/He age. The loss of alpha particles is estimated by using a geometrical and statistical correction factor (Ft) based on the dimensions of the apatite grain and an assumed homogeneity of parent abundance throughout the crystal (Farley and Stockli, 2002; Farley et al., 1996). Apatite grains were measured using computer software calibrated to the microscope through a mounted digital camera. The Ft correction works best for euhedral grains over 100 um in width. Running several aliquots per sample helped to deal with inherent correction errors resulting from the smaller size and imperfect shape of many of the analyzed grains.

The resulting (U-Th)/He mean ages shown in Tables 3.2 and 3.3 were calculated from several individual analyses (see supplementary data Tables SD3.1 and SD3.2). In most cases (N=38), three or more replicates were used to calculate the mean; however, 8 of the 46 reported ages were calculated using fewer than three replicates. These samples contained outlier analyses that were excluded from our calculated mean ages. In fact, a significant portion (N=25) of our reported mean ages had outliers that were excluded from our calculations. Of the 195 individual analyses completed, 41 or 20% of the aliquots were excluded. Outliers were determined, in most instances, as ages that were more than 2 standard deviations from the mean. Analyses with a large number of reextractions during laser He degassing were also excluded from the determined means, as this usually points to the presence of unseen mineral or fluid inclusions within the grain (House et al., 1999). The data were evaluated for other possible trends that might explain

the high degree of scatter in our ages. No apparent correlation was identified between (U-Th)/He dates and effective U concentrations that would suggest radiation damage effects on closure temperatures (Shuster et al., 2006; Flowers et al., 2007). Similarly, we did not observe grain size effects in our data (Farley,2000; Reiners and Farley, 2001). Although we cannot determine the exact cause of the scatter in our data, we suspect that microscopic mineral or fluid inclusions (e.g., House et al., 1999), inhomogeneous parent isotope distributions (e.g., Hourigan et al., 2005) and/or He implantation from adjacent minerals (e.g., Spiegel et al., 2009) may be the source of our problems.

Propagated analytical uncertainties for individual analyses are approximately 3-4% (2σ). However, analytical uncertainties generally underestimate the reproducibility of a sample because uncertainties related to the Ft correction and U and Th distributions are difficult to quantify. Common practice in (U-Th)/He dating is to apply a percentage error to individual analyses based on the reproducibility of laboratory standards: 6% for apatite and 8% for zircon (Farley et al., 2001; Reiners et al., 2002). For our mean ages, we report the error as the standard deviation (1σ) of our grain population for a given sample. However, 4 samples (BDCSR28, BDCSR 36; 12LC09, and 12LC13) are single grain ages; therefore, we show the error in the "mean" age as the standard error.

Results

The results for the northern, central, and southern thermochronology transects are discussed in separate sections because of structural and age differences between them.

Northern Transect

The northern transect crosses the Manly Pass fault and consists of 15 samples of medium-grained Stockwell diorite from both the footwall and hanging wall (Figures 3.2 and 3.3).

Hanging wall rocks are complicated in that they come from horses within the hanging wall of the offset Slate Range detachment. Samples were collected approximately parallel to the west-directed motion (Walker et al., 2005) and were taken in ~100 m vertical increments in order to represent the entire footwall section (Figure 3.3 and Table 3.2).

Table 3.2 shows that apatite (U-Th)/He mean ages from the northern transect range from as young 4.2 Ma to as old as 51.8 Ma, but no systematic relationship between cooling age and elevation is observed. The youngest cooling ages along this transect are located in the footwall immediately east of the Manly Pass fault, clustering at around 4 Ma (Table 3.2 and Figure 3.3A). The samples increase in apparent age to east (Table 3.2 and Figure 3.3A). Some of the oldest apparent ages are located west of the fault, ranging from 28.8 Ma to 51.8 Ma (Table 3.2 and Figure 3.3A).

Central Transect

The central transect crosses the Searles Valley fault and consists of 14 samples of Copper Queen alaskite and Jurassic metadiorite (Figures 3.2 and 3.3). Only one sample was collected from the hanging wall of the fault zone; all other samples are from the footwall of both the Searles Valley fault and Slate Range detachment.

Table 3.2 shows that apatite (U-Th)/He mean ages from the central transect range from as young 6.0 Ma to as old as 50.1 Ma. Like the northern transect, no systematic relationship between cooling age and elevation is observed (Table 3.2). Samples with the youngest cooling ages come from the western part of the transect (Table 3.2 and Figure 3.3B). The three westernmost samples from the Searles Valley fault footwall have ages varying from ~6 to 9 Ma. Higher in the range, two samples give consistent ages at about 14 Ma. Samples then increase in apparent age eastward over the range (Table 3.2 and Figure 3.3B). The oldest apparent ages are

located on the eastern slope, from samples located only a few hundred meters beneath the projection of the Miocene nonconformity, and have ages of ~45 to 50 Ma (Table 3.2 and Figure 3.3B).

Southern Transect

The southern transect crosses the Searles Valley fault and consists of 14 samples of Jurassic diorite, leucogranite, and metavolcanic rocks (Figures 3.2 and 3.3). Two samples were collected from the hanging wall of the fault zone; all other samples are from the footwall of both the Searles Valley fault and Slate Range detachment.

Although there are 14 samples in the southern transect, only 7 contained inclusion-free apatite grains. Table 3.2 shows that the resulting mean ages range from as young 5.2 Ma to as old as 26.0 Ma. Like the other transects, no systematic relationship between apparent age and elevation is observed (Table 3.2). Samples with the youngest cooling ages come from the western part of the transect, east of the both the Searles Valley fault and Slate Range detachment, ranging from 5.2 Ma to 6.8 Ma (Table 3.2 and Figure 3.3C). Further east, two samples give consistent ages at about 13 Ma (Table 3.2 and Figure 3.3C). The oldest apparent age is from a sample located a few hundred meters below the projection of the Miocene nonconformity (Table 3.2 and Figure 3.3C).

Zircon (U-Th)/He mean ages from the southern transect are shown in Table 3.3. Only 11 of the 14 samples had useable zircon grains. The mean ages range from as young as 44.6 Ma to as old as 56.6 Ma, with most samples clustering around 51 Ma. No systematic relationship between the age of samples and their elevation was observed in the data.

Interpretation of the (U-Th)/He thermochronologic data

Plotting the apparent (U-Th)/He ages against paleodepth provides a basis for interpreting the cooling and exhumation history of the Slate Range with respect to the mapped faults and faulting history of the area (Figure 3.6). It is important to note that the paleodepth interpretations come from basic structural mapping of the area, whereas the temperature/ partial retention zone interpretations come solely from the (U-Th)/He age data. Thus, the two datasets are independent, although we do use the apparent age data to make some adjustments to the depths in the northern profile.

Northern Transect

The northern transect is somewhat complicated in that three mapped faults cross or project into the footwall of the Searles Valley fault zone (Figure 3.3A). The amount slip on these structures is unknown. An additional complication for this transect is that three of the oldest (U-Th)/He samples are found within the hanging wall of the fault (Figure 3.3A). Clearly, any offsets from faults within the cross section must be accounted for in order to restore all of the samples to their "true" pre-extensional paleodepths. Our initial interpretations ignored footwall faults, restoring samples to paleodepths relative to our projection of the Miocene nonconformity. This yielded a clear trend of age with depth, but resulted in a somewhat jagged partial retention zone. We then made small adjustments to the paleodepths by using the cooling ages to create a smooth partial retention zone to infer offset across these structures (Figures 3.3A, 3.6A, and 3.7). Our interpretation based on cooling ages is that the western two faults have ~125 and ~150 m of down-to-the-west throw respectively, and the eastern fault ~300 m of down-to-the-east throw at the eastern flank of the northern-central Slate Range (Figure 3.3A). Hence, the down-to-the-east and down-to-the-west components are essentially the same. This means that these faults have

little effect on our depth estimates in the western part of the transect, and the relatively minor offsets restored on these structures do not quantitatively affect our conclusions. On the other hand, samples in the hanging wall of the Manly Pass fault are particularly important, as they can be used to constrain Pliocene slip on that structure and the top of the Pliocene partial retention zone. These samples (1, 2, 3, and 8) were restored by adjusting the depths of the sample until they intersected the extrapolated trend of data from the footwall of the Manly Pass fault, through the Pliocene PRZ (Figure 3.7).

After restoring the samples to their paleodepths, the apatite (U-Th)/He data from the northern Slate Range exhibit systematic apparent age versus paleodepth patterns indicative of rapid footwall exhumation of a shallow crustal block (House et al., 1999; Reiners et al., 2000; Armstrong et al., 2003; Stockli, 2005; Stockli et al., 2000; Stockli et al., 2002). Apparent ages decrease with increasing paleodepths from 51.8 Ma to 4.3 Ma at ~2.3 km paleodepth (Figure 3.7). Invariant ages at the structurally deepest paleodepths record rapid exhumation at ~4 Ma. Based on the proximity of these samples to the Manly Pass fault (Figures 3.3A and 3.6A), these invariant (U-Th)/He ages are interpreted to be related to fault slip along that structure. The invariant ages indicate that fault slip was significant enough to cool samples from just below the zero retention isotherm (> ~80°C) to below 40°C. Hence, we interpret the Manly Pass segment of the Searles Valley fault zone to have initiated at around 4 Ma. Progressively older apparent ages at structurally shallower depths record residence in the apatite He PRZ prior to early Pliocene exhumation (Figure 3.7). Exhumation and cooling directly attributed to the earlier Slate Range detachment is not observed in the data. The projected NNW strike of the Slate Range detachment and structural reconstructions suggests that the breakaway for this fault was west or

above most samples in this transect (Figure 3.6A). This may indicate that the effect of motion on this structure was not in a position to cause a significant change in the thermal structure.

Based on our paleodepth reconstructions, the relative position of the 80° C isotherm is constrained to be between 1.8 and 2.0 by samples 6 (shallowest Pliocene sample) and 7 (deepest Miocene sample). Although the relative position is tightly determined, our structural restoration (using all estimated errors) places the pre-extensional depth of the 80° C isotherm at 1.8 +/-1.5 km. Using an assumed mean annual surface temperature of 10 +/-5°C (Stockli et al., 2000), the pre-extensional geothermal gradient is 40 +/-30°C/km. The uncertainty based on absolute paleodepths is obviously quite large, but it is the most precise estimate that can be obtained with the available structural data.

The ~40°C/km geothermal gradient is elevated compared to average continental geothermal gradients of ~25°C/km; however, local volcanic activity supports high heat flow and an elevated geothermal gradient in the late Miocene and Pliocene Slate Range (Andrew and Walker, 2009). Interestingly, this value is similar to estimates of the geothermal gradient in the Wassuk Range (Stockli et al., 2002) and to modern geothermal gradients of ~35°C/km in the western Basin and Range province (e.g., Lachenbruch and Sass, 1980). Unfortunately, uncertainties in our data make drawing conclusions about the thermal structure of the Slate Range pre-extensional upper crust difficult.

Using the cooling ages, we can estimate the throw, fault slip, and west-directed heave or extension on the Manly Pass segment over the past ~4 Ma. Our principal estimate using sample 2 does not directly rely on paleodepth, but rather restoration of cooling ages in cross section. The dip-slip estimated here is ~1.5 km. This is the amount of offset of sample 2 to restore it to the appropriate age horizon of the PRZ. This estimate is similar to the ~2 km magnitude of the dip-

slip estimated along cross-section A-A' by restoring the middle Miocene rocks in the hanging wall along the fault to the projected middle Miocene nonconformity in the footwall (although this interpretation is complicated by uncertain effects of the Slate Range detachment). The present dip of the Manly Pass fault is approximately 50° to the west in the northern-central Slate Range. This dip constrains the amount of heave on the fault over the last 4 Ma to ~ 1 km. This yields an average west-directed extension rate of ~0.25 mm/yr since the early Pliocene on the basal fault of the system. This rate is the same as the slip rate of 0.21 to 0.35 mm/yr inferred for the Searles Valley fault to the south by Numelin et al. (2007) over latest Pleistocene to Holocene time. Because that fault dips shallowly, it slip rate is approximately the same as the east-west extension rate. For this reason, it appears that the modern and time averaged rates on the Searles Valley fault zone are similar along its extent. It is important to note that this estimate applies to the basal fault strand of the Searles Valley fault zone. There is significant distributed faulting in the hanging wall of this structure (not sampled by this estimate or that of Numelin et al., 2007) that probably amounts to ~3.5 km of additional regional extension (Andrew and Walker, 2009).

Central and Southern Transects

Paleodepth reconstructions of (U-Th)/He ages from the central and southern transects are somewhat simpler than for the northern one since almost all of the samples reside within the minimally faulted footwall to the Searles Valley fault zone and Slate Range detachment (Figure 3.3, 3.6B, and 3.6C). However, interpretation of the reconstructed cooling ages is significantly more complicated. Zircon (U-Th)/He ages from the southern transect cluster around ~51 Ma, suggesting there is an exhumation event at that time (Figure 3.8 and Table 3.2). While this exhumation event is significantly older than the Miocene and Pliocene fault history we are concerned with, this age is an important constraint for interpreting the apatite data (see below).

Apatite (U-Th)/He apparent ages increase with decreasing paleodepth from ~5 Ma to ~51 Ma (Figure 3.8). The oldest apatite samples from the central transect (samples 27, 28, 29, 30, 38, and 39) are similar in age to zircons from the southern transect, suggesting that these relatively old apatite samples resided near the top of a partial retention zone, and are either unreset or only minimally reset. Below 1.0 km (depth of sample 39), apatite ages get progressively younger. Figure 3.8 shows a possible interpretation of data, where a partial retention zone is identified between 0.4 and 2.5 km. Below 2.5 km, (U-Th)/He ages form a cluster around ~6 Ma, suggesting rapid exhumation at that time (Figure 3.8). Using this paleodepth reconstruction, the relative position of the 80° C isotherm is constrained to be between 2.2 and 2.5 by sample 12LC11, the shallowest ~6 Ma sample, and sample 35, the deepest sample definitively within the partial retention zone. Using an assumed mean annual surface temperature of 10 +/-5°C (Stockli et al., 2000), the calculated late Miocene geothermal gradient is 30+/-4°C/km.

Although the pattern of cooling ages and calculated geothermal gradient, using the above interpretation, are broadly similar to that of the northern transect (Figure 3.7), it implies that exhumation along Searles Valley fault zone initiated at 6 Ma in the central and southern parts of the Slate Range, and at 4 Ma in the north. Fault initiation at 6 Ma is not improbable as extension is known to occur in the Death Valley area at that time (e.g., Topping, 1993; Snow and Lux, 1999). However, Pliocene cooling and fault histories are much more common for this part of the Basin and Range (e.g., Hodges et al., 1989; Snyder and Hodges, 2000; Monastero et al., 2002; Stockli et al., 2003; Andrew and Walker, 2009; Lee et al., 2009). The interpretation shown in Figure 3.8 also ignores a group of samples between 1.7 and 2.2 km that cluster between 12-14 Ma, coincident with the timing of initiation for the Slate Range detachment (Andrew and Walker, 2009). For these reasons, we prefer an alternative interpretation of our reconstructed

samples, shown in Figure 3.9. In this interpretation, two partial retention zones are identified from the data. The first is evident between 0.4 and 1.6 km (Figure 3.9). Below 1.6 km, ages cluster between 12-14 Ma, recording an exhumation event at that time (Figure 3.9). We interpret these samples to record cooling related to motion on the Slate Range detachment, consistent with the work of Andrew and Walker (2009). While these samples were exhumed and cooled through the apatite He PRZ in the Miocene, structurally deeper samples yield younger apparent ages (between about 5 and 9 Ma). Although the data are somewhat clustered, they show inconsistent age to paleodepth scatter. We therefore interpret these rocks to have resided in a second PRZ during late Miocene to early Pliocene time, and were then exhumed and cooled during Pliocene motion on the Searles Valley fault. We accept the ~4 Ma age from the Manly Pass segment to be the most reliably time of initiation of faulting. For the central transect, motion on the fault was probably not sufficient to expose rocks that were originally below the PRZ for the Pliocene (Figures 3.3, 3.6 and 3.9). In contrast, paleodepth reconstructions of the data from the southern transect suggest that samples 12LC03 and 12LC04 resided below the Pliocene PRZ (Figure 3.6C). Unfortunately this could not be confirmed because inclusion-free apatite grains were not identified within these samples.

Structural restoration using our preferred interpretation places the pre-extensional depth of the middle Miocene 80° C isotherm at 1.6 +/-0.2 km (Figure 3.8). Based on an assumed mean annual surface temperature of 10 +/-5°C (Stockli et al., 2000), the pre-extensional geothermal gradient is 45 +/-9°C/km. The 45°C/km geothermal gradient is elevated compared to average continental geothermal gradients of ~25°C/ km and significantly higher than the ~15°C/km geothermal gradient documented for the nearby Inyo (Lee et al., 2009) and White mountains (Stockli et al., 2003). Although local volcanic activity is consistent with relatively high heat

flow and an elevated geothermal gradient during the Miocene in the Slate Range (Andrew and Walker, 2009), the high magnitude of the geothermal gradient suggests that there may be a problem with our absolute paleodepths. This is confirmed when evaluating the position of the 40° C isotherm in both Figures 3.8 and 3.9 at 0.4km, probably an unrealistically shallow depth. This suggests there was additional overburden in the central and southern parts of the Slate Range, not accounted for in our reconstructions. As noted above, Miocene sections to the east in the Panamint Range are typically 500 m thicker. If this is applied to the central and southern transects, then the 40° C isotherm would have been at a more reasonable depth of about 1 km.

Extension across the central and southern transects is somewhat larger in that we see the effects of both the Miocene and Pliocene to recent fault systems. In the Layton Canyon area, we estimate a minimum of ~9 km of east-west extension: 4 km of this is from the Slate Range detachment (the distance between the westernmost klippe and its likely footwall equivalent to the east) and 5 km from the Searles Valley fault (see Andrew and Walker, 2009). A significant component of the apparent horizontal displacement across the central Slate Range results from the post-Miocene tilting of a moderately dipping Slate Range detachment fault to low dips. This tilting seems to predate the inception of the Searles Valley fault in the northern central Slate Range that still has relatively steep dips. If there is a general westward moving wave of the initiation of transtensional deformation then extensional faults in the Death Valley extensional system may have been active before transtension began in the Slate Range [~11 Ma from Snow and Lux (1999) and ~8 Ma from Topping (1993)]. The Death Valley extensional fault system dips to the west beneath the Panamint Range and probably also below the Slate Range, therefore displacement on these systems could lead to similar amounts and orientations of tilted Miocene

units of the hanging wall Panamint and Slate ranges before transtensional deformation begins in this area.

Discussion

Our age of ~4 Ma for cooling of the Searles Valley fault zone footwall rocks provides an important regional constraint on the timing of transition to transtensional deformation. Comparing the work of Mahan et al. (2009) and Monastero et al. (2002) with this study would indicate that the onset of dextral transtensional deformation decreases in age westward at this latitude, from around 5 Ma in southern Nevada, to 4 Ma in Searles Valley/southern Panamint Valley, to 3 to 2 Ma in Indian Wells Valley. These data, therefore, support the idea presented by Stockli et al. (2003) of a westward progression in initiation of dextral transtension.

Interestingly, our ~4 Ma age is somewhat older than the 2.8 +/- 0.7 Ma age for renewed motion on the eastern Inyo fault zone and start of motion on the Hunter Mountain fault (Figure 3.1; Lee et al., 2009). This is significant in that motion on the Hunter Mountain fault is interpreted to transfer slip from the Panamint Valley fault zone onto the eastern Inyo fault zone in Saline Valley (e.g., Burchfiel et al., 1987, Lee et al., 2009), hence implying that the Panamint system started at around 3 Ma (see Figure 3.1 for structures and locations). Alternatively, Walker et al. (2005) interpreted the Searles Valley fault zone and Panamint Valley fault zones to be an integrated system of structures accomplishing dextral transtensional deformation in the region, implying a somewhat older age of initiation. This leads to several possible options for resolving this difference in age: (1) Uncertainties on the ages interpreted from the analytical data are underestimated, and the ages would overlap if larger/more reasonable errors were assigned; (2) The rapid cooling evident in age/depth profiles does not record the onset of faulting, but is imparted at somewhat different times; or (3) Slip along the Panamint/Searles system did not

initially link along the Hunter Mountain fault into Saline Valley, but rather continued northward through the Towne Pass area between the Panamint and Cottonwood mountains. Although all these scenarios are possible, we favor the last for several reasons. First, the errors seem reasonably computed and the ages are reproducible. Second, other studies show that rapid cooling is associated with fault initiation (see Stockli, 2005). Third, there is evidence for significant deformation in the Towne Pass area at the time motion began on the Searles system. Snyder and Hodges (2000) report large increase in sedimentation rate for the Nova basin starting at around 4 Ma and continuing to about 3 Ma. They also report that faulting in the area is distributed in a complex manner between the Emigrant detachment and other structures over this time interval. Thus, it is our interpretation that the Panamint/Searles system did initiate at about 4 Ma, and that for the first 1 m.y. of its history fed deformation northward through the Emigrant and Towne Pass systems. This ceased at around 3 Ma when deformation in Panamint Valley was transferred northwestward into Saline Valley via the Hunter Mountain fault.

If the above interpretations are correct for the timing of extension and the initiation of transtension in the Slate Range, then regionally there may not be a change from local extension to transtension, but instead there is a spatial wave of the local initiation of major transtensional deformation structures that overprint an earlier discrete east-west extensional event, active only in the middle to late (?) Miocene. This idea may resolve the issue of comparing timing data derived from fault studies versus from plate tectonic data. The plate tectonic data indicates that transtensional deformation should have begun at 8 to 10 Ma (Atwater and Stock, 1998) after a period of east-west extension. Transtension in Death Valley seems to begin at this time (Wernicke et al., 1988, Snow and Lux, 1999), but areas to the west (i.e., the Panamint and Slate Ranges) were not experiencing significant deformation until ~4 Ma (Hodges et al., 1989).

Transtensional deformation then migrated westward in a series of jumps to farther west structures (Hodges et al., 1989; Andrew, 2005; Monastero et al., 2002). Transtensional faulting then began at ~4 Ma in the Slate Range by the initiation of the Searles Valley fault zone.

Conclusions

Our new mapping and thermochronological data give important insights into the exhumation and extension of the Slate Range, California. The range is presently part of the eastern California shear zone/ Walker Lane system and is undergoing transtension on the Searles Valley fault zone. Transtensional activity started at around 4 Ma when footwall rocks of the Searles Valley fault zone cooled below the apatite (U-Th)/He partial retention zone.

Apatite data from the central and southern Slate Range indicate that cooling started around 14 Ma. This is probably related to motion on the mapped Slate Range detachment. This fault currently has a flat dip, but probably initiated with a dip closer to 25° to 50°, the dip of footwall Miocene strata and the cutoff angle of similar strata in the hanging wall, respectively. Overall extension during this phase was west directed, and has a minimum value of 4 km – this is the offset distance between Miocene strata in the hanging wall from the footwall nonconformity beneath coeval rocks. Assuming extension is similar between the northern and central Slate Range, this gives a combined total extension in the range of ~9 km.

Timing of extension fits well with regional patterns. The beginning of transtensional deformation is somewhat older than that in Indian Wells Valley, but somewhat younger than in southern Nevada, suggesting that transtension progressively youngs westward.

Acknowledgements

This study was partially supported by grants awarded to Walker from the Geothermal Program Office at China Lake Naval Weapons Station and the EarthScope Program of the

National Science Foundation. The authors are indebted to numerous researchers for discussions on the geology of the Panamint Valley Region, including George Dunne, Frank Monastero, Jon Spencer, Eric Kirby, and Marek Cichanski. This manuscript was significantly improved by thoughtful reviews from Ann Blythe and Phillip Armstrong.

References cited

Andrew, J.E., 2002, The Mesozoic and Tertiary tectonics of the Panamint Range and Quail Mountains, California [Ph.D. thesis]: Lawrence, University of Kansas, and 154p.

Andrew, J.E., 2005, Complexity and transtension in the Walker Lane Belt due to superposition of Neogene strain fields: Panamint Valley, California: Geological Society of America Abstracts with Programs, v. 37, p. 70.

Andrew, J.E., and Walker, J.D., 2003, Miocene and Pliocene volcanic-sedimentary successions and relationships with deformation in the extensionally dismembered Panamint Valley region, SE California: Geological Society of America Abstracts with Programs, v. 35, p. 347.

Andrew, J.E., and Walker, J.D., 2009, Reconstructing Cenozoic deformation in the Panamint Valley region, eastern California, with implications for timing and magnitude of faulting in parts of the Central Basin and Range: Geosphere, v. 5, p. 172-198.

Armstrong, P.A., Taylor, A.R., and Ehlers, T.A., Is the Wasatch fault footwall (Utah, United States) segmented over million-year time scales?: Geology, v. 32, p. 385-388.

Atwater, T., and Stock, J., 1998, Pacific-North America Plate tectonics of the Neogene Southwestern United States; an update, *in* Ernst, W.G., and Nelson, C.A., eds., Integrated Earth and environmental evolution of the Southwestern United States; the Clarence A. Hall, Jr. volume.: Columbia, MD, United States, Bellwether Publishing, p. 393-420.

Ault, A.K. and Flowers, R.M., 2012, Is apatite U-Th zonation information necessary for accurate interpretation of apatite (U-Th)/He thermochronometry data?: Geochimica et Cosmochimica Acta, v. 79, p. 60-78.

Axen, G.J., Grove, M., Stockli, D., Lovera, O.M., Rothstein, D.A., Fletcher, J.M., Farley, K., and Abbott, P.L., Thermal evolution of Monte Blanco dome: Low-angle normal faulting during Gulf of California rifting and late Eocene denudation of the eastern Peninsular Ranges: Tectonics, v. 19, p. 197-212.

Bellier, O., and Zoback, M.L., 1995, Recent state of stress change in the Walker Lane zone, western Basin and Range Province, United States: Tectonics, v. 14, p. 564-593.

Burchfiel, B.C., Hodges, K.V., and Royden, L.H., 1987, Geology of Panamint Valley-Saline Valley pull-apart system, California; palinspastic evidence for low-angle geometry of a Neogene range-bounding fault: Journal of Geophysical Research, v. 92, p. 10,422-10,426.

Davis, G.A., 1988, Enigmatic "older-over-younger" low-angle faulting of Miocene age, central Owlshead Mountains, California: Geological Society of America Abstracts with Programs, v. 20, no. 3, p. 154.

Davis, G.A., and Fleck, R.J., 1977, Chronology of Miocene volcanic and structural events, central Owlshead Mountains, eastern San Bernardino County, California: Geological Society of America Abstracts with Programs, v. 9, p. 409.

Didericksen, B., 2005, Middle Miocene to recent faulting and exhumation of the central Slate Range, Eastern California Shear Zone [M.S. thesis]: Lawrence, University of Kansas, 104 p.

Dunne, G.C., and Walker, J.D., 2004, Structure and evolution of the East Sierran thrust system, east central California: Tectonics, v. 23, p. TC4012, 1-23.

Ehlers, T.A., Willett, S.D., Armstrong, P.A., and Chapman, D.S., 2003, Exhumation of the Central Wasatch Mountains, Utah: 2. Thermo-kinematics of exhumation, erosion and thermochronometer interpretation: Journal of Geophysical Research., v. 108, 2173, doi:10.1029/2001JB001723.

Farley, K.A., 2000, Helium diffusion from apatite: General behavior as illustrated by Durango fluorapatite: Journal of Geophysical Research: v. 105, p. 2903–2914, doi:10.1029/1999JB900348.

Farley, K.A., Rusmore, M.E., and Bogue, S.W., 2001, Exhumation and uplift history of the central Coast Mountains, British Columbia, from apatite (U-Th)/He Thermochronometry: Geology, v. 29, p. 99-102.

Farley, K.A., and Stockli, D.F., 2002, (U-Th)/ He dating of phosphates; apatite, monazite, and xenotime, *in* Kohn, M.J., Rakovan, J., and Hughes, J.M., eds., Phosphates; geochemical, geobiological, and materials importance., Mineralogical Society of America and Geochemical Society. Washington, DC, United States.

Farley, K.A., Wolf, R.A., and Silver, L.T., 1996, The effects of long alpha-stopping distances on (U-Th)/ He ages: Geochimica et Cosmochimica Acta, v. 60, p. 4223-4229.

Flowers, R.M., Shuster, D.L., Wernicke, B.P., and Farley, K.A., 2007, Radiation damage control on apatite (U-Th)/He dates from the Grand Canyon region, Colorado Plateau: Geology, v. 35, p. 447–450, doi: 10.1130/G23471A.1.

Hodges, K.V., McKenna, L.W., Stock, J., Knapp, J., Page, L., Sternlof, K., Wuest, G., and Walker, J.D., 1989, Evolution of extensional basins and basin and range topography west of Death Valley, California: Tectonics, v. 8, p. 453-467.

Hourigan, J. K., Reiners, P. W., and Brandon, M. T., 2005, U-Th zonation-dependent alpha-ejection in (U-Th)/He chronometry: Geochimica et Cosmochimica Acta, v. 69, p. 3349-3365.

House, M.A., Farley, K.A., and Kohn, B.P., 1999, An empirical test of helium diffusion in apatite; borehole data from the Otway Basin, Australia: Earth and Planetary Science Letters, v. 170, p. 463-474.

House, M.A., Farley, K.A., and Stockli, D., 2000, Helium chronometry of apatite and titanite using Nd-YAG laser heating: Earth and Planetary Science Letters, v. 183, p. 365-368.

Johnson, B.K., 1957, Geology of a part of the Manly Peak Quadrangle, southern Panamint Range, California: University of California Publications in Geological Sciences, v.30, p. 353-423.

Lachenbruch, A. H., and Sass, J. H., 1980, Models of an extending lithosphere and heat flow in the Basin and Range province, *in* R. B. Smith and G. P. Eaton, eds., Cenozoic Tectonics and Regional Geophysics of the Western Cordillera, Memoir of the Geological Society of America, v.152, p. 209 – 250.

Lee, J., Stockli, D.F., Owen, L.A., Finkel, R.C., and Kislitsyn, R., 2009, Exhumation of the Inyo Mountains, California: Implications for the timing of extension along the western boundary of the Basin and Range Province and distribution of dextral fault slip rates across the eastern California shear zone: Tectonics, v. 28, TC1001, doi:10.1029/2008TC002295.

Lippolt, H.J., Leitz, M., Wernicke, R.S., and Hagedorn, B., 1994, (Uranium+thorium)/ helium dating of apatite; experience with samples from different geochemical environments: Chemical Geology, v. 112, p. 179-191.

Luckow, H.G., Pavlis, T.P., Serpa, L.F., Guest, B., Wagner, D.L., Snee, L., Hensley T. and Korjenkove, A., 2005, Late Cenozoic sedimentation and volcanism during transtensional deformation in Wingate Wash and the Owlshead Mountains, Death Valley: Earth-Science Reviews, v. 73, n. 1-4, p. 177-219.

Mahan, K.H., Guest, B., Wernicke, B., and Niemi, N.A., 2009, Low-temperature thermochronologic constraints on the kinematic history and spatial extent of the Eastern California shear zone: Geosphere; v. 5, p. 483–495, doi: 10.1130/GES00226.1

McQuarrie, N. and Wernicke, B., 2005, An animated tectonic reconstruction of southwestern North America since 36 Ma: Geosphere, v. 1, p. 147-172.

Miller, M.B., and Pavlis, T.L., 2005, The Black Mountains Turtlebacks: Rosetta Stones of Death Valley tectonics: Earth Science Reviews, v. 73, p. 115-138.

Monastero, F.C., Walker, J.D., Katzenstein, A.M., and Sabin, A.E., 2002, Neogene evolution of the Indian Wells Valley, east-central California, *in* Glazner, A.F., Walker, J.D., and Bartley, J.M., eds., Geologic evolution of the Mojave Desert and southwestern Basin and Range., Geological Society of America (GSA). Boulder, CO, United States.

Moore, S.C., 1976, Geology and thrust fault tectonics of parts of the Argus and Slate ranges, Inyo County, California.

Muehlberger, W. R., 1954, Geology of the Quail Mountains San Bernardino County, Map Sheet no. 16: In: Jahns, R. H., ed., Geology of southern California: California Division of Mines Bulletin, n. 170.

Niemi, N.A., Wernicke, B.P., Brady, R.J., Saleeby, J.B., and Dunne, G.C., 2001, Distribution and provenance of the middle Miocene Eagle Mountain Formation, and implications for regional kinematic analysis of the Basin and Range Province: Geological Society of America Bulletin, v. 113, p. 419-442.

Numelin, T., Kirby, E., Walker, J.D., and Didericksen, B., 2007, Late Pleistocene slip on a low-angle normal fault, Searles Valley, California: Geosphere, v. 3, no. 3, p. 163–176, doi: 10.1130/GES00052.1s.

Reiners, P.W., Brady, R., Farley, K.A., Fryxell, J.E., Wernicke, B.P., and Lux, D., 2000, Helium and Argon thermochronometry of the Gold Butte block, South Virgin Mountains, Nevada: Earth and Planetary Science Letters, v. 178, p. 315-326.

Reiners, P.W., and Farley, K.A., 2001, Influence of crystal size on apatite (U-Th)/He thermochronology: An example from the Bighorn Mountains, Wyoming: Earth and Planetary Science Letters, v. 188, p. 413-420.

Reiners, P.W., Farley, K.A., and Hickes, H.J., 2002, He diffusion and (U-Th)/He thermochronometry of zircon: Initial results from Fish Canyon Tuff and Gold Butte: Tectonophysics, v. 349, p. 247–308.

Reiners, P.W., Spell, T.L., Nicolescu, S., and Zanetti, K.A., 2004, Zircon (U-TH)/He thermochronometry: He diffusion and comparison with 40Ar/39Ar dating: Geochimica et Cosmochimica Acta, v. 68, p. 1857-1887.Shuster, D.L., Flowers, R.M., and Farley, K.A., 2006, The influence of natural radiation damage on helium diffusion kinetics in apatite: Earth and Planetary Science Letters, v. 249, doi: 10.1016/j.epsl.2006.07.028.

Smith, G.I., Troxel, B.W., Gray, C.H., Jr., and Von, H.R., 1968, Geologic reconnaissance of the Slate Range, San Bernardino and Inyo counties, California: Special Report – California Division of Mines and Geology, v. 96, p. 1-33.

Snow, J.K. and Lux, D.R., 1999, Tectono-sequence stratigraphy of Tertiary rocks in the Cottonwood Mountains and northern Death Valley area, California and Nevada: *in* Troxel, B.W., ed., Geological Society of America Special Paper, v. 333, p. 17-64.

Snow, J.K. and Wernicke, B.P., 1989, Uniqueness of geological correlations; an example from the Death Valley extended terrain: Geological Society of America Bulletin, v. 101, p. 1351-1362.

Snow, J.K., and Wernicke, B.P., 2000, Cenozoic tectonism in the central Basin and Range: Magnitude, rate and distribution of upper crustal strain: American Journal of Science, v. 300, p. 659-719.

Snyder, N.P. and Hodges, K.V., 2000, Depositional and tectonic evolution of a supradetachment basin: 40Ar/39Ar geochronology of the Nova Formation, Panamint Range, California: Basin Research, v. 12, p. 19-30.

Spiegel, C., Kohn, B., Belton, D., Berner, Z., and Gleadow, A., 2009, Apatite (U-Th-Sm)/He thermochronology of rapidly cooled samples: The effect of He implantation: Earth and Planetary Science Letter, v. 285, p. 105-114.Stewart, J.H., 1983, Extensional tectonics in the Death Valley area, California; transport of the Panamint Range structural block 80 km northwestward: Geology (Boulder), v. 11, p. 153-157.

Stockli, D., 2005, Application of low-temperature thermochronometry to extensional settings, *in* Reiners, P.W., and Ehlers, T.A., eds., Reviews in Mineralogy & Geochemistry, Volume 58, Mineralogical Society of America, p. 411-448.

Stockli, D.F., Dumitru, T.A., McWilliams, M.O., and Farley, K.A., 2003, Cenozoic tectonic evolution of the White Mountains, California and Nevada: Geological Society of America Bulletin, v. 115, p. 788-816.

Stockli, D.F., Farley, K.A., and Dumitru, T.A., 2000, Calibration of the apatite (U-Th)/ He thermochronometer on an exhumed fault block, White Mountains, California: Geology, v. 28, p. 983-986.

Stockli, D.F., Surpless, B.E., and Dumitru, T.A., 2002, Thermochronological constraints on the timing and magnitude of Miocene and Pliocene extension in the central Wassuk Range, western Nevada: Tectonics, v. 21, p. 10-1 – 10-19.

Topping, D.J., 1993, Paleogeographic reconstruction of the Death Valley extended region; evidence from Miocene large rock-avalanche deposits in the Amargosa Chaos Basin, California: Geological Society of America Bulletin, v. 105, p. 1090-1213.

Unruh, J., and Hauksson, E., 2009, Seismotectonics of an evolving intracontinental plate boundary, southeastern California, *in* Oldow, J.S., and Cashman, P.H., eds., Late Cenozoic Structure and Evolution of the Great Basin–Sierra Nevada Transition:

Geological Society of America Special Paper 447, p. 351–372, doi:10.1130/2009.2447(16)

Walker, J.D., Andrew, J.E., and Kirby, E., 2005, Strain transfer and partitioning between the Panamint Valley, Searles Valley, and Ash Hill fault zones, California: Geosphere, v. 1,, p. 111–118, doi: 10.1130/GES00014.1.

Walker, J.D., Berry, A.K., Davis, P.J., Andrew, J.E., and Mitsdarfer, J.M., 2002, Geologic map of northern Mojave Desert and southwestern Basin and Range, California; compilation method and references, *in* Glazner, A.F., Walker, J.D., and Bartley, J.M., eds., Geologic evolution of the Mojave Desert and southwestern Basin and Range., Geological Society of America (GSA). Boulder, CO, United States.

Walker, J.D., Martin, M.W., Stern, S.M., and Linn, J.K., 1994, Structural development of the southern Slate Range, east-central California: Geological Society of America, Cordilleran Section, 90th annual meeting., Volume 26, no. 2, p. 101.

Wernicke, B., Spencer, J.E., Burchfiel, B.C., and Guth, P.L., 1982, Magnitude of crustal extension in the southern Great Basin: Geology, v. 10, p. 499-502.

Wernicke, B.P., Axen, G.J., and Snow, J.K., 1988, Basin and Range extensional tectonics at the latitude of Las Vegas, Nevada: Geological Society of America Bulletin, v. 100, p. 1738-1757.

Wolf, R.A., Farley, K.A., and Silver, L.T., 1996, Helium diffusion and low temperature thermochronometry of apatite: Geochimica et Cosmochimica Acta, v. 60, p. 4231-4240.

Wolf, R.A., Farley, K.A., and Kass, D.M., 1998, Modeling of the temperature sensitivity of the apatite (U-Th)/He thermochronometer: Chemical Geology, v. 148, p. 105-114.

Figure captions

Figure 3.1. Color shaded relief map of study area and surrounding region. Warm colors correspond to the ranges and cool colors to the basins. Extensional and transtensional structures that are part of the eastern California shear zone are shown in black.

Figure 3.2. Simplified geologic map of the Slate Range with locations of major fault systems and zones. Black dots correspond to the locations of our thermochronology samples. Arrows with corresponding orientations show the locations of the northward projection of the Miocene nonconformity (2σ orientations) used in calculating extension magnitudes (see

text for discussion). Geology from this study, Smith et al. (1968), Walker et al. (1994), Walker et al. (2002), Andrew (2002), Dunne and Walker (2004), and Andrew and Walker (2009).

Figure 3.3. Cross sections across the (A) northern, (B) central, and (C) southern Slate Range based on work of Smith et al. (1968), Andrew and Walker (2009), and this study. Samples, shown as black dots, are projected in the plane of the cross-section. In the projected view, samples may lie above or below topography of the section line. Number above each sample corresponds to sample numbers referred to in Tables 3.2 and 3.3. Green dashed lines show the projected Miocene nonconformity (lower) and pre-extensional surface datum (upper). Dashed orange line is the approximate base of the Miocene and/or Pliocene partial retention zone(s) (hachured area). Mean (U-Th)/He ages are plotted as a function of horizontal distance above each cross section. Errors shown at 1σ standard deviation. PRZ-M – Miocene Partial Retention Zone; PRZ-P – Pliocene zone; SRD – Slate Range detachment; SVFZ – Searles Valley fault zone. Location of sections lines shown in Figure 2.

Figure 3.4. (A) Miocene volcanic rocks cropping out over Jurassic granite and metavolcanic rocks on the eastern flank of the Slate Range north of Layton Pass. The tilted nonconformity here appears to be a rotated gentle erosional surface with beds steepening in the dark volcanic rocks at the top. Field of view about 800 meters. Panamint Range in background. Panoramic view is toward the northeast. (B) Slate Range detachment west-southwest of Layton Pass. Miocene strata dipping about 45° at top of hill, an ~2m thick ground zone beneath (tan layer), and brecciated Jurassic metaplutonic rocks at base. White box is next to ~2m tall person for scale. (C) Slate Range detachment fault and

splay faults in the hanging wall of the Searles Valley normal fault, just north of Copper Queen Canyon.

Figure 3.5. Equal area projection showing the distribution of oriented planes within the Miocene sedimentary and volcanic sequence (Table 3.1). The axial mean (349° +/-16°, 24° +/-6° - bold line) of these planes should approximate the middle Miocene nonconformity or pre-extensional paleosurface used in paleodepth reconstructions within a 2σ confidence interval (gray area). Data given in Table 3.1.

Figure 3.6. Reconstructed sample positions for the (A) northern, (B) central, and (C) southern thermochronology transects. Abbreviations and line coloring as in Figure 3. Sample numbers refer to Tables 3.2 and 3.3.

Figure 3.7. Apatite (U-Th)/He ages versus middle Miocene paleodepth for the northern transect (A-A'). Error bars are 1σ standard deviations. Labeled sample numbers refer to Tables 3.2 and 3.3. Hachured area shows uncertainty in position of the 40°C and 80°C isotherms.

Figure 3.8. (U-Th)/He ages versus middle Miocene paleodepth for the central (B-B') and southern (C-C') transects. Error bars are 1σ standard deviations. Labeled sample numbers refer to Tables 3.2 and 3.3. Hachured area shows uncertainty in position of the 40°C and 80°C isotherms. PRZ – Partial Retention Zone.

Figure 3.9. Preferred middle Miocene paleodepth reconstruction for the central (B-B') and southern (C-C') transects. Error bars are 1σ standard deviations. Labeled sample numbers refer to Tables 3.2 and 3.3. Hachured area shows uncertainty in position of the 40°C and 80°C isotherms. PRZ – Partial Retention Zone.

Table 3.1. Structural data used to estimate the present day orientation of middle Miocene pre-extensional paleosurface.

Strike	Dip	Measurement Surface
335	14	TPS – nonconformity
350	16	TPS – nonconformity
325	16	TPS – nonconformity
350	18	TPS – nonconformity
008	25	TPS – nonconformity
010	43	bedding – ash deposit ~50 m thick
335	40	bedding – limestone ~50m thick
325	35	bedding – limestone ~50m thick
347	23	bedding – calcareous sandstone ~5m thick
345	25	bedding – limestone
018	25	bedding – calcareous sandstone

Note: TPS – Three point solution

Table 3.2. Summary of (U-Th)/He apatite data for the Slate Range

Sample	Longitude (W)	Latitude (N)	Elevation (m)	Mass (μg)	Ft*	U (ppm)	Th (ppm)	Sm (ppm)	Th/U	He (ncc/mg)	Mean age (Ma)	St.Dev.† (Ma)	Replicates
Northern Transect (section A-A')													
BD04CSR-8	117.2649	35.8494	840	0.57	0.56	46.9	68.8	-	1.49	223.0	51.8	0.6	3
BD04CSR-1	117.2627	35.8487	900	1.02	0.61	15.1	32.8	-	2.10	74.5	43.1	6.3	5
BD04CSR-2	117.2574	35.8468	1010	1.60	0.69	97.7	106.7	-	1.13	304.9	28.8	3.4	4
BD04CSR-3	117.2528	35.8496	1090	1.22	0.66	11.3	19.1	-	1.72	9.1	7.3	0.7	5
BD04CSR-4	117.2485	35.8498	1190	1.55	0.64	11.6	22.3	-	2.43	6.6	4.6	0.9	6
BD04CSR-5	117.2450	35.8488	1290	1.80	0.64	6.1	16.9	-	2.79	3.3	4.2	0.4	3
BD04CSR-6	117.2430	35.8474	1400	1.23	0.62	11.2	33.0	-	3.04	5.4	4.2	1.9	3
BD04CSR-7	117.2403	35.8454	1500	0.85	0.64	45.4	31.2	-	0.66	39.2	9.5	2.3	4
BD04CSR-54	117.2369	35.8433	1460	1.88	0.66	34.2	39.3	-	1.10	37.0	10.6	1.4	4
BD04CSR-51	117.2289	35.8403	1390	1.28	0.59	61.5	100.7	-	1.63	125.2	20.6	1.0	4
BD04CSR-52	117.2268	35.8396	1310	3.09	0.67	7.5	21.0	-	2.84	10.8	10.8	1.4	7
BD04CSR-4849	117.2124	35.8405	950	3.20	0.67	19.3	44.1	-	2.31	50.9	21.0	0.9	3
BD04CSR-50	117.2092	35.8402	810	5.70	0.75	8.6	16.9	-	1.93	16.7	14.9	0.7	4
BD04CSR-25	117.2062	35.8393	700	3.88	0.68	20.8	33.4	-	1.61	44.6	20.0	3.6	4
BD04CSR-26	117.2019	35.8400	600	2.27	0.64	92.1	67.7	-	0.74	326.0	39.0	3.5	3
Central Transect (section B-B')													
BDCSR27	117.1536	35.7456	800	0.68	0.59	6.0	34.0	-	10.93	40.6	44.4	7.5	4
BDCSR28	117.1568	35.7442	920	1.30	0.68	1.6	15.8	-	9.69	20.0	45.0	-	1
BDCSR29	117.1608	35.7440	1000	2.28	0.67	7.0	35.4	-	5.39	56.2	45.4	5.4	5
BDCSR30	117.1638	35.7436	1100	4.88	0.73	5.1	16.1	-	3.25	37.6	50.1	4.2	5
BDCSR-31	117.2270	35.7581	800	1.20	0.66	20.0	95.3	-	4.66	31.1	8.8	1.2	3
BDCSR-32	117.2196	35.7571	900	0.50	0.54	20.2	48.8	-	3.07	13.6	6.8	1.4	2
BDCSR33	117.2161	35.7558	1010	0.83	0.61	25.9	62.6	-	2.50	18.0	6.0	0.9	3
BDCSR-35	117.2094	35.7495	1200	1.57	0.61	23.2	57.2	-	2.54	33.4	12.4	4.0	3
BDCSR36	117.2010	35.7488	1303	0.90	0.63	26.0	61.7	-	2.37	42.3	13.6	-	1
BDCSR-37	117.2332	35.7561	710	3.47	0.69	20.8	79.1	-	3.81	76.2	23.7	6.0	3
BDCSR38	117.1767	35.7439	1400	0.65	0.58	26.8	83.9	-	3.14	135.2	42.1	7.4	2
BDCSR39	117.1866	35.7472	1440	1.10	0.60	28.2	111.6	-	3.92	140.0	34.5	6.5	6
BDCSR40	117.1936	35.7459	1320	0.60	0.56	36.6	125.6	-	3.27	138.0	27.8	6.0	6

(continued)

Table 3.2. Summary of (U-Th)/He apatite data for the Slate Range (continued)

Southern Transect (section C-C')

Sample	Longitude (W)	Latitude (N)	Elevation (m)	Mass (μg)	Ft*	U (ppm)	Th (ppm)	Sm (ppm)	Th/U	He (ncc/mg)	Mean age (Ma)	St.Dev.† (Ma)	Replicates
12LC07	117.1985	35.6792	800	1.13	0.60	49.7	49.8	26.7	1.00	1.1	5.6	0.4	2
12LC08	117.1951	35.6804	850	1.41	0.61	27.7	35.0	28.7	1.27	0.6	5.2	0.5	4
12LC09	117.1913	35.6801	850	1.83	0.64	31.3	60.3	66.9	1.92	1.1	6.8	-	2
12LC11	117.1848	35.6797	900	1.64	0.63	57.7	41.9	59.1	0.67	1.5	6.2	0.7	3
12LC13	117.1745	35.6818	980	1.61	0.61	16.7	32.4	12.0	1.94	1.1	13.7	-	1
12LC14	117.1673	35.6802	1020	0.74	0.53	6.9	45.2	65.3	6.41	0.7	12.7	0.8	2
12LC16	117.1472	35.6843	1000	1.96	0.65	30.0	46.2	24.6	1.50	3.9	26.0	3.2	3

Note: Individual analyses are given in supplementary data tables SD3.1 and SD3.2; dash—not measured.

*Ft is the alpha ejection correction of Farley et al. (1996).

†St. Dev.—standard deviation.

Table 3.3. Summary of (U-Th)/He zircon data for the Slate Range

Southern Transect (section C-C')

Sample	Longitude (W)	Latitude (N)	Elevation (m)	Mass (μg)	Ft*	U (ppm)	Th (ppm)	Sm (ppm)	Th/U	He (nmol/g)	Mean age (Ma)	St.Dev.† (Ma)	Replicates
12LC01	117.2191	35.6778	675	6.12	0.77	659.4	253.5	5.7	0.39	151.8	50.1	5.8	3
12LC02	117.2159	35.6784	700	2.88	0.72	663.6	257.2	5.0	0.38	147.2	52.1	5.1	3
12LC03	117.2129	35.6787	700	4.79	0.75	771.4	225.8	1.0	0.30	149.2	44.6	8.4	3
12LC04	117.2092	35.6798	750	5.90	0.76	644.5	355.5	0.7	0.56	135.4	45.3	2.6	3
12LC07	117.1985	35.6792	800	6.00	0.76	1171.5	312.8	0.8	0.26	257.4	50.7	7.0	3
12LC09	117.1913	35.6801	850	14.93	0.83	433.1	146.5	0.6	0.34	113.8	54.3	0.0	2
12LC10	117.1880	35.6803	900	5.86	0.77	45.8	35.7	0.5	0.76	11.7	51.3	3.6	3
12LC11	117.1848	35.6797	900	4.72	0.75	367.8	125.3	0.6	0.34	81.6	51.0	2.0	3
12LC12	117.1812	35.6792	950	7.17	0.78	190.8	221.3	1.0	1.19	46.4	46.1	3.5	3
12LC15	117.1551	35.6823	1070	5.63	0.76	381.4	114.4	0.7	0.31	92.4	55.2	3.1	3
12LC16	117.1472	35.6843	1000	4.35	0.75	195.9	135.6	0.7	0.69	52.5	56.6	2.9	3

Note: Individual analyses are given in supplementary data tables SD1 and SD2; dash—not measured.

*Ft is the alpha ejection correction of Farley et al. (1996).

†St. Dev.—standard deviation.

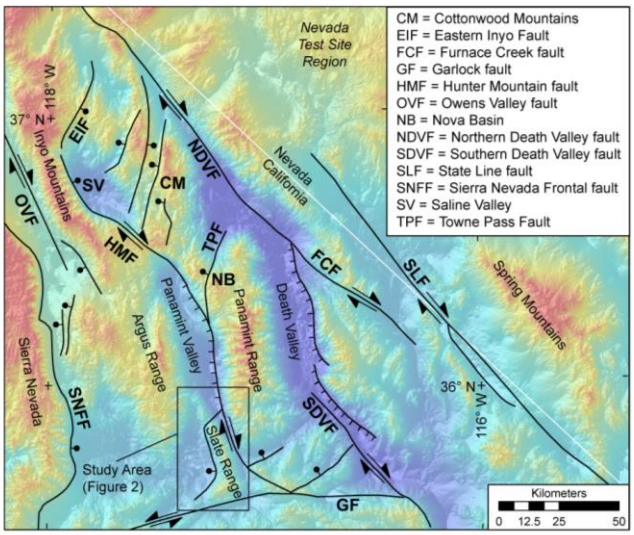
CM = Cottonwood Mountains
EIF = Eastern Inyo Fault
FCF = Furnace Creek fault
GF = Garlock fault
HMF = Hunter Mountain fault
OVF = Owens Valley fault
NB = Nova Basin
NDVF = Northern Death Valley fault
SDVF = Southern Death Valley fault
SLF = State Line fault
SNFF = Sierra Nevada Frontal fault
SV = Saline Valley
TPF = Towne Pass Fault
Nevada Test Site Region
Nevada
California
37° N
118° W
Inyo Mountains
EIF
SV
CM
NDVF
OVF
HMF
TPF
NB
FCF
SLF
Spring Mountains
Panamint Valley
Argus Range
Panamint Range
Death Valley
Sierra Nevada
SNFF
SDVF
36° N
116° W
Slate Range
Study Area
(Figure 2)
GF
Kilometers
0 12.5 25 50

Figure 3.1

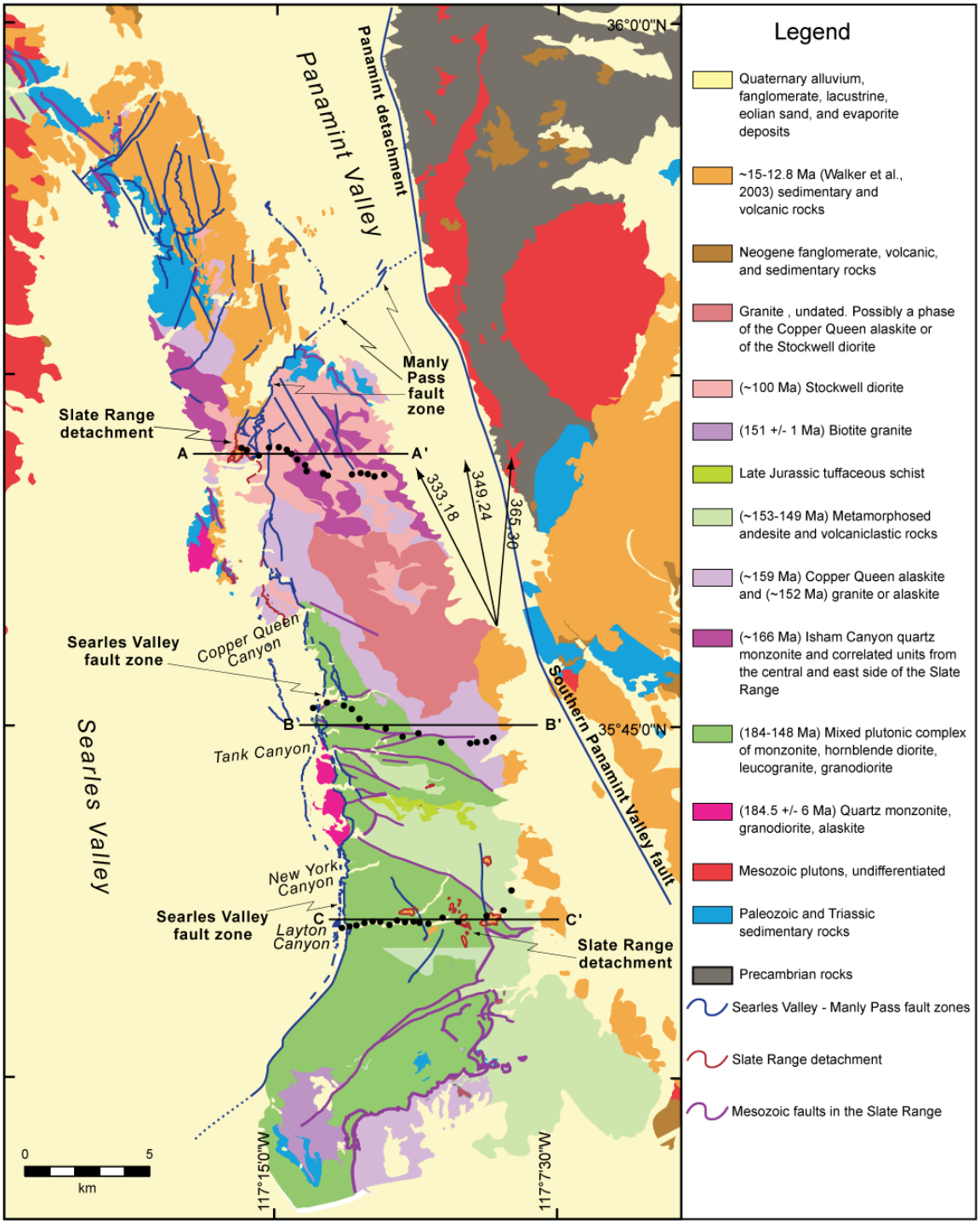
Panamint Valley
Panamint detachment
36°0'0"N
Manly Pass fault zone
Slate Range detachment
A
A'
333.18
349.24
365.30
Searles Valley fault zone
Copper Queen Canyon
B
B'
35°45'0"N
Tank Canyon
Searles Valley
Southern Panamint Valley fault
New York Canyon
Searles Valley fault zone
C
C'
Layton Canyon
Slate Range detachment
0
5
km
117°15'0"W
117°7'30"W
Legend
Quaternary alluvium, fanglomerate, lacustrine, eolian sand, and evaporite deposits
~15-12.8 Ma (Walker et al., 2003) sedimentary and volcanic rocks
Neogene fanglomerate, volcanic, and sedimentary rocks
Granite , undated. Possibly a phase of the Copper Queen alaskite or of the Stockwell diorite
(~100 Ma) Stockwell diorite
(151 +/- 1 Ma) Biotite granite
Late Jurassic tuffaceous schist
(~153-149 Ma) Metamorphosed andesite and volcaniclastic rocks
(~159 Ma) Copper Queen alaskite and (~152 Ma) granite or alaskite
(~166 Ma) Isham Canyon quartz monzonite and correlated units from the central and east side of the Slate Range
(184-148 Ma) Mixed plutonic complex of monzonite, hornblende diorite, leucogranite, granodiorite
(184.5 +/- 6 Ma) Quartz monzonite, granodiorite, alaskite
Mesozoic plutons, undifferentiated
Paleozoic and Triassic sedimentary rocks
Precambrian rocks
Searles Valley - Manly Pass fault zones
Slate Range detachment
Mesozoic faults in the Slate Range

Figure 3.2

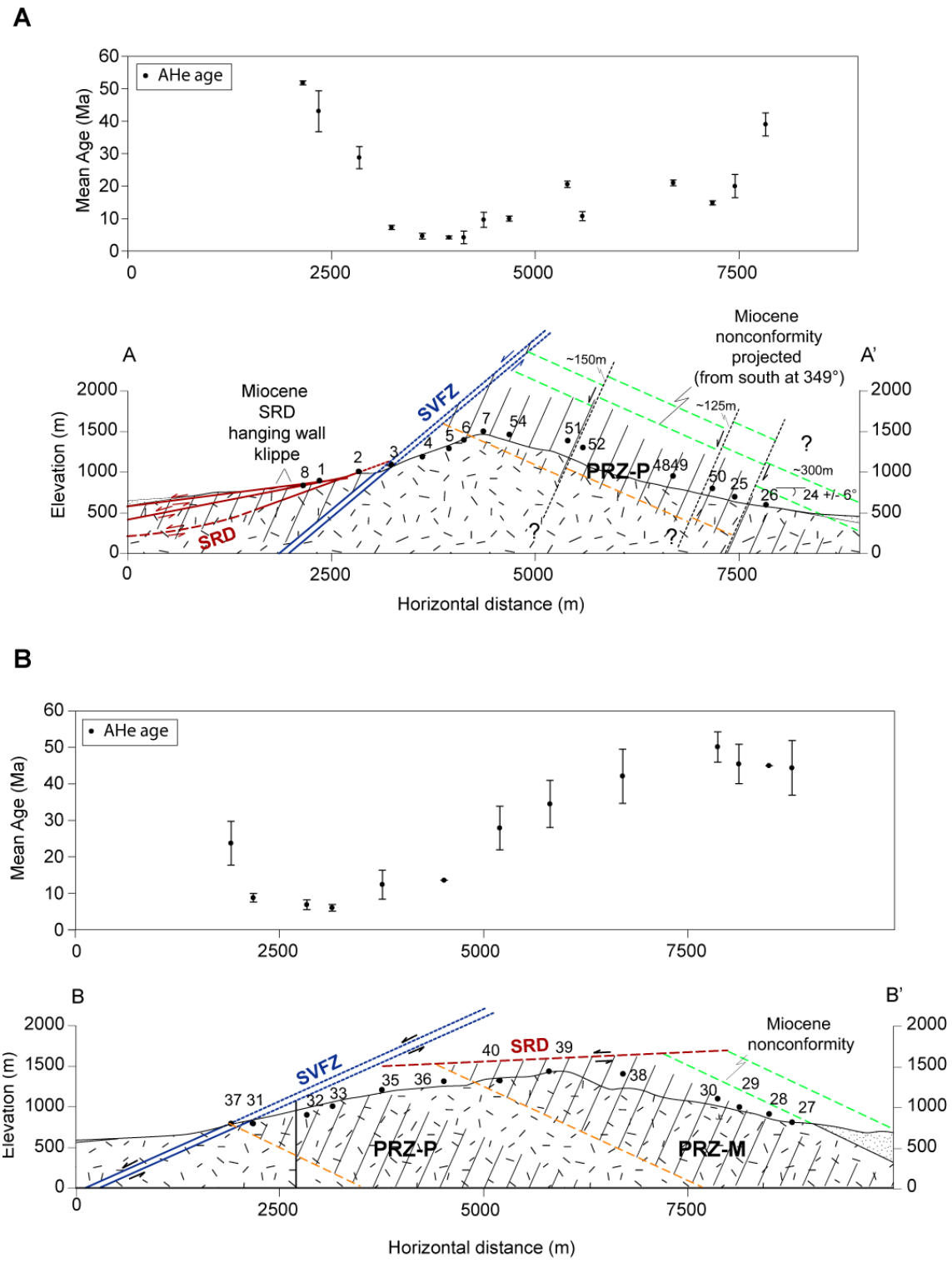
A
AHe age
Mean Age (Ma)
A
A'
Miocene
SRD
hanging wall
klippe
SVFZ
Miocene
nonconformity
projected
(from south at 349°)
~150m
~125m
~300m
24 +/- 6°
PRZ-P
SRD
Elevation (m)
Horizontal distance (m)
B
AHe age
Mean Age (Ma)
B
B'
SVFZ
SRD
Miocene
nonconformity
PRZ-P
PRZ-M
Elevation (m)
Horizontal distance (m)

Figure 3.3

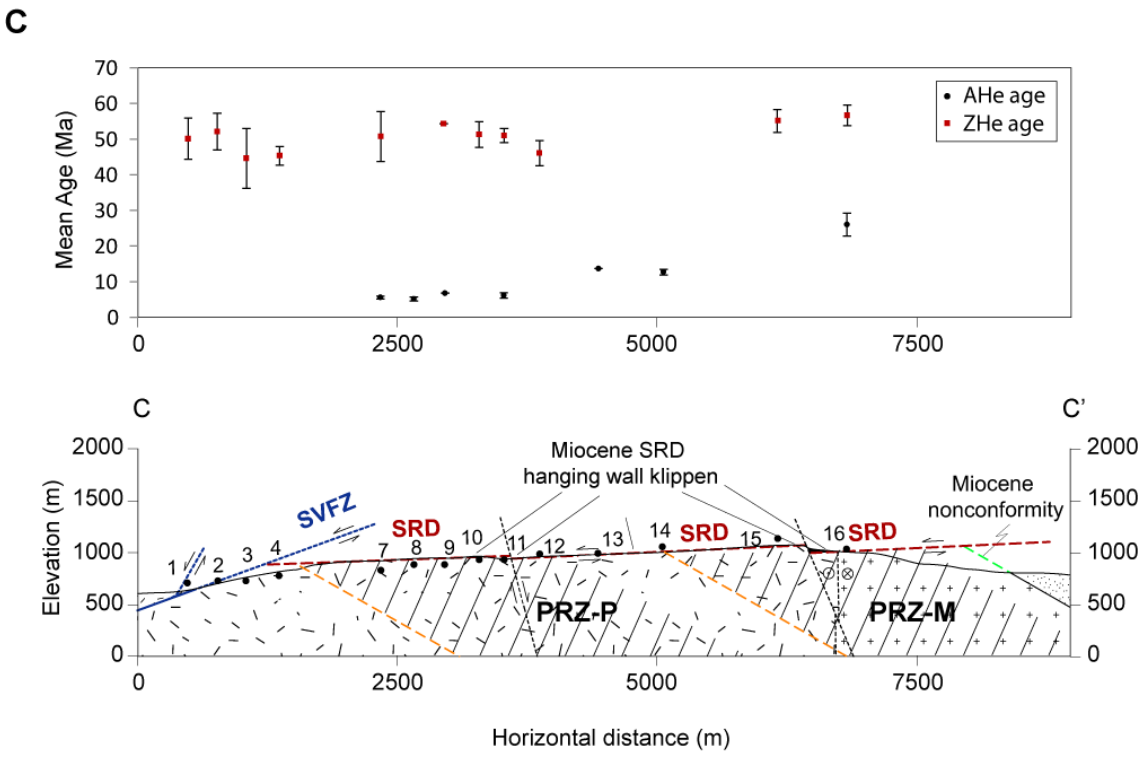

Figure 3.3 (continued)

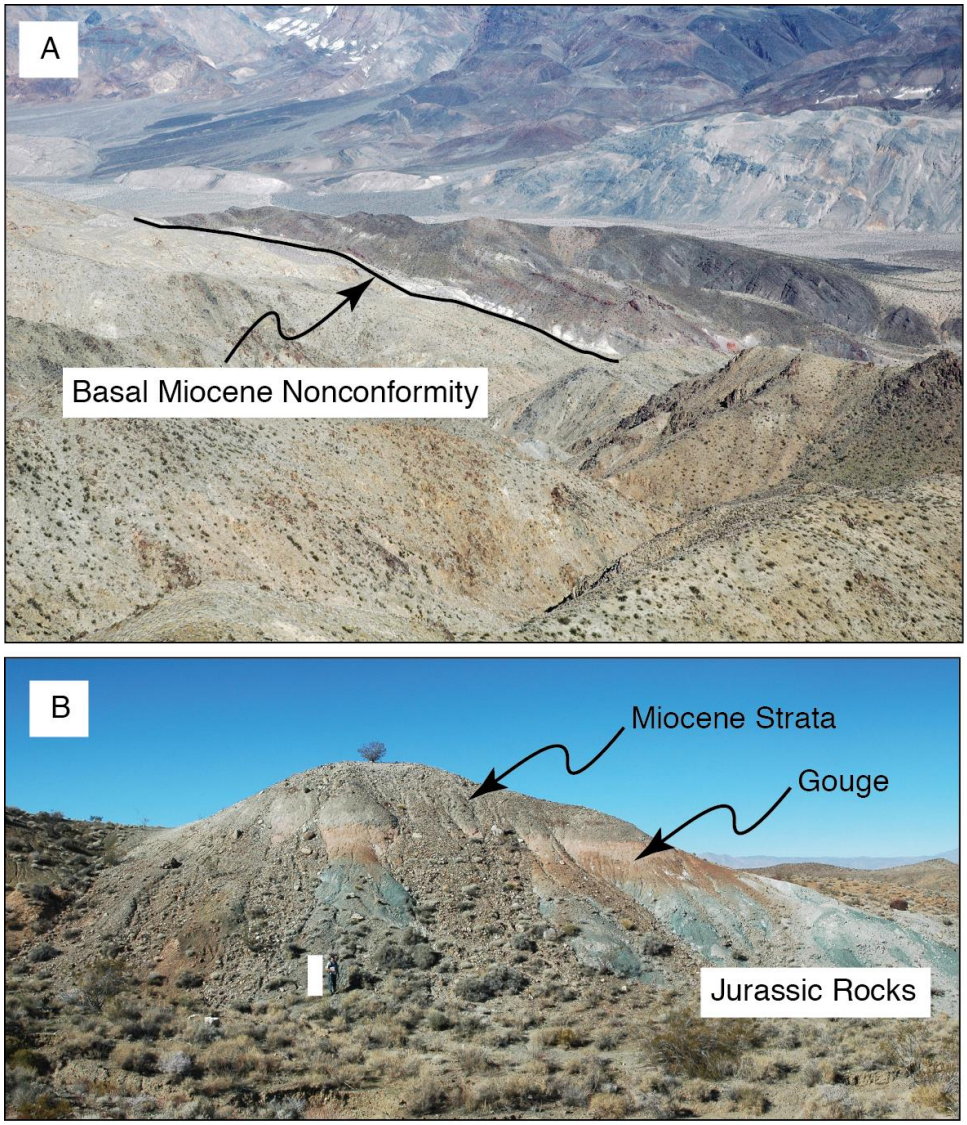
A
Basal Miocene Nonconformity
B
Miocene Strata
Gouge
Jurassic Rocks

Figure 3.4

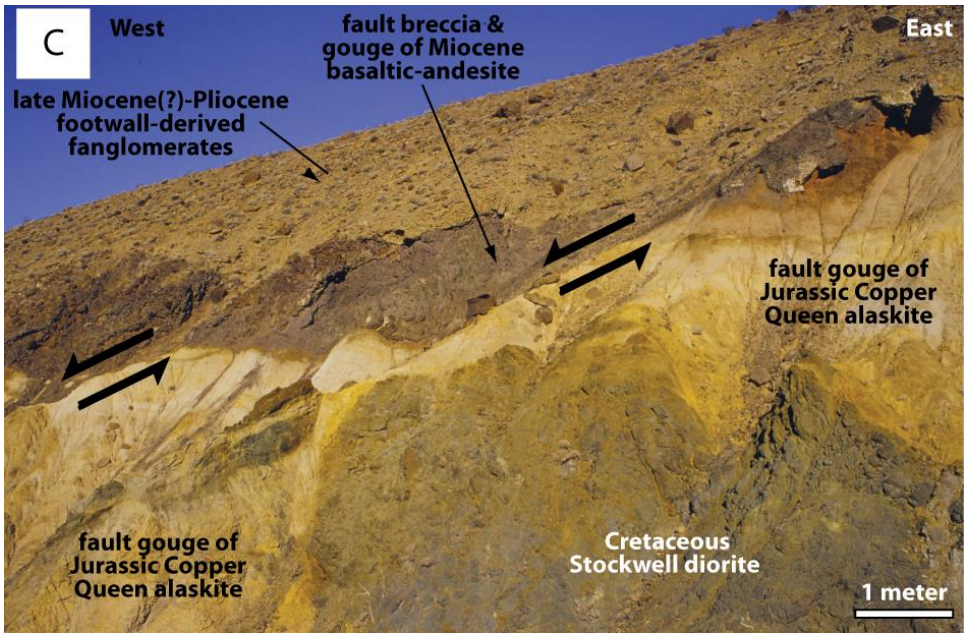

Figure 3.4 (continued)

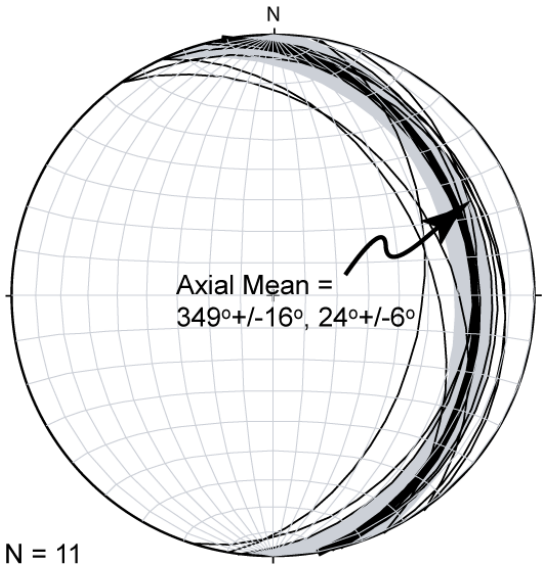

Figure 3.5

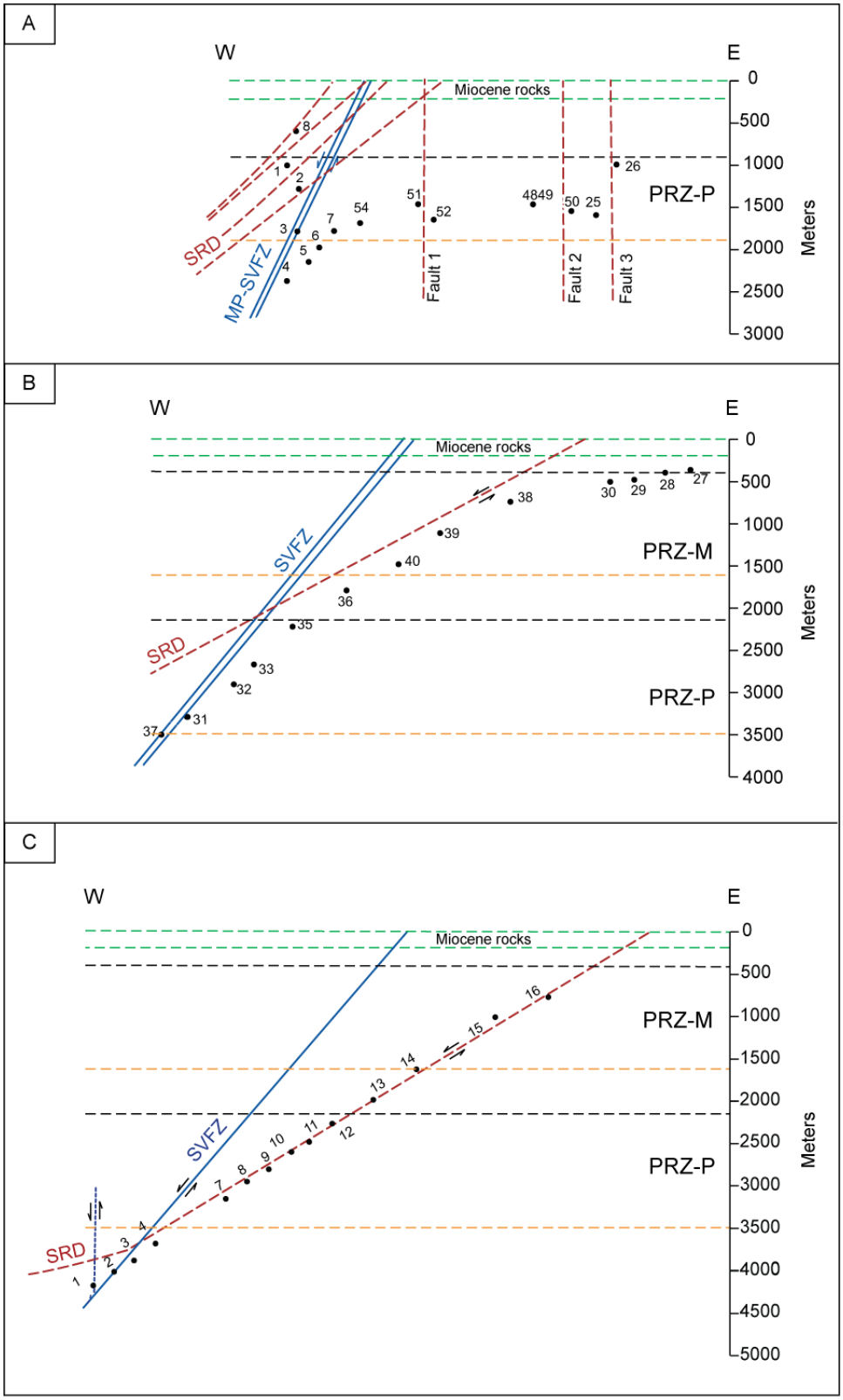
A
W
E
Miocene rocks
PRZ-P
SRD
MP-SVFZ
Fault 1
Fault 2
Fault 3
Meters
0
500
1000
1500
2000
2500
3000
B
W
E
Miocene rocks
SVFZ
SRD
PRZ-M
PRZ-P
Meters
0
500
1000
1500
2000
2500
3000
3500
4000
C
W
E
Miocene rocks
SVFZ
SRD
PRZ-M
PRZ-P
Meters
0
500
1000
1500
2000
2500
3000
3500
4000
4500
5000

Figure 3.6

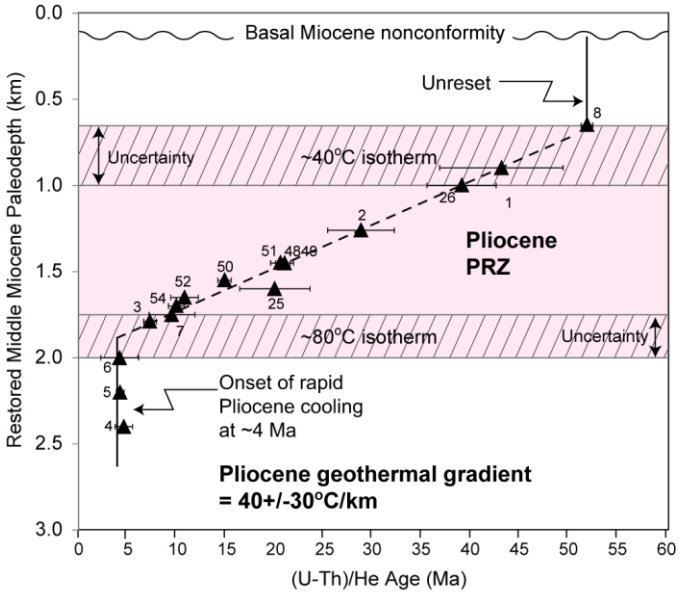
Basal Miocene nonconformity
Unreset
Uncertainty
~40°C isotherm
Pliocene
PRZ
~80°C isotherm
Uncertainty
Onset of rapid
Pliocene cooling
at ~4 Ma
Pliocene geothermal gradient
= 40+/-30°C/km
Restored Middle Miocene Paleodepth (km)
(U-Th)/He Age (Ma)
0.0
0.5
1.0
1.5
2.0
2.5
3.0
0
5
10
15
20
25
30
35
40
45
50
55
60

Figure 3.7

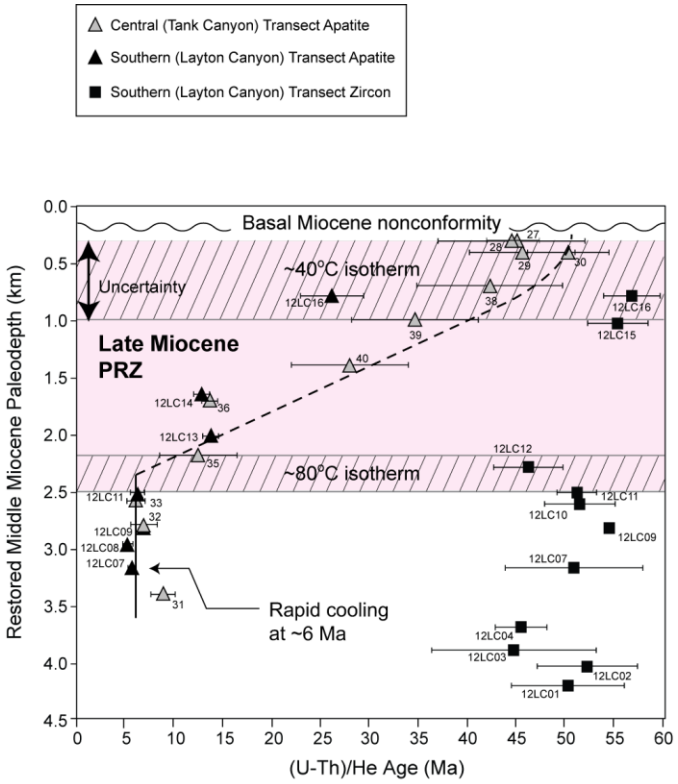
Central (Tank Canyon) Transect Apatite
Southern (Layton Canyon) Transect Apatite
Southern (Layton Canyon) Transect Zircon
Basal Miocene nonconformity
Uncertainty
~40°C isotherm
Late Miocene
PRZ
~80°C isotherm
Rapid cooling
at ~6 Ma
Restored Middle Miocene Paleodepth (km)
(U-Th)/He Age (Ma)
0.0
0.5
1.0
1.5
2.0
2.5
3.0
3.5
4.0
4.5
0
5
10
15
20
25
30
35
40
45
50
55
60
27
28
29
30
12LC16
38
39
12LC15
40
12LC14
36
12LC13
35
12LC12
33
32
12LC11
12LC10
12LC09
12LC08
12LC07
31
12LC04
12LC03
12LC02
12LC01

Figure 3.8

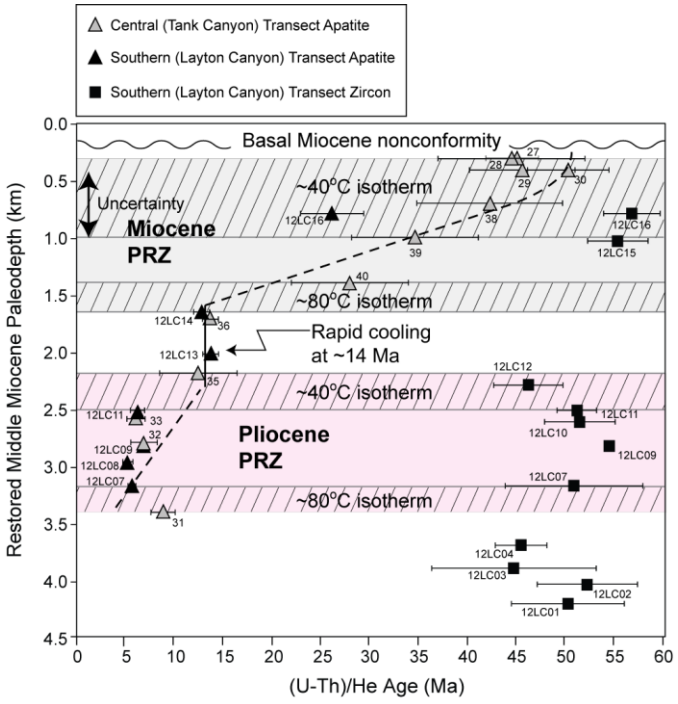
Central (Tank Canyon) Transect Apatite
Southern (Layton Canyon) Transect Apatite
Southern (Layton Canyon) Transect Zircon
Basal Miocene nonconformity
~40°C isotherm
Uncertainty
Miocene
PRZ
~80°C isotherm
Rapid cooling
at ~14 Ma
~40°C isotherm
Pliocene
PRZ
~80°C isotherm
Restored Middle Miocene Paleodepth (km)
(U-Th)/He Age (Ma)
0.0
0.5
1.0
1.5
2.0
2.5
3.0
3.5
4.0
4.5
0
5
10
15
20
25
30
35
40
45
50
55
60
12LC16
12LC15
12LC14
12LC13
12LC12
12LC11
12LC10
12LC09
12LC08
12LC07
12LC04
12LC03
12LC02
12LC01
27
28
29
30
38
39
40
36
35
33
32
31

Figure 3.9

Table SD3.1. Apatite (U-Th)/He data for the Slate Range

Sample	L (mm)	W (mm)	Mass (μg)	Ft*	U (ppm)	Th (ppm)	Sm (ppm)	Th/U	He (ncc/mg)	Corrected Age (Ma)	Mean age (Ma)	St.Dev.† (Ma)
BD04CSR-8			**0.6**	**0.56**	**46.9**	**68.8**	-	**1.49**	**223.0**		**51.8**	**0.6**
BD04CSR-8-1	104.60	46.40	0.5	0.52	36.9	51.9	-	1.41	159.0	51.1		
BD04CSR-8-2	89.50	60.20	0.7	0.60	32.5	53.8	-	1.66	172.3	52.1		
BD04CSR-8-3	97.10	52.80	0.5	0.56	71.2	100.7	-	1.41	337.8	52.1		
BD04CSR-1			**1.0**	**0.61**	**15.1**	**32.8**	-	**2.10**	**74.5**		**43.1**	**6.3**
BD04CSR-1-1	141.00	62.10	1.0	0.62	20.8	50.2	-	2.42	125.8	50.9		
BD04CSR-1-2	123.00	59.70	0.9	0.61	15.6	30.5	-	1.95	82.8	48.6		
BD04CSR-1-3	176.30	60.90	1.3	0.63	12.3	28.1	-	2.28	58.5	40.1		
BD04CSR-1-5	154.50	72.00	1.4	0.67	10.1	15.3	-	1.52	43.6	39.2		
BD04CSR-1-6	116.70	47.60	0.5	0.53	16.9	39.7	-	2.36	61.8	36.5		
BD04CSR-2			**1.6**	**0.69**	**97.7**	**106.7**	-	**1.13**	**304.9**		**28.8**	**3.4**
BD04CSR-2-1	141.50	77.20	1.6	0.69	109.3	115.0	-	1.05	362.9	31.8		
BD04CSR-2-2	164.80	74.30	1.8	0.69	106.4	114.7	-	1.08	317.6	28.4		
BD04CSR-2-3	103.30	68.80	1.0	0.65	56.0	78.4	-	1.40	141.4	24.1		
BD04CSR-2-4§	*102.30*	*61.10*	*0.8*	*0.61*	*40.3*	*78.4*	-	*1.94*	*177.4*	*40.6*		
BD04CSR-2-5	127.80	89.00	2.0	0.72	119.2	118.9	-	1.00	397.6	30.8		
BD04CSR-3			**1.2**	**0.66**	**11.3**	**19.1**	-	**1.72**	**9.1**		**7.3**	**0.7**
BD04CSR-3-1	113.70	74.50	1.3	0.67	9.1	17.0	-	1.87	8.5	7.9		
BD04CSR-3-2	101.00	84.60	1.5	0.70	13.2	21.0	-	1.58	11.5	7.4		
BD04CSR-3-3	124.10	81.70	1.7	0.70	9.4	16.0	-	1.71	7.2	6.4		
BD04CSR-3-4	96.90	67.00	0.9	0.63	8.0	14.6	-	1.82	6.9	7.9		
BD04CSR-3-5	101.70	74.40	0.7	0.60	16.9	26.8	-	1.59	11.6	6.8		
BD04CSR-4			**1.6**	**0.64**	**11.6**	**22.3**	-	**2.43**	**6.6**		**4.6**	**0.9**
BD04CSR-4-1	120.00	61.90	1.0	0.64	11.3	29.3	-	2.60	5.1	4.0		
BD04CSR-4-2	113.50	61.40	0.9	0.62	8.0	21.4	-	2.67	5.6	5.7		
BD04CSR-4-3	112.10	65.80	0.9	0.62	0.8	3.3	-	4.37	2.0	3.5		
BD04CSR-4-4	94.60	68.20	2.5	0.62	21.5	35.5	-	1.65	12.6	5.6		
BD04CSR-4-5§	*128.60*	*64.00*	*1.9*	*0.63*	*18.9*	*26.7*	-	*1.41*	*36.7*	*19.1*		
	102.60	*61.90*										
BD04CSR-4-6	138.40	87.20	2.1	0.72	15.7	21.6	-	1.38	8.7	4.8		
BD04CSR-4-7	105.00	70.00	1.9	0.64	12.0	22.8	-	1.90	5.6	4.2		
	101.30	65.20										

Sample	L (mm)	W (mm)	Mass (µg)	Ft*	U (ppm)	Th (ppm)	Sm (ppm)	Th/U	He (ncc/mg)	Corrected Age (Ma)	Mean age (Ma)	St.Dev.† (Ma)
BD04CSR-5			**1.8**	**0.64**	**6.1**	**16.9**	-	**2.79**	**3.3**		**4.2**	**0.4**
BD04CSR-5-1§	*120.80*	*54.20*	*0.9*	*0.64*	*4.8*	*15.3*	-	*3.19*	*14.8*	*22.7*		
BD04CSR-5-2§	*133.80*	*81.80*	*0.7*	*0.62*	*16.1*	*39.0*	-	*2.43*	*18.0*	*9.5*		
BD04CSR-5-3§	*88.00*	*64.80*	*1.7*	*0.68*	*2.9*	*8.0*	-	*2.77*	*24.6*	*62.0*		
BD04CSR-5-4§	*114.50*	*70.00*	*1.1*	*0.66*	*6.9*	*18.6*	-	*2.71*	*26.8*	*29.7*		
BD04CSR-5-5	115.20	60.80	1.9	0.63	6.1	16.4	-	2.70	3.6	4.7		
BD04CSR-5-6	97.70	72.80	1.9	0.65	5.5	16.4	-	2.96	3.0	4.1		
BD04CSR-5-7	93.20	80.00	1.6	0.64	6.6	17.8	-	2.71	3.3	4.0		
BD04CSR-6			**1.2**	**0.62**	**11.2**	**33.0**	-	**3.04**	**5.4**		**4.2**	**1.9**
BD04CSR-6-1	92.10	68.30	0.7	0.58	16.8	44.3	-	2.64	4.1	2.2		
BD04CSR-6-2	78.80	65.60	1.8	0.70	7.8	25.1	-	3.22	5.2	4.4		
BD04CSR-6-3	*149.30*	*74.60*	*0.7*	*0.62*	*20.3*	*68.6*	-	*3.38*	*3.7*	*1.4*		
BD04CSR-6-4	*168.40*	*87.20*	*2.6*	*0.73*	*13.4*	*40.2*	-	*3.00*	*27.1*	*13.4*		
BD04CSR-6-5	103.50	54.50	1.2	0.58	9.1	29.6	-	3.25	6.8	6.0		
BD04CSR-6-6	*87.90*	*72.30*	*1.6*	*0.61*	*10.4*	*34.9*	-	*3.36*	*15.1*	*10.9*		
BD04CSR-7			**0.8**	**0.64**	**45.4**	**31.2**	-	**0.66**	**39.2**		**9.5**	**2.3**
BD04CSR-7-1	78.60	61.00	0.6	0.59	36.0	12.8	-	0.36	21.3	7.6		
BD04CSR-7-2	89.20	52.30	0.5	0.55	58.5	47.1	-	0.81	34.6	7.4		
BD04CSR-7-3	116.40	86.00	1.7	0.70	44.4	36.3	-	0.82	53.8	11.9		
BD04CSR-7-4	116.50	53.60	0.6	0.70	42.9	28.5	-	0.66	46.9	11.1		
BD04CSR-54			**1.9**	**0.66**	**34.2**	**39.3**	-	**1.10**	**37.0**		**10.6**	**1.4**
BD04CSR-54-1	173.30	115.50	4.7	0.78	26.8	15.1	-	0.56	31.0	10.7		
BD04CSR-54-2§	*129.60*	*67.80*	*1.2*	*0.65*	*21.3*	*24.0*	-	*1.13*	*70.5*	*32.8*		
BD04CSR-54-3	142.50	55.20	0.9	0.59	53.7	72.1	-	1.34	63.1	12.4		
BD04CSR-54-4	81.60	70.80	0.8	0.64	29.6	33.5	-	1.13	26.6	9.1		
BD04CSR-54-5	137.40	63.20	1.1	0.63	26.6	36.5	-	1.38	27.4	10.1		
BD04CSR-51			**1.3**	**0.59**	**61.5**	**100.7**	-	**1.63**	**125.2**		**20.6**	**1.0**
BD04CSR-51-1	*171.70*	*66.30*	*3.0*	*0.66*	*59.0*	*99.7*	-	*1.69*	*188.2*	*28.4*		
BD04CSR-51-2	*124.70*	*71.10*	*2.5*	*0.66*	*60.9*	*92.5*	-	*1.52*	*200.5*	*30.0*		
BD04CSR-51-3	115.90	59.10	1.5	0.60	71.6	120.9	-	1.69	142.4	19.5		
BD04CSR-51-4	*119.30*	*82.30*	*2.5*	*0.67*	*67.7*	*82.1*	-	*1.21*	*203.7*	*28.8*		
BD04CSR-51-5	83.60	56.10	1.2	0.59	48.4	76.0	-	1.57	95.8	20.0		
BD04CSR-51-7	90.00	57.40	1.0	0.57	70.2	113.0	-	1.61	141.3	21.1		
BD04CSR-51-8	97.30	56.30	1.4	0.59	55.7	93.0	-	1.67	121.4	21.6		

Sample	L (mm)	W (mm)	Mass (µg)	Ft*	U (ppm)	Th (ppm)	Sm (ppm)	Th/U	He (ncc/mg)	Corrected Age (Ma)	Mean age (Ma)	St.Dev.† (Ma)
BD04CSR-52			**3.1**	**0.67**	**7.5**	**21.0**	-	**2.84**	**10.8**		**10.8**	**1.4**
BD04CSR-52-1	154.70	66.10	1.4	0.65	8.0	20.7	-	2.61	10.3	10.1		
BD04CSR-52-2	172.40	68.70	3.9	0.68	7.0	20.3	-	2.89	9.0	9.2		
BD04CSR-52-3	83.90	64.50	1.3	0.60	9.5	27.0	-	2.83	11.6	10.1		
BD04CSR-52-4	*150.90*	*65.10*	*3.2*	*0.68*	*19.7*	*10.7*	-	*0.54*	*12.0*	*6.6*		
BD04CSR-52-5	176.50	97.80	6.7	0.76	8.2	21.3	-	2.59	14.1	11.6		
BD04CSR-52-6	136.40	75.80	3.4	0.70	5.4	17.9	-	3.33	10.9	13.4		
BD04CSR-52-7	94.20	64.60	1.3	0.59	8.8	21.9	-	2.49	11.2	11.2		
BD04CSR-52-8	118.50	88.20	3.6	0.71	5.8	18.2	-	3.15	8.7	10.1		
BD04CSR-4849			**3.2**	**0.67**	**19.3**	**44.1**	-	**2.31**	**50.9**		**21.0**	**0.9**
BD04CSR-4849-1	143.80	59.10	2.6	0.67	18.0	51.2	-	2.83	52.4	21.5		
BD04CSR-4849-2	174.40	66.20	3.1	0.66	24.2	48.2	-	1.99	61.9	21.5		
BD04CSR-4849-3	*246.10*	*115.10*	*6.6*	*0.79*	*6.9*	*4.4*	-	*0.64*	*118.2*	*151.6*		
BD04CSR-4849-4	112.60	81.00	3.9	0.68	15.7	32.8	-	2.10	38.5	19.9		
BD04CSR-4849-5	*93.90*	*63.90*	*1.4*	*0.61*	*8.4*	*12.3*	-	*1.47*	*23.9*	*28.7*		
BD04CSR-4849-6	*126.60*	*53.30*	*1.4*	*0.59*	*11.3*	*23.2*	-	*2.05*	*37.9*	*31.8*		
BD04CSR-4849-7	*82.80*	*48.00*	*1.1*	*0.57*	*13.6*	*25.2*	-	*1.85*	*18.8*	*13.9*		
BD04CSR-50			**5.7**	**0.75**	**8.6**	**16.9**	-	**1.93**	**16.7**		**14.9**	**0.7**
BD04CSR-50-1	179.80	131.00	6.2	0.81	3.4	5.8	-	1.70	7.4	15.8		
BD04CSR-50-2	*163.60*	*98.20*	*3.2*	*0.75*	*21.9*	*98.6*	-	*4.50*	*9.7*	*2.4*		
BD04CSR-50-3	*127.10*	*147.40*	*4.8*	*0.79*	*8.8*	*12.0*	-	*1.35*	*8.8*	*7.8*		
BD04CSR-50-4	164.20	76.70	6.3	0.74	12.9	25.2	-	1.95	24.0	14.1		
BD04CSR-50-5	105.30	85.70	2.7	0.69	8.0	18.5	-	2.31	15.4	14.9		
BD04CSR-50-6	*157.50*	*69.70*	*4.1*	*0.71*	*9.2*	*19.3*	-	*2.09*	*8.4*	*7.1*		
BD04CSR-50-7	166.30	131.70	7.6	0.78	10.2	18.0	-	1.77	20.1	14.7		
BD04CSR-25			**3.9**	**0.68**	**20.8**	**33.4**	-	**1.61**	**44.6**		**20.0**	**3.6**
BD04CSR-25-1	129.40	50.00	2.0	0.62	18.1	31.5	-	1.74	40.2	20.7		
BD04CSR-25-2	181.60	85.90	4.5	0.72	12.3	18.7	-	1.52	35.8	24.4		
BD04CSR-25-3	129.70	62.70	1.7	0.61	31.7	49.8	-	1.57	50.8	15.8		
BD04CSR-25-4	128.50	114.40	7.3	0.77	21.0	33.5	-	1.59	51.8	19.0		
BD04CSR-26			**2.3**	**0.64**	**92.1**	**67.7**	-	**0.74**	**326.0**		**39.0**	**3.5**
BD04CSR-26-1	*84.60*	*66.60*	*1.8*	*0.64*	*13.3*	*11.0*	-	*0.83*	*34.0*	*27.6*		
BD04CSR-26-2	113.80	60.10	1.3	0.58	79.6	58.3	-	0.73	267.1	40.4		
BD04CSR-26-3	136.80	78.30	3.5	0.69	81.6	65.1	-	0.80	340.0	41.6		
BD04CSR-26-4	106.20	65.40	2.0	0.65	115.2	79.7	-	0.69	371.0	35.0		

Sample	L (mm)	W (mm)	Mass (µg)	Ft*	U (ppm)	Th (ppm)	Sm (ppm)	Th/U	He (ncc/mg)	Corrected Age (Ma)	Mean age (Ma)	St.Dev.† (Ma)
BDCSR27			**0.7**	**0.59**	**6.0**	**34.0**	-	**10.93**	**40.6**		**44.4**	**7.5**
BDCSR27-1§	*144.30*	*62.90*	*1.1*	*0.64*	*2.3*	*30.8*	-	*13.50*	*65.6*	*88.8*		
BDCSR27-2	107.70	68.60	1.0	0.65	3.3	37.8	-	11.40	42.5	44.1		
BDCSR27-3	84.10	70.30	0.8	0.64	1.1	19.9	-	18.90	24.5	54.9		
BDCSR27-4	67.50	52.00	0.4	0.53	16.8	48.8	-	2.90	68.8	37.6		
BDCSR27-5	87.70	52.90	0.5	0.55	2.8	29.4	-	10.53	26.8	40.9		
BDCSR28			**1.3**	**0.68**	**1.6**	**15.8**	-	**9.69**	**20.0**		**45.0**	-
BDCSR28-2§	*93.90*	*49.40*	*0.8*	*0.61*	*2.4*	*26.3*	-	*10.92*	*111.9*	*173.9*		
BDCSR28-3	108.10	60.80	1.3	0.68	1.6	15.8	-	9.69	20.0	45.0		
BDCSR29			**2.3**	**0.67**	**7.0**	**35.4**	-	**5.39**	**56.2**		**45.4**	**5.4**
BDCSR29-1	177.30	105.40	4.0	0.77	4.2	24.2	-	5.77	44.7	48.3		
BDCSR29-2	148.10	70.80	3.2	0.68	10.0	54.8	-	5.46	80.0	42.3		
BDCSR29-3	90.40	67.30	0.8	0.63	5.0	39.3	-	7.85	42.1	38.3		
BDCSR29-4	151.50	80.30	2.0	0.70	8.9	20.5	-	2.31	61.6	52.3		
BDCSR29-5	115.70	59.30	1.4	0.59	6.9	38.4	-	5.59	52.4	45.9		
BDCSR29-6§	*98.60*	*60.90*	*1.5*	*0.60*	*10.2*	*73.1*	-	*7.18*	*141.7*	*71.2*		
BDCSR30			**4.9**	**0.73**	**5.1**	**16.1**	-	**3.25**	**37.6**		**50.1**	**4.2**
BDCSR30-1	174.10	108.20	4.1	0.77	3.0	10.9	-	3.67	28.0	53.8		
BDCSR30-2	205.20	111.60	5.1	0.78	4.3	12.9	-	3.02	38.0	54.5		
BDCSR30-3	137.90	76.70	5.0	0.69	4.2	12.8	-	3.06	30.1	49.2		
	136.60	65.10										
	136.30	88.80										
BDCSR30-4	123.50	70.90	2.2	0.65	9.8	29.9	-	3.04	59.5	44.2		
	100.40	68.40										
BDCSR30-5	234.90	86.00	8.0	0.75	4.0	13.9	-	3.47	32.5	49.0		
	233.20	97.80										
BDCSR-31			**1.2**	**0.66**	**20.0**	**95.3**	-	**4.66**	**31.1**		**8.8**	**1.2**
BDCSR-31-1	86.80	71.50	0.9	0.65	14.8	61.2	-	4.15	18.7	8.1		
BDCSR-31-2	103.20	71.00	1.0	0.65	20.7	94.4	-	4.55	27.3	8.0		
BDCSR-31-3	148.40	75.60	1.7	0.69	24.6	130.4	-	5.30	47.2	10.2		
BDCSR-32			**0.5**	**0.54**	**20.2**	**48.8**	-	**3.07**	**13.6**		**6.8**	**1.4**
BDCSR-32-1	81.70	50.70	0.4	0.54	30.4	53.9	-	1.77	16.5	5.9		
BDCSR-32-2	127.40	50.20	0.6	0.55	10.0	43.7	-	4.37	10.7	7.8		
BDCSR-32-3§	*128.30*	*68.90*	*1.2*	*0.66*	*32.2*	*63.2*	-	*1.96*	*53.9*	*14.3*		

Sample	L (mm)	W (mm)	Mass (µg)	Ft*	U (ppm)	Th (ppm)	Sm (ppm)	Th/U	He (ncc/mg)	Corrected Age (Ma)	Mean age (Ma)	St.Dev.† (Ma)
BDCSR33			**0.8**	**0.61**	**25.9**	**62.6**	-	**2.50**	**18.0**		**6.0**	**0.9**
BDCSR33.1§	*115.60*	*45.00*	*0.5*	*0.51*	*14.7*	*46.0*	-	*3.14*	*25.8*	*16.4*		
BDCSR33.2	115.10	74.90	1.3	0.67	31.7	56.2	-	1.77	21.3	5.8		
BDCSR33.3§	*106.30*	*41.10*	*0.4*	*0.47*	*7.5*	*43.0*	-	*5.71*	*20.3*	*20.2*		
BDCSR33.4	90.80	47.90	0.4	0.52	23.2	80.2	-	3.46	18.8	7.0		
BDCSR33.5	79.70	69.60	0.8	0.63	22.7	51.2	-	2.26	14.0	5.2		
BDCSR-35			**1.6**	**0.61**	**23.2**	**57.2**	-	**2.54**	**33.4**		**12.4**	**4.0**
BDCSR-35.1	101.30 116.10	61.70 69.20	1.9	0.64	19.9	72.2	-	3.62	28.8	10.1		
BDCSR-35.2	115.50 97.90	62.60 53.90	1.5	0.60	23.4	50.2	-	2.14	43.7	16.9		
BDCSR-35.3	82.30 105.10	56.40 60.70	1.3	0.59	26.4	49.1	-	1.86	27.8	10.1		
BDCSR-35.4§	*122.90* *114.20*	*51.30* *50.60*	*1.2*	*0.56*	*33.0*	*79.8*	-	*2.42*	*65.8*	*18.7*		
BDCSR36			**0.9**	**0.63**	**26.0**	**61.7**	-	**2.37**	**42.3**		**13.6**	-
BDCSR36.1§	*87.40*	*62.50*	*0.7*	*0.61*	*16.0*	*37.1*	-	*2.32*	*87.9*	*48.0*		
BDCSR36.2	110.20	65.10	0.9	0.63	26.0	61.7	-	2.37	42.3	13.6		
BDCSR-37			**3.5**	**0.69**	**20.8**	**79.1**	-	**3.81**	**76.2**		**23.7**	**6.0**
BDCSR-37.1	110.40 123.80	60.10 72.70	2.1	0.65	15.2	58.6	-	3.85	56.8	24.8		
BDCSR-37.2§	*102.60* *99.30*	*72.40* *72.40*	*2.1*	*0.66*	*14.4*	*61.7*	-	*4.29*	*88.9*	*38.3*		
BDCSR-37.3	152.40 149.20	79.60 73.10	3.5	0.69	19.8	73.4	-	3.71	91.0	29.2		
BDCSR-37.4	141.40 128.50	83.60 105.00	4.8	0.74	27.3	105.3	-	3.86	80.7	17.3		
BDCSR38			**0.7**	**0.58**	**26.8**	**83.9**	-	**3.14**	**135.2**		**42.1**	**7.4**
BDCSR38.1§	*133.50*	*63.50*	*1.1*	*0.64*	*16.1*	*32.5*	-	*2.01*	*162.2*	*87.8*		
BDCSR38.2	93.60	65.30	0.8	0.63	30.0	92.7	-	3.09	145.6	36.9		
BDCSR38.3	99.20	47.90	0.5	0.53	23.5	75.2	-	3.20	124.8	47.4		

Sample	L (mm)	W (mm)	Mass (µg)	Ft*	U (ppm)	Th (ppm)	Sm (ppm)	Th/U	He (ncc/mg)	Corrected Age (Ma)	Mean age (Ma)	St.Dev.† (Ma)
BDCSR39			**1.1**	**0.60**	**28.2**	**111.6**	-	**3.92**	**140.0**		**34.5**	**6.5**
BDCSR39.1	107.90	51.40	0.6	0.56	24.2	107.3	-	4.44	113.3	33.9		
BDCSR39.2	87.20	45.70	0.4	0.50	47.5	146.5	-	3.08	142.5	28.6		
	100.80	41.60										
BDCSR39.3	126.70	61.00	0.9	0.62	29.0	168.4	-	5.80	222.3	42.8		
BDCSR39.4	192.80	69.10	1.9	0.67	29.0	131.3	-	4.53	195.9	39.9		
BDCSR39.5	134.20	72.60	2.0	0.64	23.2	77.0	-	3.31	115.8	35.7		
	101.90	54.20										
BDCSR39.6	93.80	63.10	0.8	0.62	16.5	39.1	-	2.38	50.0	26.0		
BDCSR40			**0.6**	**0.56**	**36.6**	**125.6**	-	**3.27**	**138.0**		**27.8**	**6.0**
BDCSR40.1	94.60	58.60	0.7	0.59	15.4	36.4	-	2.36	32.9	19.0		
BDCSR40.2	105.20	64.40	0.9	0.63	51.8	174.9	-	3.38	232.8	32.7		
BDCSR40.3	82.90	48.40	0.4	0.52	28.2	73.1	-	2.59	77.3	27.0		
BDCSR40.4	100.70	48.30	0.5	0.53	42.5	168.6	-	3.97	178.8	33.7		
BDCSR40.5	90.50	49.40	0.4	0.53	28.0	100.3	-	3.58	76.3	22.8		
BDCSR40.6	116.70	56.20	0.7	0.59	53.5	200.1	-	3.74	230.0	31.8		
12LC07			**1.1**	**0.60**	**49.67**	**49.83**	**26.68**	**1.00**	**1.1**		**5.6**	**0.4**
12LC07-1	92.32	82.89	1.3	0.62	50.1	49.4	25.4	0.99	1.2	5.9		
12LC07-2	101.44	69.34	1.0	0.58	49.2	50.2	27.9	1.02	1.0	5.3		
12LC07-3	*102.57*	*57.04*	*0.7*	*0.51*	*9.3*	*26.4*	*13.6*	*2.84*	*2.3*	*52.9*		
12LC08			**1.4**	**0.61**	**27.68**	**34.99**	**28.72**	**1.27**	**0.6**		**5.2**	**0.5**
12LC08-1	113.80	77.64	1.4	0.62	30.2	30.6	18.6	1.01	0.7	5.4		
12LC08-2	139.95	90.39	2.3	0.67	22.2	23.7	33.2	1.07	0.5	4.6		
12LC08-3	85.76	74.36	1.0	0.58	36.6	50.2	31.7	1.37	0.8	4.9		
12LC08-4	99.21	71.03	1.0	0.58	21.6	35.4	31.4	1.64	0.6	5.8		
12LC09			**1.8**	**0.64**	**31.34**	**60.30**	**66.93**	**1.92**	**1.1**		**6.8**	-
12LC09-1	137.18	81.40	1.8	0.64	31.3	60.3	66.9	1.92	1.1	6.8		
12LC09-2	*145.30*	*84.40*	*2.1*	*0.65*	*56.8*	*104.3*	*90.4*	*1.84*	*3.6*	*12.5*		
12LC09-3	*116.36*	*73.22*	*1.3*	*0.60*	*71.6*	*148.9*	*74.0*	*2.08*	*4.5*	*12.8*		
12LC11			**1.6**	**0.63**	**57.73**	**41.86**	**59.09**	**0.67**	**1.5**		**6.2**	**0.7**
12LC11-1	146.19	86.12	2.2	0.67	85.6	71.5	81.4	0.84	2.5	6.7		
12LC11-2	139.27	79.44	1.8	0.65	22.4	11.9	41.8	0.53	0.5	5.4		
12LC11-3	126.50	61.99	1.0	0.57	65.2	42.1	54.1	0.65	1.5	6.4		

Sample	L (mm)	W (mm)	Mass (µg)	Ft*	U (ppm)	Th (ppm)	Sm (ppm)	Th/U	He (ncc/mg)	Corrected Age (Ma)	Mean age (Ma)	St.Dev.† (Ma)
12LC13			**1.6**	**0.61**	**16.67**	**32.41**	**11.99**	**1.94**	**1.1**		**13.7**	-
12LC13-1	155.22	71.77	1.6	0.61	16.7	32.4	12.0	1.94	1.1	13.7		
12LC13-2	*114.20*	*62.60*	*0.9*	*0.56*	*23.1*	*28.6*	*18.2*	*1.24*	*5.2*	*56.9*		
12LC13-3	*95.73*	*50.51*	*0.5*	*0.47*	*9.6*	*29.3*	*10.5*	*3.06*	*1.3*	*31.9*		
12LC14			**0.7**	**0.53**	**6.87**	**45.23**	**65.34**	**6.41**	**0.7**		**12.7**	**0.8**
12LC14-1	*183.92*	*78.82*	*2.3*	*0.64*	*4.1*	*27.9*	*47.1*	*6.82*	*0.4*	*9.3*		
12LC14-2	87.74	60.40	0.6	0.51	5.0	29.2	73.3	5.80	0.5	13.3		
12LC14-3	89.00	68.35	0.8	0.55	8.7	61.3	57.3	7.03	0.9	12.1		
12LC16			**2.0**	**0.65**	**30.05**	**46.20**	**24.58**	**1.50**	**3.9**		**26.0**	**3.2**
12LC16-1	145.00	82.57	2.0	0.65	42.3	70.9	25.3	1.68	6.1	29.5		
12LC16-2	146.48	82.48	2.0	0.65	23.8	27.6	14.8	1.16	2.7	25.6		
12LC16-3	132.42	83.92	1.9	0.65	24.1	40.1	33.6	1.66	2.7	23.1		
12LC16-4	*102.03*	*86.46*	*1.5*	*0.63*	*40.3*	*65.6*	*30.0*	*1.63*	*9.7*	*50.4*		

Notes: See text for discussion of analytical procedures and errors; samples in italics were not used in the calculation of mean ages; dash—not measured.

*Ft is the alpha ejection correction of Farley et al. (1996).

†St. Dev.—standard deviation.

§Samples with large reextractions during He degassing.

Table SD3.2. Zircon (U-Th)/He data for the Slate Range

Sample	L (mm)	W (mm)	Mass (μg)	Ft*	U (ppm)	Th (ppm)	Sm (ppm)	Th/U	He (ncc/mg)	Corrected Age (Ma)	Mean age (Ma)	St.Dev.† (Ma)
12LC01			**6.1**	**0.77**	**659.41**	**253.47**	**5.74**	**0.39**	**151.8**		**50.1**	**5.8**
z12LC01-1	177.37	92.72	7.1	0.79	555.7	245.1	2.6	0.44	113.6	43.6		
z12LC01-2	168.29	78.92	4.9	0.76	779.3	240.3	0.6	0.31	187.1	54.6		
z12LC01-3	188.15	85.45	6.4	0.78	643.3	275.0	14.0	0.43	154.8	52.1		
12LC02			**2.9**	**0.72**	**663.57**	**257.16**	**4.96**	**0.38**	**147.2**		**52.1**	**5.1**
z12LC02-1	132.31	65.19	2.6	0.71	627.0	303.7	0.9	0.48	127.5	47.8		
z12LC02-2	158.34	67.46	3.4	0.73	577.6	157.1	1.0	0.27	122.6	50.8		
z12LC02-3	126.23	67.49	2.7	0.71	786.1	310.7	13.0	0.40	191.4	57.7		
12LC03			**4.8**	**0.75**	**771.37**	**225.79**	**1.04**	**0.30**	**149.2**		**44.6**	**8.4**
z12LC03-1	182.12	71.50	4.3	0.74	471.2	166.3	1.5	0.35	92.4	45.1		
z12LC03-2	154.24	70.34	3.5	0.74	940.5	166.9	0.7	0.18	139.8	35.9		
z12LC03-3	222.52	79.15	6.5	0.77	902.4	344.2	0.9	0.38	215.4	52.7		
12LC04			**5.9**	**0.76**	**644.46**	**355.54**	**0.72**	**0.56**	**135.4**		**45.3**	**2.6**
z12LC04-1	225.21	92.99	9.1	0.80	497.7	211.4	0.7	0.42	108.4	46.0		
z12LC04-2	156.40	83.22	5.0	0.76	626.1	519.7	0.7	0.83	130.2	42.4		
z12LC04-3	152.70	71.42	3.6	0.73	809.6	335.6	0.8	0.41	167.5	47.5		
12LC07			**6.0**	**0.76**	**1171.55**	**312.85**	**0.81**	**0.26**	**257.4**		**50.7**	**7.0**
z12LC07-1	250.29	92.60	10.0	0.80	788.7	201.6	0.7	0.26	171.5	47.4		
z12LC07-2	182.55	70.89	4.3	0.74	1464.9	448.5	1.3	0.31	289.4	46.0		
z12LC07-3	163.16	70.27	3.7	0.74	1261.0	288.4	0.4	0.23	311.3	58.8		
12LC09			**14.9**	**0.83**	**433.09**	**146.52**	**0.58**	**0.34**	**113.8**		**54.3**	**0.0**
z12LC09-1	232.28	122.89	16.3	0.84	345.5	121.5	0.5	0.35	91.9	54.3		
z12LC09-2	241.41	109.87	13.6	0.82	520.7	171.6	0.6	0.33	135.7	54.3		
12LC10			**5.9**	**0.77**	**45.81**	**35.67**	**0.51**	**0.76**	**11.7**		**51.3**	**3.6**
z12LC10-1	181.56	89.24	6.7	0.78	55.4	48.2	0.5	0.87	14.9	53.1		
z12LC10-2	176.81	92.70	7.1	0.78	45.7	35.4	0.7	0.77	12.3	53.7		
z12LC10-3	143.36	75.36	3.8	0.74	36.3	23.4	0.3	0.64	7.9	47.2		
12LC11			**4.7**	**0.75**	**367.76**	**125.31**	**0.57**	**0.34**	**81.6**		**51.0**	**2.0**
z12LC11-1	163.40	71.95	3.9	0.74	329.0	106.9	0.5	0.33	72.8	51.4		
z12LC11-2	217.35	77.59	6.1	0.76	348.5	113.0	0.5	0.32	81.9	52.8		
z12LC11-3	179.56	70.52	4.2	0.74	425.8	156.0	0.7	0.37	90.2	48.8		

Sample	L (mm)	W (mm)	Mass (μg)	Ft*	U (ppm)	Th (ppm)	Sm (ppm)	Th/U	He (ncc/mg)	Corrected Age (Ma)	Mean age (Ma)	St.Dev.† (Ma)
12LC12			**7.2**	**0.78**	**190.84**	**221.27**	**0.97**	**1.19**	**46.4**		**46.1**	**3.5**
z12LC12-1	152.60	80.74	4.6	0.75	146.2	219.0	1.2	1.50	39.5	49.3		
z12LC12-2	129.02	88.59	4.7	0.76	241.8	265.1	0.9	1.10	52.8	42.3		
z12LC12-3	159.24	128.17	12.2	0.82	184.5	179.7	0.9	0.97	47.0	46.6		
12LC15			**5.6**	**0.76**	**381.37**	**114.41**	**0.72**	**0.31**	**92.4**		**55.2**	**3.1**
z12LC15-1	195.32	70.17	4.5	0.74	345.2	135.0	0.8	0.39	79.9	52.9		
z12LC15-2	179.96	74.06	4.6	0.75	455.1	107.9	0.7	0.24	105.3	54.0		
z12LC15-3	206.11	90.33	7.8	0.79	343.7	100.3	0.7	0.29	92.1	58.7		
12LC16			**4.4**	**0.75**	**195.91**	**135.60**	**0.73**	**0.69**	**52.5**		**56.6**	**2.9**
z12LC16-1	154.00	90.73	5.9	0.77	217.8	173.2	0.8	0.80	64.9	60.0		
z12LC16-2	136.12	76.42	3.7	0.74	206.2	121.4	0.8	0.59	51.6	54.9		
z12LC16-3	151.22	70.26	3.5	0.73	163.8	112.2	0.7	0.69	41.1	55.0		

Notes: See text for discussion of analytical procedures and errors; samples in italics were not used in calculated mean ages.

*Ft is the alpha ejection correction of Farley et al. (1996).

†St. Dev.—standard deviation.

CHAPTER 4

Low-temperature thermochronology of the Black and Panamint mountains, Death Valley, CA: Implications for geodynamic controls on Cenozoic intraplate strain

Tandis S. Bidgoli[1]

Erika Amir[2]

J. Douglas Walker[1]

Daniel F. Stockli[3]

Joseph E. Andrew[1]

S. John Caskey[2]

[1]*Department of Geology, University of Kansas, Lawrence, Kansas 66045, USA*

[2]*Department of Earth and Climate Sciences, San Francisco State University, San Francisco, CA 94132, USA*

[3]*Jackson School of Geosciences, University of Texas, Austin, Texas 78712, USA*

Abstract

We use apatite and zircon (U-Th)/He thermochronometry to evaluate the temporal and spatial patterns and tectonic drivers of Miocene to Pliocene deformation within the Death Valley area, eastern California. We analyzed 48 samples from the footwalls of the Amargosa-Black Mountains and Panamint-Emigrant detachment faults in the Black and Panamint mountains, respectively. Zircon He ages from the Black Mountains record continuous footwall cooling and exhumation from 9 to 3 Ma. Thermal modeling of these data suggest that cooling took place during two discrete intervals: a period of rapid (~5-10 mm/yr) footwall exhumation from 10-6 Ma, followed by slower (<5 mm/yr) exhumation since 6 Ma. Total cumulative exhumation is estimated to be 10-16 km. Paleodepth reconstruction and cooling ages from the central Panamint

Range samples also show two periods of cooling. Zircon He ages record late Miocene cooling via a completely exhumed partial retention zone, whereas apatite He ages show a punctuated phase of exhumation at ca. 4 Ma. The results suggest the western Panamint Range experienced a minimum of 7.2 km of exhumation since ~12 Ma. The new data, when evaluated within the context of published fault timing data, suggest that the transition from Basin and Range extension to dextral transtension is spatially and temporally distinct. The transition begins at ~8 Ma in ranges to the east and north of the Black Mountains, migrating westward into eastern Death Valley at 6 Ma. Initiation of this event is coincident with a major change in plate boundary relative motion vectors. Data from Panamint Range and several ranges to the west of Death Valley indicate transtension initiated over a large area at ca. 3-4 Ma. This distributed deformation is coeval with lithospheric delamination in the central and southern Sierra Nevada Range. Our results suggest that the transition from extension to dextral transtension reflects an evolution in driving mechanism from plate boundary kinematics to intraplate lithospheric delamination.

Introduction

Plate motions may be accommodated across broad zones of diffuse and variable style deformation within continental lithosphere (e.g., England, 1987). One of the best known examples of a diffuse zone is the Pacific-North American plate boundary, where ~25% of the current plate motion is accommodated far inboard of the San Andreas transform fault (Minster and Jordan, 1987; Dokka and Travis, 1990; Bennett et al., 2003). Geodetic data from across western North America show that most of this intraplate strain is focused in the eastern California shear zone (ECSZ; also the Walker Lane belt), a system of active, mostly northwest-striking, strike-slip faults that account for ~9-12 mm/yr of displacement of the Sierran mircoplate

relative to the Great Basin (Figure 4.1; Dixon et al., 1995; Bennett et al., 2003; Dokka and Travis, 1990).

Global circuit reconstructions of the Pacific plate relative to North America suggest that at ca. 10-8 Ma the plate boundary changed from NW oblique to dominantly coast-parallel motion (Atwater, 1970; Atwater and Stock, 1998). It is proposed that this motion change initiated the change from more Basin and Range style deformation to the transcurrent ECSZ and attendant structures (e.g., Dokka and Travis, 1990). [Plate boundary and intraplate deformation patterns are shown spectacularly in the animations of Atwater and Stock (1998), available at http://emvc.geol.ucsb.edu/download/nepac.php, and McQuarrie and Wernicke (2005)]. However, timing data from individual structures within the ECSZ range from middle Miocene to late Pleistocene (see Hodges et al., 1989; Holm and Dokka, 1991, 1993; Holm and Snow, 1992; Hoish and Simpson, 1993;; Snow and Lux, 1999; Snyder and Hodges, 2000; Niemi et al., 2001; Monastero et al., 2002; Stockli et al., 2003; Lee et al., 2009; Mahan et al., 2009; Beyene, 2011; Walker et al., 2014), suggesting that the transition from intraplate extension to intraplate dextral transtension may not be simply related to plate boundary kinematics, and that other geodynamic factors may play a role in the temporal and spatial patterns. One possible factor is lithospheric delamination, proposed to occur in the central and southern parts of the Sierra Nevada at ca. 3.5 Ma (Jones et al., 2004; Zandt et al., 2005; Gilbert et al., 2007).

In this paper, we present new zircon and apatite (U-Th)/He thermochronologic data from the Black and Panamint mountains bordering Death Valley in eastern California (Figure 4.1). Death Valley lies within a region that has experienced both Basin and Range extension and more recent dextral transtension related to the ECSZ and Walker Lane belt, and is therefore an ideal place to study the inboard part of the evolving Pacific-North American plate boundary. The new

timing data are integrated with published thermochronologic and sedimentologic data of a regional scale to show that the initiation of the dextral shear varies from east to west across the region, possibly reflecting an interplay between plate boundary effects and intraplate drivers such as lithospheric delamination.

Geologic background

The Black Mountains are located on the eastern margin of Death Valley (Figure 4.1). The range is host to the Amargosa-Black Mountains detachment (ABMD), a normal fault system that exposes 1.7 Ga gneiss and late Precambrian metasedimentary rocks intruded by 11.6 Ma Willow Springs pluton (Asmerom et al., 1990) and 10.4 Ma Smith Mountain Granite (Miller et al., 2004). Published $^{40}Ar/^{39}Ar$ and zircon fission-track ages from the Black Mountains show that exhumation and cooling along the ABMD began at ~12 Ma in the southern Black Mountains, however, major unroofing of the northern and central parts of the range took place between ~8 and 6 Ma (Holm et al., 1992; Holm and Dokka, 1993). The sedimentological record of the lower part of the adjacent Furnace Creek basin matches the timing of exhumation recorded in the thermochronology data; however, a significant portion of the basin shows rapid deposition beginning at 6 Ma, suggesting a major reorganization of the basin at that time (Wright et al., 1999).

The Panamint Range, on the western flank of Death Valley, is the relatively intact hanging wall to the ABMD. The range hosts two major Tertiary structures: the Eastern Panamint fault system (EPFS) and the Panamint-Emigrant detachment (PED) (Figure 4.1). These structures expose a core of 1.7 Ga gneiss, middle and late Precambrian metasedimentary rocks, and Cretaceous and Tertiary plutons. The EPFS is a low-angle normal fault system, exposed in the eastern part of the range. The timing of motion on the EPFS is poorly constrained, but it

likely post-dates intrusion of the 10.6 Ma Little Chief stock in the center of the range, and most of the Trail Canyon volcanic sequence (ca. 10.5-9.4 Ma), exposed on east side of the range (McKenna and Hodges, 1990; Hodges et al., 1990). The Trail Canyon volcanic sequence is tilted 20-40°, indicating significant eastward tilting of the EPFS and range since ~9 Ma.

The PED, exposed on the west side of the Panamint Range, includes the Emigrant and Town Pass faults, and the Panamint detachment. Timing constraints for the PED come from the sedimentary succession of the Nova Formation preserved in its hanging wall, and suggest fault initiation and basin development after ~12 Ma (Hodges et al., 1989; Synder and Hodges, 2000). However, the bulk of the Nova Formation was deposited rapidly between ~4.4 and 3.0 Ma, indicating that much of the activity related to this fault system is young (Synder and Hodges, 2000).

(U-Th)/He thermochronometry

We analyzed 48 samples from the footwalls of the ABMD and PED using zircon and apatite (U-Th)/He thermochronometry (Figure 4.1). Two additional samples were also analyzed: one from the western base of the Nopah Range and another from the northern base of the Avawatz Mountains (Figure 4.1). Samples represent a range of units, including Proterozoic gneiss and metasedimentary rocks, Cretaceous gneiss and leucogranite, and Tertiary diorite and granite. Laboratory and analytical work was performed at Isotope Geochemistry Laboratories at the University of Kansas, the (U-Th)/He Geo- and Thermochronometry Lab at the University of Texas at Austin, and the (U-Th)/He Thermochronology Lab at the University of California, Santa Cruz. Data tables, descriptions of analytical procedures, and error reporting are given in Tables SD4.1 and SD4.2 and Appendix 4.1.

He age results

Black Mountains

Cross-section A-A' (Figure 4.2) is oriented east-west and shows the geometry of the ABMD and the projected positions of our thermochronology samples from Sheep Canyon in the central Black Mountains. Zircon (U-Th)/He mean ages range from 5.4 ± 0.6 to 9.3 ± 3.9Ma and systematically increase with increasing elevation (Figures 4.2 and 4.3; Tables SD4.1). Samples also systematically increase in age eastward across the range (Figure 4.2). A similar pattern of cooling ages is observed from the footwall of AMBD in Confidence Wash in the southern Black Mountains (cross-section B-B' in Figure 4.2). Zircon (U-Th)/He mean ages there range from 5.4 ± 0.2 to 8.5 ± 1.4 Ma. Mean ages from this transect also systematically increase from west to east; however, the age-elevation relationship is much more subdued when compared with data from the central Black Mountains (Figures 4.2 and 4.3).

In addition to the above transects, we analyzed several samples from along the range front of the Black Mountains (Figure 4.1). Zircon (U-Th)/He mean ages span from 3.3 ± 0.3 to 5.5 ± 0.3 Ma, with most samples clustering at around 4 Ma (Figure 4.1). These samples also show a modest correlation between mean age and elevations (Figure 4.3).

Panamint Mountains

Cross-section C-C' (Figure 4.2) shows the geometry of the Miocene to Pliocene faults in the Panamint Range and projected positions of our thermochronology samples from the footwall of the PED in Surprise Canyon and Pleasant Canyon in the central part of the range. Zircon (U-Th)/He mean ages range from 6.4 ± 1.0 to 45.3 ± 4.9 Ma and systematically increase with increasing elevation (Table SD4.1). Samples also increase in age eastward across the range. In

contrast, mean apatite ages from these transects appear to cluster at ~3-4 Ma. The exception is our structurally highest sample, which had a mean age of 19.4 ± 0.3 Ma.

Thermal modeling and paleodepth reconstruction

In order to evaluate possible cooling histories and apparent exhumation rates, we modeled footwall transects from the central Black Mountains and Panamint Range using the numerical modeling software HeMP (Hager and Stockli, 2009). The software searches for viable thermal histories for multi-sample transects by modeling He production, stopping, and diffusion for randomly generated temperature-time paths using algorithms and goodness-of-fit tests described in Ketcham (2005). Details of the required model inputs and constraints are given in Appendix 4.1.

The modeling results for the central Black Mountains are shown in Figure 4.4. The model show continuous exhumation since ~10 Ma. There is a distinct change in the slope of model fits at ~6 Ma and a corresponding change in exhumations rates, from 10-5 mm/yr between 10 to 6 Ma, to <5 mm/yr after 6 Ma. The cumulative exhumation from our models ranges from 9 to 16 km, which is similar to earlier geobarometric estimates for the Willow Springs pluton (Holm et al., 1992). The modeling results also show that most of the model fits correspond to reasonable geothermal gradients between 20 and 50°C/km, although geothermal gradients as high as ~140°C/km were not excluded.

In contrast, thermal models for the Panamint Range could only be satisfied by model fits at very high geothermal gradients (100+°C), suggesting that our samples and paleoisotherms have been rotated and that a different approach is needed to evaluate the data. To account for the rotation, we restored samples to their middle Miocene paleodepths using the unconformity below the east-tilted Trail Canyon volcanic sequence as a pre-extensional ~paleohorizontal datum. The

restoration assumes that the range is a simple, tilted fault block; therefore, hinge position for tilting is not a factor (e.g., Armstrong et al., 2003). Our reconstruction adds ~500 m of overburden above the unconformity based on the thickness of the sequence in the north-central part of the range (McKenna and Hodges, 1990). A simple check on the accuracy of the reconstruction is that it places outcrops of the Little Chief stock at 1.8 to 2.2 km below the middle Miocene surface, consistent with crystallization pressures estimated for the stock (McDowell, 1974).

The resulting paleodepth reconstruction (Figure 4.5) shows two distinct periods of cooling. The structurally lowest zircon ages overlap within errors and show a period of late Miocene cooling. Samples above 7.5 km then steadily increase in age with decreasing paleodepth, defining a He partial retention zone. The shallowest zircon samples cluster at ~45 Ma and are not reset, defining the top of the partial retention zone. In contrast, apatite ages from these same samples are invariant at ~ 4 Ma, consistent with rapid exhumation at that time.

Assuming a mean surface temperature of 10°C, our paleodepth reconstruction indicates that the Panamint Range has experienced a minimum of 180°C of cooling since the late Miocene. The estimated geothermal gradient from our reconstruction is ~25°C/km, which translates to ~7.2 km of vertical exhumation. However, our structurally deepest sample resides 1.2 km below the approximate position of the 190°C isotherm in our paleodepth reconstruction. Therefore, the total vertical exhumation since the late Miocene is probably closer to 8.4 km.

Discussion and conclusions

The new data from the Black Mountains, combined with earlier thermochronologic constraints from the range, show a continuous exhumation history that begins at ~12 Ma. A marked change in the thermal history and inferred exhumation rate occurs at ~6 Ma, which is

coincident with a major change in the character of sediment and depositional rates within the Furnace Creek basin (Wright et al., 1999). The Panamint Range similarly shows two periods of exhumation: one in the late Miocene and the other in the Pliocene. The Pliocene cooling coincides with a period of rapid sedimentation within the adjacent Nova basin (Snyder and Hodges, 2000), suggesting a major reorganization at that time.

Timing constraints for the major faults within the ECSZ are variable. Faults located east and north of the Black Mountains (e.g., Stateline fault, Boundary Canyon Detachment, Furnace Creek fault, Northern Death Valley-Fish Lake Valley fault) initiate between 11 to 8 Ma, around the time of the plate boundary change (Figure 4.1; Mahan et al., 2009; Snow and Lux, 1999; Niemi et al., 2001; Holm and Dokka, 1991, 1993; Hoisch and Simpson, 1993; Beyene, 2011, Reheis and Sawyer, 1997). It is unclear if these structures initiate at the onset of regional extension or dextral transtension. However, timing data across much of the ECSZ suggest that extension and transtension occur in discrete phases. The Northern Death Valley-Fish Lake Valley fault system, for example, initiates at ca. 10 Ma, but reorganizes at ~6 Ma, similar to the Black Mountains (Reheis and Sawyer, 1997, Stockli et al., 2003). Like the Panamint Range, the Slate Range, and Inyo and White Mountains show two phases of rapid exhumation: one in the middle Miocene and another at ~3-4 Ma (Figure 4.1; Walker et al., 2014; Lee et al., 2009; Stockli et al., 2003). The earlier of these events is linked to Basin and Range extension, while the latter to the initiation of dextral transtension.

The new thermochronology data, when placed within the context of published fault timing data, demonstrate that the very eastern part of the ECSZ experienced a transition to dextral transtension that may have been coincident with the plate boundary change, while areas to the west lag the plate boundary change by several million years. The data also suggest that

areas to the west of Death Valley experience the near simultaneous transition at ~3-4 Ma. This space-time pattern seems to indicate that, in addition to the plate boundary change at 10-8 Ma, other geodynamic drivers may need to be considered.

One factor that may be imparting a control on the temporal and spatial pattern of intraplate strain is lithospheric delamination, which is interpreted to have occurred in the central and southern Sierra Nevada at ca. 3.5 Ma (Jones et al., 2004; Zandt et al., 2004; Gilbert et al., 2007). Mantle tomographic studies have identified a large, dense lithospheric body (the Isabella anomaly) spreading out from the base of the crust into the asthenosphere beneath the western Sierras and Great Valley, while the topographically-high eastern Sierras are made up of relatively thin crust (~35 km) and low-velocity mantle (Gilbert et al., 2012 and references therein). Aside from the geophysical evidence for delamination, garnet-rich xenoliths, present in 12-8 Ma basalts, are conspicuously missing from eruptions younger than ca. 4 Ma, suggesting that a portion of the lithosphere was removed during the intervening interval (Ducea and Saleeby, 1996, 1998). The timing of delamination is inferred from a brief pulse of small volume, but widespread volcanism at ca. 3.5 Ma, interpreted to have been caused by asthenospheric upwelling in the wake of lithospheric removal (Manly et al., 2000; Farmer et al., 2002; Jones et al., 2004).

The nearly identical timing of lithospheric delamination and the development of the ECSZ west of Death Valley suggests these events are linked. Such a connection has been postulated and modeled by a number of authors (e.g., Jones et al., 2004, Oldow et al., 2008; Le Pourhiet et al., 2006; Saleeby et al., 2012), but major gaps in fault timing constraints have rendered the relationship between the two ambiguous. Data from this study, combined with published fault timing constraints, indicate that the initiation of dextral transtension occurs as a

westward migrating wave, with strain localized in the east at ~8 Ma, in Death Valley and Fish Lake Valley at 6 Ma, and in areas west of Death Valley at 3-4 Ma. This pattern can be readily explained by progressive westward delamination of mantle lithosphere and its associated thermomechanical consequences.

Acknowledgements

This research was supported by a University of Kanas - Patterson Fellowship and student research grants from the Geological Society of America and the American Association of Petroleum Geologists. We would like to thank Michael Giallorenzo for providing apatite separates from the Nopah Range, and Roman Kislitsyn and Jeremey Hourigan for assistance with sample preparation and analysis. We are grateful to Chad La Fever, Edward Morehouse, Gabriel Creason, and Rachelle Warren for assistance with sample collection.

References cited

Armstrong, P.A., Ehlers, T.A., Chapman, D.S., Farley, K.A., and Kamp, P.J., 2003, Exhumation of the central Wasatch Mountains, Utah:1. Patterns and timing of exhumation deduced from low-temperature thermochronology data: Journal of Geophysical Research, v. 108, 2172, doi:10.1029/2001JB001708,2003

Asmerom, Y., Snow, J. K., Holm, D. K., Jacobsen, S. B., Wernicke, B. P., and Lux, D. R., 1990, Rapid uplift and crustal growth in extensional environments: An isotopic study from the Death Valley region, California: Geology, v. 18, p. 223-226.

Atwater, T., 1970, Implications of plate tectonics for the Cenozoic tectonic evolution of western North America: Bulletin of the Geological Society of America, v. 81, p. 3513–3536.

Atwater, T., and Stock, J., 1998, Pacific-North America plate tectonics of the Neogene southwestern United States: An update: International Geological Review, v. 40, p. 375–402.Bennett, R.A., Wernicke, B.P., Niemi, N.A., Friedrich, A.M., and Davis, J.L., 2003, Contemporary strain rates in the northern Basin and Range province from GPS data: Tectonics, v. 22, p. 1008.

Beyene, M., 2011, Mesozoic burial, and Mesozoic and Cenozoic exhumation of the Funeral Mountains core complex, Death Valley, southeastern California [Ph.D. thesis]: Las Vegas, University of Nevada, 362 p.

Dixon, T.H., Robaudo, S., Lee, J., and Reheis, M.C., 1995, Constraints on present-day Basin and Range deformation from space geodesy: Tectonics, v. 14, p. 755–772.

Dokka, R.K., and Travis, C.J., 1990, Role of the eastern California shear zone in accommodating Pacific-North American plate motion: Geophysical Research Letters, v. 17, p. 1323–1326.

Drewes, H., 1963, Geology of the Funeral Peak quadrangle, California, on the eastern flank of Death Valley: U.S. Geological Survey Professional Paper 413, 78 p.

Ducea, M.N., and Saleeby, J.B., 1996, Buoyancy sources for a large, unrooted mountain range, the Sierra Nevada, California: Evidence from xenoliths thermobarometry: Journal of Geophysical Research, v. 101, p. 8229–8244.

Ducea, M.N., and Saleeby, J.B., 1998, A case for delamination of the deep batholithic crust beneath the Sierra Nevada, California: International Geology Review, v. 40, p. 78–93.

England, P.C., 1987, Diffuse continental deformation: length scales, rates and metamorphic evolution: Philosophical Transactions of the Royal Society of London, v. 321, p. 3-22.

Farmer, G.L., Glazner, A.F., and Manley, C.R., 2002, Did lithospheric delamination trigger late Cenozoic potassic volcanism in the southern Sierra Nevada, California?: Geological Society of America Bulletin, v. 114, p. 754–768.

Gilbert, H.J., Jones, C., Owens, T.J., Zandt, G., 2007, Imaging Sierra Nevada lithospheric sinking: Eos (Transactions, American Geophysical Union), v. 88, p. 225.

Gilbert, H., Yang, Y., Forsyth, D.W., Jones, C.H., Owens, T.J., Zandt, G., and Stachnik, J.C., 2012, Imaging lithospheric foundering in the structure of the Sierra Nevada: Geosphere, v. 8, p. 1310-1330.

Hager, C. and Stockli, D.F., 2009, A new MATLAB©-based helium modeling package ("HeMP") for thermal history recovery from single and multi-thermochronometer (U-Th)/He data and data arrays: Geological Society of America, Abstracts with Program, v. 41, p. 487.

Hodges, K.V., McKenna, L.W., Stock, J.M., Knapp, J.H., and Walker, J.D., 1989, Structural relationships between Neogene extensional basins, Panamint Valley area, southeast California: New perspectives of Basin and Range topography: Tectonics, v. 8, p. 453–467.

Hodges, K.V., McKenna, L.W., and Harding, M.B., 1990, Structural unroofing of the central Panamint Mountains, Death Valley region, southeastern California, in Wernicke, B.P., ed., Basin and Range extensional tectonics near the latitude of Las Vegas, Nevada: Geological Society of America Memoir 176, p. 377–390.

Holm, D.K., and R.K. Dokka, 1991, Major late Miocene cooling of the middle crust associated with extensional orogenesis in the Funeral Mountains, California, Geophysical Research Letters, v. 18, p. 1775–1778.

Holm, D. K., and R.K. Dokka, 1993, Interpretation and tectonic implications of cooling histories: An example from the Black Mountains, Death Valley extended terrane, California: Earth and Planetary Science Letters, v. 116, p. 63–80.

Holm, D.K., Snow, J.K., and Lux, D.R., 1992, Thermal and barometric constraints on the intrusive and unroofing history of the Black Mountains—Implications for timing, initial dip, and kinematics of detachment faulting in the Death Valley region, California: Tectonics, v. 11, p. 507–522.

Hoisch, T.D., and Simpson, C., 1993, Rise and tilt of metamorphic rocks in the lower plate of a detachment fault in the Funeral Mountains, Death Valley, California: Journal of Geophysical Research, v. 98, p. 6805-6827.

Hunt, C.B. and Mabey, D.R., 1966, Stratigraphy and structure, Death Valley, California: U.S. Geological Survey Professional Paper 494A, 162 p.

Jones, C.H., Farmer, G.L., and Unruh, J., 2004, Tectonics of Pliocene removal of lithosphere of the Sierra Nevada, California: Geological Society of America Bulletin, v. 116, p. 1408–1422.

Ketcham, R.A., 2005, Forward and inverse modeling of low temperature thermochronometry data, Reviews in Mineralogy and Geochemistry, v. 58, p. 275-314.

Lee, J., Stockli, D.F., Owen, L.A., Finkel, R.C., and Kislitsyn, R., 2009, Exhumation of the Inyo Mountains, California: Implications for the timing of extension along the western boundary of the Basin and Range Province and distribution of dextral fault slip rates across the eastern California shear zone: Tectonics, v. 28, TC1001, doi: 10.1029/2008TC002295.

Le Pourhiet, L., Gurnis, M., and Saleeby, J., 2006, Mantle instability beneath the Sierra Nevada mountains in California and Death Valley extension: Earth and Planetary Science Letters, v. 251, p. 104-119.

Mahan, K.H., Guest, B., Wernicke, B., and Niemi, N.A., 2009, Low-temperature thermochronologic constraints on the kinematic history and spatial extent of the Eastern California shear zone. Geosphere, v. 5, 1–13.

Manley, C.R., Glazner, A.F., and Farmer, G.L., 2000, Timing of volcanism in the Sierra Nevada of California: Evidence for the Pliocene delamination of the batholithic root?: Geology, v. 28, p. 811–814.

McDowell, D., 1974, Emplacement of the Little Chief stock, Panamint Range, California: Geological Society of America Bulletin, v. 85, p. 1535-1546.

McKenna, L.W., and Hodges, K.V., 1990, Constraints on the kinematics and timing of late Miocene–recent extension between the Panamint and Black Mountains, southeastern California, in Wernicke, B.P., ed., Basin and Range extensional tectonics near the latitude of Las Vegas, Nevada: Geological Society of America Memoir 176, p. 363–376.

Minster, J.B., and Jordan, T.H., 1987, Vector constraints on Western US deformation from space geodesy, neotectonics, and plate motions: Journal of Geophysical Research, v. 92, p. 4798–4804.

Miller, M., Friedman, R.M., Dee, S., 2004, Pre-10 Ma TIMS U-PB zircon age for the Smith Mountain Granite, Death Valley, California: implications for timing of major extension: Geological Society of America, Abstracts with Program, v. 36, p. 501.

Monastero, F.C., Walker, J.D., Katzenstein, A.M., and Sabin, A.E., 2002, Neogene evolution of the Indian Wells Valley, east-central California, *in* Glazner, A.F., Walker, J.D., and Bartley, J.M., eds., Geologic evolution of the Mojave Desert and southwestern Basin and Range., Geological Society of America (GSA). Boulder, CO, United States.

Niemi, N.A., Wernicke, B.P., Brady, R.J., Saleeby, J.B., and Dunne, G.C., 2001, Distribution and provenance of the middle Miocene Eagle Mountain Formation, and implications for regional kinematic analysis of the Basin and Range province: Geological Society of America, Bulletin, v. 113, p. 419-442.

Oldow, J. S., Geissman, J. W., & Stockli, D. F., 2008, Evolution and strain reorganization within late Neogene structural stepovers linking the central Walker Lane and northern Eastern California shear zone, western Great Basin: International Geology Review, v. 50, p. 270-290.

Reheis, M.C. and Sawyer, T.L., 1997, Late Cenozoic history and slip rates of the fish lake valley, emigrant peak, and deep springs fault zones, Nevada and California: Geological Society of America Bulletin, v. 109, p. 280-299.

Reinert, E., Cowan, D.S., and Reiners, P.W., 2003, Transpression within the Eastern California shear zone and low-temperature thermochronometry of the Avawatz Mountains, southern California, U.S.A: Geological Society of America, Abstracts with Program, v. 35, p. 64.

Saleeby, J., Le Pourhiet, L., Saleeby, Z., & Gurnis, M., 2012, Epeirogenic transients related to mantle lithosphere removal in the southern Sierra Nevada region, California, part I: Implications of thermomechanical modeling: Geosphere, v. 8, p. 1286-1309.

Snow, J.K., and Lux, D.R., 1999, Tectono-sequence stratigraphy of Tertiary rocks in the Cottonwood Mountains and northern Death Valley area, California and Nevada, in

Wright, L.A., and Troxel, B.W., eds., Cenozoic Basins of the Death Valley Region: Geological Society of America, Special Paper 333, p. 17-64.

Snyder, N.P. and Hodges, K.V., 2000, Depositional and tectonic evolution of a supradetachment basin:40Ar/39Ar geochronology of the Nova Formation, Panamint Range, California: Basin Research, v. 12, p. 18-30.

Stockli, D.F., T.A. Dumitru, M.O. McWilliams, and K.A. Farley, 2003, Cenozoic tectonic evolution of the White Mountains, California and Nevada, Geological Society of America Bulletin, v. 115, 788–816.

Walker, J.D., Bidgoli, T.S., Didericksen, B.D., Stockli, D.F., and Andrew, J.E., 2014, Middle Miocene to Recent Exhumation of the Slate Range, eastern California, and implication for the timing of extension and the transition to transtension: Geosphere, v. X. p. XX-XX.

Workman, J.B., Menges, C.M., Page, W.R., Taylor, E.M., Ekren, E.B., Rowley, P.D., Dixon, G.L., Thompson, R.A., and Wright, L.A., 2002, Geologic Map of the Death Valley Ground-water Model Area, Nevada and California, in USGS MF2381, http://pubs.usgs.gov/mf/2002/mf-2381/ (accessed December 2013).

Wright, L.A., Greene, R.C., Cemen, I., Johnson, F.C., Prave, A.R., and Drake, R.E., 1999, Tectonostratigraphic development of the Miocene-Pliocene Furnace Creek Basin and related features, Death Valley region, California, in Wright, L.A., and Troxel, B.W., eds., Cenozoic Basins of the Death Valley Region: Geological Society of America Special Paper 333, p. 115–126.

Zandt, G., Gilbert, H., Owens, T.J., Ducea, M., Saleeby, J., and Jones, C.H., 2004, Active foundering of a continental arc root beneath the southern Sierra Nevada in California: Nature, v. 431, p. 41–46.

Figure captions

Figure 4.1. Color shaded relief map of the greater Death Valley area with major detachment (ticks), normal (ball and stick), and strike-slip (arrows with relative motion) faults shown in black. Faults after Wernicke et al. (1988). Published fission-track and (U-Th)/He ages (Ma) are shown in ovals. Mean zircon (black text) and apatite (red text) (U-Th)/He ages and age ranges are shown for samples from this study. Inset map shows area of figure (dashed box) with respect to western North America. AHe – Apatite Helium; AFT – Apatite Fission Track; BM – Black Mountains; CM – Clark Mountains; CW –

Cottonwood Mountains; HM – Hunter Mountain; NR – Nopah Range; ZHe – Zircon Helium; ZFT – Zircon Fission Track. Data sources: McCullough Range – Mahan et al. (2009); Avawatz Mountains – Reinert et al. (2003); Black Mountains – Holm et al. (1992), Holm and Dokka (1993); Funeral Mountains – Holm and Dokka (1991), Hoisch and Simpson (1993); Panamint Range – B. Wernicke (2011, pers. comm.); Slate Range – Walker et al. (2014); Inyo Mountains – Lee et al. (2009); White Mountains – Stockli et al. (2003).

Figure 4.2. Geologic cross sections across the central Black Mountains (A-A'), southern Black Mountains (B-B'), and central Panamint Range (C-C'). Thermochronology samples, shown as dots, are projected into the plane of each cross-section. In this projected view, samples may lie above or below topography of the section line. Mean zircon (black diamonds) and apatite (white diamonds) (U-Th)/He ages and errors (1σ standard deviation) are shown above each sample. Cross section locations are shown in Figure 1. Geology from Drewes (1963), Hunt and Mabey (1966), and the compilation of Workman et al. (2002).

Figure 4.3. Plot of zircon (U-Th)/He age versus elevation for the Black Mountains showing a strong age-elevation relationship for the Sheep Canyon data, while data from Confidence Wash show a more modest correlation.

Figure 4.4. (a) Modeled temperature-time (T-t) paths (acceptable fits) for the Sheep Canyon transect, central Black Mountains. Dashed line shows that most of the modeled paths have an inflection point or change in slope and cooling rate at ~6 Ma. Black boxes show the model constraints based on biotite and hornblende $^{40}Ar/^{39}Ar$ ages from Holm et al. (1992) and an assumed mean annual surface temperature. (b) Exhumation rates from

modeled (t-T) histories that satisfy a 30˚C/km geothermal gradient (1000 fits). Results suggest that from10 to 6 Ma rates ranged from ~10 to 5 mm/yr. Rates have decreased since 6 Ma to <5 mm/yr.

Figure 4.5. Mean (U-Th)/He ages versus middle Miocene paleodepth for samples from the central Panamint Range. Zircon ages are shown as black diamond, apatite ages as white diamond. Error bars are 1σ standard deviations. Shaded area corresponds to the approximate position of the zircon He partial retention zone. Two periods of rapid exhumation are evident in the data: one in the late Miocene and another in the Pliocene. ZHe-PRZ – Zircon Helium Partial Retention Zone.

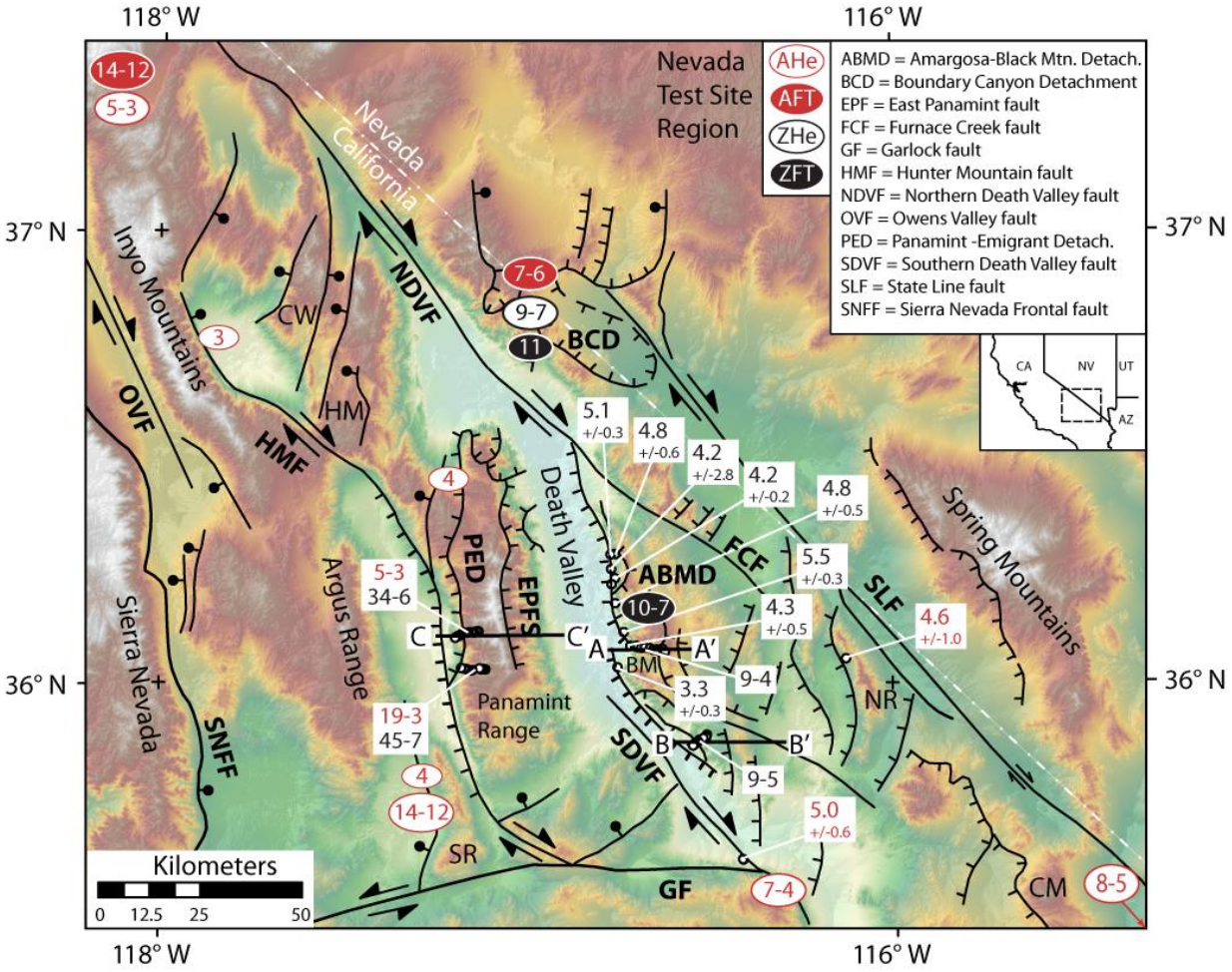
118° W
116° W
37° N
36° N
Nevada Test Site Region
AHe
AFT
ZHe
ZFT
ABMD = Amargosa-Black Mtn. Detach.
BCD = Boundary Canyon Detachment
EPF = East Panamint fault
FCF = Furnace Creek fault
GF = Garlock fault
HMF = Hunter Mountain fault
NDVF = Northern Death Valley fault
OVF = Owens Valley fault
PED = Panamint -Emigrant Detach.
SDVF = Southern Death Valley fault
SLF = State Line fault
SNFF = Sierra Nevada Frontal fault
CA
NV
UT
AZ
Nevada
California
Inyo Mountains
Sierra Nevada
Death Valley
Argus Range
Panamint Range
Spring Mountains
NDVF
OVF
HMF
SNFF
BCD
PED
EPFS
FCF
ABMD
SLF
SDVF
GF
CW
HM
BM
NR
CM
SR
14-12
5-3
7-6
9-7
11
3
4
10-7
9-4
9-5
7-4
8-5
34-6
19-3
45-7
5.1 +/-0.3
4.8 +/-0.6
4.2 +/-2.8
4.2 +/-0.2
4.8 +/-0.5
5.5 +/-0.3
4.3 +/-0.5
4.6 +/-1.0
3.3 +/-0.3
5.0 +/-0.6
A
A′
B
B′
C
C′
Kilometers
0 12.5 25 50

Figure 4.1

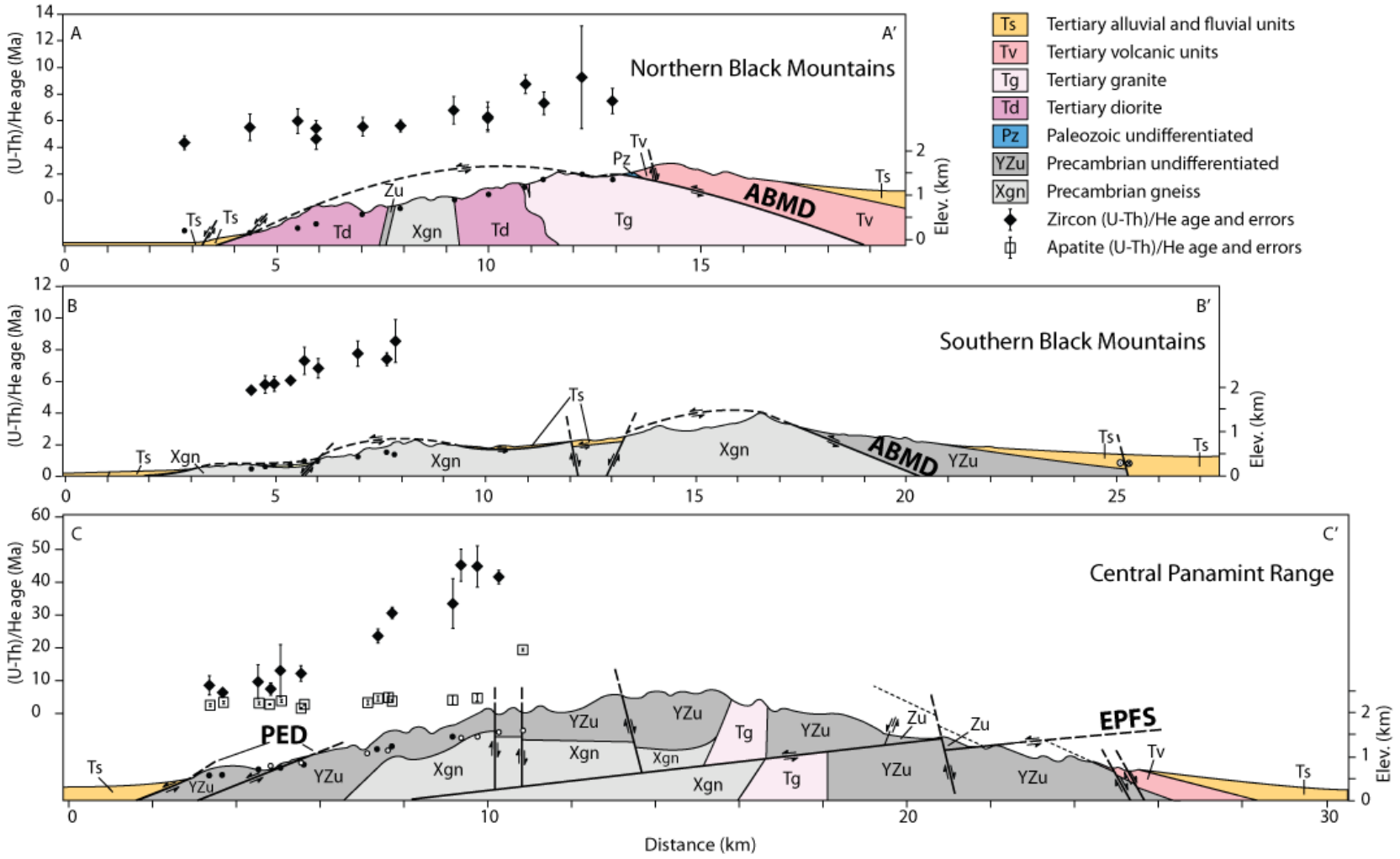
A
A′
Northern Black Mountains
B
B′
Southern Black Mountains
C
C′
Central Panamint Range
(U-Th)/He age (Ma)
Elev. (km)
Distance (km)
ABMD
EPFS
PED
Ts
Tv
Tg
Td
Pz
YZu
Xgn
Zu
Tertiary alluvial and fluvial units
Tertiary volcanic units
Tertiary granite
Tertiary diorite
Paleozoic undifferentiated
Precambrian undifferentiated
Precambrian gneiss
Zircon (U-Th)/He age and errors
Apatite (U-Th)/He age and errors

Figure 4.2

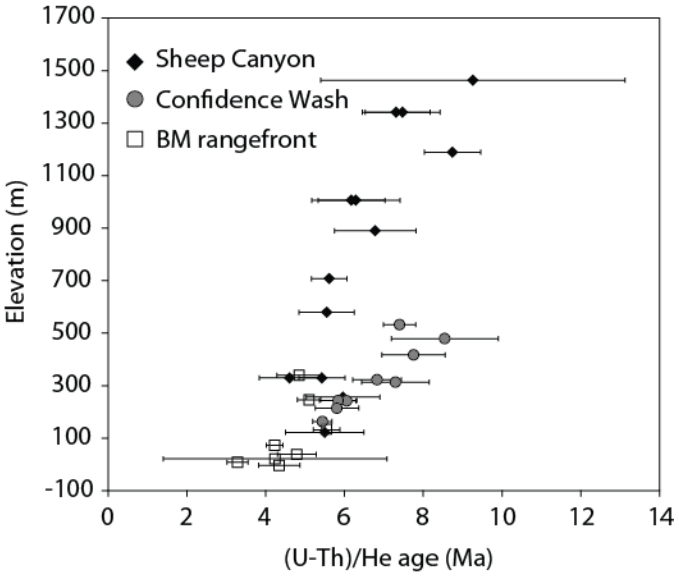
Sheep Canyon
Confidence Wash
BM rangefront
Elevation (m)
1700
1500
1300
1100
900
700
500
300
100
-100
0
2
4
6
8
10
12
14
(U-Th)/He age (Ma)

Figure 4.3

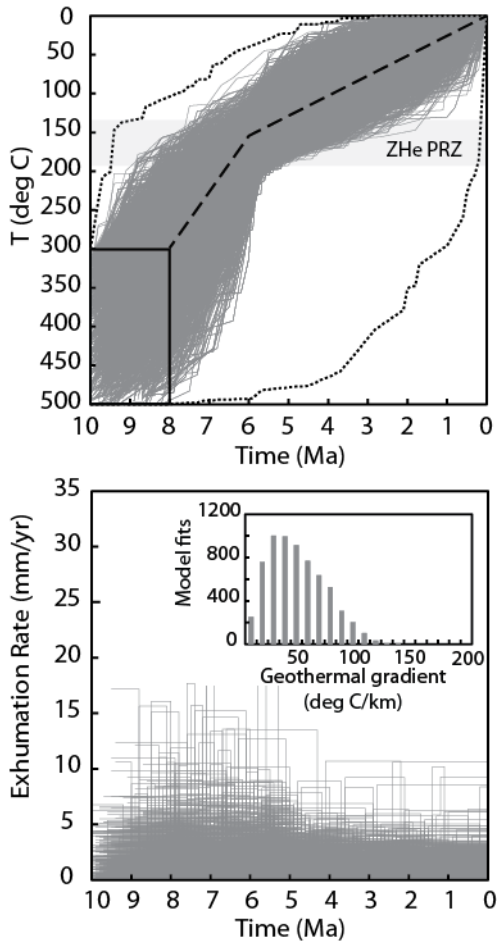
T (deg C)
Time (Ma)
ZHe PRZ
Exhumation Rate (mm/yr)
Model fits
Geothermal gradient
(deg C/km)

Figure 4.4

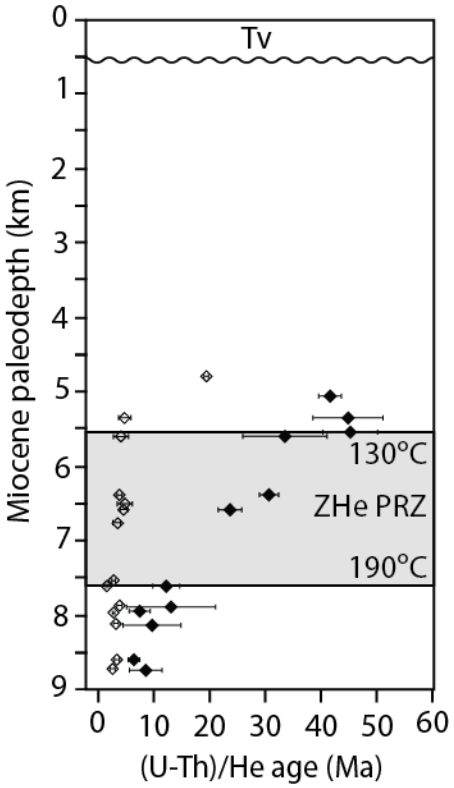
Tv
130°C
ZHe PRZ
190°C
Miocene paleodepth (km)
(U-Th)/He age (Ma)
0
1
2
3
4
5
6
7
8
9
0
10
20
30
40
50
60

Figure 4.5

Appendix 4.1

Analytical Procedures

Standard mineral separation techniques were used to isolate and concentrate apatite and zircon from our rock samples. Individual grains were inspected, measured, and photographed using a 180X Nikon stereomicroscope with crossed polarizers and mounted digital camera. In general, grains that were selected were near euhedral grains, greater than 70 µm in width that appeared inclusion-free. These guidelines increase the accuracy and reproducibility of (U-Th)/He ages by minimizing the effects of U and Th-bearing inclusions and the alpha-ejection (Ft) correction (Farley et al., 1996). Each single-grain was then loaded into a 1-mm platinum packet. Apatite grains were heated for 5 minutes at 1070°C using a continuous-mode laser. Zircon grains were heated for 10 minutes at 1300°C. The extracted He gas was then spiked with ^{3}He, purified using a gettering and cryogenic gas system, and measured on a Blazers Prisma QMS-200 quadrupole mass spectrometer. The degassed apatite grains were then dissolved in a spiked (^{230}Th, ^{235}U, ^{149}Sm) HNO_3 solution and analyzed using a Thermo Scientific Element-2 inductively coupled plasma mass spectrometer (ICP-MS). After laser degassing, zircon grains were removed from packets and dissolved using standard U-Pb high-pressure vessel digestion procedures (HF-HNO_3 and HCl). Following dissolution, samples were spiked (^{230}Th, ^{235}U, ^{149}Sm) and analyzed for U, Th, and Sm using an ICP-MS. Laboratory and analytical work was performed at the Isotope Geochemistry Laboratories at the University of Kansas, the (U-Th)/He Geo- and Thermochronometry Lab at the University of Texas at Austin, and the (U-Th)/He Thermochronology Lab at the University of California, Santa Cruz.

Error Reporting

Analytical uncertainties for individual (U-Th)/He analyses are approximately 3-4% (2σ). Because analytical uncertainties generally underestimate the reproducibility of a given sample due to uncertainties related to the Ft correction and parent isotope distributions, we follow common practice in (U-Th)/He dating and apply percentage errors to individual analyses based on the reproducibility of laboratory standards (Farley et al., 2001; Reiners et al., 2002; Tables SD4.1 and SD4.2). These are 6% for apatite and 8% for zircon. For mean ages, we report the error as the standard deviation (1σ) of our grain population for a given sample (Table SD4.1). However, 3 samples (12BM01, 12SC08, 12PC09) are single grain ages; therefore, we show the error in the "mean" age as the standard error in figures.

Table SD4.1 shows our resulting (U-Th)/He mean ages and associated errors (1σ). For most of our samples (N=48), three or more replicates were used to calculate the mean; however, 11 of the 59 reported mean ages were calculated using a smaller number of replicates. These samples contained outliers that were excluded from our calculations. Out of the 239 single-grain analyses completed, 39 or ~16% of the aliquots were excluded. We determined outliers as ages that were more than 2 standard deviations from the mean. Analyses with a large number of reextractions during laser He degassing were also excluded from our means, as this usually points to the presence of unseen mineral or fluid inclusions within the grain (House et al., 1999).

Thermal Modeling

We modeled footwall transects from the central Black Mountains and Panamint Range using the numerical modeling software Helium Modeling Package (HeMP; Hager and Stockli, 2009). The software searches for viable thermal histories for multi-sample transects by calculating model ages for temperature-time paths generated using a Monte Carlo approach, and

comparing those ages to the measured data. The algorithms used to model He production, stopping, and diffusion, and the goodness-of-fit tests are described in Ketcham (2005). Model inputs include sample elevation, mean age and uncertainty, isotopic concentrations, and grain size. User-defined parameters for our models include the model precision, set to 3.5 and 0.1 Ma increments; the geothermal gradient, which we allowed to range from 10 to 200°C; and the number of nodes between model constraints, set to 10. For the Sheep Canyon transect, central Black Mountains, we applied two T-t constraints: a starting temperature of 300 to 500°C between 10 to 8 Ma based on published hornblende and biotite ages (Holm et al., 1992; Holm and Dokka, 1993) in the vicinity of our transect, and a final temperature of 5 to 15°C . Thermal models for the Panamint Range use the same final temperature, but had a starting temperature of 350 to 500°C between 110 and 80 Ma, constrained by muscovite and hornblende K-Ar ages from the range (Lanphere, 1962). Models were allowed a maximum of 3 outliers and ran until 1000 acceptable fits were achieved.

References Cited

Farley, K.A., Rusmore, M.E., and Bogue, S.W., 2001, Exhumation and uplift history of the central Coast Mountains, British Columbia, from apatite (U-Th)/He Thermochronometry: Geology, v. 29, p. 99-102.

Farley, K.A., Wolf, R.A., and Silver, L.T., 1996, The effects of long alpha-stopping distances on (U-Th)/ He ages: Geochimica et Cosmochimica Acta, v. 60, p. 4223-4229.

Hager, C. and Stockli, D.F., 2009, A new MATLAB©-based helium modeling package ("HeMP") for thermal history recovery from single and multi-thermochronometer (U-Th)/He data and data arrays: Geological Society of America, Abstracts with Program, v. 41, p. 487.

Holm, D. K., and R.K. Dokka, 1993, Interpretation and tectonic implications of cooling histories: An example from the Black Mountains, Death Valley extended terrane, California: Earth and Planetary Science Letters, v. 116, p. 63–80.

Holm, D.K., Snow, J.K., and Lux, D.R., 1992, Thermal and barometric constraints on the intrusive and unroofing history of the Black Mountains—Implications for timing, initial

dip, and kinematics of detachment faulting in the Death Valley region, California: Tectonics, v. 11, p. 507–522.

House, M.A., Farley, K.A., and Kohn, B.P., 1999, An empirical test of helium diffusion in apatite; borehole data from the Otway Basin, Australia: Earth and Planetary Science Letters, v. 170, p. 463-474.

Ketcham, R.A., 2005, Forward and inverse modeling of low temperature thermochronometry data, Reviews in Mineralogy and Geochemistry, v. 58, p. 275-314.

Lanphere, M.A., 1962, I. Geology of the Wildrose area, Panamint Range, California; II. Geochronologic studies in Death Valley-Mojave Desert region, California [Ph.D. thesis]: Pasadena, California Institute of Technology.

Reiners, P.W., Farley, K.A., and Hickes, H.J., 2002, He diffusion and (U-Th)/He thermochronometry of zircon: Initial results from Fish Canyon Tuff and Gold Butte: Tectonophysics, v. 349, p. 247–308.

Stockli, D. F., Farley, K. A., and Dumitru, T. A., 2000, Calibration of the apatite (U-Th)/He thermochronometer on an exhumed fault block, White Mountains, California: Geology, v. 28, p. 983–986, 2000.

Wolf, R.A., Farley, K.A., and Silver, L.T., 1996, Helium diffusion and low temperature thermochronometry of apatite: Geochimica et Cosmochimica Acta, v. 60, p. 4231-4240.

Wolf, R.A., Farley, K.A., and Kass, D.M., 1998, Modeling of the temperature sensitivity of the apatite (U-Th)/He thermochronometer: Chemical Geology, v. 148, p. 105-114.

Wolfe, M.R. and Stockli, D.F., 2010, Zircon (U-Th)/He thermochronometry in the KTB drillhole, Germany, and its implications for bulk He diffusion kinetics in zircon, Earth and Planetary Science Letters v. 295, p. 69-82.

Table SD4.1. Summary of (U-Th)/He data

Sample	Longitude	Latitude	Elevation (m)	Mass (µg)	Ft*	U (ppm)	Th (ppm)	Sm (ppm)	Th/U	He (nmol/g)	Mean age (Ma)	St.Dev.† (Ma)	Replicates
Sheep Canyon zircon													
GV-2	-116.63310	36.077115	1463	0.77	0.55	384.5	112.3	n.m.	0.38	0.86	9.26	3.86	5
SC-9	-116.64328	36.072439	1341	10.18	0.78	317.6	124.0	n.m.	0.39	11.06	7.31	0.86	5
GV-1	-116.62521	36.070510	1341	6.29	0.75	389.9	295.4	n.m.	0.75	8.53	7.48	0.95	5
SC-8	-116.64804	36.075145	1189	6.44	0.72	742.5	2254.2	n.m.	2.85	19.51	8.74	0.71	4
SC-10	-116.65775	36.074620	1006	3.55	0.69	461.8	398.6	n.m.	0.82	5.02	6.29	1.12	2
SC-11	-116.65775	36.074620	1006	2.61	0.64	1146.6	1150.3	n.m.	0.85	3.94	6.18	0.85	2
SC-1	-116.66641	36.078071	890	5.14	0.75	161.7	156.1	n.m.	0.97	2.88	6.78	1.03	4
SC-2	-116.68060	36.079366	707	12.27	0.77	172.8	159.9	n.m.	0.91	5.46	5.62	0.45	4
SC-3	-116.69049	36.079115	579	3.49	0.70	507.3	167.7	n.m.	0.49	3.04	5.55	0.70	5
SC-5a	-116.70257	36.083810	329	6.41	0.71	428.4	314.7	n.m.	0.79	5.97	5.43	0.59	5
SC-5b	-116.70257	36.083810	329	7.18	0.74	100.0	86.0	n.m.	0.84	1.74	4.61	0.77	5
SC-6	-116.70727	36.082991	256	2.53	0.66	179.5	48.1	n.m.	0.55	1.03	5.96	0.93	5
SC-7	-116.71988	36.083660	122	2.06	0.60	499.1	138.9	n.m.	0.21	3.11	5.50	1.00	3
Black Mountains range front apatite													
12BM01	-116.76033	36.286186	328	0.52	0.52	16.3	0.8	16.9	0.05	0.07	1.5	-	1
12BM07	-116.76115	36.177779	132	0.68	0.51	11.9	24.2	29.8	2.22	0.15	2.8	2.2	4
12BM09	-116.75526	36.035909	8	2.39	0.66	6.7	4.0	49.4	0.89	0.05	1.6	1.1	4
Black Mountains range front zircon													
12BM02	-116.76127	36.287203	339	4.25	0.74	612.7	51.8	0.6	0.09	11.84	4.8	0.6	3
12BM03	-116.76217	36.286247	246	3.21	0.72	328.1	48.2	0.6	0.15	6.78	5.1	0.3	3
12BM04	-116.77231	36.254035	21	3.56	0.72	57.5	24.5	0.5	0.51	1.13	4.2	2.8	4
12BM05	-116.76184	36.233222	73	16.27	0.83	341.6	68.0	0.5	0.19	6.77	4.2	0.2	3
12BM06	-116.77074	36.220020	38	10.45	0.79	166.7	269.0	1.0	1.61	4.55	4.8	0.5	3
12BM07	-116.76115	36.177779	132	5.64	0.75	378.0	507.1	1.9	1.12	11.38	5.5	0.3	3
12BM08	-116.73845	36.114283	-4	4.54	0.74	394.5	79.6	0.5	0.22	7.01	4.3	0.5	3
12BM09	-116.75526	36.035909	8	18.06	0.82	38.5	56.7	0.8	1.46	0.76	3.3	0.3	3
Confidence Wash zircon													
12CW01	-116.51200	35.886307	479	3.22	0.72	655.1	71.9	0.8	0.13	22.11	8.5	1.4	3
12CW02	-116.51421	35.880763	532	4.92	0.75	482.0	72.9	1.5	0.15	14.78	7.4	0.4	3
12CW03	-116.52175	35.878388	417	6.06	0.77	462.3	103.6	1.7	0.22	15.86	7.8	0.8	5
12CW04	-116.53210	35.875175	322	11.61	0.81	538.1	72.5	1.2	0.13	16.95	6.8	0.6	3
12CW05	-116.53593	35.871230	313	7.21	0.78	614.1	85.7	1.3	0.14	19.77	7.3	0.9	5
12CW06	-116.53961	35.868324	242	4.67	0.75	582.1	93.0	1.1	0.15	14.78	6.1	0.2	3
12CW07	-116.54398	35.866795	243	5.21	0.75	543.2	111.1	13.4	0.19	13.42	5.8	0.5	3
12CW08	-116.54624	35.864399	214	9.86	0.79	603.3	75.8	0.9	0.15	15.00	5.8	0.6	3
12CW09	-116.54991	35.862237	163	3.95	0.74	546.6	66.6	0.7	0.12	12.16	5.4	0.2	3

(continued)

Table SD4.1. Summary of (U-Th)/He data (continued)

Sample	Longitude	Latitude	Elevation (m)	Mass (µg)	Ft*	U (ppm)	Th (ppm)	Sm (ppm)	Th/U	He (nmol/g)	Mean age (Ma)	St.Dev.† (Ma)	Replicates
Surprise Canyon apatite													
12SC01	-117.13505	36.115919	1446	1.72	0.66	7.8	2.2	3.9	0.28	0.12	4.1	1.4	4
12SC04	-117.15092	36.113839	1230	1.33	0.63	34.0	2.4	36.5	0.07	0.43	3.8	0.4	3
12SC05	-117.15494	36.114349	1172	1.91	0.66	44.0	13.0	68.2	0.30	0.83	4.5	0.6	4
12SC08	-117.17406	36.112891	819	0.84	0.55	1.4	8.1	3.1	5.96	0.03	2.8	-	1
12SC09	-117.18034	36.110764	754	1.22	0.60	2.4	3.0	3.1	1.35	0.04	3.8	0.4	3
12SC10	-117.18618	36.106805	724	1.14	0.59	25.1	3.2	15.7	0.15	0.25	3.1	0.5	4
12SC12	-117.19570	36.103297	597	0.68	0.53	16.9	19.8	11.9	1.34	0.20	3.3	0.5	2
12SC13	-117.19915	36.101602	584	0.88	0.57	16.0	7.9	24.0	0.49	0.14	2.6	0.5	3
Surprise Canyon zircon													
12SC01	-117.13505	36.115919	1446	4.20	0.74	100.7	40.0	0.5	0.40	11.25	33.5	7.6	2
12SC04	-117.15092	36.113839	1230	5.17	0.77	337.2	43.0	0.5	0.14	44.08	30.6	1.7	4
12SC05	-117.15494	36.114349	1172	3.51	0.73	526.6	67.8	0.7	0.13	51.46	23.7	2.1	4
12SC09	-117.18034	36.110764	754	3.72	0.71	124.9	79.1	1.2	0.65	7.19	13.0	8.0	2
12SC10	-117.18618	36.106805	724	2.82	0.70	522.5	84.4	0.7	0.18	19.74	9.6	5.2	4
12SC12	-117.19570	36.103297	597	2.25	0.69	109.4	56.7	0.8	0.53	2.96	6.4	1.0	3
12SC13	-117.19915	36.101602	584	4.11	0.74	856.7	125.5	0.5	0.15	28.70	8.5	2.9	5
Pleasant Canyon apatite													
12PC01	-117.11634	36.031701	1589	1.05	0.59	34.5	25.5	75.0	0.74	2.57	19.4	0.3	2
12PC03	-117.12819	36.031582	1451	1.01	0.58	35.9	17.8	54.3	0.50	0.59	4.7	1.2	3
12PC05	-117.15183	36.029646	1150	0.78	0.56	18.3	9.7	25.3	0.78	0.28	4.8	1.4	3
12PC06	-117.15756	36.029400	1085	0.59	0.52	7.0	6.8	4.4	0.94	0.08	3.5	0.6	2
12PC09	-117.17460	36.032835	877	1.68	0.61	1.0	3.8	21.5	3.85	0.01	1.5	-	1
12PC10	-117.18268	36.034612	799	0.93	0.54	19.7	51.6	17.0	2.66	0.26	2.7	0.1	2
Pleasant Canyon zircon													
12PC02	-117.12261	36.032303	1550	2.75	0.71	300.2	92.4	1.9	0.31	51.15	41.6	2.1	3
12PC03	-117.12819	36.031582	1451	5.52	0.76	199.6	75.0	1.1	0.41	38.35	44.9	6.3	3
12PC04	-117.13260	36.033366	1422	3.35	0.73	391.6	167.6	3.3	0.55	77.85	45.3	4.9	3
12PC09	-117.17460	36.032835	877	3.71	0.73	389.7	66.8	0.7	0.19	19.59	12.2	2.4	5
12PC10	-117.18268	36.034612	799	2.93	0.69	135.5	94.7	1.8	0.72	4.28	7.5	1.9	6

Note: See Appendix 4.1 for discussion of analytical procedures and errors
*Ft is the alpha ejection correction of Farley et al. (1996)
†St. Dev.—standard deviation

Table SD4.2. (U-Th)/He data

Name	W_1	W_2	L_1	L_2	Mass (µg)	Ft*	U (ppm)	Th (ppm)	Th/U	He (nmol/g)	Corrected Age [Ma]	Error (Ma)	Mean age (Ma)	St.Dev.† (Ma)
SC-1	**84.50**	**82.25**	**160.50**	**156.50**	**5.14**	**0.75**	**161.73**	**156.08**	**0.97**	**2.88**	-	**0.54**	**6.8**	**1.0**
SC-1-1	82.00	88.00	170.00	170.00	5.70	0.76	131.8	178.9	1.36	2.88	7.1	0.6		
SC-1-2	81.00	80.00	164.00	147.00	4.69	0.74	275.4	254.6	0.92	5.15	8.1	0.6		
SC-1-3	94.00	81.00	168.00	167.00	5.93	0.76	120.1	83.1	0.69	2.02	5.9	0.5		
SC-1-4	81.00	80.00	140.00	142.00	4.25	0.74	119.6	107.7	0.9	1.49	6.0	0.5		
SC-1-5	*46.00*	*50.00*	*94.00*	*97.00*	*1.02*	*0.59*	*265.8*	*288.0*	*1.08*	*1.21*	*11.1*	*0.9*		
SC-2	**95.75**	**98.00**	**214.50**	**211.00**	**12.27**	**0.77**	**172.80**	**159.88**	**0.91**	**5.46**	-	**0.45**	**5.6**	**0.5**
SC-2-1	74.00	83.00	214.00	214.00	6.11	0.75	142.8	114.5	0.8	2.60	6.1	0.5		
SC-2-2	78.00	84.00	218.00	215.00	6.60	0.76	195.5	258.1	1.32	3.57	5.1	0.4		
SC-2-3	*98.00*	*130.00*	*177.00*	*188.00*	*10.81*	*0.81*	*97.4*	*63.2*	*0.65*	*1.46*	*2.7*	*0.2*		
SC-2-4	147.00	162.00	302.00	302.00	33.44	0.86	143.9	100.4	0.7	14.05	5.4	0.4		
SC-2-5	84.00	63.00	124.00	113.00	2.92	0.71	209.0	166.5	0.8	1.61	5.8	0.5		
SC-3	**69.60**	**66.00**	**154.00**	**151.40**	**3.49**	**0.70**	**507.30**	**167.72**	**0.49**	**3.04**	**5.55**	**0.44**	**5.5**	**0.7**
SC-3-1	74.00	66.00	134.00	125.00	2.94	0.71	183.8	51.5	0.28	1.18	5.3	0.4		
SC-3-2	59.00	58.00	148.00	148.00	2.36	0.68	1399.0	41.3	0.03	5.47	4.5	0.4		
SC-3-3	91.00	87.00	187.00	188.00	6.90	0.77	214.4	72.7	0.34	3.88	5.8	0.5		
SC-3-4	57.00	51.00	141.00	137.00	1.88	0.65	503.3	476.8	0.95	2.32	5.7	0.5		
SC-3-5	67.00	68.00	160.00	159.00	3.38	0.71	236.0	196.3	0.83	2.35	6.4	0.5		
SC-5a	**76.00**	**74.60**	**173.60**	**173.40**	**6.41**	**0.71**	**428.38**	**314.72**	**0.79**	**5.97**	-	**0.43**	**5.4**	**0.6**
SC-5a-1	136.00	133.00	244.00	247.00	20.65	0.84	281.8	121.7	0.43	16.38	5.6	0.4		
SC-5a-2	73.00	72.00	178.00	175.00	4.31	0.73	715.5	138.5	0.19	8.15	6.4	0.5		
SC-5a-3	44.00	52.00	124.00	122.00	1.31	0.60	494.1	611.1	1.24	1.45	5.3	0.4		
SC-5a-4	75.00	67.00	169.00	172.00	3.98	0.72	248.7	216.7	0.87	2.27	4.8	0.4		
SC-5a-5	52.00	49.00	153.00	151.00	1.80	0.63	401.8	485.6	1.21	1.61	5.0	0.4		
SC-5b	**73.80**	**81.20**	**220.00**	**221.40**	0.00 **7.18**	**0.74**	**100.02**	**85.98**	**0.84**	**1.74**	-	**0.37**	**4.6**	**0.8**
SC-5b-1	101.00	118.00	308.00	311.00	17.15	0.82	100.9	84.8	0.84	4.25	4.6	0.4		
SC-5b-2	75.00	80.00	274.00	279.00	7.71	0.76	94.1	80.4	0.85	2.03	5.7	0.5		
SC-5b-3	61.00	66.00	200.00	199.00	3.73	0.70	171.9	158.1	0.92	1.49	5.0	0.4		
SC-5b-4	51.00	62.00	148.00	149.00	2.18	0.66	62.0	55.1	0.89	0.22	3.8	0.3		
SC-5b-5	81.00	80.00	170.00	169.00	5.11	0.75	71.2	51.5	0.72	0.68	3.9	0.3		
SC-6	**56.00**	**60.20**	**154.80**	**153.20**	**2.53**	**0.66**	**179.46**	**48.08**	**0.55**	**1.03**	-	**0.48**	**6.0**	**0.9**
SC-6-1	52.00	47.00	171.00	168.00	1.93	0.63	127.3	92.7	0.73	0.66	6.7	0.5		
SC-6-2	66.00	68.00	173.00	173.00	3.61	0.71	66.2	58.9	0.89	0.69	6.2	0.5		
SC-6-3	48.00	61.00	131.00	136.00	1.82	0.64	37.1	35.3	0.95	0.13	4.6	0.4		
SC-6-4	42.00	53.00	131.00	129.00	1.35	0.61	432.9	29.7	0.07	1.08	5.5	0.4		
SC-6-5	72.00	72.00	168.00	160.00	3.95	0.73	233.8	23.8	0.1	2.58	6.9	0.6		

Name	W_1	W_2	L_1	L_2	Mass (µg)	Ft*	U (ppm)	Th (ppm)	Th/U	He (nmol/g)	Corrected Age [Ma]	Error (Ma)	Mean age (Ma)	St.Dev.† (Ma)
SC-7	**52.67**	**57.33**	**111.00**	**110.33**	**2.06**	**0.60**	**499.13**	**138.90**	**0.21**	**3.11**	-	**0.44**	**5.5**	**1.0**
SC-7-1	81.00	95.00	133.00	131.00	4.72	0.75	878.1	348.1	0.4	8.55	4.6	0.4		
SC-7-2	42.00	42.00	122.00	122.00	1.00	0.57	327.8	44.9	0.14	0.56	5.3	0.4		
SC-7-3	35.00	35.00	78.00	78.00	0.44	0.48	291.5	23.7	0.08	0.23	6.6	0.5		
SC-7-4	*32.00*	*48.00*	*123.00*	*124.00*	*0.88*	*0.54*	*363.8*	*91.4*	*0.25*	*23.00*	*225.0*	*18.0*		
SC-7-5	*54.00*	*57.00*	*108.00*	*106.00*	*1.53*	*0.64*	*-2.2*	*-0.8*	*0.38*	*0.01*	*-9.7*	*-0.8*		
SC-8	**72.75**	**90.75**	**160.00**	**159.25**	**6.44**	**0.72**	**742.45**	**2254.18**	**2.85**	**19.51**	-	**0.70**	**8.7**	**0.7**
SC-8-1	97.00	152.00	262.00	257.00	17.79	0.82	436.0	647.4	1.48	38.78	8.3	0.7		
SC-8-3	69.00	69.00	134.00	132.00	2.94	0.69	788.8	2617.8	3.32	13.31	8.5	0.7		
SC-8-4	54.00	70.00	130.00	131.00	2.29	0.66	893.7	2816.7	3.15	12.63	9.8	0.8		
SC-8-5	71.00	72.00	114.00	117.00	2.75	0.69	851.3	2934.8	3.45	13.30	8.3	0.7		
SC-9	**94.00**	**96.20**	**221.20**	**223.00**	**10.18**	**0.78**	**317.64**	**124.00**	**0.39**	**11.06**	-	**0.59**	**7.3**	**0.9**
SC-9-1	99.00	108.00	256.00	257.00	12.75	0.81	262.6	103.6	0.39	10.87	6.8	0.5		
SC-9-2	87.00	90.00	200.00	201.00	7.30	0.77	362.2	138.0	0.38	8.77	7.2	0.6		
SC-9-3	139.00	123.00	244.00	249.00	19.60	0.84	325.0	59.0	0.18	25.12	8.3	0.7		
SC-9-4	79.00	85.00	228.00	233.00	7.20	0.76	219.5	111.0	0.51	5.88	8.0	0.6		
SC-9-5	66.00	75.00	178.00	175.00	4.06	0.72	418.9	208.4	0.5	4.65	6.2	0.5		
SC-10	**71.00**	**70.50**	**139.00**	**137.00**	**3.55**	**0.69**	**461.75**	**398.60**	**0.82**	**5.02**	-	**0.50**	**6.3**	**1.1**
SC-10-1	94.00	87.00	145.00	146.00	5.53	0.76	528.4	582.1	1.1	8.35	5.5	0.4		
SC-10-2	*50.00*	*56.00*	*104.00*	*105.00*	*1.36*	*0.63*	*212.9*	*125.2*	*0.59*	*26.40*	*231.0*	*18.5*		
SC-10-3	48.00	54.00	133.00	128.00	1.57	0.63	395.1	215.1	0.54	1.70	7.1	0.6		
SC-10-4	*63.00*	*58.00*	*105.00*	*106.00*	*1.79*	*0.66*	*308.4*	*226.1*	*0.73*	*11.60*	*49.8*	*4.0*		
SC-10-5	*33.00*	*47.00*	*103.00*	*105.00*	*0.75*	*0.54*	*950.2*	*383.0*	*0.4*	*6.31*	*27.8*	*2.2*		
SC-11	**56.50**	**57.50**	**139.00**	**140.50**	**2.61**	**0.64**	**1146.55**	**1150.25**	**0.85**	**3.94**	**6.18**	**0.49**	**6.2**	**0.9**
SC-11-1	71.00	74.00	182.00	181.00	4.43	0.73	344.9	212.4	0.62	4.71	6.8	0.5		
SC-11-2	*46.00*	*55.00*	*118.00*	*108.00*	*1.33*	*0.62*	*156.3*	*115.9*	*0.74*	*1.05*	*12.8*	*1.0*		
SC-11-3	*39.00*	*47.00*	*104.00*	*103.00*	*0.88*	*0.56*	*92.7*	*73.4*	*0.79*	*2.02*	*67.9*	*5.4*		
SC-11-4	*37.00*	*46.00*	*97.00*	*95.00*	*0.76*	*0.54*	*153.9*	*128.8*	*0.84*	*3.25*	*78.0*	*6.2*		
SC-11-5	42.00	41.00	96.00	100.00	0.78	0.55	1948.2	2088.1	1.07	3.17	5.6	0.4		
GV-1	**79.60**	**84.20**	**194.40**	**193.60**	**6.29**	**0.75**	**389.92**	**295.38**	**0.75**	**8.53**	-	**0.60**	**7.5**	**0.9**
GV-1-1	89.00	102.00	279.00	277.00	11.74	0.80	280.2	149.6	0.53	14.53	9.1	0.7		
GV-1-2	68.00	94.00	205.00	206.00	6.11	0.75	362.9	264.9	0.73	7.59	7.2	0.6		
GV-1-3	81.00	78.00	186.00	184.00	5.44	0.75	571.4	359.5	0.63	10.56	7.3	0.6		
GV-1-4	79.00	70.00	173.00	174.00	4.46	0.73	320.0	215.2	0.67	4.32	6.6	0.5		
GV-1-5	81.00	77.00	129.00	127.00	3.71	0.73	415.1	487.7	1.17	5.68	7.3	0.6		

Name	W_1	W_2	L_1	L_2	Mass (µg)	Ft*	U (ppm)	Th (ppm)	Th/U	He (nmol/g)	Corrected Age [Ma]	Error (Ma)	Mean age (Ma)	St.Dev.† (Ma)
GV-2	**41.80**	**41.20**	**96.00**	**96.00**	**0.77**	**0.55**	**384.48**	**112.28**	**0.38**	**0.86**	-	**0.74**	**9.3**	**3.9**
GV-2-1	50.00	41.00	93.00	92.00	0.88	0.57	183.8	169.8	0.92	0.44	7.1	0.6		
GV-2-2	42.00	46.00	97.00	96.00	0.87	0.57	350.6	180.6	0.52	1.67	15.8	1.3		
GV-2-3	34.00	45.00	79.00	87.00	0.59	0.52	384.9	101.7	0.26	0.65	9.5	0.8		
GV-2-4	42.00	35.00	84.00	82.00	0.57	0.52	484.7	46.1	0.1	0.58	7.4	0.6		
GV-2-5	41.00	39.00	127.00	123.00	0.93	0.56	518.4	63.2	0.12	0.96	6.4	0.5		
12BM01	**91.33**	**53.23**	**0.52**	**0.52**	**16.34**	**0.78**	**16.85**	**16.60**	**0.05**	**0.07**	-	**0.09**	**1.5**	-
12BM01-1	*87.05*	*59.94*	*0.63*	*0.57*	*5.8*	*-1.1*	*48.2*	*5.8*	*-0.18*	*0.01*	*0.4*	*0.0*		
12BM01-2	91.33	53.23	0.52	0.52	16.3	0.8	16.9	16.6	0.05	0.07	1.5	0.1		
12BM01-3	*67.43*	*66.51*	*0.60*	*0.58*	*7.3*	*-1.7*	*38.9*	*7.1*	*-0.24*	*0.03*	*1.3*	*0.1*		
12BM01-4	*95.75*	*62.38*	*0.75*	*0.36*	*1.0*	*-1.3*	*26.5*	*0.8*	*-1.32*	*0.04*	*22.7*	*1.4*		
12BM07	**104.07**	**57.05**	**0.68**	**0.51**	**11.93**	**24.23**	**29.76**	**17.66**	**2.22**	**0.15**	-	**0.17**	**2.8**	**2.2**
12BM07-1	132.61	52.16	0.73	0.50	2.2	6.6	28.6	3.9	2.97	0.03	3.0	0.2		
12BM07-2	80.91	61.51	0.62	0.52	16.6	39.2	32.4	25.8	2.37	0.43	5.9	0.4		
12BM07-3	133.03	59.19	0.94	0.55	12.7	24.1	25.6	18.4	1.89	0.04	0.7	0.0		
12BM07-4	69.73	55.35	0.43	0.47	16.2	27.0	32.3	22.6	1.66	0.11	1.9	0.1		
12BM09	**179.40**	**80.96**	**2.39**	**0.66**	**6.70**	**4.03**	**49.44**	**7.87**	**0.89**	**0.05**	-	**0.10**	**1.6**	**1.1**
12BM09-1	169.62	96.09	3.15	0.71	6.1	2.4	34.1	6.8	0.40	0.08	2.8	0.2		
12BM09-2	170.30	83.92	2.41	0.68	9.3	2.8	49.7	10.2	0.30	0.08	2.1	0.1		
12BM09-3	168.68	67.21	1.53	0.60	2.1	4.6	52.4	3.4	2.16	0.01	0.5	0.0		
12BM09-4	209.01	76.63	2.47	0.66	9.3	6.3	61.6	11.0	0.69	0.04	0.9	0.1		
12BM02	**191.35**	**69.11**	**4.25**	**0.74**	**612.74**	**51.83**	**0.64**	**624.68**	**0.09**	**11.84**	-	**0.39**	**4.8**	**0.6**
z12BM02-1	192.73	71.28	4.55	0.75	441.6	24.4	0.3	447.2	0.06	9.89	5.5	0.4		
z12BM02-2	206.06	68.17	4.45	0.74	833.2	53.0	0.7	845.4	0.06	14.84	4.4	0.4		
z12BM02-3	175.27	67.89	3.76	0.73	563.4	78.1	0.9	581.4	0.14	10.79	4.7	0.4		
12BM03	**157.77**	**66.10**	**3.21**	**0.72**	**328.12**	**48.25**	**0.58**	**339.22**	**0.15**	**6.78**	-	**0.41**	**5.1**	**0.3**
z12BM03-1	151.93	68.85	3.35	0.73	461.4	35.2	0.4	469.5	0.08	9.94	5.4	0.4		
z12BM03-2	155.62	61.61	2.75	0.71	340.1	87.3	1.0	360.2	0.26	6.57	4.8	0.4		
z12BM03-3	*207.96*	*68.45*	*4.53*	*0.74*	*1192.2*	*242.9*	*1.8*	*1248.2*	*0.20*	*1.16*	*0.2*	*0.0*		
z12BM03-4	165.77	67.85	3.55	0.73	182.9	22.3	0.3	188.0	0.12	3.84	5.2	0.4		
z12BM03-5	*137.36*	*61.20*	*2.39*	*0.70*	*267.5*	*30.8*	*0.2*	*274.6*	*0.12*	*6.85*	*6.6*	*0.5*		
12BM04	**155.76**	**68.52**	**3.56**	**0.72**	**57.48**	**24.52**	**0.48**	**63.13**	**0.51**	**1.13**	-	**0.34**	**4.2**	**2.8**
z12BM04-1	171.83	81.37	5.29	0.76	67.1	38.5	0.5	75.9	0.57	1.04	3.3	0.3		
z12BM04-2	150.45	72.70	3.70	0.74	70.3	18.8	0.3	74.7	0.27	1.07	3.6	0.3		
z12BM04-3	127.16	53.31	1.68	0.65	27.6	26.5	0.6	33.7	0.96	0.21	1.7	0.1		
z12BM04-4	173.59	66.70	3.59	0.73	64.9	14.2	0.5	68.2	0.22	2.23	8.3	0.7		

Name	W_1	W_2	L_1	L_2	Mass (µg)	Ft*	U (ppm)	Th (ppm)	Th/U	He (nmol/g)	Corrected Age [Ma]	Error (Ma)	Mean age (Ma)	St.Dev.[†] (Ma)
z12BM04-5	*131.64*	*80.84*	*4.00*	*0.75*	*231.3*	*95.7*	*0.9*	*253.3*	*0.41*	*63.58*	*61.8*	*4.9*		
12BM05	**260.41**	**113.75**	**16.27**	**0.83**	**341.56**	**67.97**	**0.53**	**357.21**	**0.19**	**6.77**	-	**0.34**	**4.2**	**0.2**
z12BM05-1	274.38	121.22	18.75	0.84	369.8	87.9	0.6	390.1	0.24	7.26	4.1	0.3		
z12BM05-2	279.10	126.72	20.84	0.85	182.0	27.3	0.3	188.2	0.15	3.53	4.1	0.3		
z12BM05-3	227.76	93.32	9.22	0.80	472.9	88.8	0.7	493.3	0.19	9.51	4.5	0.4		
12BM06	**250.91**	**93.08**	**10.45**	**0.79**	**166.66**	**268.96**	**1.00**	**228.58**	**1.61**	**4.55**	-	**0.38**	**4.8**	**0.5**
z12BM06-1	300.37	101.18	14.30	0.81	101.6	128.4	0.8	131.2	1.26	2.68	4.6	0.4		
z12BM06-2	254.20	95.43	10.76	0.80	122.8	242.8	1.7	178.7	1.98	4.13	5.3	0.4		
z12BM06-3	198.17	82.62	6.29	0.76	275.6	435.6	0.6	375.8	1.58	6.83	4.4	0.4		
12BM07	**198.67**	**77.91**	**5.64**	**0.75**	**377.97**	**507.08**	**1.87**	**494.71**	**1.12**	**11.38**	-	**0.44**	**5.5**	**0.3**
z12BM07-1	184.39	73.53	4.64	0.74	306.5	318.0	1.3	379.7	1.04	8.84	5.8	0.5		
z12BM07-2	209.80	75.33	5.54	0.75	718.2	1121.8	3.3	976.4	1.56	22.52	5.7	0.5		
z12BM07-3	201.83	84.86	6.76	0.77	109.3	81.5	1.0	128.0	0.75	2.77	5.2	0.4		
12BM08	**167.49**	**73.95**	**4.54**	**0.74**	**394.53**	**79.63**	**0.47**	**412.86**	**0.22**	**7.01**	-	**0.35**	**4.3**	**0.5**
z12BM08-1	193.53	90.80	7.42	0.79	166.0	38.1	0.3	174.8	0.23	3.63	4.9	0.4		
z12BM08-2	181.21	66.08	3.68	0.73	104.6	26.1	0.5	110.6	0.25	1.67	3.8	0.3		
z12BM08-3	127.72	64.98	2.51	0.71	913.0	174.7	0.7	953.2	0.19	15.74	4.3	0.3		
12BM09	**351.74**	**103.86**	**18.06**	**0.82**	**38.51**	**56.71**	**0.81**	**51.57**	**1.46**	**0.76**	-	**0.26**	**3.3**	**0.3**
z12BM09-1	370.37	98.53	16.72	0.81	33.3	42.3	0.8	43.1	1.27	0.65	3.4	0.3		
z12BM09-2	313.89	93.29	12.70	0.80	53.6	84.2	1.0	73.0	1.57	1.09	3.5	0.3		
z12BM09-3	370.97	119.77	24.75	0.84	28.6	43.6	0.6	38.6	1.53	0.52	3.0	0.2		
12CW01	**155.93**	**65.48**	**3.22**	**0.72**	**655.07**	**71.94**	**0.76**	**671.63**	**0.13**	**22.11**	**8.55**	**0.68**	**8.5**	**1.4**
z12CW01-1	*212.21*	*67.53*	*4.50*	*0.74*	*385.5*	*47.6*	*0.8*	*396.4*	*0.12*	*6.95*	*4.4*	*0.4*		
z12CW01-2	*133.55*	*66.59*	*2.75*	*0.71*	*526.6*	*173.3*	*1.2*	*566.5*	*0.33*	*39.55*	*18.1*	*1.4*		
z12CW01-3	149.01	64.65	2.90	0.72	555.6	65.7	0.7	570.7	0.12	15.47	7.0	0.6		
z12CW01-4	139.05	57.36	2.13	0.69	1010.5	72.1	0.7	1027.1	0.07	34.69	9.1	0.7		
z12CW01-5	*129.95*	*56.42*	*1.92*	*0.68*	*390.4*	*62.7*	*0.9*	*404.8*	*0.16*	*39.74*	*26.7*	*2.1*		
z12CW01-6	179.74	74.42	4.63	0.75	399.2	78.1	0.9	417.2	0.20	16.17	9.6	0.8		
12CW02	**205.03**	**71.53**	**4.92**	**0.75**	**481.98**	**72.95**	**1.55**	**498.78**	**0.15**	**14.78**	-	**0.59**	**7.4**	**0.4**
z12CW02-1	236.93	72.85	5.85	0.76	603.9	97.9	1.5	626.4	0.16	17.78	6.9	0.6		
z12CW02-2	189.16	77.05	5.22	0.76	321.0	49.1	1.3	332.3	0.15	10.25	7.5	0.6		
z12CW02-3	189.01	64.68	3.68	0.73	521.1	71.8	1.8	537.6	0.14	16.31	7.7	0.6		
12CW03	**200.20**	**80.27**	**6.06**	**0.77**	**462.35**	**103.60**	**1.73**	**486.21**	**0.22**	**15.86**	-	**0.62**	**7.8**	**0.8**
z12CW03-1	207.45	85.99	7.13	0.78	606.2	162.0	0.7	643.5	0.27	23.80	8.8	0.7		

Name	W_1	W_2	L_1	L_2	Mass (µg)	Ft*	U (ppm)	Th (ppm)	Th/U	He (nmol/g)	Corrected Age [Ma]	Error (Ma)	Mean age (Ma)	St.Dev.† (Ma)
z12CW03-2	222.54	82.43	7.03	0.78	381.2	69.6	0.6	397.2	0.18	11.00	6.6	0.5		
z12CW03-3	199.17	79.21	5.81	0.77	476.1	84.9	1.8	495.6	0.18	16.41	8.0	0.6		
z12CW03-4	211.07	79.55	6.21	0.77	471.4	138.5	4.6	503.3	0.29	15.51	7.4	0.6		
z12CW03-5	160.76	74.15	4.11	0.75	376.9	63.0	0.9	391.4	0.17	12.60	8.0	0.6		
12CW04	**244.61**	**100.87**	**11.61**	**0.81**	**538.13**	**72.48**	**1.24**	**554.83**	**0.13**	**16.95**	-	**0.55**	**6.8**	**0.6**
z12CW04-1	254.73	87.90	9.15	0.79	597.1	80.7	1.9	615.7	0.14	18.21	6.9	0.6		
z12CW04-2	235.81	108.07	12.81	0.82	697.2	95.4	1.1	719.2	0.14	23.61	7.4	0.6		
z12CW04-3	243.30	106.63	12.86	0.82	320.0	41.4	0.7	329.6	0.13	9.01	6.2	0.5		
12CW05	**220.76**	**83.32**	**7.21**	**0.78**	**614.15**	**85.72**	**1.33**	**633.89**	**0.14**	**19.77**	-	**0.58**	**7.3**	**0.9**
z12CW05-1	266.97	82.29	8.41	0.78	852.9	109.0	2.5	878.0	0.13	31.84	8.6	0.7		
z12CW05-2	219.34	71.75	5.25	0.75	563.2	134.4	1.3	594.1	0.24	17.69	7.3	0.6		
z12CW05-3	194.35	76.35	5.27	0.76	737.1	60.9	1.3	751.1	0.08	20.82	6.7	0.5		
z12CW05-4	191.75	90.98	7.38	0.79	549.4	74.4	0.6	566.5	0.14	18.10	7.5	0.6		
z12CW05-5	231.37	95.25	9.76	0.80	368.2	50.0	1.0	379.7	0.14	10.39	6.3	0.5		
12CW06	**184.38**	**73.28**	**4.67**	**0.75**	**582.05**	**92.96**	**1.07**	**603.46**	**0.15**	**14.78**	**6.06**	**0.48**	**6.1**	**0.2**
z12CW06-1	171.58	76.63	4.69	0.76	819.4	158.1	1.8	855.8	0.19	21.05	6.0	0.5		
z12CW06-2	177.30	64.33	3.41	0.72	525.6	64.7	0.8	540.5	0.12	13.30	6.3	0.5		
z12CW06-3	204.27	78.87	5.91	0.77	401.2	56.1	0.6	414.1	0.14	10.00	5.8	0.5		
12CW07	**208.42**	**73.60**	**5.21**	**0.75**	**543.23**	**111.07**	**13.44**	**568.87**	**0.19**	**13.42**	-	**0.47**	**5.8**	**0.5**
z12CW07-1	186.93	75.54	4.96	0.76	530.8	86.4	0.9	550.7	0.16	14.33	6.4	0.5		
z12CW07-2	237.70	64.84	4.65	0.73	642.8	187.5	38.0	686.1	0.29	14.87	5.5	0.4		
z12CW07-3	200.62	80.43	6.03	0.77	456.1	59.3	1.4	469.8	0.13	11.06	5.7	0.5		
12CW08	**282.32**	**86.46**	**9.86**	**0.79**	**603.31**	**75.79**	**0.85**	**620.76**	**0.15**	**15.00**	-	**0.46**	**5.8**	**0.6**
z12CW08-1	310.62	90.12	11.73	0.80	417.2	73.8	1.0	434.2	0.18	11.23	6.0	0.5		
z12CW08-2	273.62	84.50	9.08	0.79	463.2	89.8	1.0	483.8	0.19	12.89	6.3	0.5		
z12CW08-3	262.71	84.76	8.78	0.79	929.5	63.8	0.6	944.2	0.07	20.88	5.2	0.4		
12CW09	**171.70**	**70.34**	**3.95**	**0.74**	**546.62**	**66.57**	**0.71**	**561.94**	**0.12**	**12.16**	-	**0.44**	**5.4**	**0.2**
z12CW09-1	169.82	68.24	3.68	0.73	683.1	80.8	0.9	701.7	0.12	15.57	5.6	0.4		
z12CW09-2	151.32	72.06	3.65	0.74	602.4	71.1	0.5	618.8	0.12	12.74	5.2	0.4		
z12CW09-3	193.97	70.71	4.51	0.75	354.3	47.8	0.7	365.3	0.13	8.17	5.6	0.4		
12SC01	**102.59**	**90.00**	**1.72**	**0.66**	**7.80**	**2.21**	**3.95**	**8.32**	**0.28**	**0.12**	-	**0.24**	**4.1**	**1.4**
12SC01-1	112.89	106.43	2.57	0.71	7.1	0.8	4.0	7.4	0.11	0.10	3.6	0.2		
12SC01-2	88.81	82.51	1.22	0.62	6.9	3.3	5.4	7.6	0.48	0.08	3.3	0.2		
12SC01-3	115.35	88.50	1.82	0.67	7.9	1.5	3.1	8.3	0.19	0.10	3.4	0.2		
12SC01-4	93.30	82.57	1.28	0.63	9.2	3.2	3.3	10.0	0.34	0.21	6.1	0.4		

Name	W_1	W_2	L_1	L_2	Mass (µg)	Ft*	U (ppm)	Th (ppm)	Th/U	He (nmol/g)	Corrected Age [Ma]	Error (Ma)	Mean age (Ma)	St.Dev.† (Ma)
12SC04	**97.53**	**79.99**	**1.33**	**0.63**	**33.99**	**2.39**	**36.48**	**34.72**	**0.07**	**0.43**	-	**0.23**	**3.8**	**0.4**
12SC04-1	116.02	94.48	2.09	0.69	23.3	1.6	42.2	23.9	0.07	0.33	3.7	0.2		
12SC04-2	*153.75*	*85.75*	*2.28*	*0.68*	*16.4*	*2.1*	*38.0*	*17.1*	*0.13*	*0.36*	*5.7*	*0.3*		
12SC04-3	89.92	78.32	1.11	0.63	22.1	1.2	28.4	22.5	0.05	0.32	4.2	0.3		
12SC04-4	86.65	67.18	0.79	0.58	56.7	4.3	38.9	57.8	0.08	0.62	3.4	0.2		
12SC05	**130.74**	**83.44**	**1.91**	**0.66**	**43.99**	**12.98**	**68.21**	**47.31**	**0.30**	**0.83**	-	**0.29**	**4.5**	**0.6**
12SC05-1	147.59	104.01	3.21	0.72	35.5	12.5	65.3	38.7	0.35	0.58	3.8	0.2		
12SC05-2	152.29	84.44	2.19	0.68	51.4	7.6	82.9	53.5	0.15	1.02	5.2	0.3		
12SC05-3	136.88	74.82	1.54	0.64	42.9	13.6	68.9	46.3	0.32	0.67	4.2	0.3		
12SC05-4	104.33	82.04	1.41	0.64	39.0	12.1	43.0	42.0	0.31	0.72	4.9	0.3		
12SC05-5	*112.60*	*71.87*	*1.17*	*0.61*	*51.2*	*19.0*	*81.0*	*56.0*	*0.37*	*1.16*	*6.3*	*0.4*		
12SC08	**77.21**	**73.31**	**0.84**	**0.55**	**1.35**	**8.05**	**3.06**	**3.22**	**5.96**	**0.03**	-	**0.17**	**2.8**	-
12SC08-1	*112.44*	*94.14*	*2.01*	*0.65*	*0.5*	*2.2*	*1.2*	*1.0*	*4.54*	*0.09*	*24.3*	*1.5*		
12SC08-2	*99.24*	*84.21*	*1.42*	*0.62*	*1.0*	*3.5*	*0.4*	*1.8*	*3.58*	*-0.05*	*-8.4*	*-0.5*		
12SC08-3	77.21	73.31	0.84	0.55	1.4	8.1	3.1	3.2	5.96	0.03	2.8	0.2		
12SC09	**116.58**	**72.49**	**1.22**	**0.60**	**2.39**	**3.01**	**3.13**	**3.10**	**1.35**	**0.04**	-	**0.23**	**3.8**	**0.4**
12SC09-1	122.05	69.27	1.18	0.59	1.7	3.2	2.5	2.5	1.88	0.03	4.1	0.2		
12SC09-2	97.53	87.66	1.51	0.64	2.5	3.0	3.9	3.2	1.19	0.04	3.4	0.2		
12SC09-3	*117.06*	*69.21*	*1.13*	*0.59*	*1.6*	*2.8*	*2.8*	*2.3*	*1.72*	*0.17*	*22.5*	*1.4*		
12SC09-4	130.16	60.55	0.96	0.56	2.9	2.8	2.9	3.6	0.97	0.04	4.0	0.2		
12SC10	**103.69**	**65.61**	**1.14**	**0.59**	**25.09**	**3.24**	**15.67**	**25.91**	**0.15**	**0.25**	-	**0.17**	**3.1**	**0.5**
12SC10-1	*82.04*	*61.20*	*0.62*	*0.54*	*12.6*	*3.0*	*6.9*	*13.3*	*0.24*	*0.06*	*1.5*	*0.1*		
12SC10-2	96.61	66.51	0.86	0.58	18.3	3.5	16.2	19.2	0.19	0.16	2.7	0.2		
12SC10-3	109.82	67.17	1.00	0.60	26.9	3.4	16.3	27.7	0.13	0.33	3.6	0.2		
12SC10-4	115.61	62.39	0.91	0.58	37.7	3.9	22.7	38.7	0.10	0.33	2.7	0.2		
12SC10-5	114.39	70.79	2.34	0.62	30.0	2.5	16.4	30.6	0.08	0.36	3.5	0.2		
12SC12	**85.07**	**62.48**	**0.68**	**0.53**	**16.85**	**19.85**	**11.86**	**21.48**	**1.34**	**0.20**	-	**0.20**	**3.3**	**0.5**
12SC12-1	93.03	66.17	0.82	0.56	9.8	17.0	7.9	13.8	1.73	0.15	3.7	0.2		
12SC12-2	77.11	58.80	0.54	0.51	23.9	22.6	15.8	29.2	0.95	0.24	3.0	0.2		
12SC12-3	*102.80*	*60.97*	*0.77*	*0.55*	*8.8*	*9.3*	*7.2*	*11.0*	*1.05*	*-0.09*	*-2.9*	*-0.2*		
12SC12-4	*126.71*	*67.03*	*1.15*	*0.58*	*0.4*	*0.6*	*0.1*	*0.5*	*1.66*	*0.09*	*57.4*	*3.4*		
12SC13	**98.86**	**66.13**	**0.88**	**0.57**	**16.01**	**7.85**	**24.01**	**17.94**	**0.49**	**0.14**	**2.58**	**0.15**	**2.6**	**0.5**
12SC13-1	91.42	58.44	0.63	0.53	22.0	11.2	37.4	24.7	0.51	0.15	2.1	0.1		
12SC13-2	106.98	63.80	0.88	0.57	15.7	7.1	22.3	17.5	0.45	0.17	3.1	0.2		
12SC13-3	98.19	76.16	1.15	0.61	10.3	5.2	12.3	11.6	0.50	0.10	2.6	0.2		

Name	W_1	W_2	L_1	L_2	Mass (µg)	Ft*	U (ppm)	Th (ppm)	Th/U	He (nmol/g)	Corrected Age [Ma]	Error (Ma)	Mean age (Ma)	St.Dev.† (Ma)
12SC01	**173.56**	**71.74**	**4.20**	**0.74**	**100.65**	**39.96**	**0.52**	**109.85**	**0.40**	**11.25**	**27.10**	**2.17**	**33.5**	**7.6**
z12SC01-1	182.50	59.08	2.96	0.70	115.4	41.4	0.6	124.9	0.36	14.98	31.6	2.5		
z12SC01-2	*151.18*	*75.90*	*4.05*	*0.74*	*107.1*	*46.3*	*0.6*	*117.8*	*0.43*	*3.70*	*7.8*	*0.6*		
z12SC01-3	187.01	80.25	5.60	0.76	79.5	32.1	0.5	86.9	0.40	15.06	41.9	3.4		
12SC04	**166.21**	**81.69**	**5.17**	**0.77**	**337.18**	**43.03**	**0.53**	**347.09**	**0.14**	**44.08**	-	**2.45**	**30.6**	**1.7**
z12SC04-1	*244.07*	*94.36*	*10.10*	*0.80*	*435.3*	*66.5*	*0.8*	*450.6*	*0.15*	*79.18*	*40.4*	*3.2*		
z12SC04-2	175.15	80.87	5.33	0.77	283.2	32.2	0.5	290.6	0.11	35.04	29.1	2.3		
z12SC04-3	164.45	88.41	5.98	0.78	401.5	33.7	0.5	409.3	0.08	50.48	29.3	2.3		
z12SC04-4	149.26	78.54	4.28	0.76	407.8	44.4	0.7	418.0	0.11	55.54	32.5	2.6		
z12SC04-5	175.98	78.93	5.10	0.76	256.2	61.8	0.4	270.4	0.24	35.27	31.7	2.5		
12SC05	**152.54**	**69.60**	**3.51**	**0.73**	**526.62**	**67.84**	**0.74**	**542.24**	**0.13**	**51.46**	-	**1.89**	**23.7**	**2.1**
z12SC05-1	150.15	79.16	4.38	0.76	346.6	39.1	1.2	355.7	0.11	34.99	24.1	1.9		
z12SC05-2	*149.73*	*68.83*	*3.30*	*0.73*	*224.8*	*73.0*	*0.7*	*241.6*	*0.32*	*13.83*	*14.6*	*1.2*		
z12SC05-3	155.16	64.31	2.98	0.72	518.8	75.6	1.0	536.2	0.15	46.32	22.3	1.8		
z12SC05-4	128.81	61.68	2.28	0.70	953.5	122.2	0.4	981.6	0.13	98.39	26.5	2.1		
z12SC05-5	176.03	73.25	4.39	0.75	287.5	34.5	0.3	295.5	0.12	26.14	21.9	1.7		
12SC09	**185.01**	**63.10**	**3.72**	**0.71**	**124.89**	**79.07**	**1.23**	**143.10**	**0.65**	**7.19**	**9.60**	**0.77**	**13.0**	**8.0**
z12SC09-1	213.91	66.72	4.43	0.73	50.3	35.6	0.9	58.5	0.71	1.70	7.4	0.6		
z12SC09-2	*136.67*	*53.07*	*1.79*	*0.66*	*125.3*	*53.8*	*0.8*	*137.6*	*0.43*	*2.28*	*4.6*	*0.4*		
z12SC09-3	*171.45*	*52.87*	*2.23*	*0.67*	*107.5*	*91.4*	*2.0*	*128.5*	*0.85*	*1.96*	*4.2*	*0.3*		
z12SC09-4	218.03	79.72	6.44	0.77	216.6	135.5	1.3	247.8	0.63	22.80	22.2	1.8		
12SC10	**159.56**	**73.70**	**2.82**	**0.70**	**522.48**	**84.37**	**0.75**	**541.91**	**0.18**	**19.74**	-	**0.77**	**9.6**	**5.2**
z12SC10-1	171.35	69.77	3.88	0.74	321.2	85.8	0.6	340.9	0.27	5.57	4.1	0.3		
z12SC10-2	161.80	70.37	3.73	0.74	365.4	76.5	0.9	383.0	0.21	24.29	15.9	1.3		
z12SC10-4	154.91	75.70	1.79	0.65	612.1	73.0	0.7	628.9	0.12	15.29	6.9	0.6		
z12SC10-5	150.18	78.98	1.89	0.66	791.2	102.2	0.8	814.8	0.13	33.81	11.6	0.9		
12SC12	**123.58**	**62.27**	**2.25**	**0.69**	**109.38**	**56.68**	**0.75**	**122.44**	**0.53**	**2.96**	-	**0.51**	**6.4**	**1.0**
z12SC12-1	118.95	65.42	2.37	0.70	99.0	64.1	0.5	113.8	0.65	2.92	6.8	0.5		
z12SC12-2	121.46	54.66	1.69	0.66	138.9	57.4	1.0	152.1	0.41	3.92	7.2	0.6		
z12SC12-3	130.34	66.74	2.70	0.71	90.3	48.6	0.7	101.5	0.54	2.05	5.3	0.4		
12SC13	**166.79**	**72.17**	**4.11**	**0.74**	**856.68**	**125.54**	**0.54**	**885.59**	**0.15**	**28.70**	-	**0.68**	**8.5**	**2.9**
z12SC13-1	212.55	78.49	6.09	0.77	699.1	108.8	0.6	724.1	0.16	33.83	11.3	0.9		
z12SC13-2	180.49	74.80	4.70	0.75	1284.4	171.8	0.6	1324.0	0.13	33.30	6.2	0.5		
z12SC13-3	149.19	68.05	3.21	0.73	765.8	103.1	0.5	789.5	0.13	34.13	11.0	0.9		
z12SC13-4	167.90	68.32	3.64	0.73	641.4	102.5	0.5	665.0	0.16	25.01	9.5	0.8		
z12SC13-5	123.82	71.21	2.92	0.73	892.7	141.6	0.5	925.3	0.16	17.21	4.7	0.4		

Name	W_1	W_2	L_1	L_2	Mass (µg)	Ft*	U (ppm)	Th (ppm)	Th/U	He (nmol/g)	Corrected Age [Ma]	Error (Ma)	Mean age (Ma)	St.Dev.† (Ma)
12PC01	**97.06**	**73.28**	**1.05**	**0.59**	**34.51**	**25.51**	**74.99**	**40.76**	**0.74**	**2.57**	-	**1.17**	**19.4**	**0.3**
12PC01-1	117.23	73.54	1.28	0.61	36.2	27.7	65.3	42.9	0.77	2.8	19.6	1.18		
12PC01-2	*94.87*	*67.60*	*0.87*	*0.55*	*31.9*	*124.0*	*66.1*	*60.7*	*3.89*	*21.7*	*116.9*	*7.02*		
12PC01-3	76.89	73.02	0.83	0.57	32.8	23.3	84.6	38.6	0.71	2.3	19.2	1.15		
12PC03	**124.34**	**63.76**	**1.01**	**0.58**	**35.91**	**17.83**	**54.33**	**40.29**	**0.50**	**0.59**	-	**0.28**	**4.7**	**1.2**
12PC03-1	103.49	65.09	0.88	0.58	31.5	9.4	16.9	33.7	0.30	0.4	3.3	0.20		
12PC03-2	121.94	66.15	1.07	0.59	58.8	32.9	85.4	66.8	0.56	1.1	5.0	0.30		
12PC03-3	147.60	60.03	1.07	0.57	17.5	11.1	60.7	20.3	0.64	0.4	5.8	0.35		
12PC05	**79.58**	**68.47**	**0.78**	**0.56**	**18.33**	**9.70**	**25.28**	**20.69**	**0.78**	**0.28**	-	**0.29**	**4.8**	**1.4**
12PC05-1	95.48	76.21	1.12	0.60	0.8	1.0	12.2	1.1	1.13	0.0	6.2	0.37		
12PC05-2	79.22	68.88	0.76	0.56	5.1	3.6	2.5	5.9	0.71	0.1	3.3	0.20		
12PC05-3	64.03	60.32	0.47	0.51	49.1	24.5	61.1	55.0	0.50	0.8	5.0	0.30		
12PC06	**79.63**	**60.47**	**0.59**	**0.52**	**6.97**	**6.82**	**4.43**	**8.57**	**0.94**	**0.08**	**3.51**	**0.21**	**3.5**	**0.6**
12PC06-1	81.24	65.20	0.70	0.55	5.4	4.2	2.2	6.4	0.77	0.1	4.0	0.24		
12PC06-2	78.02	55.74	0.49	0.49	8.5	9.5	6.6	10.7	1.11	0.1	3.1	0.18		
12PC06-3	*77.98*	*54.33*	*0.46*	*0.49*	*3.7*	*3.7*	*2.2*	*4.6*	*0.99*	*0.1*	*11.1*	*0.66*		
12PC09	**155.69**	**73.14**	**1.68**	**0.61**	**0.98**	**3.78**	**21.49**	**1.96**	**3.85**	**0.01**	-	**0.09**	**1.5**	-
12PC09-1	*83.85*	*61.56*	*0.64*	*0.53*	*4.4*	*6.2*	*21.4*	*6.0*	*1.41*	*0.0*	*-1.2*	*-0.07*		
12PC09-2	*93.53*	*64.90*	*0.79*	*0.55*	*1.9*	*4.0*	*19.3*	*2.9*	*2.14*	*0.0*	*-1.1*	*-0.06*		
12PC09-3	155.69	73.14	1.68	0.61	1.0	3.8	21.5	2.0	3.85	0.0	1.5	0.09		
12PC09-4	*129.45*	*60.00*	*0.94*	*0.55*	*1.3*	*2.6*	*23.5*	*2.1*	*1.97*	*1.6*	*252.2*	*15.13*		
12PC10	**126.17**	**59.79**	**0.93**	**0.54**	**19.67**	**51.60**	**16.97**	**31.63**	**2.66**	**0.26**	**2.73**	**0.16**	**2.7**	**0.1**
12PC10-2	140.04	65.22	1.20	0.58	22.5	54.6	21.1	35.2	2.43	0.3	2.7	0.16		
12PC10-3	112.30	54.36	0.67	0.50	16.8	48.6	12.9	28.0	2.89	0.2	2.8	0.17		
12PC10-4	*99.09*	*50.46*	*0.51*	*0.47*	*11.1*	*29.2*	*18.1*	*18.0*	*2.63*	*0.0*	*0.6*	*0.03*		
12PC02	**140.65**	**65.41**	**2.75**	**0.71**	**300.17**	**92.35**	**1.88**	**321.44**	**0.31**	**51.15**	**41.63**	**3.33**	**41.6**	**2.1**
z12PC02-1	182.14	60.59	3.11	0.71	342.9	108.0	2.9	367.8	0.31	57.55	40.8	3.3		
z12PC02-2	119.95	65.78	2.41	0.71	221.4	75.6	1.4	238.8	0.34	40.12	44.0	3.5		
z12PC02-3	119.85	69.85	2.72	0.72	336.2	93.5	1.3	357.7	0.28	55.79	40.1	3.2		
12PC03	**197.56**	**77.19**	**5.52**	**0.76**	**199.57**	**75.05**	**1.08**	**216.85**	**0.41**	**38.35**	**44.86**	**3.59**	**44.9**	**6.3**
z12PC03-1	191.88	89.97	7.22	0.78	202.1	100.4	1.4	225.2	0.50	38.93	40.7	3.3		
z12PC03-2	181.51	71.07	4.26	0.74	295.9	76.1	0.8	313.4	0.26	52.59	41.8	3.3		
z12PC03-3	219.30	70.52	5.07	0.74	100.8	48.6	1.1	112.0	0.48	23.53	52.1	4.2		

Name	W_1	W_2	L_1	L_2	Mass (µg)	Ft*	U (ppm)	Th (ppm)	Th/U	He (nmol/g)	Corrected Age [Ma]	Error (Ma)	Mean age (Ma)	St.Dev.† (Ma)
12PC04	**128.20**	**74.80**	**3.35**	**0.73**	**391.56**	**167.65**	**3.35**	**430.17**	**0.55**	**77.85**	**45.29**	**3.62**	**45.3**	**4.9**
z12PC04-1	139.21	80.79	4.23	0.76	589.1	89.6	0.5	609.8	0.15	120.47	48.3	3.9		
z12PC04-2	137.66	66.55	2.84	0.71	375.0	229.7	6.0	427.9	0.61	65.40	39.6	3.2		
z12PC04-3	107.72	77.07	2.98	0.72	210.6	183.6	3.6	252.9	0.87	47.68	48.0	3.8		
12PC09	**160.82**	**69.79**	**3.71**	**0.73**	**389.69**	**66.83**	**0.66**	**405.08**	**0.19**	**19.59**	**12.21**	**0.98**	**12.2**	**2.4**
z12PC09-1	176.38	69.15	3.92	0.74	755.2	105.3	0.4	779.4	0.14	37.37	12.0	1.0		
z12PC09-2	*154.83*	*52.08*	*1.95*	*0.67*	*2707.6*	*417.5*	*0.9*	*2803.7*	*0.15*	*53.21*	*5.3*	*0.4*		
z12PC09-3	128.39	67.50	2.72	0.72	204.4	38.0	0.3	213.1	0.19	10.16	12.3	1.0		
z12PC09-4	183.49	79.41	5.38	0.76	232.8	65.6	0.5	247.9	0.28	9.36	9.2	0.7		
z12PC09-5	151.40	63.36	2.83	0.71	446.4	81.1	0.9	465.1	0.18	20.87	11.7	0.9		
z12PC09-6	164.45	69.54	3.70	0.74	309.8	44.2	1.2	319.9	0.14	20.20	15.9	1.3		
12PC10	**159.81**	**75.33**	**2.93**	**0.69**	**135.46**	**94.74**	**1.80**	**157.28**	**0.72**	**4.28**	**7.45**	**0.60**	**7.5**	**1.9**
z12PC10-1	173.45	80.85	5.27	0.76	70.1	47.5	0.4	81.0	0.68	1.95	5.9	0.5		
z12PC10-2	167.44	65.94	3.39	0.72	118.4	89.2	0.5	139.0	0.75	4.93	9.1	0.7		
z12PC10-3	133.25	64.59	2.58	0.70	97.1	79.0	0.4	115.3	0.81	2.29	5.2	0.4		
z12PC10-4	157.12	72.14	1.65	0.63	263.3	164.9	6.6	301.3	0.63	6.37	6.2	0.5		
z12PC10-5	162.37	87.85	2.52	0.68	134.8	98.0	1.2	157.4	0.73	4.97	8.6	0.7		
z12PC10-6	165.26	80.64	2.16	0.66	129.1	89.9	1.9	149.8	0.70	5.16	9.7	0.8		

Notes: See Appendix 4.1 for discussion of analytical procedures and errors; samples in italics were not used in calculated mean ages.

*Ft is the alpha ejection correction of Farley et al. (1996)

†St. Dev.—standard deviation.

CHAPTER 5

Latest Cretaceous exhumation and Eocene erosional beveling of the Nevadaplano, western Nevada and southern California, from low-temperature thermochronology

Tandis S. Bidgoli[1]

J. Douglas Walker[1]

Daniel F. Stockli[2]

[1]*Department of Geology, University of Kansas, Lawrence, Kansas 66045, USA*

[2]*Jackson School of Geosciences, University of Texas, Austin, Texas 78712, USA*

Abstract

New basement and detrital apatite and zircon (U-Th)/He ages, combined with published (U-Th)/He, fission-track, $^{40}Ar/^{39}Ar$, and K/Ar ages from the Sierra Nevada, western Basin and Range, and Mojave Desert, show two distinct periods of cooling affecting this geographically broad region. The first is a Late Cretaceous cooling event that may be related to widespread extension, crustal refrigeration, and tectonic exhumation associated with Laramide flat-slab subduction. The second event corresponds to a pulse of rapid exhumation during the Eocene. Eocene cooling is problematic because there are no known structures of that age, suggesting the region was tectonically quiescent at that time. Instead, it appears that this exhumation event may be related to rapid erosion, following major shifts in global climate related to the hyperthermal Late Paleocene Thermal Maximum (LPTM) and Early Eocene Climatic Optimum (EECO). We postulate that widespread laterites, indicative of intense weathering during a warm and humid Cretaceous and early Eocene climate, were eroded and deposited in fluvial-fandeltas and offshore during or shortly after these events. The provenance of marine and nonmarine successions also changes from local to more distal sources, suggesting a transition to well-

integrated, low to moderate-gradient drainage networks typical of semi-arid climates. Pedogenic carbonate within paleosols across the region also implies a change to more arid and/or seasonal conditions. Early Eocene exhumation is followed by prolonged (~35 Ma) inactivity in cooling histories across the region, suggesting subsequent erosional exhumation was very slow. Collectively, the data suggest that rapid tectonic exhumation of the Nevadaplano occurred in the latest Cretaceous, whereas erosional beveling and stabilization of the plateau was dominantly an early to middle Eocene phenomenon related to a changing climate.

Introduction

The Late Cretaceous to early Cenozoic hinterland of the Sevier retroarc fold-thrust belt in western North America is widely interpreted as a broad plateau, coined the Nevadaplano by analogy to the modern Andean Puna-Altiplano (e.g., Coney and Harms, 1984; Dilek and Moores, 1999; DeCelles, 2004; Best et al., 2009; Cassel et al., 2009; Henry et al., 2012). Although there is general consensus that this erosional highland was in place by the mid-Eocene based on widely distributed ash-flow tuffs that fill major paleovalleys extending from central Nevada to the western Sierra Nevada, the details of the history of the Nevadaplano remains controversial (Wakabayashi and Sawyer, 2001; Mulch et al., 2006; Molnar, 2010; Henry et al., 2012; Chamberlain et al., 2012).

Most of the studies to date have focused on the estimating the absolute elevation and topographic relief of the Sierra Nevada, which formed the western margin of the Nevadaplano (e.g., Lindgren, 1911; Unruh, 1991; Wernicke et al., 1996; Chamberlain and Poage, 2000; Wakabayashi and Sawyer, 2001; Jones et al., 2004; Horton et al., 2004; Cecil et al., 2006; Mulch et al., 2006; Crowley et al., 2008; Mulch et al., 2008; Cassel et al., 2009; Hren et al., 2010). These studies have used a range of techniques (e.g., stream gradients, paleobotany, stable

isotopes, clumped isotopes, low-temperature thermochronology) and have resulted in several competing models for the evolving landscape of the Sierra Nevada. In contrast to these numerous investigations, few studies have focused on the western Great Basin or Mojave portions of the plateau where the timing of plateau development, its regional extent, and the processes that shaped it are largely unknown.

In this paper, we use new bedrock and detrital apatite and zircon (U-Th)/He ages, combined with published thermochronology data from the Sierra Nevada, western Great Basin, and Mojave Desert to constrain the timing, spatial pattern, and magnitude of Late Cretaceous to early Cenozoic cooling. The results are used to evaluate dynamic controls on the cooling history of this broad region. We show that late Cretaceous exhumation of the western Nevadaplano was followed by a brief, but rapid episode of Eocene erosional beveling related to changing global climate.

Previous studies

Thermochronology studies show that exhumation of the Sierra Nevada occurred principally in the latest Cretaceous and early Cenozoic, forming a well-preserved low-relief surface that mimics the modern topography (Dumitru, 1990; House et al., 1997, 1998, 2001; Clark et al., 2005; Cecil et al., 2006; Maheo et al., 2009, Blythe and Longinotti, 2013). Long-term erosion rates determined by these studies also show that subsequent exhumation of the range has been slow, on the order of 0.02-0.06 mm/yr (Clark et al., 2006; Cecil et al., 2006; Maheo et al., 2009)

The western Great Basin, east of the Sierra Nevada, has also been a host to a number of thermochronology studies (e.g., Surpless et al., 2002; Stockli et al., 2002, 2003; Lee et al., 2009; Mahan et al., 2009; Ferrill et al., 2012). Although the emphasis of these investigations was on

middle Miocene to Pliocene exhumation related to Basin and Range extension and later dextral transtension, these studies inadvertently provide constraints on the latest Cretaceous and early Cenozoic cooling history of the region. Similarly, a large dataset of cooling ages from several pioneering geochronology studies of the Mojave, south of the Sierras, also provide important constraints (e.g., Armstrong and Suppe, 1973; Miller and Morton, 1980). The results of these studies are summarized in Figure 5.1.

(U-Th)/He thermochronometry

New apatite and zircon (U-Th)/He ages were obtained from 35 bedrock samples from the Argus Range, Avawatz Mountains, Clark Mountains, Lucy Gray Range, and Spring Mountains (Figures 5.1 and 5.2). Bedrock samples were collected from a range of lithologic units, including Proterozoic gneiss and metasedimentary rocks, and Cretaceous granitoids and volcanic rocks. We also present new detrital apatite and zircon (U-Th)/He ages from 39 samples of the Miocene Bedrock Spring Formation in the Lava Mountains (Figure 5.1). Detailed maps of the Bedrock Spring Formation and sample locations are available in Andrew et al. (2014). Laboratory and analytical work was performed at the Isotope Geochemistry Laboratories at the University of Kansas and the (U-Th)/He Geo- and Thermochronometry Lab at the University of Texas at Austin. Data tables and descriptions of analytical procedures and error reporting are given in Tables SD5.1 and SD5.2 and Appendix 5.1.

He age results

Basement He ages

Figure 5.2 summarizes basement (U-Th)/He ages from four of the sampled areas. These simplified cross-sections are oriented roughly EW and show the projected positions of our thermochronology samples and their associated cooling ages. Cross-section A-A' is located

across Wilson Canyon in the Argus Range and shows that zircon (U-Th)/He mean ages range from 49.8 ± 4.0 to 66.8 ± 11.0 and systematically increase with elevation and distance eastward across the range. In contrast, apatite mean ages are mostly elevation invariant and cluster at ~45 Ma. Cross-section B-B' is located across Mountain Pass in the Clark Mountains and shows that zircon (U-Th)/He ages from this area are elevation invariant, clustering at ~65 Ma. Cross-section C-C' is located across the central part of the Lucy Gray Range. Zircon mean ages are unreset, ranging from 119.6 ± 14.8 to 227.2 ± 143.9; whereas apatite mean ages range from 45.7 ± 4.7 to 83.2 ± 5.0 and systematically increase with elevation and distance eastward across the range. Cross-section D-D' crosses the northern part of the Spring Mountains and shows that zircon mean ages range from 40.1 ± 3.2 to 72.7 ± 33.5. Although errors for this transect are quite large due to suspected radiation damage effects, the ages broadly cluster at ~55 Ma.

Detrital He ages

Apatite and zircon (U-Th)/He single grain ages from the Miocene Bedrock Spring Formation in the Lava Mountains are summarized in Figure 5.3. The Bedrock Springs Formation is a thick (600 m) succession of arkosic sandstone interbedded with conglomerate, siltstone, limestone, and volcanic rocks that has been correlated to the Dove Springs Formation in the El Paso Basin (Smith, 1964; Loomis and Burbank, 1988; Smith et al., 2002; Frankel et al., 2008). Paleocurrent indicators and clast provenance demonstrate that basin sediment was derived from the south-southeast (Smith, 1964); thus, detrital cooling ages from the Bedrock Springs Formation may be used as a proxy for the cooling age of basement sources within the northern Mojave Desert.

Although the single grains ages are aggregated from more than 30 samples, the histograms of apparent (U-Th)/He ages show two distinct peaks. Zircon (U-Th)/He ages have a

peak frequency at ~65 Ma, with ~60% of the 85 grains analyzed ranging from 70-60 Ma. In contrast, apatite (U-Th)/He ages have a strong peak at ~52 Ma, with > 30% of the 101 grains analyzed between 55-50 Ma and >50% between 60-45 Ma.

Regional cooling age patterns

In addition to obtaining new cooling ages, we compiled published (U-Th)/He, fission-track, $^{40}Ar/^{39}Ar$, and K/Ar ages from a broad region covering the Sierra Nevada, western Great Basin, and Mojave Desert. The compilation includes over 450 samples and ~600 individual cooling ages, summarized in Figure 5.1.

Although the Mojave Desert shows widespread cooling prior ~70 Ma, the vast majority of the cooling ages are distributed between the latest Cretaceous and early Eocene, with a high degree of overlap between these periods of cooling. The map-based patterns indicate that cooling was areally extensive, but the details of the individual ranges are lost at this scale. A more instructive view is provided by the age versus paleodepth or elevation profiles summarized in Figure 5.4. For most of the ranges, paleodepths are shown relative to a middle Miocene paleohorizontal surface. For the Spring Mountains, paleodepth is determined relative to a stratigraphic reference in the Cambrian. For ranges that lack a paleohorizontal reference, ages are plotted against the samples current elevation.

The compilation shows that cooling ages are invariant with paleodepth or elevation at two distinct periods, ~65 Ma and/or ~50-55 Ma. The exception is the Wassuk Range, where gradual overlap of cooling ages with paleodepth suggests a more protracted cooling history. Although the precise magnitude of cooling is difficult to estimate because of erosion and tilting, the reconstructions show that exhumation during these events was rapid and on the order of kilometers. Lee et al. (2009) estimated ~7.5 km of latest Cretaceous and ~3.9 km of Eocene

exhumation for the Inyo Mountains. Approximate cooling rates of 4˚ to 15˚ C/m.y. were determined by using differences in closure temperatures and cooling ages between pairs of thermochronometers; however, the overlap between apatite (U-Th)/He ages and apatite fission-track or zircon (U-Th)/He ages in several of the ranges (e.g., White, Inyo, Argus and Slate ranges) is indicative of more rapid (>40˚ C/m.y) cooling rates.

Another critical observation that can be made from the paleodepth profiles is that early Eocene exhumation is followed by ~35 Ma of inactivity in cooling histories across the region. Ranges across the region do not experience cooling again until the Miocene, which suggests erosional exhumation during the intervening period was very slow.

Discussion

The new (U-Th)/He ages combined with published cooling ages show that there are two relatively distinct periods of cooling: one at ~65 Ma and another at ~55-50 Ma. Late Cretaceous cooling is well documented in the region and has been linked to a several possible causes, including (1) refrigeration associated with Laramide flat-slab subduction (e.g., Dumitru, 1990), (2) magmatic arc cooling (e.g., Stockli et al., 2003), (3) erosional exhumation (e.g., House et al., 1997; Stockli et al., 2002; Surpless et al., 2002; Clark et al., 2005); (4) contractional deformation (e.g., Yin, 2002), and (4) extensional deformation (e.g., Wells and Hoisch, 2008 and references therein). Subduction refrigeration is a viable explanation for Late Cretaceous cooling in the western Mojave, where the Pelona, Orocopia, Rand, and associated schists provide direct evidence of a low-angle slab and lithospheric delamination (Grove et al., 2003, Saleeby, 2003, Jacobson et al., 2007), but is difficult to apply to the region to the north, where mantle xenoliths indicate that the North American lithosphere was intact and the Farallon slab likely had a steeper geometry (Ducea and Saleeby, 1998). For these areas, tectonic exhumation seems more likely,

as cooling ages are broadly compatible with the timing of (1) exhumation associated with a belt of extensional structures in the eastern Mojave, active from ~75-67 Ma (Wells and Hoisch, 2008), (2) slip along the Boundary Canyon Detachment in the Funeral Mountains, which was active from 72-70 Ma (Hodges and Walker, 1990; Applegate et al., 1992), (3) dextral shear across Owens Valley (Glazner et al., 2005; Bartley et al., 2007), and (4) unroofing of the southern Sierras associated with an inferred low-angle detachment system (Wood and Saleeby, 1997; Chapman et al., 2012; Blythe and Longinotti, 2013). Thus, it appears that tectonic exhumation in the hinterland of the Sevier orogen during the latest Cretaceous affected a much broader region than previously estimated (e.g., Hodges and Walker, 1992).

In contrast, widespread Eocene cooling is more difficult to explain. Tectonic exhumation (contractional or extensional) seems unlikely because there are no known structures of that age and plate convergence rates are inferred to have slowed significantly during the Eocene (Engebretson et al., 1985). Regional igneous rocks, which are either Mesozoic or mid- to late-Tertiary in age, indicate that magmatic cooling is highly implausible as a cause for the observed cooling age pattern. Thermal relaxation related to asthenospheric processes is also doubtful given that the lower dip of the Farallon slab would have restricted mantle wedge circulation at that time, and that the timing of slab roll-back, documented by the mid-Tertiary ignimbrite flare-up, significantly post-dates this period of cooling (Coney and Reynolds, 1977; Humphreys, 1995).

One possible explanation for widespread cooling in the Eocene is rapid erosion associated with major changes in global climate. The early Cenozoic climate was characterized by pronounced warming that concluded with the early Eocene Climatic Optimum (EECO; 52 to 50 Ma), during which global temperatures and greenhouse gas concentrations reached a long-

term maximum (Figure 5.5). This warming period was punctuated by the Late Paleocene Thermal Maximum (LPTM; ca. 55 Ma; Figure 5.5), a brief (100 k.y.) hyperthermal episode, documented in strata worldwide by a significant negative carbon isotope excursion (Chase et al., 1998; Zachos et al., 2001) and a notable increase in kaolinite in the sedimentary successions (Robert and Chamley, 1991; Gibson et al., 1993; Bolle et al., 1998; Knox 1998). The source of the kaolinites is debated (e.g., Schmitz et al., 2001; Thiry and Dupuis, 2000), but it likely reflects deeper levels of continental erosion that stripped and transported kaolinite-rich soils formed during Cretaceous and early Tertiary hothouses.

Although the early Cenozoic sedimentary record is somewhat limited, changes in sedimentary provenance and maturity suggest important transitions were taking place in the early Eocene that may be evidence of enhanced erosion and a changing climate. Upper Cretaceous through Paleocene marine and nonmarine successions are dominated by locally-derived sediment, suggestive of relatively short transport systems draining Sierran and Peninsular Range sources (Nilsen and Clarke, 1975; Cox, 1982; Kies and Abbott, 1983; Critelli and Nilsen, 2000; Lechler and Niemi, 2011). In contrast, lower to middle Eocene cobble conglomerates are more mature and contain exotic clasts derived from Great Basin, Mojave, and Sonoran sources, implying that drainage networks expanded their reach and became increasingly integrated (Nilsen and Clarke, 1975; Cox, 1982; Kies and Abbott, 1983; Howard, 2000; Lechler and Niemi, 2011). These paleorivers are interpreted to have low to moderate gradients and high bed loads, which are more typical of semi-arid climates (Peterson and Abbott, 1979; Kies and Abbott, 1983).

The paleosol record also supports a major shift in regional paleoclimate in the early Cenozoic. Lateritic paleosols in the western foothills of the Sierra (Allen, 1929; Bateman and

Wahrhaftig, 1966) and in southern California and the Baja peninsula (Peterson and Abbott, 1979) suggest that warm and humid conditions prevailed during the Late Cretaceous through early Eocene, consistent with paleo-fauna and -flora from foreland areas (e.g., Wilf, 2000). A detrital origin for kaolinite-rich deposits in the Eocene Ione Formation is debated, but would also support widespread laterite development during an earlier period (Allen, 1928; Pask and Turner, 1952; Wood, 1994; Gillam, 1974; Rodgers, 1986). In contrast, late Paleocene and middle Eocene paleosols contain pedogenic carbonate, consistent with a change to more arid and/or seasonal conditions (Peterson and Abbott, 1979; Torres and Gaines, 2013).

Cooling ages from across the region suggest that Eocene erosional denudation proceeded quickly. We speculate that high rates of surface denudation may have been enhanced by (1) relief generated by Late Cretaceous tectonic exhumation across the region, (2) earlier phases of hothouse climate, which may have provided a deeply weathered soil/regolith profiles, (3) changes in vegetative cover, which may have temporarily destabilized surfaces, and/or (4) enhanced chemical weathering due to high levels of atmospheric CO_2 during the LPTM and EECO (Suchet and Probst, 1995; Smith et al., 2008). A similar pulse of rapid erosion is documented in the Sevier hinterland in Idaho and preserved as a major outpouring of sediment into the Franciscan trench and the Tyee, Great Valley, and Green River basins during the early to middle Eocene (Dumitru et al., 2013), suggesting that this event may have affected much of western North America.

The cooling history data also demonstrate that exhumation in the Eocene was succeeded by protracted quiescence across region. For most the region, exhumation does not begin again until the early to middle Miocene (Wernicke et al., 1988; Glazner et al., 2002), supporting earlier

studies that suggest erosion rates over this interval were very low (e.g., Clark et al., 2005; Maheo et al., 2009).

Collectively, the data suggest that rapid tectonic exhumation of the Nevadaplano occurred in the latest Cretaceous, whereas erosional beveling and stabilization of the plateau was a widespread and dominantly an early to middle Eocene phenomenon related to a changing climate.

Acknowledgements

This research was supported by grants from the Geothermal Program Office of the U.S. Department of the Navy, China Lake and the NSF EarthScope Program, and a University of Kanas - Patterson Fellowship. We are grateful to Chad La Fever, Joseph Andrew, Sarah Evans, Kurt Sundell, and Steve Alm for assistance with sample collection, and to Roman Kislitsyn for assistance with sample preparation and analysis.

References

Andrew, J.E., Rittase, W.M., Monastero, F.M., Bidgoli, T., and Walker, J.D., 2014, Geologic Map of the Northern Lava Mountains and Summit Range, San Bernardino County, California: Geological Society of America Digital Map and Chart Series 19, doi:10.1130/2014.DMCH019.

Allen, V.T., 1929, The Ione Formation of California: University of California Department of Geological Sciences Bulletin, v. 18, p. 347–448.

Applegate, J.D.R., Walker, J.D., and Hodges, K.V., 1992, Late Cretaceous extensional unroofing in the Funeral Mountains metamorphic core complex, California: Geology, v. 20, p. 519-522.

Armstrong, R.L. and Suppe, J., 1973, Potassium-argon geochronometry of Mesozoic igneous rocks in Nevada, Utah, and southern California: Geological Society of America Bulletin, v. 84, p. 1375-1392.

Bartley, J.M., Glazner, A.F., Coleman, D.S. Kylander-Clark, A., Mapes, R., and Friedrich, A.M., 2007, Large Laramide dextral offset across Owens Valley, California, and its possible relation to tectonic unroofing of the southern Sierra Nevada, in Till, A.B., Roeske, S.M., Sample, J.C., and Foster, D.A., eds., Exhumation Associated With

Continental Strike-Slip Fault Systems: Geological Society of American Special Paper 434, p.129-148.

Bateman, P.C., and Wahrhaftig, C., 1966, Geology of the Sierra Nevada, in Bailey, E.H., ed., Geology of Northern California: California Division of Mines and Geology Bulletin, v. 190, p. 107–172.

Best, M.G., Barr, D.L., Christiansen, E.H., Gromme, S., Deino, A.L., and Tingey, D.G., 2009, The Great Basin Altiplano during the middle Cenozoic ignimbrite flareup: Insights from volcanic rocks: International Geology Review, v. 51, p. 589–633.

Blythe, A.E. and Longinotti, N., 2013, Exhumation of the southern Sierra Nevada–eastern Tehachapi Mountains constrained by low-temperature thermochronology: Implications for the initiation of the Garlock fault: Lithosphere, v. 5, p. 321-327.

Bolle, M.P., Adatte, T., Keller, G., Von Salis, K., and Hunziker, J., 1998, Biostratigraphy, mineralogy, and geochemistry of the Trabakua Pass and Ermua sections in Spain: Paleocene-Eocene transition: Eclogae Geologicae Helvetiae, v. 91, p. 1–25.

Cassel, E.J., Calvert, A., and Graham, S.A., 2009, Age, geochemical composition, and distribution of Oligocene ignimbrites in the northern Sierra Nevada, California: Implications for landscape morphology, elevation, and drainage divide geography of the Nevadaplano: International Geology Review, v. 51, p. 723–742.

Cecil, M.R., Ducea, M.N., Reiners, P.W., and Chase, C.G., 2006, Cenozoic exhumation of the northern Sierra Nevada, California, from (U-Th)/He thermochronology: Geological Society of America Bulletin, v. 118,p. 1481–1488, doi: 10.1130/B25876.1.

Cecil, M.R., Ducea, M.N., Reiners, P.W., and Chase, C.G., 2006, Cenozoic exhumation of the northern Sierra Nevada, California, from (U-Th)/He thermochronology: Geological Society of America Bulletin, v. 118, p. 1481–1488, doi: 10.1130/B25876.1.

Chamberlain, C.P., and Poage, M.A., 2000, Reconstructing the paleotopography of mountain belts from the isotopic composition of authigenic minerals: Geology, v. 28, p. 115–118.

Chamberlain, C.P., Mix, H.T., Mulch, A., Hren, M.T., Kent-Corson, M.L., Davis, S. J., and Graham, S.A., 2012, The Cenozoic climatic and topographic evolution of the western North American Cordillera: American Journal of Science, v. 312, p. 213-262.

Chapman, A.D., Saleeby, J.B., Wood, D.J., Piasecki, A., Kidder, S., Ducea, M.N., and Farley, K.A., 2012, Late Cretaceous gravitational collapse of the southern Sierra Nevada batholith, California: Geosphere, v. 8, p. 314-341.

Chase, C.G., Gregory-Wodzicki, K.M., Parrish-Jones, J.T., and DeCelles, P., 1998, Topographic history of the western Cordillera of North America and controls on climate, in Crowley, T.J., and Burke, K., eds., Tectonic boundary conditions for climate model simulations:

Oxford, UK, Oxford University Press, Oxford Monographs on Geology and Geophysics 39, p. 73–99.

Clark, M.K., Maheo, G., Saleeby, J., and Farley, K.A., 2005, The non-equilibrium landscape of the southern Sierra Nevada, California: GSA Today, v. 15, p. 4–10.

Coney, P.J., and Harms, T.J., 1984, Cordilleran metamorphic core complexes: Cenozoic extensional relics of Mesozoic compression: Geology, v. 12, p. 550–554.

Coney, P.J., and Reynolds, S.J., 1977, Cordilleran Benioff zones: Nature, v. 270, p. 403–406.

Cox, B.F., 1982, Stratigraphy, sedimentology, and structure of the Goler Formation (Paleocene), El Paso Mountains, California: Implications for Paleogene tectonism on the Garlock Fault Zone [Ph.D. thesis]: Riverside, University of California, 248 p.

Critelli, S., and Nilsen, T.H., 2000, Provenance and stratigraphy of the Eocene Tejon Formation, Western Tehachapi Mountains, San Emigdio Mountains, and Southern San Joaquin Basin, California: Sedimentary Geology, v. 136, p. 7–27

Crowley, B.E., Koch, P.L., and Davis, E.B., 2008, Stable isotope constraints on the elevation history of the Sierra Nevada Mountains, California: Geology, v. 120, p. 588–598.

DeCelles, P.G., 2004, Late Jurassic to Eocene evolution of the Cordilleran thrust belt and foreland basin system, western U.S.A.: American Journal of Science, v. 304, p. 105–168, doi:10.2475/ajs.304.2.105.

Dilek, Y., and Moores, E.M., 1999, A Tibetan model for the early Tertiary western United States: Geological Society of London Journal, v. 156, p. 929–941.

Ducea, M.N., and Saleeby, J.B., 1998, The age and origin of a thick mafic-ultramafic c keel from beneath the Sierra Nevada Batholith: Contributions to Mineralogy and Petrology, v. 133, p. 169–185.

Dumitru, T.A., 1990, Subnormal Cenozoic geothermal gradients in the extinct Sierra Nevada magmatic arc: Consequences of Laramide and Post-Laramide shallow-angle subduction: Journal of Geophysical Research, v. 95, p. 4925-4941.

Dumitru, T.A., Ernst, W.G., Wright, J.E., Wooden, J.L., Wells, R.E., Farmer, L.P., and Graham, S.A., 2013, Eocene extension in Idaho generated massive sediment floods into the Franciscan trench and into the Tyee, Great Valley, and Green River basins: Geology, v. 41, p. 187-190.

Dumitru, T.A., Gans, P.B., Foster, D.A., & Miller, E.L., 1991, Refrigeration of the western Cordilleran lithosphere during Laramide shallow-angle subduction: Geology, v. 19, p. 1145-1148.

Engebretson, D.C., Cox, A., and Gordon, R.G., 1985, Relative Motions between Oceanic and Continental Plates in the Pacific Basin: Geological Society of America Special Paper 206, 59 p.

Farmer, G.L., Glazner, A.F., and Manley, C.R., 2002, Did lithospheric delamination trigger late Cenozoic potassic volcanism in the southern Sierra Nevada, California?: Geological Society of America Bulletin, v. 114, p. 754–768.

Ferrill, D.A., Morris, A.P., Stamatakos, J.A., Waiting, D.J., Donelick, R.A., and Blythe, A.E., 2012, Constraints on exhumation and extensional faulting in southwestern Nevada and eastern California, USA, from zircon and apatite thermochronology: Lithosphere, v. 4, p. 63-76.

Frankel, K.L., Glazner, A.F., Kirby, E., Monastero, F.C., Strane, M.D., Oskin, M.E., Unruh, J.R., Walker, J.D., Anandakrishnan, S., Bartley, J.M., Coleman, D.S., Dolan, J.F., Finkel, R.C., Greene, D., Kylander-Clark, A., Morrero, S., Owen, L.A., and Phillips, F., 2008, Active tectonics of the eastern California shear zone, in Duebendorfer, E.M., and Smith, E.I., eds.: Geological Society of America Field Guide 11, p. 43-81, doi: 10.1130/2008.fld011.

Foster, D.A., Miller, D.S., and Miller, C.F., 1991, Tertiary extension in the Old Woman Mountains area, California: Evidence from apatite fission track analysis: Tectonics, v. 10, p. 875-886.

Foster, D.A., Miller, C.F., Harrison, T.M., and Hoisch, T.D., 1992, $^{40}Ar/^{39}Ar$ thermochronology and thermobarometry of metamorphism, plutonism, and tectonic denudation in the Old Woman Mountains area, California: Geological Society of America Bulletin, v. 104, p. 176-191.

Giallorenzo, M., 2013, Application of (U-Th)/He and 40Ar/39Ar Thermochronology to the Age of Thrust Faulting in the Sevier Orogenic Belt [Ph.D. thesis]: Las Vegas, University of Nevada, 296 p.

Gibson, T.G., Bybell, L.M., and Owens, J.P., 1993, Latest Paleocene lithological biotic events in neritic deposits from southwestern New Jersey: Paleoceanography, v. 8, p. 495–514.

Gillam, M.L., 1974, Contact relations of the Ione and Valley Springs formations in the Buena Vista area, Amador County, California [M.S. thesis]: Stanford University, Palo Alto, California, 180 p.

Glazner, A.F., Walker, J.D., Bartley, J.M., and Fletcher, J.M., 2002, Cenozoic evolution of the Mojave block, southern California, in Glazner, A.F., Walker, J.D., and Bartley, J.M., editors, Geologic Evolution of the Mojave Desert and Southwestern Basin and Range: Geological Society of America Memoir 195, p. 19-42.

Glazner, A.F., Lee, J. Bartley, J.M., Coleman, D.S., Kylander-Clark, A., Greene, D.C., and Le, K., 2005, Large dextral offset across Owens Valley, California from 148 Ma to 1872 A.D., in Stevens, C. and Cooper, J., eds., Western Great Basin Geology: Pacific Section, SEPM, v. 99, p. 1-35.

Gorynski, K.E., Stockli, D.F., and Douglas Walker, J., 2013, Thermochronometrically constrained anatomy and evolution of a Miocene extensional accommodation zone and tilt domain boundary: The southern Wassuk Range, Nevada: *Tectonics*, v. *32*, p. 516-539.

Grove, M., Jacobson, C.E., Barth, A.P., and Vucic, A., 2003, Temporal and spatial trends of Late Cretaceous–early Tertiary underplating Pelona and related schist beneath southern California and southwestern Arizona: Geological Society of America Special Paper 374, p. 381–406.

Henry, C.D., Hinz, N.H., Faulds, J.E., Colgan, J.P., John, D.A., Brooks, E.R., Cassel, E.J., Garside, L.J., Davis, D.A., and Castor, S.B., 2012, Eocene–Early Miocene paleotopography of the Sierra Nevada–Great Basin–Nevadaplano based on widespread ash-flow tuffs and paleovalleys: Geosphere, v. 8, p. 1–27.

Hodges, K.V., and Walker, J.D., 1990, Petrologic constraints on the unroofing history of the Funeral Mountains metamorphic core complex, California: Journal of Geophysical Research, vol. 95, p. 8,437-8,445.

Hodges, K.V., and Walker, J.D., 1992, Extension in the Cretaceous Sevier orogen, North American Cordillera: Geological Society of America Bulletin, vol. 104, p. 560-569.

Hoisch, T.D., and Simpson, C., 1993, Rise and tilt of metamorphic rocks in the lower plate of a detachment fault in the Funeral Mountains, Death Valley, California: Journal of Geophysical Research, v. 98, p. 6805-6827.

Horton, T.W., Sjostrom, D.J., Abruzzese, M.J., Poage, M.A., Waldbauer, J.R., Hren, M., Wooden, J., and Chamberlain, C.P., 2004, Spatial and temporal variation of Cenozoic surface elevation in the Great Basin and Sierra Nevada: American Journal of Science, v. 304, p. 862–888.

House, M.A., Wernicke, B.P., Farley, K.A., and Dumitru, T.A., 1997, Cenozoic thermal evolution of the central Sierra Nevada, California, from (U-Th)/He thermochronometry: Earth and Planetary Science Letters, v. 151, p. 167–179.

House, M.A., Wernicke, B.P., and Farley, K.A., 1998, Dating topography of the Sierra Nevada, California, using apatite (U-Th)/He ages: Nature, v. 396, p. 66–69.

House, M.A., Wernicke, B.P., and Farley, K.A., 2001, Paleogeomorphology of the Sierra Nevada, California, from the (U-Th)/He ages in apatite: American Journal of Science, v. 301, p. 77–102.

Howard, J.L., 2000, Provenance of quartzite clasts in the Eocene-Oligocene Sespe Formation: Paleogeographic implications for southern California and the ancestral Colorado River: Geological Society of America Bulletin, v. 112, p. 1635–1649.

Hren, M.T., Pagani, M., Erwin, D.M., and Brandon, M., 2010, Biomarker reconstruction of the early Eocene paleotopography and paleoclimate of the northern Sierra Nevada: Geology, v. 38, p. 7–10.

Humphreys, E., 2009, Relation of flat subduction to magmatism and deformation in the western United States, in Kay, S.M., Ramos, V.A., and Dickinson, W.R., eds., Backbone of the Americas: Shallow Subduction, Plateau Uplift, and Ridge and Terrane Collision: Geological Society of America Memoir 204, p. 85–98.

Humphreys, E., Hessler, E., Dueker, K., Farmer, G.L., Erslev, E., and Atwater, T., 2003, How Laramide-age hydration of North American lithosphere by the Farallon slab controlled subsequent activity in the western United States: International Geology Review, v. 45, p. 575–595.

Humphreys, E.D., 1995, Post-Laramide removal of the Farallon slab, western United States: Geology, v. 23, p. 987-990.

Jacobson, C.E., Grove, M., Vucic, A., Pedrick, J.N., and Ebert, K.A., 2007, Exhumation of the Orocopia Schist and associated rocks of southeastern California: Relative roles of erosion, synsubduction tectonic denudation, and middle Cenozoic extension: Geological Society of America Special Paper 419, p. 1–37.

Jones, C.H., Farmer, G.L., and Unruh, J., 2004, Tectonics of Pliocene removal of lithosphere of the Sierra Nevada, California: Geological Society of America Bulletin, v. 116, p. 1408–1422.

Kies, R.P., and Abbott, P.L., 1983, Rhyolite clast populations and tectonics in the California continental borderland: Journal of Sedimentary Petrology, v. 53, p. 461–476

Knox, R.W.O., 1998, Kaolinite influx within Paleocene-Eocene boundary strata of western Europe: Newsletters on Stratigraphy, v. 36, p. 49–53.

Lechler, A.R. and Niemi, N.A., 2011, Sedimentologic and isotopic constraints on the Paleogene paleogeography and paleotopography of the southern Sierra Nevada, California: Geology, v. 39, p. 379–382

Lee, J., Stockli, D.F., Owen, L.A., Finkel, R.C., and Kislitsyn, R., 2009, Exhumation of the Inyo Mountains, California: Implications for the timing of extension along the western boundary of the Basin and Range Province and distribution of dextral fault slip rates across the eastern California shear zone: Tectonics, v. 28, TC1001, doi: 10.1029/2008TC002295.

Lindgren, W., 1911, The Tertiary Gravels of the Sierra Nevada of California: U.S. Geological Survey Professional Paper 73, 226 p.

Loomis, D.P. and Burbank, D.W., 1988, The stratigraphic evolution of the El Paso basin, southern California: Implications for the Miocene development of the Garlock fault and uplift of the Sierra Nevada: Geological Society of America Bulletin, v. 100, p. 12-28.

Ludington, S., Moring, D.C., Miller, R.J., Stone, P.A., Bookstrom, A.A., Bedford, D.R., Evans, J.G., Haxel, G.A., Nutt, C.J., Flyn, K.S., and Hopkins, M.J., 2007, Preliminary integrated geologic map of databases for the United States, Western States: California, Nevada, Arizona, Washington, Oregon, Idaho, and Utah: United States Geological Survey Open-File Report (2005-1305), 44 p.

Mahan, K.H., Guest, B., Wernicke, B., and Niemi, N.A., 2009, Low-temperature thermochronologic constraints on the kinematic history and spatial extent of the Eastern California shear zone. Geosphere, v. 5, 1–13.

Maheo, G., Saleeby, J., Saleeby, Z., and Farley, K.A., 2009, Tectonic control on southern Sierra Nevada topography, California: Tectonics, v. 28, TC6006, doi: 10.1029/2008TC002340.

Miller, F.K., and Morton, D.M., 1980, Potassium-Argon Geochronology of the Eastern Transverse Ranges and Southern Mojave Desert, Southern California: U.S. Geological Survey Professional Paper P1152, 30 p.

Miller, M.G., and Friedman, R.M., 1999, Early Tertiary magmatism and probable Mesozoic fabrics in the Black Mountains, Death Valley, California: Geology, v. 27, p. 19-22.

Molnar, P., 2010, Deuterium and oxygen isotopes, paleoelevations of the Sierra Nevada, and Cenozoic climate: Geological Society of America Bulletin, v. 122, p. 1106–1115.

Mulch, A., Graham, S.A., and Chamberlain, C.P., 2006, Hydrogen isotopes in Eocene river gravels and paleoelevation of the Sierra Nevada: Science, v. 313, p. 87–89.

Nilsen, T.H. and Clarke, S.H., 1975, Sedimentation and tectonics in the Early Tertiary continental borderland of central California: United States Geological Survey Professional Paper, 925, p. 64.

Pask, J.A., and Turner, M.D., 1952, Geology and Ceramic Properties of the Ione Formation, Buena Vista Area, Amador County, California: State of California, Department of Natural Resources, Division of Mines.

Peterson, G.L. and Abbott, P.L., 1979, Mid-Eocene climatic change, southwestern California and northwestern Baja California: Palaeogeography, Palaeoclimatology, Palaeoecology, v. 26, p. 73-87.

Robert, C. and Chamley, H., 1991, Development of early Eocene warm climates, as inferred from clay mineral variations in oceanic sediments: Palaeogeography, Palaeoclimatology, Palaeoecology, v. 89, p. 315-331.

Rodgers, C.L., 1986, Depositional environments of the Ione Formation, east-central California [M.S. thesis]: California State University at Fresno, Fresno, California, 114p.

Saleeby, J., 2003, Segmentation of the Laramide slab: Evidence from the southern Sierra Nevada region: Geological Society of America Bulletin, v. 115, no. 6, p. 655–668.

Schmitz, B., Pujalte, V., and Nunez-Betelu, K., 2001, Climate and sea-level perturbations during the Initial Eocene Thermal Maximum: Evidence from siliciclastic units in the Basque Basin (Ermua, Zumaia and Trabakua Pass), northern Spain: Palaeogeography, Palaeoclimatology, Palaeoecology, v. 165, p. 299–320.

Smith, E.I., Sánchez, A., Keenan, D.L., & Monastero, F.C., 2002, Stratigraphy and geochemistry of volcanic rocks in the Lava Mountains, California: Implications for the Miocene development of the Garlock fault. Geologic evolution of the Mojave Desert and southwestern Basin and Range: Geological Society of America Memoir, 195, p. 151-160.

Smith, G.I., 1964, Geology and volcanic petrology of the Lava Mountains, San Bernardino County, California: U.S. Geologic Survey Professional Paper 457, 97 p.

Smith, M.E., Carroll, A.R., and Mueller, E.R., 2008, Elevated weathering rates in the Rocky Mountains during the Early Eocene Climatic Optimum: Nature Geoscience, v. 1, p. 370-374.

Stockli, D.F., Surpless, B.E., and Dumitru, T.A., 2002, Thermochronological constraints on the timing and magnitude of Miocene and Pliocene extension in the central Wassuk Range, western Nevada: Tectonics, v. 21, p. 10-1 – 10-19.

Stockli, D.F., T.A. Dumitru, M.O. McWilliams, and K.A. Farley, 2003, Cenozoic tectonic evolution of the White Mountains, California and Nevada, Geological Society of America Bulletin, v. 115, 788–816.

Suchet, P.A. and Probst, J.L., 1995, A global model for present-day atmospheric/soil CO_2 consumption by chemical erosion of continental rocks (GEM-CO_2): Tellus B, v. 47, p. 273-280.

Surpless, B.E., Stockli, D.F., Dumitru, T.A., and Miller, E.L., 2002, Two-phase westward encroachment of Basin and Range extension into the northern Sierra Nevada: Tectonics, v. 21, p. 2-1 – 2-13.

Thiry, M., and Dupuis, M., 2000, Use of clay minerals for paleoclimatic reconstructions: Limits of the method with special reference to the Paleocene–lower Eocene interval: GFF, v. 122, p. 166–167.

Torres, M.A. and Gaines, R.R., 2013, Paleoenvironmental and Paleoclimatic Interpretations of the Late Paleocene Goler Formation, Southern California, USA, Based on Paleosol Geochemistry: Journal of Sedimentary Research, v. 83, p. 591-605.

Unruh, J.R., 1991, The uplift of the Sierra Nevada and implications for late Cenozoic epeirogeny in the western Cordillera: Geological Society of America Bulletin, v. 103, p. 1395–1404.

Wakabayashi, J., and Sawyer, T.L., 2001, Stream incision, tectonics, uplift and evolution of topography of the Sierra Nevada, California: The Journal of Geology, v. 109, p. 539–562.

Walker, J.D., Bidgoli, T.S., Didericksen, B.D., Stockli, D.F., and Andrew, J.E., 2014, Middle Miocene to Recent Exhumation of the Slate Range, eastern California, and implication for the timing of extension and the transition to transtension: Geosphere, doi:10.1130;GES00947.1.

Wells, M.L., Beyene, M.A., Spell, T.L., Kula, J.L., Miller, D.M., and Zanetti, K.A., 2005, The Pinto shear zone; a Laramide synconvergent extensional shear zone in the Mojave Desert region of the southwestern United States: Journal of structural geology, v. 27, p. 1697-1720.

Wells, M.L. and Hoisch, T.D., 2008, The role of mantle delamination in widespread Late Cretaceous extension and magmatism in the Cordilleran orogen, western United States: Geological Society of America Bulletin, v. 120, p. 515-530.

Wernicke, B.P., Axen, G.J., and Snow, J.K., 1988, Basin and Range extensional tectonics at the latitude of Las Vegas, Nevada: Geological Society of America Bulletin, v. 100, p. 1738-1757.

Wernicke, B., Clayton, R., Ducea, M., Jones, C.H., Park, S., Ruppert, S., Saleeby, J., Snow, J.K., Squires, L., Fliedner, M., Jiracek, G., Keller, R., Klemperer, S., Luetgert, J., Malin, P., Miller, K., Mooney, W., Oliver, H., and Phinney, R., 1996, Origin of high mountains in the continents: The southern Sierra Nevada: Science, v. 271, p. 190–193.

Wilf, P., 2000, Late Paleocene–early Eocene climate changes in southwestern Wyoming: Paleobotanical analysis: Geological Society of America Bulletin, v. 112, p. 292–307

Wood, J., and Saleeby, J., 1997, Late Cretaceous-Paleocene extensional collapse and disaggregation of the southernmost Sierra Nevada batholith: International Geology Review, v. 39, p. 973-1009.

Wood, J.L, 1994, A re-evaluation of the origin of kaolinite in the Ione Depositional System (Eocene), Sierra Foothills, California [M.S. thesis]: California State University – Los Angeles, Los Angeles, California, 86 p.

Yin, A., 2002, Passive-roof thrust model for the emplacement of the Pelona-Orocopia Schist in southern California, United States: Geology, v. 30, p. 183-186.

Zachos, J., Pagani, M., Sloan, L., Thomas, E., and Billups, K., 2001, Trends, rhythms, and aberrations in global climate 65 Ma to present: Science, v. 292, p. 686-693.

Figure captions

Figure 5.1. Shaded relief map of southern California and western Nevada showing the spatial and temporal distribution of cooling ages from the Sierra Nevada, western Great Basin and Mojave Desert. Cooling age data are scaled and stacked with age. AHe – Apatite Helium; AFT – Apatite Fission Track; BAr – Biotite K/Ar or $^{40}Ar/^{39}Ar$; ZHe – Zircon Helium; ZFT – Zircon Fission Track. Data sources: Mojave – Armstrong and Suppe (1973), Miller and Morton (1980); Foster et al. (1991, 1992); Wells et al. (2005); Sierra Nevada – Dumitru et al. (1990), House et al. (1997; 2001), Cecil et al. (2006), Clark et al. (2005), Maheo et al. (2009), Blythe et al. (2013); Western Great Basin – Surpless et al. (2002), Stockli et al. (2002; 2003), Lee et al. (2009), Mahan et al. (2009); Ferril et al. (2012), Gorynski et al. (2013), and Walker et al. (2014).

Figure 5.2. Simplified cross-sections across the Argus Range (A-A'), Clark Mountains (B-B'), Lucy Gray Range (C-C'), and Spring Mountains (D-D'). Thermochronology samples, shown as black dots, are projected into the plane of the cross-section, oriented ~EW. In this projected view, they may lie above or below topography of the section line. Mean zircon (black text) and apatite (blue text) (U-Th)/He ages and errors (1σ standard deviation) are shown above each sample. Cross section locations shown on Figure 1. Geology from compilation of Ludington et al. (2007).

Figure 5.3. Histograms of detrital zircon (blue) and apatite (yellow) (U-Th)/He ages from the Miocene Bedrock Springs Formation. Data are binned in 5 Ma intervals and show

distinct peaks at ~65 Ma and ~50 Ma, suggesting exhumation of northern Mojave basement sources at those time.

Figure 5.4. Age versus paleodepth or elevation for the western Great Basin including the ranges analyzed in this study. Individual reconstructions are modified from Surpless et al. (2002, Singatse Range); Gorynski et al. (2013, Wassuk Range); Stockli et al. (2003, White Mountains); Lee et al. (2009, Inyo Mountains); Walker et al. (2014; Slate Range); and Giallorenzo (2013; Spring Mountains).

Figure 5.5. Global oxygen and carbon isotope curves from DSP and ODP sites, after Zachos, et al. (2001).

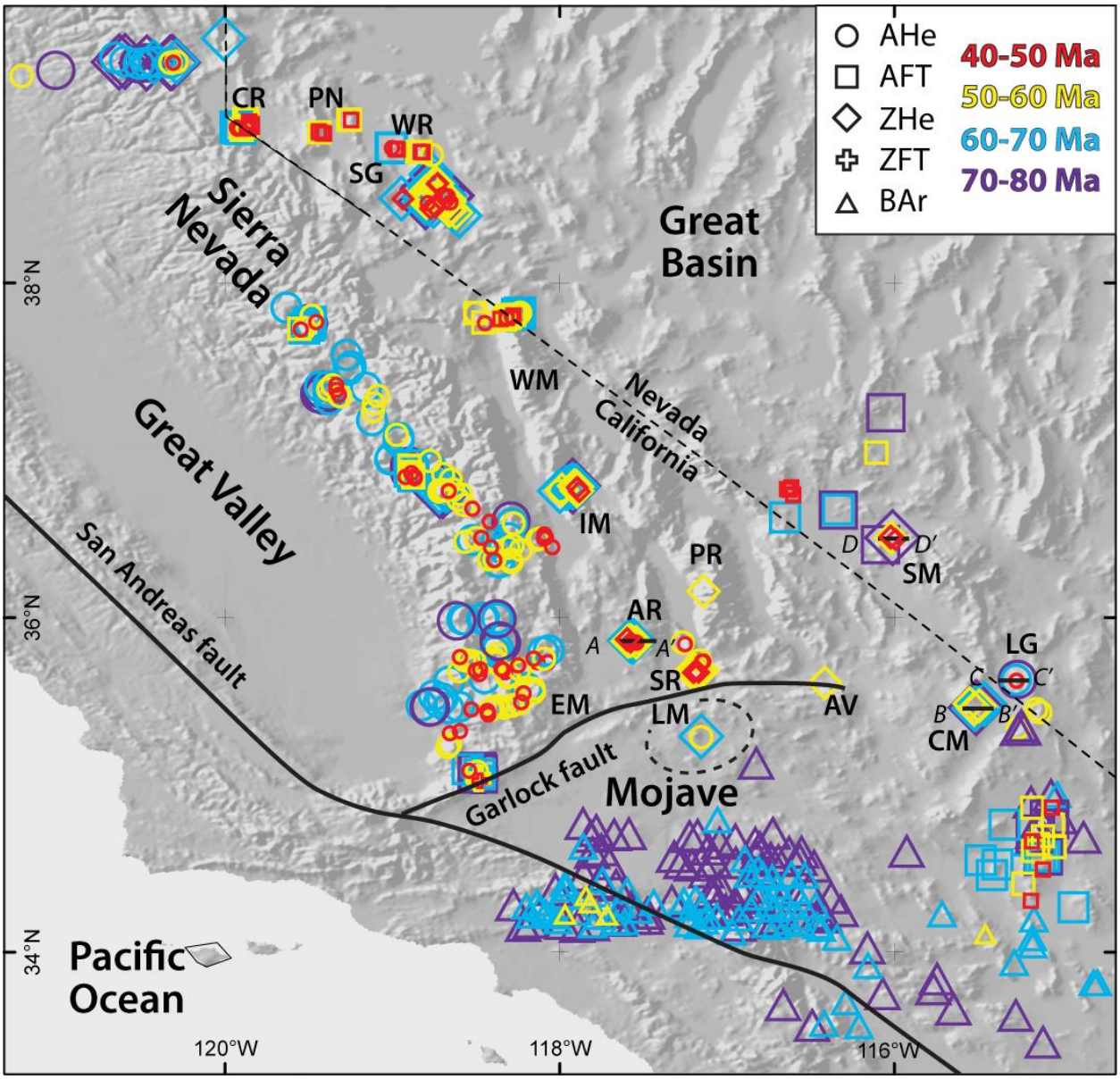
AHe
AFT
ZHe
ZFT
BAr
40-50 Ma
50-60 Ma
60-70 Ma
70-80 Ma
CR
PN
WR
SG
Sierra Nevada
Great Basin
WM
Nevada
California
Great Valley
IM
PR
D
D′
SM
San Andreas fault
AR
A
A′
SR
LG
C
C′
EM
LM
AV
B
B′
CM
Garlock fault
Mojave
Pacific Ocean
38°N
36°N
34°N
120°W
118°W
116°W

Figure 5.1

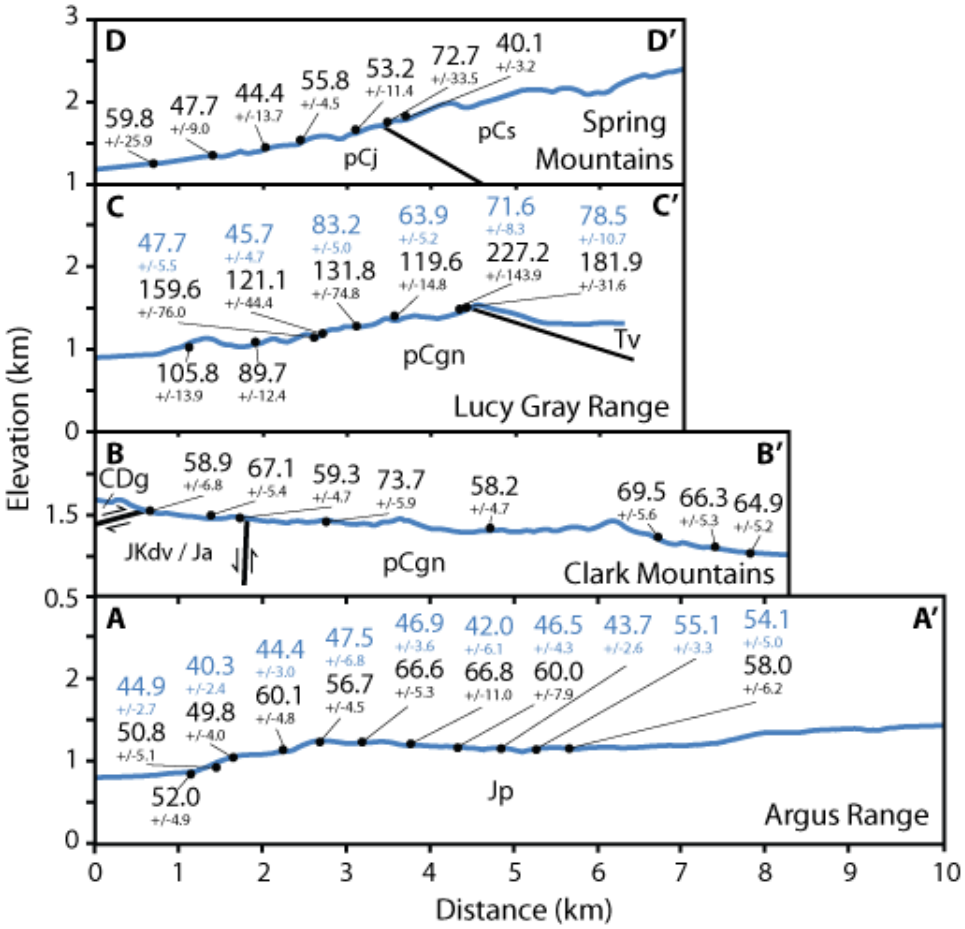
D
D′
59.8 +/-25.9
47.7 +/-9.0
44.4 +/-13.7
55.8 +/-4.5
53.2 +/-11.4
72.7 +/-33.5
40.1 +/-3.2
pCj
pCs
Spring Mountains
C
C′
47.7 +/-5.5
159.6 +/-76.0
45.7 +/-4.7
121.1 +/-44.4
83.2 +/-5.0
131.8 +/-74.8
63.9 +/-5.2
119.6 +/-14.8
71.6 +/-8.3
227.2 +/-143.9
78.5 +/-10.7
181.9 +/-31.6
105.8 +/-13.9
89.7 +/-12.4
pCgn
Tv
Lucy Gray Range
B
B′
CDg
58.9 +/-6.8
67.1 +/-5.4
59.3 +/-4.7
73.7 +/-5.9
58.2 +/-4.7
69.5 +/-5.6
66.3 +/-5.3
64.9 +/-5.2
JKdv / Ja
pCgn
Clark Mountains
A
A′
44.9 +/-2.7
50.8 +/-5.1
40.3 +/-2.4
49.8 +/-4.0
44.4 +/-3.0
60.1 +/-4.8
47.5 +/-6.8
56.7 +/-4.5
46.9 +/-3.6
66.6 +/-5.3
42.0 +/-6.1
66.8 +/-11.0
46.5 +/-4.3
60.0 +/-7.9
43.7 +/-2.6
55.1 +/-3.3
54.1 +/-5.0
58.0 +/-6.2
52.0 +/-4.9
Jp
Argus Range
Elevation (km)
Distance (km)
0
0.5
1
1.5
2
3
4
5
6
7
8
9
10

Figure 5.2

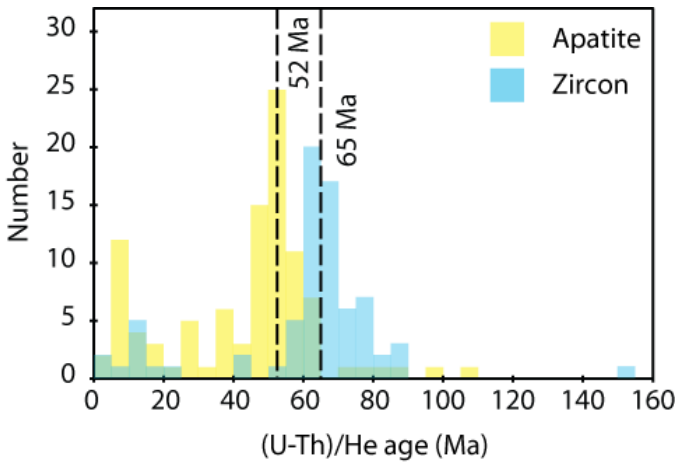
Apatite
Zircon
52 Ma
65 Ma
Number
(U-Th)/He age (Ma)
0
5
10
15
20
25
30
0
20
40
60
80
100
120
140
160

Figure 5.3

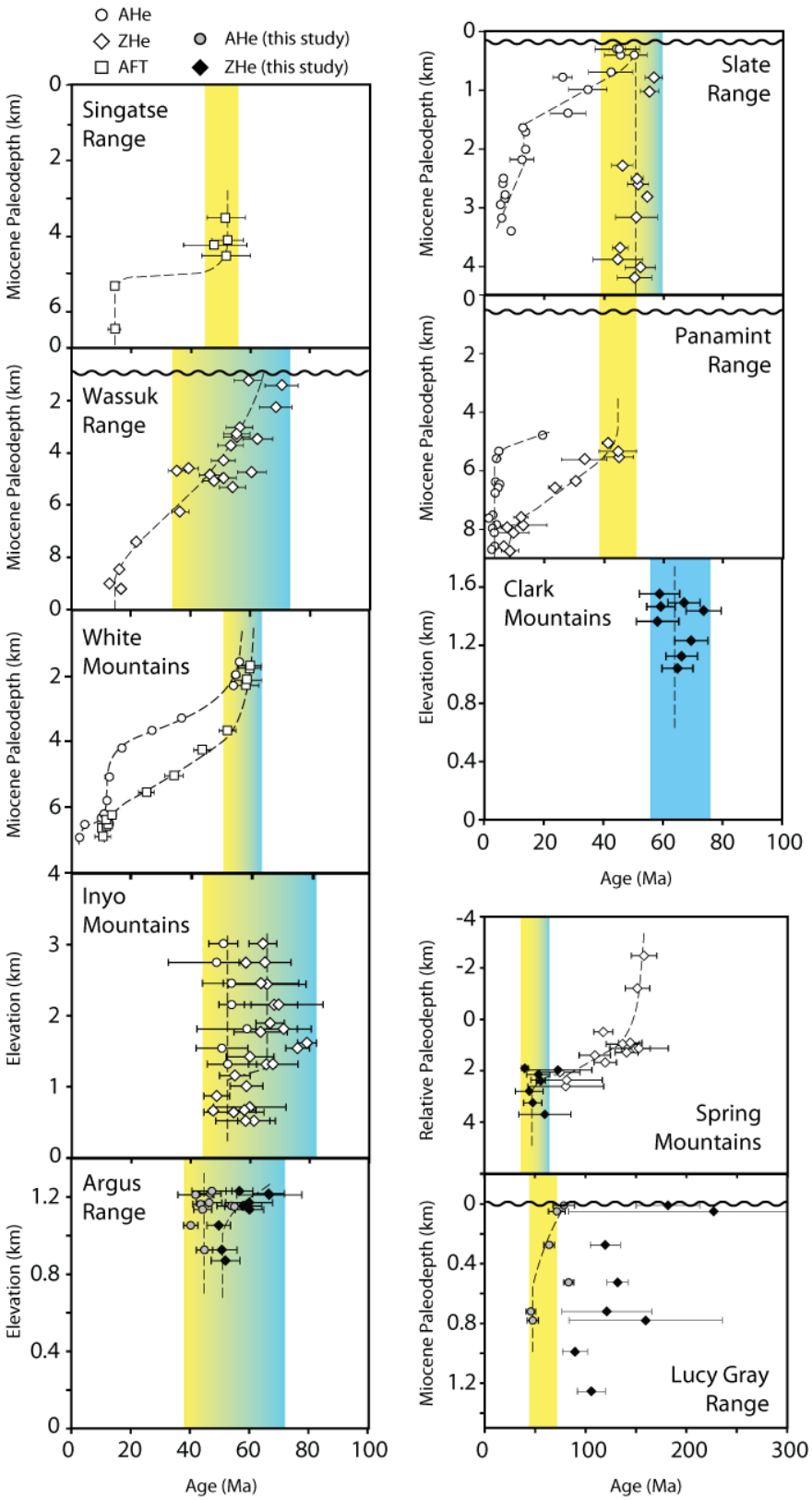
AHe
ZHe
AFT
AHe (this study)
ZHe (this study)
Singatse Range
Wassuk Range
White Mountains
Inyo Mountains
Argus Range
Slate Range
Panamint Range
Clark Mountains
Spring Mountains
Lucy Gray Range
Miocene Paleodepth (km)
Elevation (km)
Relative Paleodepth (km)
Age (Ma)

Figure 5.4

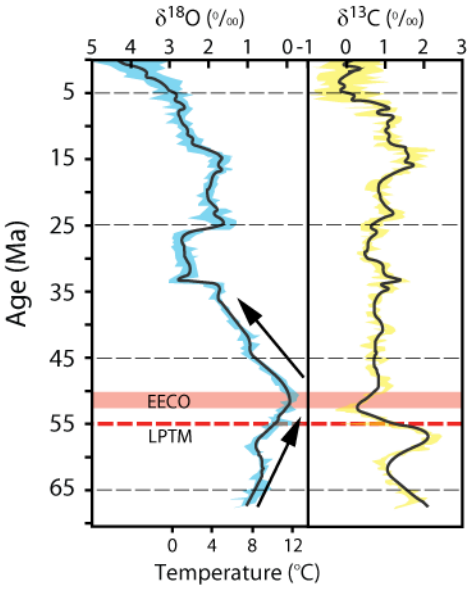
δ18O (‰)
δ13C (‰)
5 4 3 2 1 0 -1
0 1 2 3
Age (Ma)
5
15
25
35
45
55
65
EECO
LPTM
0 4 8 12
Temperature (°C)

Figure 5.5

Appendix 5.1

Analytical Procedures

We used standard mineral separation techniques to isolate and concentrate apatite and zircon from our rock samples. Individual grains were evaluated for size and clarity using a 180X Nikon stereo microscope with crossed polarizers and mounted digital camera. When possible, we selected near euhedral grains, greater than 70 μm in width that appeared inclusion-free. These guidelines minimize the effects of U and Th-bearing inclusion, which increase the accuracy and reproducibility of (U-Th)/He ages by minimizing the effects of U and Th-bearing inclusions and the alpha-ejection (Ft) correction (Farley et al., 1996). Each single-grain was then loaded into a 1-mm platinum packet. Apatite grains were heated for 5 minutes at 1070°C using a continuous-mode laser. Zircon grains were heated for 10 minutes at 1300°C. The extracted He gas was spiked with ^{3}He, purified using a gettering and cryogenic gas system, and measured on a Blazers Prisma QMS-200 quadrupole mass spectrometer. The degassed apatite grains were then dissolved (in their Pt packets) in a spiked (^{230}Th, ^{235}U, ^{149}Sm) HNO_3 solution and analyzed using a Thermo Scientific Element-2 inductively coupled plasma mass spectrometer (ICP-MS). After laser degassing, zircon grains were removed from packets and dissolved using standard U-Pb high-pressure vessel digestion procedures (HF-HNO_3 and HCl). Following dissolution, samples were spiked (^{230}Th, ^{235}U, ^{149}Sm) and analyzed for U, Th, and Sm using an ICP-MS. Laboratory and analytical work was performed at the Isotope Geochemistry Laboratories at the University of Kansas and the (U-Th)/He Geo- and Thermochronology Lab at the University of Texas at Austin.

Error Reporting

Propagated analytical uncertainties for individual analyses are approximately 3-4% (2σ). However, analytical uncertainties generally underestimate the reproducibility of a sample because uncertainties related to the Ft correction and U and Th distributions are difficult to quantify. We follow common practice in (U-Th)/He dating and apply percentage errors of 6% for apatite and 8% for zircon to individual analyses based on the reproducibility of laboratory standards (Farley et al., 2001; Reiners et al., 2002; Tables SD5.1 and SD5.2). For our mean ages, we report the error as the standard deviation (1σ) of our grain population for a given sample (Table SD5.1). However, 2 samples (12WC10, 11CM09) are single grain ages; therefore, we show the error in the "mean" age as the standard error in figures.

Table SD5.1 shows our (U-Th)/He mean ages and associated errors (1σ). In most cases (N=39), three replicates were used to calculate the mean; however, 11 of the 50 mean ages were calculated using fewer than three replicates. These samples contained outliers that were excluded from our calculated mean ages. Of the 169 single-grain analyses completed, 17 or ~10% of the aliquots were excluded. Outliers were determined as ages that were more than 2 standard deviations from the mean. Analyses with a large number of reextractions during laser He degassing were also excluded from the determined means, as this usually points to the presence of unseen mineral or fluid inclusions within the grain (House et al., 1999).

Although most of our mean ages were calculated with 3 or more replicates, many of the reported standard deviations in Table SD5.1 are quite large (>20%) and show that there is a wide span of dates captured by our mean (U-Th)/He ages, particularly for zircon. Individual zircon dates for some of our samples (e.g., Spring Mountains) are negatively correlated with both [He] and the [U]e, which suggests radiation damage effects are a contributing factor (Figure 3;

Reiners et al., 2002; 2004; Nasdala, 2004; Reich et al., 2007; Guenthner et al., 2013). Likewise radiation damage effects are observed for apatite (U-Th)/He ages in the Lucy Gray Range (Shuster et al., 2006; Flowers et al., 2009).

References

Farley, K.A., Rusmore, M.E., and Bogue, S.W., 2001, Exhumation and uplift history of the central Coast Mountains, British Columbia, from apatite (U-Th)/He Thermochronometry: Geology, v. 29, p. 99-102.

Farley, K.A., Wolf, R.A., and Silver, L.T., 1996, The effects of long alpha-stopping distances on (U-Th)/ He ages: Geochimica et Cosmochimica Acta, v. 60, p. 4223-4229.

Flowers R.M., Ketcham R.A., Shuster D.L., Farley K.A., 2009, Apatite (U-Th)/He thermochronometry using a radiation damage accumulation and annealing model, Geochimica et Cosmochimica Acta, v. 73, p. 2347-2365.

Guenthner, W., Reiners, P.W., Ketcham, R.A., Nasdala, L., and Giester, G., 2013, Helium diffusion in natural zircon: Radiation damage, anisotropy, and the interpretation of zircon (U-Th)/He thermochronology: American Journal of Science, v. 313, p. 145-198.

House, M.A., Farley, K.A., and Kohn, B.P., 1999, An empirical test of helium diffusion in apatite; borehole data from the Otway Basin, Australia: Earth and Planetary Science Letters, v. 170, p. 463-474.

Nasdala, L., Reiners, P.W., Garver, J.I., Kennedy, A.K., Stern, R.A., Balan, E, and Wirth, R., 2004, Incomplete retention of radiation damage in zircon from Sri Lanka: American Mineralogist, v. 89, p. 219-231.

Reich, M., Ewing, R.C., Ehlers, T.A., and Becker, U., 2007, Low-temperature anisotropic diffusion of helium in zircon: Implications for zircon (U-Th)/He thermochronometry, Geochimica et Cosmochimica Acta, v. 71, p. 3119-3130.

Reiners, P.W., Farley, K.A., and Hickes, H.J., 2002, He diffusion and (U-Th)/He thermochronometry of zircon: Initial results from Fish Canyon Tuff and Gold Butte: Tectonophysics, v. 349, p. 247–308.

Reiners, P.W., Spell, T.L., Nicolescu, S., and Zanetti, K.A., 2004, Zircon (U-TH)/He thermochronometry: He diffusion and comparison with 40Ar/39Ar dating: Geochimica et Cosmochimica Acta, v. 68, p. 1857-1887.Shuster, D.L., Flowers, R.M., and Farley, K.A., 2006, The influence of natural radiation damage on helium diffusion kinetics in apatite: Earth and Planetary Science Letters, v. 249, doi: 10.1016/j.epsl.2006.07.028.

Shuster D. L., Flowers R. M., and Farley K. A., 2006, The influence of natural radiation damage on helium diffusion kinetics in apatite. Earth and Planetary Science Letters 249(3-4), 148-161.

Stockli, D. F., Farley, K. A., and Dumitru, T. A., 2000, Calibration of the apatite (U-Th)/He thermochronometer on an exhumed fault block, White Mountains, California: Geology, v. 28, p. 983–986, 2000.

Wolf, R.A., Farley, K.A., and Silver, L.T., 1996, Helium diffusion and low temperature thermochronometry of apatite: Geochimica Cosmochimica Acta, v. 60, p. 4231-4240.

Wolf, R.A., Farley, K.A., and Kass, D.M., 1998, Modeling of the temperature sensitivity of the apatite (U-Th)/He thermochronometer: Chemical Geology, v. 148, p. 105-114.

Wolfe, M.R. and Stockli, D.F., 2010, Zircon (U-Th)/He thermochronometry in the KTB drillhole, Germany, and its implications for bulk He diffusion kinetics in zircon, Earth and Planetary Science Letters v. 295, p. 69-82.

Table SD5.1. Mean zircon and apatite (U-Th)/He ages

Sample	Longitude	Latitude	Elevation (m)	Mass (µg)	Ft*	U (ppm)	Th (ppm)	Sm (ppm)	Th/U	He (nmol/g)	Mean age (Ma)	St.Dev.† (Ma)	Replicates
Argus Range apatite													
12WC01	-117.5434	35.8522	1153	1.83	0.63	4.8	15.3	37.5	3.25	1.6	54.1	5.0	2
12WC02	-117.5477	35.8558	1150	1.59	0.62	27.3	69.1	63.6	5.04	8.1	55.1	2.2	4
12WC03	-117.5524	35.8583	1162	0.79	0.54	10.0	5.4	48.1	0.57	1.5	43.7	1.4	2
12WC04	-117.5580	35.8586	1170	1.55	0.61	10.0	32.5	25.9	3.26	2.7	46.5	4.3	2
12WC05	-117.5641	35.8580	1211	1.19	0.57	13.7	41.0	21.9	3.01	3.1	42.0	6.1	3
12WC06	-117.5705	35.8586	1217	1.40	0.59	11.2	32.6	25.8	2.91	2.8	46.9	3.6	3
12WC07	-117.5759	35.8618	1230	1.62	0.61	10.2	33.1	26.5	3.46	2.9	47.5	6.8	3
12WC08	-117.5808	35.8634	1135	1.69	0.61	9.2	24.1	24.7	2.64	2.2	44.4	3.0	4
12WC09	-117.5873	35.8598	1053	0.88	0.54	4.7	14.7	21.9	3.21	1.0	40.3	0.3	2
12WC10	-117.5894	35.8618	926	1.45	0.58	7.9	21.1	28.0	2.68	1.9	44.9	-	1
12WC11	-117.5928	35.8591	870	1.57	0.61	18.6	50.3	21.6	2.70	0.7	6.5	0.8	4
Argus Range zircon													
12WC01	-117.5434	35.8522	1153	6.29	0.76	84.1	78.9	0.6	0.91	24.7	58.0	6.2	3
12WC04	-117.5580	35.8586	1170	4.33	0.72	352.9	271.3	0.9	0.73	99.4	60.0	7.9	3
12WC05	-117.5641	35.8580	1211	6.43	0.76	46.2	39.8	0.4	0.86	15.2	66.8	11.0	2
12WC06	-117.5705	35.8586	1217	5.72	0.76	55.9	43.3	0.6	0.77	18.1	66.6	2.7	3
12WC07	-117.5759	35.8618	1230	7.86	0.79	43.6	35.0	0.3	0.80	12.5	56.7	4.4	3
12WC08	-117.5808	35.8634	1135	5.94	0.76	41.0	33.6	0.3	0.82	12.2	60.1	1.2	3
12WC09	-117.5873	35.8598	1053	5.76	0.76	110.2	63.4	0.6	0.61	25.4	49.8	2.7	3
12WC10	-117.5894	35.8618	926	6.13	0.77	108.2	58.6	0.7	0.55	26.3	50.8	5.1	3
12WC11	-117.5928	35.8591	870	6.46	0.77	227.4	211.3	0.7	0.93	60.2	52.0	4.9	2
Avawatz Mountains zircon													
12CC01	-116.4166	35.6099	435	6.49	0.76	365.4	254.9	1.6	0.65	91.3	52.6	6.1	3
Clark Mountains zircon													
11CM01	-115.5505	35.4862	1553	4.24	0.74	333.1	270.2	11.7	0.87	91.9	58.9	6.8	3
11CM01B	-115.5228	35.4536	1492	10.15	0.79	110.1	203.5	1.8	1.83	45.0	67.1	3.5	2
11CM02	-115.5206	35.4566	1465	5.63	0.77	366.4	106.3	1.3	0.29	96.2	59.3	1.5	2
11CM04	-115.5115	35.4626	1437	6.95	0.78	346.5	43.0	1.8	0.12	112.4	73.7	4.5	2
11CM06	-115.4928	35.4718	1363	6.46	0.77	617.9	94.9	6.4	0.17	152.8	58.2	7.1	3

(continued)

Table SD5.1. Mean zircon and apatite (U-Th)/He ages (continued)

Sample	Longitude	Latitude	Elevation (m)	Mass (μg)	Ft*	U (ppm)	Th (ppm)	Sm (ppm)	Th/U	He (nmol/g)	Mean age (Ma)	St.Dev.† (Ma)	Replicates
11CM09	-115.4732	35.4806	1231	3.55	0.74	503.8	256.6	2.0	0.51	156.6	69.5	-	1
11CM10	-115.4656	35.4826	1124	2.76	0.71	589.5	140.1	1.7	0.23	155.9	66.3	2.7	4
11CM11	-115.4614	35.4824	1041	4.81	0.75	554.4	76.8	1.2	0.13	151.8	64.9	2.0	3
Lucy Gray Range apatite													
11LG03	-115.2842	35.6307	1142	3.29	0.69	33.8	90.9	35.3	2.68	10.0	47.7	5.5	3
11LG04	-115.2830	35.6292	1194	1.21	0.58	37.9	166.8	54.1	4.63	11.7	45.7	4.7	3
11LG05	-115.2785	35.6289	1297	2.17	0.65	44.3	170.9	66.6	3.87	24.8	83.2	2.5	3
11LG06	-115.2734	35.6283	1440	0.91	0.54	72.1	290.1	88.0	4.01	27.2	63.9	5.2	3
11LG07	-115.2650	35.6301	1506	2.10	0.63	52.2	218.7	117.7	4.26	25.4	71.6	8.3	3
11LG08	-115.2641	35.6301	1528	1.06	0.55	66.1	260.1	71.0	3.94	30.4	78.5	10.7	3
Lucy Gray Range zircon													
11LG01	-115.3002	35.6252	1014	10.71	0.79	915.6	455.6	4.0	0.49	470.4	105.8	13.9	3
11LG02	-115.2920	35.6311	1098	6.47	0.77	646.3	136.6	1.4	0.22	243.8	89.7	12.4	3
11LG03	-115.2842	35.6307	1142	13.10	0.81	321.9	142.6	1.5	0.45	234.7	159.6	76.0	3
11LG04	-115.2830	35.6292	1194	7.07	0.77	796.6	215.9	5.0	0.39	325.2	121.1	44.4	3
11LG05	-115.2785	35.6289	1297	7.99	0.78	262.6	109.0	2.4	0.41	159.6	131.8	7.4	3
11LG06	-115.2734	35.6283	1440	7.76	0.77	372.5	217.0	3.9	0.58	207.9	119.6	14.8	3
11LG07	-115.2650	35.6301	1506	9.12	0.78	309.1	168.2	2.0	0.53	264.9	227.2	143.9	3
11LG08	-115.2641	35.6301	1528	4.85	0.74	195.9	107.1	2.6	0.55	162.2	181.9	31.6	3
Spring Mountains zircon													
11SM01	-116.0060	36.4732	1832	6.17	0.77	284.2	66.0	1.1	0.23	50.0	40.1	2.1	3
11SM02	-116.0079	36.4747	1751	23.68	0.83	84.7	76.5	1.7	0.97	23.2	72.7	33.5	5
11SM03	-116.0113	36.4770	1669	4.79	0.75	290.4	125.1	2.5	0.48	62.2	53.2	11.4	5
11SM04	-116.0189	36.4771	1559	15.27	0.83	115.5	60.8	2.0	0.66	33.0	55.8	4.0	3
11SM05	-116.0229	36.4790	1448	7.23	0.78	220.6	75.5	3.3	0.33	40.5	44.4	13.7	3
11SM06	-116.0289	36.4819	1361	9.96	0.81	145.1	62.1	1.8	0.55	30.6	47.7	9.0	3
11SM07	-116.0363	36.4840	1256	1.61	0.66	183.6	104.1	1.5	0.56	43.1	59.8	25.9	3

Note: Details of analytical procedures and error reporting are given in Appendix 5.1; See Table SD 5.2 for individual aliquot analyses used in mean age.

*Ft is the alpha ejection correction of Farley et al. (1996).

†St. Dev.—standard deviation.

Table SD5.2. Zircon and apatite (U-Th)/He data

Sample	L (μm)	W (μm)	Mass (μg)	Ft*	U (ppm)	Th (ppm)	Sm (ppm)	[U]e	Th/U	He (nmol/g)	Corrected Age (Ma)	Mean age (Ma)	St.Dev.† (Ma)
Wilson Canyon, Argus Range													
12WC01	**124.1**	**85.1**	**1.83**	**0.63**	**4.8**	**15.3**	**37.5**	**8.5**	**3.25**	**1.6**	-	**54.1**	**5.0**
12WC01-1	*134.70*	*70.21*	*1.34*	*0.59*	*5.3*	*23.1*	*43.8*	*10.8*	*4.37*	*1.2*	*33.5*		
12WC01-2	127.55	72.96	1.37	0.60	6.7	20.8	44.4	11.7	3.12	2.0	50.6		
12WC01-3	*134.60*	*80.43*	*1.75*	*0.63*	*3.2*	*6.8*	*28.1*	*4.9*	*2.12*	*0.4*	*21.0*		
12WC01-4	120.67	97.24	2.30	0.67	2.9	9.8	30.5	5.3	3.39	1.1	57.7		
12WC02	**128.18**	**78.67**	**1.59**	**0.62**	**27.32**	**69.09**	**63.63**	**43.54**	**5.04**	**8.06**	**55.11**	**55.1**	**2.2**
12WC02-1	153.09	66.61	1.37	0.59	41.4	114.5	77.4	68.2	2.76	12.6	57.5		
12WC02-2	118.36	93.66	2.09	0.65	4.0	44.4	46.2	14.5	11.05	2.8	53.2		
12WC02-3	113.10	75.73	1.31	0.61	36.5	48.3	67.3	47.9	1.32	8.7	54.6		
12WC02-4	*129.08*	*87.63*	*2.00*	*0.66*	*23.5*	*39.2*	*38.2*	*32.7*	*1.67*	*7.6*	*64.8*		
12WC03	**125.2**	**56.0**	**0.79**	**0.54**	**10.0**	**5.4**	**48.1**	**11.5**	**0.57**	**1.5**	-	**43.7**	**1.4**
12WC03-2	128.59	55.42	0.80	0.54	6.5	4.4	37.4	7.7	0.67	1.0	42.7		
12WC03-3	121.81	56.49	0.78	0.54	13.6	6.5	58.9	15.3	0.48	2.0	44.7		
12WC04	**135.11**	**74.39**	**1.55**	**0.61**	**10.0**	**32.5**	**25.9**	**17.6**	**3.26**	**2.72**	-	**46.5**	**4.3**
12WC04-1	146.80	82.11	1.99	0.64	9.8	29.6	22.2	16.8	3.02	2.6	43.5		
12WC04-2	*132.35*	*66.67*	*1.18*	*0.58*	*18.8*	*30.4*	*17.9*	*25.9*	*1.61*	*2.7*	*32.5*		
12WC04-3	123.42	66.67	1.10	0.57	10.1	35.4	29.6	18.4	3.50	2.9	49.6		
12WC04-4	*177.18*	*85.33*	*2.60*	*0.66*	*4.4*	*14.2*	*20.0*	*7.8*	*3.18*	*1.7*	*58.0*		
12WC05	**137.9**	**65.2**	**1.19**	**0.57**	**13.7**	**41.0**	**21.9**	**23.2**	**3.01**	**3.1**	-	**42.0**	**6.1**
12WC05-1	141.58	67.33	1.29	0.59	14.2	42.2	23.5	24.1	2.97	3.1	40.2		
12WC05-2	146.68	65.33	1.26	0.58	11.0	35.4	19.6	19.3	3.21	2.3	37.0		
12WC05-3	125.58	63.04	1.00	0.56	15.8	45.2	22.5	26.3	2.86	3.9	48.7		
12WC06	**156.48**	**66.58**	**1.40**	**0.59**	**11.2**	**32.6**	**25.8**	**18.9**	**2.91**	**2.83**	-	**46.9**	**3.6**
12WC06-1	190.31	69.52	1.85	0.61	9.6	27.7	24.2	16.1	2.89	2.5	46.2		
12WC06-2	131.87	69.27	1.27	0.59	13.0	34.4	24.6	21.0	2.65	2.9	42.2		
12WC06-3	145.40	67.33	1.33	0.59	9.5	28.8	24.0	16.3	3.04	2.6	50.4		
12WC06-4	158.33	60.20	1.16	0.56	13.0	39.6	30.2	22.2	3.06	3.3	49.0		

Sample	L (μm)	W (μm)	Mass (μg)	Ft*	U (ppm)	Th (ppm)	Sm (ppm)	[U]e	Th/U	He (nmol/g)	Corrected Age (Ma)	Mean age (Ma)	St.Dev.† (Ma)
12WC07	**141.19**	**74.37**	**1.62**	**0.61**	**10.2**	**33.1**	**26.5**	**17.9**	**3.46**	**2.94**	-	**47.5**	**6.8**
12WC07-1	149.18	77.23	1.79	0.63	3.2	12.6	25.7	6.2	3.92	0.9	40.6		
12WC07-2	148.22	83.97	2.10	0.65	16.5	47.6	30.4	27.7	2.88	4.7	47.7		
12WC07-3	126.16	61.90	0.97	0.55	10.8	39.0	23.5	19.9	3.60	3.3	54.1		
12WC08	**162.44**	**72.43**	**1.69**	**0.61**	**9.2**	**24.1**	**24.7**	**14.8**	**2.64**	**2.21**	-	**44.4**	**3.0**
12WC08-1	132.75	81.84	1.79	0.64	8.2	22.7	19.3	13.5	2.77	1.9	40.2		
12WC08-2	178.28	67.74	1.65	0.60	10.8	27.3	29.4	17.2	2.54	2.7	47.5		
12WC08-3	150.81	75.12	1.71	0.62	8.3	22.8	24.6	13.7	2.74	2.1	45.2		
12WC08-4	187.92	65.04	1.60	0.59	9.3	23.5	25.5	14.9	2.51	2.2	44.6		
12WC09	**113.19**	**62.08**	**0.88**	**0.54**	**4.7**	**14.7**	**21.9**	**8.2**	**3.21**	**0.99**	-	**40.3**	**0.3**
12WC09-3	130.75	62.63	1.03	0.56	5.3	14.4	21.2	8.7	2.74	1.1	40.1		
12WC09-4	95.63	61.52	0.73	0.53	4.1	15.1	22.7	7.7	3.68	0.9	40.5		
12WC10	**174.69**	**64.30**	**1.45**	**0.58**	**7.9**	**21.1**	**28.0**	**12.9**	**2.68**	**1.9**	-	**44.9**	-
12WC10-2	174.69	64.30	1.45	0.58	7.9	21.1	28.0	12.9	2.68	1.9	44.9		
12WC01	**217.1**	**77.3**	**6.29**	**0.76**	**84.1**	**78.9**	**0.6**	**102.3**	**0.91**	**24.7**	-	**58.0**	**6.2**
z12WC01-1	235.60	81.06	7.20	0.77	76.0	85.2	0.6	95.6	1.12	21.2	53.2		
z12WC01-2	171.23	66.16	3.49	0.72	139.0	125.3	0.6	167.9	0.90	42.6	65.0		
z12WC01-3	244.49	84.79	8.17	0.78	37.4	26.3	0.5	43.4	0.70	10.3	55.8		
12WC04	**220.4**	**65.4**	**4.33**	**0.72**	**352.9**	**271.3**	**0.9**	**415.3**	**0.73**	**99.4**	-	**60.0**	**7.9**
z12WC04-1	256.12	62.85	4.70	0.72	618.9	546.5	1.2	744.7	0.88	177.2	60.8		
z12WC04-2	225.26	58.42	3.58	0.70	297.2	155.5	0.8	333.0	0.52	85.9	67.6		
z12WC04-3	179.84	74.98	4.70	0.75	142.5	112.1	0.8	168.3	0.79	35.3	51.7		
12WC05	**218.1**	**79.6**	**6.43**	**0.76**	**46.2**	**39.8**	**0.4**	**55.3**	**0.86**	**15.2**	-	**66.8**	**11.0**
z12WC05-1	219.48	81.12	6.72	0.77	49.7	43.1	0.4	59.6	0.87	14.7	59.0		
z12WC05-3	216.78	78.09	6.15	0.76	42.7	36.5	0.4	51.1	0.86	15.8	74.6		
12WC06	**204.5**	**77.6**	**5.72**	**0.76**	**55.9**	**43.3**	**0.6**	**65.9**	**0.77**	**18.1**	-	**66.6**	**2.7**
z12WC06-1	210.99	75.89	5.65	0.75	50.5	39.5	0.4	59.6	0.78	15.7	64.2		
z12WC06-2	211.13	79.98	6.28	0.76	56.5	40.9	0.5	65.9	0.72	18.1	66.0		
z12WC06-3	191.26	76.80	5.24	0.75	60.7	49.4	0.8	72.1	0.81	20.5	69.5		

Sample	L (μm)	W (μm)	Mass (μg)	Ft*	U (ppm)	Th (ppm)	Sm (ppm)	[U]e	Th/U	He (nmol/g)	Corrected Age (Ma)	Mean age (Ma)	St.Dev.† (Ma)
12WC07	**170.7**	**99.3**	**7.86**	**0.79**	**43.6**	**35.0**	**0.3**	**51.6**	**0.80**	**12.5**	-	**56.7**	**4.4**
z12WC07-1	168.42	92.12	6.65	0.78	40.1	32.2	0.4	47.5	0.80	11.9	59.0		
z12WC07-2	174.99	104.24	8.84	0.80	53.5	43.1	0.3	63.4	0.81	14.2	51.7		
z12WC07-3	168.70	101.55	8.09	0.79	37.1	29.8	0.4	44.0	0.80	11.3	59.5		
12WC08	**154.6**	**88.2**	**5.94**	**0.76**	**41.0**	**33.6**	**0.3**	**48.7**	**0.82**	**12.2**	-	**60.1**	**1.2**
z12WC08-1	176.95	104.89	9.05	0.80	42.6	33.0	0.3	50.2	0.78	13.4	61.2		
z12WC08-2	152.37	89.78	5.71	0.77	39.2	30.1	0.3	46.1	0.77	11.3	58.7		
z12WC08-3	134.55	69.87	3.05	0.72	41.2	37.7	0.3	49.9	0.91	11.8	60.4		
12WC09	**192.9**	**80.1**	**5.76**	**0.76**	**110.2**	**63.4**	**0.6**	**124.8**	**0.61**	**25.4**	-	**49.8**	**2.7**
z12WC09-1	214.79	74.59	5.56	0.75	78.0	62.2	0.4	92.3	0.80	19.8	52.7		
z12WC09-2	185.84	73.69	4.69	0.75	167.5	82.9	0.8	186.6	0.50	37.2	49.3		
z12WC09-3	178.08	92.12	7.03	0.78	85.2	45.0	0.5	95.6	0.53	19.2	47.4		
12WC10	**166.8**	**88.3**	**6.13**	**0.77**	**108.2**	**58.6**	**0.7**	**121.7**	**0.55**	**26.3**	-	**50.8**	**5.1**
z12WC10-1	187.70	95.11	7.90	0.79	125.0	64.1	1.1	139.8	0.51	33.6	56.0		
z12WC10-2	155.31	87.60	5.54	0.77	111.7	58.6	0.5	125.2	0.53	26.4	50.6		
z12WC10-3	157.26	82.29	4.95	0.76	87.9	53.0	0.6	100.1	0.60	18.9	45.8		
12WC11	**191.9**	**85.0**	**6.46**	**0.77**	**227.4**	**211.3**	**0.7**	**276.1**	**0.93**	**60.2**	-	**52.0**	**4.9**
z12WC11-1	185.54	83.41	6.00	0.77	231.3	224.2	0.7	282.9	0.97	65.3	55.5		
z12WC11-2	*235.91*	*89.07*	*8.70*	*0.79*	*115.0*	*93.3*	*0.5*	*136.5*	*0.81*	*41.8*	*71.6*		
z12WC11-3	198.21	86.63	6.92	0.78	223.5	198.5	0.8	269.2	0.89	55.1	48.6		
CC Wash, Avawatz Mountains													
12CC01	**200.28**	**81.53**	**6.49**	**0.76**	**365.43**	**254.92**	**1.60**	**424.13**	**0.65**	**91.28**	-	**52.6**	**6.1**
z12CC01-1	128.27	71.54	3.05	0.72	334.2	203.6	1.4	381.1	0.61	71.2	47.7		
z12CC01-2	251.46	77.41	7.01	0.77	222.3	112.1	2.0	248.1	0.50	61.2	59.4		
z12CC01-3	221.12	95.64	9.41	0.80	539.8	449.1	1.4	643.2	0.83	141.5	50.9		
Mountain Pass, Clark Mountains													
11CM01	**170.9**	**72.7**	**4.2**	**0.7**	**333.1**	**270.2**	**11.7**	**395.3**	**0.9**	**91.9**	-	**58.9**	**6.8**
z11CM01-1	168.97	73.23	4.21	0.74	466.9	170.3	10.4	506.2	0.36	119.9	58.8		
z11CM01-2	201.87	75.44	5.34	0.75	310.8	499.2	17.1	425.8	1.61	90.3	52.1		
z11CM01-3	141.76	69.44	3.18	0.72	221.5	141.1	7.7	254.0	0.64	65.4	65.7		

Sample	L (μm)	W (μm)	Mass (μg)	Ft*	U (ppm)	Th (ppm)	Sm (ppm)	[U]e	Th/U	He (nmol/g)	Corrected Age (Ma)	Mean age (Ma)	St.Dev.† (Ma)
11CM01B	**191.9**	**100.9**	**10.2**	**0.8**	**110.1**	**203.5**	**1.8**	**156.9**	**1.8**	**45.0**	-	**67.1**	**3.5**
z11CM01B-1	228.78	121.26	15.64	0.83	81.3	143.6	1.9	114.4	1.77	33.4	64.6		
z11CM01B-2	*156.07*	*88.60*	*5.70*	*0.76*	*254.0*	*549.7*	*13.1*	*380.6*	*2.16*	*125.6*	*79.1*		
z11CM01B-3	154.94	80.48	4.67	0.75	138.8	263.4	1.6	199.4	1.90	56.6	69.6		
11CM02	**176.0**	**82.0**	**5.6**	**0.8**	**366.4**	**106.3**	**1.3**	**390.9**	**0.3**	**96.2**	-	**59.3**	**1.5**
z11CM02-1	164.92	73.89	4.19	0.74	361.4	153.9	1.8	396.8	0.43	93.2	58.3		
z11CM02-2	186.99	90.14	7.06	0.79	371.4	58.7	0.8	384.9	0.16	99.2	60.4		
z11CM02-3	*224.90*	*94.42*	*9.32*	*0.80*	*408.8*	*61.9*	*0.7*	*423.0*	*0.15*	*144.0*	*78.3*		
11CM04	**189.64**	**87.15**	**6.95**	**0.78**	**346.53**	**42.98**	**1.75**	**356.43**	**0.12**	**112.36**	-	**73.7**	**4.5**
z11CM04-1	213.12	96.34	9.20	0.80	392.4	53.6	1.8	404.8	0.14	135.4	76.8		
z11CM04-2	*172.46*	*93.05*	*6.94*	*0.79*	*187.4*	*22.1*	*0.6*	*192.5*	*0.12*	*74.9*	*90.7*		
z11CM04-3	166.16	77.96	4.70	0.76	300.6	32.4	1.7	308.1	0.11	89.3	70.5		
11CM06	**194.64**	**83.40**	**6.46**	**0.77**	**617.9**	**94.9**	**6.4**	**639.8**	**0.17**	**152.8**	-	**58.2**	**7.1**
z11CM06-1	194.86	82.50	6.17	0.77	486.6	120.7	3.2	514.4	0.25	140.6	65.3		
z11CM06-2	179.34	72.86	4.43	0.75	805.3	51.2	10.0	817.1	0.06	169.6	51.1		
z11CM06-3	209.72	94.84	8.77	0.80	561.8	112.7	6.0	587.8	0.20	148.3	58.3		
11CM08	**167.39**	**92.68**	**6.95**	**0.77**	**2049.4**	**20583.6**	**1808.2**	**6796.8**	**9.91**	**7123.8**	-	**229.8**	**93.6**
z11CM08-1	178.84	98.17	8.02	0.78	1644.6	16747.1	1630.0	5508.0	10.18	5265.8	220.2		
z11CM08-2	177.30	104.15	8.94	0.79	2119.1	12983.7	1436.4	5115.1	6.13	3161.8	141.4		
z11CM08-3	146.04	75.72	3.89	0.73	2384.6	32020.1	2358.1	9767.4	13.43	12943.7	327.8		
11CM09	**129.99**	**76.59**	**3.55**	**0.74**	**503.8**	**256.6**	**2.0**	**562.9**	**0.51**	**156.6**	-	**69.5**	-
z11CM09-1	*187.91*	*75.68*	*5.00*	*0.76*	*253.4*	*39.1*	*1.4*	*262.4*	*0.15*	*116.5*	*107.9*		
z11CM09-2	129.99	76.59	3.55	0.74	503.8	256.6	2.0	562.9	0.51	156.6	69.5		
z11CM09-3	*116.60*	*70.64*	*2.71*	*0.72*	*286.0*	*25.8*	*0.9*	*291.9*	*0.09*	*197.5*	*171.4*		
11CM10	**147.23**	**63.09**	**2.76**	**0.71**	**589.5**	**140.1**	**1.7**	**621.8**	**0.23**	**155.9**	-	**66.3**	**2.7**
z11CM10-1	150.15	59.19	2.45	0.70	613.8	190.9	3.0	657.8	0.31	159.0	64.2		
z11CM10-2	147.34	56.40	2.18	0.69	735.1	162.9	1.1	772.7	0.22	183.3	64.0		
z11CM10-3	142.05	77.59	3.98	0.75	436.1	41.8	1.7	445.8	0.10	126.1	69.5		
z11CM10-4	149.36	59.16	2.43	0.70	573.1	164.7	1.0	611.0	0.29	155.2	67.5		

Sample	L (µm)	W (µm)	Mass (µg)	Ft*	U (ppm)	Th (ppm)	Sm (ppm)	[U]e	Th/U	He (nmol/g)	Corrected Age (Ma)	Mean age (Ma)	St.Dev.† (Ma)
11CM11	**191.3**	**73.3**	**4.8**	**0.8**	**554.4**	**76.8**	**1.2**	**572.1**	**0.1**	**151.8**	-	**64.9**	**2.0**
z11CM11-1	178.02	72.22	4.32	0.75	429.3	54.7	0.8	441.9	0.13	118.3	66.2		
z11CM11-2	177.90	71.50	4.23	0.75	518.3	57.3	1.5	531.5	0.11	134.4	62.7		
z11CM11-3	217.89	76.11	5.87	0.76	715.6	118.5	1.3	742.9	0.17	202.7	66.0		
Lucy Gray Range													
11LG01	-	-	-	-	-	-	-	-	-	-	-	-	-
11LG01-1	*82.17*	*52.44*	*0.45*	*0.54*	*-3.4*	*1.1*	*-0.5*	*-3.2*	*-0.31*	*0.0*	*-0.6*		
11LG01-2	*56.58*	*50.87*	*0.29*	*0.49*	*-5.0*	*1.5*	*-0.8*	*-4.6*	*-0.31*	*0.0*	*-0.7*		
11LG01-3	*54.40*	*40.04*	*0.18*	*0.43*	*-7.0*	*3.0*	*-1.3*	*-6.3*	*-0.43*	*0.0*	*2.4*		
11LG02	-	-	-	-	-	-	-	-	-	-	-	-	-
11LG02-1	*94.48*	*71.50*	*0.97*	*0.57*	*2.2*	*12.7*	*42.9*	*5.3*	*5.84*	*9.3*	*537.1*		
11LG02-2	*83.42*	*49.90*	*0.42*	*0.47*	*24.0*	*16.9*	*123.9*	*28.5*	*0.70*	*4.7*	*63.8*		
11LG02-3	*109.19*	*42.07*	*0.39*	*0.44*	*31.0*	*6.3*	*142.6*	*33.2*	*0.20*	*7.7*	*95.4*		
11LG03	**169.8**	**97.3**	**3.3**	**0.7**	**33.8**	**90.9**	**35.3**	**54.9**	**2.7**	**10.0**	-	**47.7**	**5.5**
11LG03-1	135.55	106.43	3.09	0.70	26.3	58.6	27.8	40.0	2.22	7.6	49.6		
11LG03-2	201.85	106.54	4.61	0.72	11.8	35.5	21.4	20.1	3.01	3.3	41.4		
11LG03-3	172.04	78.98	2.16	0.64	63.3	178.6	56.5	104.6	2.82	19.1	51.9		
11LG04	**127.1**	**67.9**	**1.2**	**0.6**	**37.9**	**166.8**	**54.1**	**76.6**	**4.6**	**11.7**	-	**45.7**	**4.7**
11LG04-1	123.50	64.77	1.04	0.56	57.2	255.8	70.4	116.4	4.47	18.0	50.2		
11LG04-2	145.58	76.28	1.71	0.62	47.3	195.2	65.5	92.5	4.13	14.5	46.1		
11LG04-3	112.19	62.69	0.89	0.54	9.4	49.6	26.3	20.9	5.29	2.6	40.8		
11LG05	**157.98**	**82.96**	**2.17**	**0.65**	**44.25**	**170.90**	**66.61**	**83.93**	**3.87**	**24.76**	-	**83.19**	**2.5**
11LG05-1	132.32	90.26	2.17	0.66	33.0	121.6	38.7	61.2	3.68	18.0	81.5		
11LG05-2	164.96	84.26	2.36	0.65	45.7	208.4	96.7	94.2	4.56	29.1	86.0		
11LG05-3	176.65	74.38	1.97	0.63	54.0	182.7	64.5	96.4	3.38	27.1	82.0		
11LG06	**115.15**	**63.01**	**0.91**	**0.54**	**72.11**	**290.13**	**87.96**	**139.33**	**4.01**	**27.19**	-	**63.93**	**5.2**
11LG06-1	91.29	66.00	0.80	0.54	118.6	479.0	119.0	229.4	4.04	47.7	69.7		
11LG06-2	99.85	62.56	0.79	0.54	69.4	278.6	95.1	134.0	4.02	23.4	59.5		
11LG06-3	154.33	60.46	1.14	0.55	28.4	112.8	49.8	54.6	3.98	10.4	62.6		

Sample	L (μm)	W (μm)	Mass (μg)	Ft*	U (ppm)	Th (ppm)	Sm (ppm)	[U]e	Th/U	He (nmol/g)	Corrected Age (Ma)	Mean age (Ma)	St.Dev.† (Ma)
11LG07	**154.8**	**80.4**	**2.1**	**0.6**	**52.2**	**218.7**	**117.7**	**103.1**	**4.3**	**25.4**	-	**71.6**	**8.3**
11LG07-1	189.44	89.48	3.05	0.68	28.8	103.9	56.1	53.0	3.61	14.3	72.4		
11LG07-2	152.42	80.77	2.00	0.64	47.9	269.0	164.8	110.6	5.62	24.4	62.9		
11LG07-3	122.44	71.09	1.25	0.59	79.8	283.2	132.1	145.6	3.55	37.5	79.4		
11LG08	**139.54**	**61.22**	**1.06**	**0.55**	**66.11**	**260.12**	**71.00**	**126.34**	**3.94**	**30.40**	-	**78.50**	**10.7**
11LG08-1	148.46	61.03	1.11	0.56	61.1	246.4	79.0	118.2	4.04	25.8	71.5		
11LG08-2	155.12	62.49	1.22	0.57	54.9	215.2	63.3	104.7	3.92	23.8	73.2		
11LG08-3	115.03	60.14	0.84	0.53	82.4	318.8	70.7	156.1	3.87	41.6	90.8		
11LG01	**284.11**	**88.46**	**10.71**	**0.79**	**915.60**	**455.59**	**4.04**	**1020.50**	**0.49**	**470.40**	-	**105.77**	**13.9**
z11LG01-1	196.15	78.62	5.64	0.76	1588.8	835.7	8.6	1781.2	0.53	869.8	117.8		
z11LG01-2	306.92	97.99	13.70	0.81	384.3	190.2	1.6	428.0	0.50	205.9	108.8		
z11LG01-3	349.25	88.76	12.79	0.80	773.8	340.9	1.9	852.3	0.44	335.6	90.6		
11LG02	**204.22**	**79.81**	**6.47**	**0.77**	**646.29**	**136.63**	**1.35**	**677.74**	**0.22**	**243.78**	-	**89.69**	**12.4**
z11LG02-1	254.70	94.68	10.62	0.80	435.6	95.1	1.0	457.5	0.22	185.9	93.0		
z11LG02-2	201.28	74.50	5.19	0.76	921.0	139.4	1.7	953.1	0.15	297.2	76.0		
z11LG02-3	156.67	70.26	3.60	0.73	582.3	175.4	1.3	622.6	0.30	248.2	100.1		
11LG03	**301.58**	**96.24**	**13.10**	**0.81**	**321.93**	**142.64**	**1.55**	**354.77**	**0.45**	**234.66**	-	**159.63**	**76.0**
z11LG03-1	347.96	88.25	12.60	0.80	250.3	128.3	1.1	279.8	0.51	303.5	247.2		
z11LG03-2	269.12	87.03	9.48	0.79	372.1	156.8	1.9	408.2	0.42	195.4	111.3		
z11LG03-3	287.66	113.44	17.21	0.83	343.4	142.8	1.6	376.3	0.42	205.2	120.4		
11LG04	**231.6**	**80.4**	**7.1**	**0.8**	**796.6**	**215.9**	**5.0**	**846.3**	**0.4**	**325.2**		**121.1**	**44.4**
z11LG04-1	226.21	66.75	4.69	0.73	345.1	179.3	1.4	386.3	0.52	187.9	121.8		
z11LG04-2	246.47	80.40	7.41	0.77	187.6	80.6	1.4	206.2	0.43	143.9	165.2		
z11LG04-3	222.09	93.92	9.11	0.80	1857.1	387.8	12.2	1946.4	0.21	643.7	76.3		
11LG05	**256.5**	**81.9**	**8.0**	**0.8**	**262.6**	**109.0**	**2.4**	**287.7**	**0.4**	**159.6**	-	**131.8**	**7.4**
z11LG05-1	268.33	73.89	6.81	0.76	293.0	154.7	3.2	328.6	0.53	167.7	123.4		
z11LG05-2	264.00	78.19	7.51	0.77	222.0	84.3	1.9	241.4	0.38	139.3	137.2		
z11LG05-3	237.10	93.56	9.65	0.80	272.8	88.1	2.0	293.1	0.32	171.9	134.7		

Sample	L (μm)	W (μm)	Mass (μg)	Ft*	U (ppm)	Th (ppm)	Sm (ppm)	[U]e	Th/U	He (nmol/g)	Corrected Age (Ma)	Mean age (Ma)	St.Dev.† (Ma)
11LG06	**231.24**	**83.66**	**7.76**	**0.77**	**372.47**	**216.99**	**3.86**	**422.44**	**0.58**	**207.85**	-	**119.61**	**14.8**
z11LG06-1	265.21	95.91	11.34	0.81	405.5	163.1	4.4	443.1	0.40	241.6	124.3		
z11LG06-2	237.03	75.62	6.30	0.76	482.8	348.6	5.8	563.1	0.72	239.4	103.0		
z11LG06-3	191.49	79.46	5.62	0.76	229.1	139.2	1.3	261.2	0.61	142.6	131.6		
11LG07	**290.41**	**81.12**	**9.12**	**0.78**	**309.13**	**168.17**	**1.99**	**347.86**	**0.53**	**264.89**	-	**227.19**	**143.9**
z11LG07-1	242.06	71.88	5.82	0.75	486.1	277.6	2.9	550.0	0.57	266.5	118.6		
z11LG07-2	298.40	84.75	9.97	0.79	147.5	77.2	0.9	165.2	0.52	282.2	390.4		
z11LG07-3	330.78	86.73	11.57	0.79	293.8	149.7	2.2	328.3	0.51	245.9	172.6		
11LG08	**210.92**	**70.21**	**4.85**	**0.74**	**195.92**	**107.06**	**2.59**	**220.58**	**0.55**	**162.17**	-	**181.87**	**31.6**
z11LG08-1	221.48	70.41	5.11	0.74	164.0	89.9	1.6	184.7	0.55	136.8	182.1		
z11LG08-2	212.30	72.55	5.20	0.75	213.3	120.1	3.6	241.0	0.56	147.7	150.1		
z11LG08-3	199.00	67.67	4.24	0.73	210.4	111.2	2.6	236.0	0.53	202.1	213.4		
Spring Mountains													
11SM01	**186.4**	**82.6**	**6.2**	**0.8**	**284.2**	**66.0**	**1.1**	**299.4**	**0.2**	**50.0**	-	**40.1**	**2.1**
z11SM01-1	162.23	75.69	4.32	0.75	247.4	55.4	1.1	260.2	0.22	43.8	41.5		
z11SM01-2	169.70	77.72	4.77	0.76	377.2	96.6	1.7	399.5	0.26	67.3	41.1		
z11SM01-3	227.42	94.33	9.41	0.80	227.9	45.8	0.5	238.5	0.20	38.9	37.7		
11SM02	**279.5**	**125.6**	**23.7**	**0.8**	**84.7**	**76.5**	**1.7**	**102.3**	**1.0**	**23.2**	-	**72.7**	**33.5**
z11SM02-1	*219.41*	*145.17*	*21.50*	*0.85*	*252.3*	*209.9*	*5.4*	*300.7*	*0.83*	*40.6*	*29.3*		
z11SM02-2	200.59	92.31	7.95	0.79	51.7	55.0	1.2	64.4	1.06	18.6	67.4		
z11SM02-3	204.37	89.35	7.59	0.78	46.9	56.2	0.9	59.9	1.20	17.1	67.3		
z11SM02-4	*405.96*	*146.84*	*40.70*	*0.87*	*30.2*	*30.2*	*0.6*	*37.2*	*1.00*	*21.7*	*123.1*		
z11SM02-5	367.12	154.30	40.64	0.87	42.3	31.3	0.6	49.5	0.74	18.0	76.6		
11SM03	**161.7**	**78.2**	**4.8**	**0.7**	**290.4**	**125.1**	**2.5**	**319.2**	**0.5**	**62.2**	-	**53.2**	**11.4**
z11SM03-1	141.23	64.22	2.71	0.70	319.0	294.5	8.5	386.8	0.92	84.8	57.5		
z11SM03-2	*159.54*	*63.51*	*2.99*	*0.71*	*654.5*	*161.5*	*0.8*	*691.7*	*0.25*	*116.1*	*43.4*		
z11SM03-3	160.05	81.56	4.95	0.76	108.4	48.9	0.9	119.6	0.45	32.2	65.2		
z11SM03-4	*195.45*	*88.85*	*7.17*	*0.79*	*253.6*	*57.8*	*0.7*	*266.9*	*0.23*	*44.2*	*39.0*		
z11SM03-5	152.19	93.01	6.12	0.78	116.3	62.7	1.7	130.8	0.54	33.7	61.0		

Sample	L (μm)	W (μm)	Mass (μg)	Ft*	U (ppm)	Th (ppm)	Sm (ppm)	[U]e	Th/U	He (nmol/g)	Corrected Age (Ma)	Mean age (Ma)	St.Dev.† (Ma)
11SM04	**240.4**	**116.2**	**15.3**	**0.8**	**115.5**	**60.8**	**2.0**	**129.5**	**0.7**	**33.0**	-	**55.8**	**4.0**
z11SM04-1	240.88	128.69	18.55	0.84	36.8	38.4	0.7	45.6	1.04	10.7	51.3		
z11SM04-2	240.37	120.99	16.36	0.84	160.8	62.3	3.2	175.2	0.39	45.1	56.9		
z11SM04-3	239.84	98.90	10.91	0.81	149.0	81.6	2.0	167.8	0.55	43.4	59.1		
11SM05	**201.1**	**87.0**	**7.2**	**0.8**	**220.6**	**75.5**	**3.3**	**238.0**	**0.3**	**40.5**	-	**44.4**	**13.7**
z11SM05-1	216.57	98.85	9.84	0.80	159.8	47.6	1.1	170.8	0.30	36.1	48.6		
z11SM05-2	190.51	85.95	6.54	0.78	335.1	125.9	8.2	364.1	0.38	44.5	29.1		
z11SM05-3	196.16	76.34	5.32	0.76	166.8	53.1	0.8	179.0	0.32	40.8	55.5		
11SM06	**192.6**	**105.3**	**10.0**	**0.8**	**145.1**	**62.1**	**1.8**	**159.4**	**0.5**	**30.6**	-	**47.7**	**9.0**
z11SM06-1	184.77	117.84	11.93	0.82	266.1	81.5	2.4	284.9	0.31	50.1	39.5		
z11SM06-2	195.01	97.84	8.68	0.80	117.6	64.5	1.1	132.4	0.55	26.6	46.4		
z11SM06-3	198.16	100.27	9.26	0.80	51.5	40.3	2.0	60.8	0.78	15.1	57.3		
11SM07	**114.9**	**55.5**	**1.6**	**0.7**	**183.6**	**104.1**	**1.5**	**207.5**	**0.6**	**43.1**	-	**59.8**	**25.9**
z11SM07-1	141.76	51.34	1.74	0.65	250.7	156.7	0.5	286.8	0.63	79.7	78.4		
z11SM07-2	118.68	55.73	1.71	0.67	80.4	43.6	2.7	90.5	0.54	23.1	70.7		
z11SM07-3	84.16	59.38	1.38	0.66	219.5	112.1	1.3	245.3	0.51	26.4	30.3		

Notes: See appendix 5.1 for discussion of analytical procedures and errors; samples in italics were not included in our calculated mean ages.

*Ft is the alpha ejection correction of Farley et al. (1996).

†St. Dev.—standard deviation.

Table SD5.3. Lava Mountains detrital (U-Th)/He data

Sample	Latitude	Longitude	L (μm)	W (μm)	Mass (μg)	Ft*	U (ppm)	Th (ppm)	Sm (ppm)	[U]e	Th/U	He (nmol/g)	Corrected Age (Ma)	Error (Ma)
Apatite data														
LV2010A1-1	35.441913	-117.489229	107.97	91.34	1.81	0.66	13.1	14.8	49.1	16.7	1.13	0.6	9.9	0.29
LV2010A1-2	35.441913	-117.489229	204.15	133.72	7.35	0.77	34.5	41.7	24.3	44.2	1.21	1.2	6.6	0.04
LV2010A1-3	35.441913	-117.489229	166.63	85.70	2.46	0.66	46.3	96.9	22.1	68.7	2.09	2.1	8.5	0.04
LV2010A2-1	35.456516	-117.491592	197.81	108.96	4.73	0.73	69.4	92.8	69.4	91.1	1.34	19.6	54.1	4.33
LV2010A2-2	35.456516	-117.491592	211.43	97.29	4.03	0.70	8.2	21.7	15.4	13.3	2.63	0.3	6.7	0.54
LV2010A2-3	35.456516	-117.491592	156.18	74.55	1.75	0.63	19.6	29.1	38.5	26.5	1.49	2.6	28.2	2.26
LV2010A3-1	35.469007	-117.491959	109.57	78.92	1.37	0.61	52.2	126.2	64.2	81.6	2.42	15.0	54.9	0.47
LV2010A3-2	35.469007	-117.491959	160.49	92.44	2.76	0.70	77.3	28.6	58.7	84.2	0.37	16.6	52.1	0.40
LV2010A3-3	35.469007	-117.491959	186.95	66.68	1.67	0.61	33.0	36.7	28.1	41.6	1.11	13.7	99.1	0.94
LV2010A4-1	35.48105	-117.497988	157.24	84.50	2.26	0.66	99.4	164.8	77.5	137.7	1.66	36.6	73.9	0.46
LV2010A4-2	35.48105	-117.497988	159.58	110.52	3.92	0.72	64.8	72.5	28.8	81.6	1.12	16.7	52.0	0.27
LV2010A4-3	35.48105	-117.497988	149.93	83.31	2.10	0.66	39.0	27.4	22.9	45.5	0.70	8.0	49.0	0.38
LV2010B0-1	35.424063	-117.474731	128.77	83.28	1.80	0.65	39.0	44.2	28.4	49.3	1.13	9.3	53.8	4.31
LV2010B0-2	35.424063	-117.474731	228.87	103.28	4.91	0.73	125.3	164.3	41.7	163.3	1.31	38.1	59.1	4.73
LV2010B0-3	35.424063	-117.474731	144.47	68.59	1.37	0.59	8.4	19.1	11.7	12.9	2.28	0.4	8.9	0.71
LV2010B1-1	35.440217	-117.474208	168.41	77.22	2.02	0.64	5.7	14.9	10.2	9.1	2.63	0.2	6.3	0.50
LV2010B1-2	35.440217	-117.474208	118.46	62.60	0.93	0.56	14.2	25.0	19.1	20.0	1.76	0.7	11.5	0.92
LV2010B1-3	35.440217	-117.474208	182.43	74.78	2.05	0.63	7.7	23.1	12.6	13.1	2.99	0.4	7.9	0.64
LV2010B2-1	35.454661	-117.472725	175.89	79.74	2.25	0.64	7.4	22.9	19.7	12.8	3.11	1.2	26.9	0.55
LV2010B2-2	35.454661	-117.472725	194.47	89.13	3.11	0.67	5.4	39.0	22.7	14.5	7.27	0.7	12.2	0.20
LV2010B2-3	35.454661	-117.472725	163.48	74.48	1.83	0.63	78.1	138.3	154.8	110.7	1.77	23.2	60.9	0.76
LV2010B3-1	35.46934	-117.477482	126.87	68.27	1.19	0.59	38.9	42.9	48.2	49.0	1.10	7.1	45.1	3.61
LV2010B3-2	35.46934	-117.477482	150.77	94.25	2.70	0.68	23.4	30.4	15.3	30.5	1.30	6.9	60.5	4.84
LV2010B3-3	35.46934	-117.477482	155.45	70.03	1.54	0.61	101.3	163.3	32.1	139.1	1.61	24.4	52.9	4.23
LV2010C1-1	35.442091	-117.460916	122.17	86.45	1.84	0.65	68.0	62.6	47.9	82.7	0.92	12.7	43.3	0.31
LV2010C1-2	35.442091	-117.460916	165.12	106.92	3.80	0.72	48.4	52.0	47.1	60.6	1.07	12.1	51.0	0.41
LV2010C1-3	35.442091	-117.460916	181.91	92.28	3.12	0.69	28.5	35.4	26.4	36.7	1.24	5.1	36.8	0.30
LV2010C2-1	35.455612	-117.459634	131.72	75.86	1.53	0.63	83.4	68.3	104.5	99.7	0.82	17.1	50.3	4.02
LV2010C2-2	35.455612	-117.459634	173.48	101.48	3.60	0.71	71.6	94.3	26.5	93.4	1.32	18.3	50.7	4.05
LV2010C2-3	35.455612	-117.459634	126.99	83.35	1.78	0.65	22.0	24.3	10.6	27.7	1.10	4.1	41.9	3.36
LV2010C3-1	35.46878	-117.455469	206.06	97.03	3.91	0.71	89.5	85.8	88.6	109.7	0.96	21.5	50.7	4.05
LV2010C3-2	35.46878	-117.455469	229.48	127.33	7.49	0.76	94.4	148.3	37.5	128.7	1.57	29.8	55.6	4.45
LV2010C3-3	35.46878	-117.455469	158.86	96.26	2.96	0.69	14.0	23.7	22.4	19.6	1.69	3.6	49.0	3.92

Sample	Latitude	Longitude	L (μm)	W (μm)	Mass (μg)	Ft*	U (ppm)	Th (ppm)	Sm (ppm)	[U]e	Th/U	He (nmol/g)	Corrected Age (Ma)	Error (Ma)
LV2010C4-1	35.481655	-117.456325	165.72	111.05	4.12	0.73	90.2	96.4	27.4	112.5	1.07	26.7	60.1	0.28
LV2010C4-2	35.481655	-117.456325	171.90	96.49	3.22	0.70	90.4	74.1	64.2	107.7	0.82	21.7	52.9	0.36
LV2010C4-3	35.481655	-117.456325	122.16	72.02	1.28	0.61	42.6	38.0	25.5	51.5	0.89	1.4	8.5	0.08
LV2010D1-1	35.444131	-117.445099	182.76	86.33	2.74	0.67	5.0	15.9	11.7	8.7	3.19	0.8	25.3	0.56
LV2010D1-2	35.444131	-117.445099	142.79	73.69	1.56	0.62	99.9	136.2	38.4	131.4	1.36	25.2	56.9	0.29
LV2010D1-3	35.444131	-117.445099	169.59	93.96	3.01	0.69	10.0	14.9	29.2	13.6	1.48	2.7	52.0	1.11
LV2010D2-1	35.459692	-117.442789	118.07	93.55	2.08	0.67	197.2	120.3	136.7	225.6	0.61	46.7	56.6	4.53
LV2010D2-2	35.459692	-117.442789	125.26	77.22	1.50	0.63	30.1	36.5	41.8	38.7	1.21	6.7	50.6	4.05
LV2010D2-3	35.459692	-117.442789	142.60	88.05	2.23	0.67	133.0	161.2	66.7	170.4	1.21	38.4	62.2	4.97
LV2010D3-1	35.469091	-117.442575	135.93	70.17	1.35	0.59	9.8	46.4	62.0	20.8	4.72	0.6	9.5	0.28
LV2010D3-2	35.469091	-117.442575	198.00	98.67	3.88	0.70	9.4	28.6	34.5	16.2	3.03	0.8	12.6	0.24
LV2010D3-3	35.469091	-117.442575	153.44	71.00	1.56	0.61	11.2	29.7	15.9	18.1	2.65	0.6	9.5	0.17
LV2010D4-1	35.483994	-117.444674	164.70	79.97	2.12	0.66	144.9	77.4	99.3	163.2	0.53	31.7	54.3	0.38
LV2010D4-2	35.483994	-117.444674	234.15	110.40	5.75	0.74	74.2	106.3	37.1	98.9	1.43	24.4	61.1	0.31
LV2010D4-3	35.483994	-117.444674	166.17	109.75	4.03	0.72	47.2	54.9	17.4	60.0	1.16	12.7	53.6	0.27
LV2010D5-1	35.494537	-117.44038	171.63	116.06	4.66	0.73	22.7	30.9	26.9	29.9	1.37	4.6	38.7	0.35
LV2010D5-2	35.494537	-117.44038	144.03	88.31	2.26	0.66	6.3	28.8	15.3	13.0	4.60	0.7	15.5	0.28
LV2010D5-3	35.494537	-117.44038	160.11	97.70	3.08	0.70	57.5	69.9	61.0	73.9	1.21	12.8	45.6	0.38
LV2010E1-1	35.442243	-117.424836	171.72	72.58	1.82	0.63	33.3	33.1	30.5	41.1	0.99	6.9	48.9	3.91
LV2010E1-2	35.442243	-117.424836	121.72	68.82	1.16	0.59	57.2	84.8	23.1	76.8	1.48	12.6	51.0	4.08
LV2010E1-3	35.442243	-117.424836	111.66	76.84	1.33	0.61	154.4	207.5	33.7	202.4	1.34	33.2	49.1	3.93
LV2010E2-1	35.451667	-117.426872	142.93	76.12	1.67	0.63	3.8	4.7	23.6	5.0	1.25	0.1	4.0	0.27
LV2010E2-2	35.451667	-117.426872	164.46	96.77	3.10	0.69	2.8	5.6	25.7	4.2	2.00	0.1	7.3	0.45
LV2010E2-3	35.451667	-117.426872	118.81	74.01	1.31	0.60	2.9	8.9	30.0	5.1	3.05	0.1	4.6	0.37
LV2010E2b-1	35.451601	-117.427208	179.12	86.01	2.67	0.67	27.1	32.8	22.9	34.8	1.21	10.6	83.3	5.00
LV2010E2b-2	35.452739	-117.42445	161.30	88.72	2.56	0.68	19.1	21.7	39.8	24.3	1.14	4.5	49.9	2.99
LV2010E2b-3	35.452739	-117.42445	109.26	75.94	1.27	0.61	44.4	38.3	12.5	53.2	0.86	9.7	54.3	3.26
LV2010E3-1	35.468975	-117.425712	130.44	81.61	1.75	0.65	117.1	51.8	41.7	129.2	0.44	24.8	54.3	0.31
LV2010E3-2	35.468975	-117.425712	161.54	85.02	2.35	0.66	31.2	44.1	84.1	41.8	1.41	7.9	52.1	0.93
LV2010E3-3	35.468975	-117.425712	168.67	95.31	3.09	0.69	34.4	63.5	57.1	49.3	1.85	9.7	52.1	0.56
LV2010E4-1	35.482968	-117.422065	90.16	77.18	1.08	0.60	30.1	26.1	18.6	36.2	0.87	1.2	9.8	0.13
LV2010E4-2	35.482968	-117.422065	135.96	70.35	1.35	0.60	2.9	5.0	25.6	4.2	1.69	6.3	436.6	40.35
LV2010E4-3	35.482968	-117.422065	111.23	66.65	0.99	0.57	7.5	11.7	6.4	10.2	1.56	1.3	39.1	1.75
LV2010E5-1	35.494013	-117.426342	99.44	77.17	1.19	0.61	57.9	53.7	42.1	70.5	0.93	12.5	53.5	4.28
LV2010E5-2	35.494013	-117.426342	160.49	80.44	2.09	0.65	186.1	226.3	47.4	238.5	1.22	49.7	58.8	4.70

Sample	Latitude	Longitude	L (μm)	W (μm)	Mass (μg)	Ft*	U (ppm)	Th (ppm)	Sm (ppm)	[U]e	Th/U	He (nmol/g)	Corrected Age (Ma)	Error (Ma)
LV2010E5-3	35.494013	-117.426342	166.38	90.53	2.75	0.68	12.9	22.2	11.7	18.1	1.72	3.6	53.9	4.32
LV2010F1-1	35.441395	-117.40987	124.32	99.45	2.48	0.68	23.8	29.0	31.6	30.7	1.22	5.4	47.4	3.79
LV2010F1-2	35.441395	-117.40987	162.73	105.54	3.65	0.72	23.2	20.5	17.9	28.0	0.88	5.2	47.7	3.81
LV2010F1-3	35.441395	-117.40987	181.76	117.51	5.05	0.74	12.1	16.8	20.7	16.1	1.39	2.4	37.2	2.97
LV2010F3-1	35.469372	-117.408585	122.62	87.30	1.88	0.65	20.7	23.4	18.1	26.1	1.13	1.0	10.7	0.12
LV2010F3-2	35.469372	-117.408585	155.99	80.12	2.02	0.65	16.0	19.2	50.0	20.6	1.20	3.6	49.6	1.16
LV2010F3-3	35.469372	-117.408585	151.20	92.92	2.63	0.68	38.8	54.0	55.9	51.5	1.39	10.5	55.1	0.58
LV2010F5-1	35.494766	-117.408959	137.78	68.21	1.29	0.60	142.3	106.0	78.9	167.1	0.74	33.8	61.8	4.94
LV2010F5-2	35.494766	-117.408959	120.79	74.09	1.33	0.61	26.3	30.1	20.1	33.4	1.14	6.6	59.6	4.77
LV2010F5-3	35.494766	-117.408959	143.98	89.49	2.32	0.67	14.6	23.7	18.9	20.1	1.63	3.6	49.1	3.93
LV2010G0-1	35.426988	-117.397354	250.33	92.22	4.29	0.70	3.1	11.2	48.0	5.9	3.61	1.3	55.2	4.41
LV2010G0-2	35.426988	-117.397354	155.92	73.70	1.71	0.62	13.2	25.3	40.5	19.3	1.91	1.8	27.7	2.21
LV2010G0-3	35.426988	-117.397354	165.27	81.65	2.22	0.65	5.2	17.1	25.5	9.3	3.28	1.1	33.2	2.66
LV2010G4-1	35.48394	-117.397006	128.27	66.03	1.13	0.59	30.4	29.8	24.1	37.4	0.98	5.9	49.4	2.97
LV2010G4-2	35.48394	-117.397006	125.89	68.19	1.18	0.60	47.6	30.3	35.8	54.7	0.64	7.1	39.8	2.39
LV2010G4-3	35.48394	-117.397006	159.70	72.94	1.71	0.62	8.2	25.6	26.3	14.2	3.13	0.8	16.3	0.98
LV2010G5-1	35.495302	-117.392862	167.92	85.88	2.49	0.69	109.1	21.9	121.8	114.7	0.20	12.6	29.6	1.77
LV2010G5-2	35.495302	-117.392862	126.84	70.22	1.26	0.60	33.9	45.3	15.6	44.4	1.34	7.8	53.9	3.24
LV2010G5-3	35.495302	-117.392862	215.69	77.40	2.60	0.65	19.5	28.5	20.9	26.2	1.46	9.9	105.9	6.35
LV2010G6-1	35.508173	-117.389622	158.92	83.31	2.22	0.66	78.0	143.0	23.6	111.0	1.83	24.4	61.6	0.28
LV2010G6-2	35.508173	-117.389622	150.55	78.16	1.85	0.63	9.8	26.0	6.9	15.8	2.66	3.1	56.6	0.91
LV2010G6-3	35.508173	-117.389622	132.74	73.92	1.46	0.61	18.0	48.7	13.2	29.2	2.71	2.0	20.2	0.23
LV2010H5-1	35.493709	-117.375908	154.37	72.14	1.62	0.62	15.2	21.3	34.5	20.3	1.40	4.1	59.3	1.20
LV2010H5-2	35.493709	-117.375908	140.26	76.67	1.66	0.63	38.8	45.2	22.7	49.3	1.17	9.0	53.4	0.42
LV2010H5-3	35.493709	-117.375908	212.01	82.63	2.91	0.66	7.2	24.9	12.5	13.0	3.47	0.8	16.6	0.24
LV2010H6-1	35.504998	-117.378452	162.96	77.15	1.95	0.64	16.5	29.0	21.4	23.3	1.76	4.5	55.1	2.76
LV2010H6-2	35.504998	-117.378452	163.59	90.54	2.70	0.68	51.7	89.0	46.2	72.4	1.72	13.2	49.4	2.96
LV2010H6-3	35.504998	-117.378452	215.96	82.56	2.96	0.67	36.8	58.8	47.2	50.5	1.60	10.0	54.2	3.25
LV2010I5-1	35.497302	-117.364384	139.10	70.77	1.40	0.61	45.8	51.0	39.0	57.8	1.11	7.9	41.2	3.29
LV2010I5-2	35.497302	-117.364384	249.87	126.84	8.09	0.77	11.8	18.5	8.9	16.1	1.57	2.5	37.4	3.00
LV2010I5-3	35.497302	-117.364384	161.01	97.90	3.11	0.69	5.6	11.9	7.5	8.4	2.12	1.5	48.5	3.88
LV2010J6-1	35.513406	-117.346305	110.10	63.80	0.90	0.55	10.6	42.5	22.8	20.5	4.00	5.5	88.8	7.11
LV2010J6-2	35.513406	-117.346305	132.49	60.62	0.98	0.55	6.2	28.1	18.2	12.7	4.54	2.9	75.9	6.08
LV2010J6-3	35.513406	-117.346305	142.17	67.76	1.31	0.59	41.5	164.0	32.0	79.4	3.95	12.7	50.0	4.00

Sample	Latitude	Longitude	L (μm)	W (μm)	Mass (μg)	Ft*	U (ppm)	Th (ppm)	Sm (ppm)	[U]e	Th/U	He (nmol/g)	Corrected Age (Ma)	Error (Ma)
Zircon data														
zLV2010A0-1	35.423571	-117.489408	195.42	86.25	6.76	0.78	578.2	155.8	1.5	614.1	0.27	159.6	61.5	0.29
zLV2010A0-2	*35.423571*	*-117.489408*	*158.68*	*81.85*	*4.94*	*0.75*	*3.2*	*5.6*	*5.3*	*4.5*	*1.77*	*-0.1*	*-3.3*	*-0.08*
zLV2010A0-3	35.423571	-117.489408	187.29	98.90	8.52	0.80	498.7	103.1	0.4	522.4	0.21	135.6	59.8	0.29
zLV2010A1-1	35.441913	-117.489229	267.42	97.70	11.87	0.81	528.0	139.4	0.9	560.1	0.26	32.1	13.1	0.06
zLV2010A1-2	35.441913	-117.489229	240.77	101.72	11.59	0.81	374.2	143.7	1.1	407.3	0.38	125.0	69.7	0.32
zLV2010A1-3	35.441913	-117.489229	250.01	99.96	11.62	0.81	308.3	84.3	0.6	327.7	0.27	96.5	67.0	0.31
zLV2010A2-1	35.456516	-117.491592	166.03	75.13	4.36	0.75	226.3	71.3	0.4	242.7	0.32	68.0	69.0	0.32
zLV2010A2-2	35.456516	-117.491592	221.85	114.14	13.44	0.82	721.1	318.3	3.1	794.4	0.44	38.3	10.8	0.05
zLV2010A2-3	35.456516	-117.491592	168.71	95.36	7.13	0.79	233.7	69.2	0.3	249.6	0.30	120.3	112.1	0.52
zLV2010A3-1	35.469007	-117.491959	178.07	74.16	4.55	0.75	113.4	30.8	0.6	120.5	0.27	31.3	63.9	0.31
zLV2010A3-3	35.469007	-117.491959	238.72	90.91	9.17	0.80	124.3	34.6	0.8	132.3	0.28	37.0	64.9	0.31
zLV2010A4-1	35.48105	-117.497988	198.66	73.78	5.03	0.75	451.9	141.0	2.6	484.3	0.31	133.5	67.6	0.31
zLV2010A4-2	35.48105	-117.497988	224.62	80.20	6.72	0.77	497.3	126.4	0.7	526.4	0.25	128.0	58.1	0.27
zLV2010A4-3	35.48105	-117.497988	217.28	96.00	9.31	0.80	364.3	113.2	0.7	390.3	0.31	70.5	41.7	0.19
zLV2010B0-1	35.424063	-117.474731	158.06	77.85	4.45	0.75	619.0	131.2	1.7	649.2	0.21	182.4	68.7	0.33
zLV2010B0-2	35.424063	-117.474731	135.59	70.69	3.15	0.73	646.7	193.4	1.2	691.3	0.30	187.1	68.6	0.32
zLV2010B0-3	35.424063	-117.474731	162.41	72.08	3.92	0.74	175.9	41.9	0.7	185.5	0.24	45.6	61.3	0.29
zLV2010B1-1	35.440217	-117.474208	187.98	100.29	8.79	0.80	275.4	67.4	0.7	290.9	0.24	67.2	53.2	0.25
zLV2010B1-2	35.440217	-117.474208	228.75	99.41	10.51	0.81	914.6	224.3	2.2	966.3	0.25	279.2	66.0	0.31
zLV2010B1-3	35.440217	-117.474208	174.96	99.50	8.05	0.80	167.4	82.8	0.5	186.5	0.49	58.6	72.8	0.33
zLV2010B2-1	35.454661	-117.472725	167.65	73.46	4.21	0.74	141.3	87.1	0.4	161.4	0.62	46.6	71.8	0.32
zLV2010B2-2	35.454661	-117.472725	187.30	111.63	10.85	0.82	231.7	76.0	0.7	249.2	0.33	70.8	64.2	0.30
zLV2010B2-3	35.454661	-117.472725	201.78	75.31	5.32	0.76	493.6	139.8	1.1	525.8	0.28	44.3	20.6	0.10
zLV2010B3-1	35.46934	-117.477482	166.81	66.96	3.48	0.73	821.4	140.7	1.8	853.8	0.17	282.0	83.6	6.68
zLV2010B3-2	35.46934	-117.477482	162.35	60.01	2.72	0.70	264.0	73.7	0.6	280.9	0.28	91.2	85.2	6.82
zLV2010B3-3	35.46934	-117.477482	155.66	96.24	6.70	0.79	160.5	44.4	0.5	170.8	0.28	47.1	64.5	5.16
zLV2010B4-1	35.482585	-117.479187	294.79	88.75	10.80	0.80	434.0	113.7	2.2	460.1	0.26	144.5	72.6	0.34
zLV2010B4-2	35.482585	-117.479187	285.13	123.98	20.38	0.84	462.8	120.1	1.2	490.5	0.26	145.1	64.6	0.30
zLV2010B4-3	35.482585	-117.479187	258.24	108.16	14.05	0.83	1221.5	184.3	0.5	1263.9	0.15	397.1	70.3	0.34
zLV2010C0-1	35.424524	-117.464592	208.21	79.41	6.10	0.77	1034.2	146.1	0.6	1067.8	0.14	271.0	60.9	0.29
zLV2010C0-2	35.424524	-117.464592	190.04	84.65	6.33	0.78	205.7	68.1	0.6	221.4	0.33	58.8	63.2	0.29
zLV2010C0-3	35.424524	-117.464592	211.02	71.17	4.97	0.75	487.7	160.0	1.3	524.6	0.33	144.4	68.0	0.32
zLV2010C1-1	35.442091	-117.460916	154.56	74.37	3.97	0.74	114.3	84.5	0.0	133.7	0.74	34.1	63.5	0.28
zLV2010C1-2	35.442091	-117.460916	165.10	92.04	6.50	0.78	291.1	70.2	0.1	307.2	0.24	77.9	59.7	0.28

Sample	Latitude	Longitude	L (μm)	W (μm)	Mass (μg)	Ft*	U (ppm)	Th (ppm)	Sm (ppm)	[U]e	Th/U	He (nmol/g)	Corrected Age (Ma)	Error (Ma)
zLV2010C1-3	35.442091	-117.460916	117.42	71.87	2.82	0.72	182.3	71.5	-0.3	198.7	0.39	49.9	64.2	0.30
zLV2010C2-1	35.455612	-117.459634	236.36	112.29	13.86	0.82	172.6	68.5	0.6	188.4	0.40	55.6	65.9	0.30
zLV2010C2-2	35.455612	-117.459634	261.52	101.40	12.50	0.81	328.5	156.6	4.4	364.6	0.48	120.0	74.6	0.34
zLV2010C2-3	35.455612	-117.459634	135.08	67.43	2.86	0.72	534.4	135.0	1.3	565.5	0.25	145.0	65.8	0.31
zLV2010C3-1	35.46878	-117.455469	220.10	86.18	7.60	0.78	280.5	99.6	1.7	303.4	0.35	79.8	61.9	0.29
zLV2010C3-2	35.46878	-117.455469	195.78	86.26	6.77	0.78	541.9	148.3	0.8	576.1	0.27	151.4	62.2	0.29
zLV2010C3-3	35.46878	-117.455469	222.71	75.35	5.88	0.76	583.6	165.1	1.1	621.6	0.28	175.7	68.6	0.32
zLV2010D1-1	35.444131	-117.445099	136.28	80.05	4.06	0.75	206.9	77.4	0.0	224.7	0.37	59.1	64.7	0.30
zLV2010D1-2	35.444131	-117.445099	214.29	85.94	7.36	0.78	912.8	245.2	2.0	969.2	0.27	287.8	70.0	0.33
zLV2010D1-3	35.444131	-117.445099	194.93	99.67	9.00	0.80	176.5	64.7	0.5	191.4	0.37	52.6	63.3	0.29
zLV2010D2-1	35.459692	-117.442789	290.54	101.76	13.99	0.82	595.9	118.8	1.1	623.3	0.20	170.9	61.8	0.30
zLV2010D2-2	35.459692	-117.442789	254.74	88.48	9.27	0.79	468.9	136.5	0.8	500.3	0.29	163.7	76.1	0.36
zLV2010D2-3	35.459692	-117.442789	194.68	96.33	8.40	0.80	486.9	186.9	1.4	530.0	0.38	92.9	40.6	0.19
zLV2010D3-1	35.469091	-117.442575	185.26	110.71	10.56	0.81	0.3	0.1	0.0	0.3	0.46	0.0	4.1	0.60
zLV2010D3-2	*35.469091*	*-117.442575*	*162.27*	*81.89*	*5.06*	*0.76*	*1.4*	*0.7*	*0.4*	*1.5*	*0.51*	*0.0*	*1.5*	*0.09*
zLV2010D3-3	35.469091	-117.442575	197.94	71.69	4.73	0.75	195.0	80.2	0.4	213.5	0.41	60.2	69.8	0.32
zLV2010D4-1	35.483994	-117.444674	169.14	86.13	5.83	0.77	1221.4	398.2	5.3	1313.1	0.33	325.7	59.2	0.27
zLV2010D4-2	35.483994	-117.444674	197.56	84.07	6.49	0.78	422.2	130.6	0.0	452.3	0.31	26.1	13.8	0.06
zLV2010D4-3	35.483994	-117.444674	186.30	84.62	6.20	0.78	504.9	117.7	0.8	532.0	0.23	154.0	68.8	0.33
zLV2010D5-1	35.494537	-117.44038	124.96	80.04	3.72	0.75	155.9	39.2	-0.3	164.9	0.25	45.1	67.5	0.32
zLV2010D5-2	35.494537	-117.44038	172.65	81.22	5.30	0.76	412.1	160.8	0.4	449.1	0.39	144.0	77.4	0.35
zLV2010D5-3	35.494537	-117.44038	168.75	75.05	4.42	0.75	662.5	162.9	0.7	700.0	0.25	190.0	66.8	0.32
zLV2010E2b-1	35.451601	-117.427208	228.29	104.70	11.64	0.82	236.2	61.8	1.1	250.4	0.26	93.2	84.1	6.73
zLV2010E2b-2	35.452739	-117.42445	275.34	106.50	14.52	0.82	664.9	177.9	1.4	705.9	0.27	42.1	13.4	1.07
zLV2010E2b-3	35.452739	-117.42445	240.07	99.45	11.04	0.81	188.8	64.7	1.2	203.7	0.34	61.1	68.4	5.47
zLV2010E3-1	35.468975	-117.425712	206.80	99.72	9.56	0.80	98.5	61.6	0.3	112.6	0.63	38.1	77.6	0.34
zLV2010E3-2	35.468975	-117.425712	201.86	87.41	7.17	0.78	167.1	50.3	0.5	178.6	0.30	58.3	76.8	0.36
zLV2010E3-3	35.468975	-117.425712	154.08	72.88	3.81	0.74	598.7	201.6	1.0	645.1	0.34	181.5	70.2	0.33
zLV2010E4-1	35.482968	-117.422065	157.19	67.64	3.34	0.72	102.3	69.8	-0.3	118.4	0.68	40.3	86.8	0.39
zLV2010E4-2	35.482968	-117.422065	196.16	83.79	6.40	0.78	331.0	82.6	0.2	350.0	0.25	128.0	86.9	0.41
zLV2010E4-3	35.482968	-117.422065	160.82	67.88	3.45	0.72	50.9	29.8	-0.3	57.7	0.59	15.4	67.8	0.34
zLV2010E5-1	35.494013	-117.426342	184.56	97.21	8.11	0.80	509.1	138.4	0.2	541.0	0.27	158.3	67.7	0.32
zLV2010E5-2	35.494013	-117.426342	172.21	85.58	5.86	0.77	160.2	125.3	1.2	189.0	0.78	51.1	64.8	0.28
zLV2010E5-3	35.494013	-117.426342	177.08	93.78	7.24	0.79	92.9	67.7	0.0	108.5	0.73	27.9	60.4	0.26
zLV2010F1-1	35.441395	-117.40987	274.90	108.53	15.06	0.83	610.3	144.4	0.7	643.6	0.24	169.1	58.7	0.28

Sample	Latitude	Longitude	L (μm)	W (μm)	Mass (μg)	Ft*	U (ppm)	Th (ppm)	Sm (ppm)	[U]e	Th/U	He (nmol/g)	Corrected Age (Ma)	Error (Ma)
zLV2010F1-2	35.441395	-117.40987	274.16	103.27	13.60	0.82	337.0	105.6	1.4	361.3	0.31	94.9	59.2	0.28
zLV2010F1-3	35.441395	-117.40987	278.09	110.26	15.72	0.83	157.6	33.2	0.4	165.2	0.21	56.7	76.3	0.36
zLV2010F3-1	35.469372	-117.408585	270.37	83.52	8.77	0.79	769.2	164.1	1.0	807.0	0.21	209.2	60.9	0.29
zLV2010F3-2	35.469372	-117.408585	219.49	73.74	5.55	0.76	410.0	143.6	0.7	443.0	0.35	116.4	64.2	0.30
zLV2010F3-3	35.469372	-117.408585	208.03	110.33	11.78	0.82	275.0	69.9	0.6	291.1	0.25	88.9	68.7	0.32
zLV2010F4-1	35.48308	-117.409566	151.39	87.44	5.38	0.77	527.5	216.7	0.7	577.4	0.41	35.1	14.6	0.07
zLV2010F4-2	35.48308	-117.409566	137.94	82.84	4.40	0.76	460.4	147.0	2.8	494.2	0.32	17.4	8.6	0.04
zLV2010F4-3	35.48308	-117.409566	152.58	70.49	3.53	0.73	347.8	144.3	1.3	381.0	0.41	25.6	17.0	0.08
zLV2010F5-1	35.494766	-117.408959	257.85	121.29	17.64	0.84	109.3	15.6	0.1	112.9	0.14	78.7	152.1	0.74
zLV2010F5-2	35.494766	-117.408959	268.09	114.29	16.28	0.83	372.9	105.9	3.0	397.3	0.28	18.4	10.3	0.05
zLV2010F5-3	35.494766	-117.408959	260.14	114.52	15.87	0.83	582.3	157.3	1.1	618.5	0.27	39.7	14.3	0.07
zLV2010G6-1	35.508173	-117.389622	155.52	80.80	4.72	0.76	229.0	45.6	-0.2	239.5	0.20	60.3	61.1	0.29
zLV2010G6-2	35.508173	-117.389622	175.70	86.85	6.16	0.77	123.3	79.6	0.3	141.7	0.65	40.7	68.4	0.30
zLV2010G6-3	35.508173	-117.389622	223.13	105.66	11.58	0.82	161.0	51.2	0.3	172.8	0.32	47.9	62.8	0.29
zLV2010H5-1	35.493709	-117.375908	157.26	75.95	4.22	0.75	184.2	57.6	0.2	197.4	0.31	61.7	77.0	0.36
zLV2010H5-2	35.493709	-117.375908	260.11	106.19	13.64	0.82	202.4	59.4	0.7	216.1	0.29	59.2	61.5	0.29
zLV2010H5-3	35.493709	-117.375908	163.54	73.54	4.11	0.74	568.2	300.7	2.1	637.4	0.53	193.8	75.6	0.34

Notes: See appendix 5.1 for discussion of analytical procedures and errors; samples in italics are erroneous and excluded from histograms.

*Ft is the alpha ejection correction of Farley et al. (1996).

APPENDIX

Appendix: (U-Th)/He data from Frenchman Mountain, the Mesquite Range, and the Kingston Range

Sample	Latitude	Longitude	L (μm)	W (μm)	Mass (μg)	Ft*	U (ppm)	Th (ppm)	Sm (ppm)	[U]e	Th/U	He (nmol/g)	Corrected Age (Ma)	Error (Ma)
Frenchman Mountain apatite														
11FM02-1	36.187505	-115.009623	94.48	81.07	1.25	0.61	9.1	14.8	48.3	12.8	1.62	0.9	20.5	1.2
11FM02-2	36.187505	-115.009623	100.48	63.31	0.81	0.53	1.1	229.0	46.2	54.1	207.04	2.6	16.5	1.0
11FM02-3	36.187505	-115.009623	107.81	62.20	0.84	0.53	0.2	230.6	50.8	53.5	1187.47	1.9	12.3	0.7
11FM03-1	*36.187364*	*-115.011581*	*68.96*	*56.45*	*0.44*	*0.53*	*-3.5*	*0.8*	*-0.5*	*-3.3*	*-0.24*	*0.0*	*-4.3*	*-0.3*
11FM03-2	*36.187364*	*-115.011581*	*96.21*	*56.83*	*0.63*	*0.56*	*-2.1*	*0.3*	*-0.4*	*-2.0*	*-0.14*	*0.0*	*-0.2*	*0.0*
11FM03-3	*36.187364*	*-115.011581*	*92.04*	*56.08*	*0.58*	*0.50*	*9.2*	*19.0*	*64.9*	*13.9*	*2.06*	*6.3*	*163.4*	*9.8*
11FM03-4	*36.187364*	*-115.011581*	*63.49*	*53.12*	*0.36*	*0.49*	*-4.5*	*0.3*	*-0.3*	*-4.5*	*-0.07*	*0.0*	*0.5*	*0.0*
11FM04-1	36.188260	-115.012824	75.94	33.09	0.17	0.30	4.4	4.3	59.2	5.7	0.97	0.3	36.3	2.2
11FM04-2	36.188260	-115.012824	81.96	45.63	0.34	0.46	30.6	4.1	93.1	32.0	0.14	0.7	9.0	0.5
11FM04-3	36.188260	-115.012824	93.82	48.87	0.45	0.49	20.8	2.1	54.9	21.5	0.10	0.7	11.9	0.7
Frenchman Mountain zircon														
z11FM02-1	36.187505	-115.009623	132.38	76.00	3.56	0.73	76.2	109.0	3.2	101.3	1.43	366.1	862.0	69.0
z11FM02-2	36.187505	-115.009623	180.54	92.51	7.18	0.78	90.4	71.2	2.0	106.8	0.79	323.4	679.4	54.4
z11FM02-3	36.187505	-115.009623	157.16	83.20	5.06	0.76	115.8	113.7	6.6	142.0	0.98	465.6	757.0	60.6
z11FM02-6	36.187505	-115.009623	177.79	73.72	4.49	0.74	70.6	96.9	1.8	93.0	1.37	287.3	735.3	58.8
z11FM02-7	36.187505	-115.009623	181.58	87.79	6.51	0.78	139.1	76.5	2.2	156.7	0.55	412.6	599.5	48.0
z11FM02-8	36.187505	-115.009623	190.99	122.49	13.32	0.83	55.8	35.8	0.7	64.0	0.64	243.9	797.8	63.8
z11FM02-9	36.187505	-115.009623	148.58	73.06	3.69	0.73	96.9	119.8	3.9	124.4	1.24	287.8	564.1	45.1
z11FM02-50	36.187505	-115.009623	136.29	72.18	3.30	0.73	96.2	87.0	2.8	116.2	0.90	275.9	582.0	46.6
z11FM02-51	36.187505	-115.009623	116.06	69.63	2.62	0.71	67.3	95.0	2.6	89.2	1.41	180.3	512.4	41.0
z11FM02-52	36.187505	-115.009623	144.85	60.86	2.49	0.69	139.9	141.7	3.1	172.5	1.01	447.9	665.3	53.2
z11FM02-53	36.187505	-115.009623	114.24	65.71	2.29	0.69	208.8	315.5	11.5	281.4	1.51	246.2	229.9	18.4
z11FM02-54	36.187505	-115.009623	116.53	58.15	1.83	0.67	69.1	97.6	3.7	91.6	1.41	70.4	210.1	16.8
z11FM02-55	36.187505	-115.009623	156.25	71.49	3.71	0.73	62.6	73.4	2.0	79.5	1.17	236.2	718.3	57.5
z11FM02-56	36.187505	-115.009623	155.88	72.74	3.84	0.73	78.3	67.9	2.0	93.9	0.87	273.3	698.8	55.9
z11FM02-57	36.187505	-115.009623	214.68	77.98	6.07	0.76	69.9	98.1	5.6	92.5	1.40	93.4	242.4	19.4
z11FM02-58	36.187505	-115.009623	159.62	76.70	4.37	0.74	152.2	129.3	6.3	181.9	0.85	191.9	257.2	20.6
z11FM02-59	36.187505	-115.009623	169.38	73.76	4.29	0.74	98.2	91.1	3.7	119.2	0.93	364.7	726.8	58.1
z11FM02-60	36.187505	-115.009623	155.42	89.10	5.74	0.77	239.0	245.1	7.5	295.4	1.03	356.9	284.7	22.8
z11FM02-61	36.187505	-115.009623	168.56	87.40	5.99	0.77	658.6	659.0	27.3	810.5	1.00	194.7	57.4	4.6

Sample	Latitude	Longitude	L (μm)	W (μm)	Mass (μg)	Ft*	U (ppm)	Th (ppm)	Sm (ppm)	[U]e	Th/U	He (nmol/g)	Corrected Age (Ma)	Error (Ma)
z11FM03-1	36.187364	-115.011581	207.23	85.55	7.05	0.78	636.5	63.2	4.2	651.0	0.10	83.1	30.2	2.4
z11FM03-2	36.187364	-115.011581	192.29	92.90	7.72	0.79	766.2	76.1	26.2	783.8	0.10	50.4	15.0	1.2
z11FM03-3	36.187364	-115.011581	212.04	89.63	7.92	0.79	540.0	177.1	21.6	580.8	0.33	58.0	23.4	1.9
z11FM04-1	36.188260	-115.012824	165.65	76.67	4.53	0.76	964.4	15.6	2.5	968.0	0.02	30.1	7.6	0.6
z11FM04-2	36.188260	-115.012824	184.13	101.53	8.83	0.81	664.7	23.5	8.1	670.2	0.04	23.5	8.1	0.6
z11FM04-3	36.188260	-115.012824	230.47	111.02	13.21	0.83	525.0	19.0	4.3	529.4	0.04	134.5	56.8	4.5
z11FM05-1	36.188473	-115.014908	275.77	113.15	16.42	0.83	291.6	26.6	5.7	297.7	0.09	103.9	77.2	6.2
z11FM05-2	36.188473	-115.014908	332.97	153.20	36.34	0.87	390.0	33.6	19.5	397.9	0.09	45.2	24.1	1.9
z11FM05-3	36.188473	-115.014908	279.38	130.54	22.14	0.85	713.2	77.5	10.4	731.1	0.11	41.4	12.3	1.0
Mesquite Range apatite														
11MQ05-1	35.658695	-115.711922	109.14	65.24	0.94	0.58	41.1	13.4	99.5	44.7	0.33	2.2	15.5	0.9
11MQ05-2	35.658695	-115.711922	110.56	61.24	0.83	0.56	5.8	4.2	76.2	7.2	0.72	0.5	20.7	1.2
11MQ05-3	35.658695	-115.711922	101.06	67.34	0.92	0.58	11.0	5.3	63.4	12.6	0.48	1.0	24.9	1.5
11MQ06-1	35.698935	-115.717058	90.39	67.28	0.82	0.57	7.4	5.0	69.4	8.9	0.67	1.4	50.1	3.0
11MQ06-2	35.698935	-115.717058	91.72	62.48	0.72	0.56	23.6	7.8	49.9	25.7	0.33	1.4	18.6	1.1
11MQ06-3	35.698935	-115.717058	88.49	82.47	1.21	0.63	18.1	3.8	54.6	19.2	0.21	1.2	18.9	1.1
11MQ06-4	35.698935	-115.717058	86.62	52.26	0.48	0.50	32.4	7.6	46.1	34.4	0.24	1.0	10.9	0.7
11MQ08-1	35.686343	-115.733612	118.40	51.56	0.63	0.47	-2.2	21.2	57.0	2.9	-9.55	0.9	106.2	6.4
11MQ08-2	35.686343	-115.733612	83.62	62.57	0.66	0.49	-2.4	10.0	50.8	0.2	-4.21	0.3	241.3	14.5
11MQ08-3	35.686343	-115.733612	99.49	46.83	0.44	0.47	25.4	7.7	83.0	27.6	0.30	1.4	19.0	1.1
11MQ08-4	35.686343	-115.733612	52.20	46.15	0.22	0.41	60.3	9.6	63.7	62.8	0.16	1.5	11.0	0.7
11MQ09-1	35.679554	-115.741551	95.14	77.22	1.14	0.62	12.5	1.7	77.3	13.2	0.13	1.3	28.4	1.7
11MQ09-2	35.679554	-115.741551	91.21	87.83	1.42	0.63	15.5	17.0	29.8	19.5	1.10	34.3	497.6	29.9
11MQ09-3	35.679554	-115.741551	109.85	83.51	1.54	0.64	4.1	2.1	60.2	4.9	0.52	0.8	44.2	2.7
11MQ10-1	35.672848	-115.749058	120.73	78.60	1.50	0.65	63.4	6.8	58.3	65.2	0.11	3.0	13.0	0.8
11MQ10-2	35.672848	-115.749058	100.37	67.75	0.93	0.59	49.1	10.8	87.0	52.0	0.22	2.7	16.0	1.0
11MQ10-3	35.672848	-115.749058	105.51	73.90	1.16	0.60	3.9	4.5	61.6	5.3	1.16	0.4	23.2	1.4

Sample	Latitude	Longitude	L (µm)	W (µm)	Mass (µg)	Ft*	U (ppm)	Th (ppm)	Sm (ppm)	[U]e	Th/U	He (nmol/g)	Corrected Age (Ma)	Error (Ma)
11MQ11-1	35.666522	-115.757875	150.23	54.98	0.91	0.56	41.1	9.1	61.0	43.5	0.22	1.4	10.7	0.6
11MQ11-2	35.666522	-115.757875	113.78	65.04	0.97	0.59	20.8	5.7	45.1	22.4	0.27	0.8	11.5	0.7
11MQ11-3	35.666522	-115.757875	152.94	53.26	0.87	0.54	48.3	25.8	25.4	54.4	0.53	1.8	11.5	0.7
11MQ13-1	35.708485	-115.700269	148.96	85.74	2.20	0.67	11.7	4.5	32.9	12.9	0.38	1.0	20.8	1.2
11MQ13-2	35.708485	-115.700269	235.44	100.55	4.79	0.73	10.9	4.8	20.6	12.1	0.44	0.9	19.1	1.1
11MQ13-3	35.708485	-115.700269	238.35	86.93	3.63	0.70	8.0	4.6	30.1	9.2	0.57	0.6	17.3	1.0
Mesquite Range zircon														
z11MQ01-1	35.730909	-115.680880	175.00	54.87	2.45	0.68	330.1	90.3	0.9	350.9	0.27	91.2	70.1	5.6
z11MQ01-2	35.730909	-115.680880	127.66	44.24	1.16	0.61	132.5	101.5	0.8	155.9	0.77	35.9	70.0	5.6
z11MQ01-3	35.730909	-115.680880	98.64	41.50	0.79	0.57	77.3	70.3	7.5	93.5	0.91	23.6	81.2	6.5
z11MQ01-4	35.730909	-115.680880	92.58	43.06	0.80	0.57	255.2	328.1	8.8	330.8	1.29	90.8	87.8	7.0
z11MQ02-1	35.718572	-115.687146	130.92	67.94	2.81	0.72	262.8	87.3	1.7	282.9	0.33	105.3	95.5	7.6
z11MQ02-2	35.718572	-115.687146	145.99	66.09	2.97	0.71	104.7	57.8	5.1	118.0	0.55	49.3	107.4	8.6
z11MQ02-3	35.718572	-115.687146	167.75	59.66	2.78	0.70	394.4	262.9	0.7	454.9	0.67	15.6	9.1	0.7
z11MQ03-1	35.712358	-115.695110	128.28	54.53	1.77	0.66	478.4	514.5	30.0	597.0	1.08	125.4	58.7	4.7
z11MQ03-2	35.712358	-115.695110	111.06	50.74	1.33	0.63	417.6	396.6	22.3	509.0	0.95	111.2	63.5	5.1
z11MQ03-3	35.712358	-115.695110	148.54	46.68	1.51	0.63	591.6	296.5	2.3	659.9	0.50	20.2	9.0	0.7
z11MQ03-4	35.712358	-115.695110	109.88	45.48	1.06	0.61	496.9	282.0	21.5	561.9	0.57	99.5	53.7	4.3
z11MQ04-1	35.666123	-115.710326	161.72	61.41	2.84	0.70	273.6	164.6	10.4	311.6	0.60	47.0	39.7	3.2
z11MQ04-2	35.666123	-115.710326	155.62	60.35	2.64	0.69	81.0	62.6	5.5	95.4	0.77	15.4	42.8	3.4
z11MQ04-3	35.666123	-115.710326	131.01	52.26	1.66	0.66	131.8	69.8	4.0	147.9	0.53	19.5	37.2	3.0
z11MQ05-1	35.658695	-115.711922	128.86	57.40	1.97	0.68	184.2	52.3	0.7	196.3	0.28	26.8	37.0	3.0
z11MQ05-2	35.658695	-115.711922	121.32	59.89	2.02	0.69	209.3	45.2	1.8	219.7	0.22	24.2	29.6	2.4
z11MQ05-3	35.658695	-115.711922	162.03	59.48	2.67	0.70	575.1	159.1	4.1	611.8	0.28	45.6	19.7	1.6
z11MQ05-4	35.658695	-115.711922	172.66	62.36	3.12	0.71	238.0	82.5	0.9	257.0	0.35	24.5	24.7	2.0
z11MQ06-1	35.698935	-115.717058	150.99	72.74	3.71	0.74	343.3	125.0	1.7	372.0	0.36	53.5	36.0	2.9
z11MQ06-2	35.698935	-115.717058	205.98	106.11	10.78	0.81	399.9	114.5	1.6	426.3	0.29	85.9	45.8	3.7
z11MQ06-3	35.698935	-115.717058	194.06	84.86	6.50	0.78	282.1	74.9	1.6	299.4	0.27	52.3	41.6	3.3

Sample	Latitude	Longitude	L (µm)	W (µm)	Mass (µg)	Ft*	U (ppm)	Th (ppm)	Sm (ppm)	[U]e	Th/U	He (nmol/g)	Corrected Age (Ma)	Error (Ma)
z11MQ07-1	35.690467	-115.723473	146.82	66.67	3.03	0.71	422.7	350.8	2.4	503.5	0.83	52.4	26.9	2.2
z11MQ07-2	35.690467	-115.723473	151.50	64.33	2.92	0.71	398.6	105.4	3.1	422.9	0.26	44.5	27.2	2.2
z11MQ07-3	35.690467	-115.723473	113.54	68.02	2.44	0.71	144.4	38.5	0.9	153.3	0.27	28.8	48.9	3.9
z11MQ07-4	35.690467	-115.723473	135.01	64.06	2.58	0.71	210.9	77.1	1.1	228.7	0.37	43.7	50.0	4.0
z11MQ09-1	35.679554	-115.741551	172.67	97.66	7.66	0.80	147.8	38.3	0.4	156.7	0.26	20.5	30.4	2.4
z11MQ09-2	35.679554	-115.741551	163.36	117.66	10.52	0.82	180.5	18.3	0.2	184.7	0.10	25.2	30.8	2.5
z11MQ09-3	35.679554	-115.741551	156.39	70.89	3.65	0.74	712.7	98.6	0.5	735.4	0.14	61.2	20.9	1.7
z11MQ10-1	35.672848	-115.749058	153.79	80.95	4.69	0.76	365.7	43.5	0.6	375.7	0.12	29.0	18.8	1.5
z11MQ10-2	35.672848	-115.749058	160.85	94.30	6.65	0.79	351.1	54.3	0.9	363.6	0.15	28.9	18.7	1.5
z11MQ10-3	35.672848	-115.749058	123.22	67.96	2.65	0.72	242.8	42.3	0.8	252.6	0.17	24.5	25.0	2.0
z11MQ11-1	35.666522	-115.757875	122.30	63.67	2.31	0.70	283.6	40.5	0.8	293.0	0.14	16.8	15.1	1.2
z11MQ11-2	35.666522	-115.757875	149.57	67.21	3.14	0.72	138.5	95.3	1.5	160.5	0.69	49.0	78.3	6.3
z11MQ11-3	35.666522	-115.757875	124.53	61.67	2.20	0.70	341.3	41.4	0.6	350.8	0.12	22.2	16.8	1.3
z11MQ11-4	35.666522	-115.757875	125.26	66.84	2.60	0.72	256.8	41.6	1.3	266.4	0.16	12.9	12.6	1.0
Kingston Range apatite														
11KR03-1	35.843042	-115.794954	*69.07*	*62.40*	*0.54*	*0.28*	*-7.0*	*8.9*	*47.4*	*-4.7*	*-1.27*	*0.2*	*-26.2*	*-1.6*
11KR03-2	35.843042	-115.794954	59.03	50.49	0.30	0.40	-0.8	16.1	66.6	3.2	-19.71	0.3	44.0	2.6
11KR03-3	35.843042	-115.794954	*62.01*	*60.22*	*0.45*	*1.95*	*-8.0*	*7.7*	*51.0*	*-6.0*	*-0.96*	*0.2*	*-2.9*	*-0.2*
11KR04-1	35.838220	-115.800382	77.16	66.39	0.68	0.52	-0.7	40.6	67.3	9.0	-56.09	0.6	23.8	1.4
11KR04-2	35.838220	-115.800382	*73.03*	*56.18*	*0.46*	*0.43*	*-9.4*	*26.8*	*84.8*	*-2.8*	*-2.84*	*0.4*	*-70.4*	*-4.2*
11KR04-3	35.838220	-115.800382	73.16	57.09	0.48	0.46	-4.8	64.8	65.8	10.4	-13.43	0.6	22.2	1.3
11KR06-1	35.832173	-115.815586	103.26	62.16	0.80	0.57	35.9	6.2	22.4	37.5	0.17	4.7	40.9	2.5
11KR06-2	35.832173	-115.815586	103.84	69.60	1.01	0.58	28.8	52.8	20.1	41.1	1.83	2.2	17.2	1.0
11KR06-3	35.832173	-115.815586	126.54	67.44	1.16	0.59	27.3	39.3	63.3	36.6	1.44	1.8	15.1	0.9
11KR07-1	35.828291	-115.817839	113.62	86.44	1.71	0.65	17.7	13.9	35.5	21.1	0.78	1.9	26.0	1.6
11KR07-2	35.828291	-115.817839	107.15	86.07	1.60	0.65	35.7	10.4	81.3	38.5	0.29	2.0	14.9	0.9
11KR07-3	35.828291	-115.817839	126.55	75.18	1.44	0.62	20.0	27.7	93.9	26.8	1.38	2.0	22.3	1.3

Sample	Latitude	Longitude	L (μm)	W (μm)	Mass (μg)	Ft*	U (ppm)	Th (ppm)	Sm (ppm)	[U]e	Th/U	He (nmol/g)	Corrected Age (Ma)	Error (Ma)
11KR10-1	35.821891	-115.836374	166.17	74.03	1.83	0.65	15.2	3.0	67.3	16.2	0.20	1.1	18.8	1.1
11KR10-2	35.821891	-115.836374	167.68	87.51	2.59	0.69	17.2	4.5	47.7	18.4	0.26	1.1	15.5	0.9
11KR10-3	35.821891	-115.836374	149.85	111.01	3.72	0.72	6.3	5.8	32.0	7.8	0.92	0.8	24.4	1.5
11KR12-1	35.792522	-115.853065	162.21	67.69	1.50	0.61	27.9	15.7	79.0	31.9	0.56	1.4	13.1	0.8
11KR12-2	35.792522	-115.853065	108.85	70.43	1.09	0.61	37.7	3.0	90.9	38.8	0.08	3.2	24.4	1.5
11KR12-3	35.792522	-115.853065	98.48	59.54	0.70	0.55	10.5	3.7	84.1	11.8	0.36	0.6	18.2	1.1
Kingston Range zircon														
z11KR03-1	35.843042	-115.794954	153.82	72.05	3.71	0.74	315.6	105.7	6.7	339.9	0.33	160.3	117.6	9.4
z11KR03-2	35.843042	-115.794954	133.90	76.64	3.66	0.73	43.5	76.5	2.8	61.1	1.76	46.2	188.0	15.0
z11KR03-3	35.843042	-115.794954	128.35	68.05	2.76	0.71	118.6	70.7	2.4	134.9	0.60	110.6	209.9	16.8
z11KR05-1	35.834912	-115.807392	187.52	78.49	5.37	0.76	122.7	101.0	2.6	145.9	0.82	83.4	138.4	11.1
z11KR05-2	35.834912	-115.807392	220.04	112.73	13.00	0.82	101.9	88.2	5.1	122.2	0.87	59.1	108.2	8.7
z11KR05-3	35.834912	-115.807392	261.54	98.18	11.72	0.80	70.5	80.7	1.6	89.1	1.14	48.2	123.3	9.9
z11KR06-1	35.832173	-115.815586	212.93	101.38	10.18	0.80	281.6	330.9	6.6	357.8	1.17	132.8	84.9	6.8
z11KR06-2	35.832173	-115.815586	234.90	73.50	5.90	0.75	418.2	716.3	21.6	583.2	1.71	235.4	98.9	7.9
z11KR06-3	35.832173	-115.815586	218.36	100.64	10.28	0.80	104.1	257.8	3.6	163.5	2.48	72.4	101.3	8.1
z11KR07-1	35.828291	-115.817839	214.91	93.88	8.81	0.79	13.4	24.4	8.6	19.1	1.81	18.6	224.0	17.9
z11KR07-2	35.828291	-115.817839	194.91	103.10	9.63	0.80	67.6	81.8	41.0	86.7	1.21	34.9	92.0	7.4
z11KR07-3	35.828291	-115.817839	202.19	103.66	10.10	0.80	32.2	34.6	4.7	40.2	1.07	18.8	106.6	8.5
z11KR08-1	35.825810	-115.826853	131.45	77.38	3.66	0.74	140.4	116.9	2.4	167.3	0.83	69.5	103.5	8.3
z11KR08-2	35.825810	-115.826853	156.86	74.10	4.01	0.74	292.1	200.9	3.5	338.3	0.69	107.0	78.8	6.3
z11KR08-3	35.825810	-115.826853	187.66	80.65	5.68	0.77	520.0	95.0	3.9	541.8	0.18	181.7	80.5	6.4
z11KR09-1	35.819851	-115.845348	170.35	86.96	5.99	0.78	308.2	75.9	2.7	325.7	0.25	92.8	67.7	5.4
z11KR09-2	35.819851	-115.845348	170.96	91.74	6.69	0.79	336.2	67.4	0.8	351.7	0.20	104.2	69.6	5.6
z11KR09-3	35.819851	-115.845348	182.47	69.26	4.07	0.74	458.6	153.7	3.9	494.0	0.34	108.8	55.2	4.4
z11KR10-1	35.821891	-115.836374	182.42	67.98	3.92	0.74	484.8	77.1	1.5	502.6	0.16	122.9	61.4	4.9
z11KR10-2	35.821891	-115.836374	183.91	69.09	4.08	0.74	507.6	147.9	6.7	541.7	0.29	238.7	110.0	8.8
z11KR10-3	35.821891	-115.836374	201.32	70.54	4.66	0.75	532.0	105.7	4.2	556.3	0.20	122.7	54.6	4.4

Sample	Latitude	Longitude	L (μm)	W (μm)	Mass (μg)	Ft*	U (ppm)	Th (ppm)	Sm (ppm)	[U]e	Th/U	He (nmol/g)	Corrected Age (Ma)	Error (Ma)
z11KR11-1	35.812645	-115.849267	145.06	79.80	4.29	0.75	363.1	84.4	3.6	382.6	0.23	101.0	64.6	5.2
z11KR11-2	35.812645	-115.849267	173.45	86.05	5.97	0.77	348.8	196.5	3.1	394.0	0.56	96.9	58.7	4.7
z11KR11-3	35.812645	-115.849267	202.88	73.67	5.12	0.75	224.2	98.8	4.1	247.0	0.44	85.2	84.6	6.8
z11KR12-1	35.792522	-115.853065	197.07	98.52	8.89	0.80	83.7	41.1	0.5	93.1	0.49	43.8	108.2	8.7
z11KR12-2	35.792522	-115.853065	202.45	131.72	16.33	0.84	168.2	65.8	2.1	183.4	0.39	94.3	112.6	9.0
z11KR12-3	35.792522	-115.853065	172.22	80.74	5.22	0.77	460.8	56.4	2.9	473.8	0.12	133.6	67.9	5.4
Kingston Pluton apatite														
12KP13-1	35.752146	-116.003527	150.01	74.72	1.69	0.62	16.6	62.5	82.9	31.4	3.77	0.9	8.8	0.5
12KP13-2	35.752146	-116.003527	172.43	51.54	0.92	0.52	13.7	21.1	100.8	19.0	1.54	0.3	6.0	0.4
12KP13-3	35.752146	-116.003527	217.56	59.62	1.56	0.57	7.4	22.7	64.6	13.0	3.05	0.3	6.1	0.4
12KP14-1	35.753170	-116.010617	201.61	69.90	1.98	0.61	13.0	63.9	57.0	27.9	4.93	0.9	9.4	0.6
12KP14-2	35.753170	-116.010617	148.07	62.73	1.17	0.56	15.8	68.6	68.6	32.0	4.33	0.8	8.1	0.5
12KP14-3	35.753170	-116.010617	166.49	65.40	1.43	0.58	8.2	47.0	56.9	19.3	5.71	0.6	10.4	0.6

Notes: Analytical procedures and errors follow descriptions in chapters 2-5; analyses in italics are erroneous.
*Ft is the alpha ejection correction of Farley et al. (1996).